# Porosity and permeability development in evolving fragmental volcanic systems

Thesis submitted in accordance with the requirements of the University of Liverpool for the degree of Doctor in Philosophy
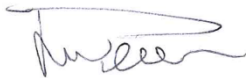
by

## Joshua Stephen Weaver

30/03/2022

# Declaration of authorship

I, Joshua Weaver, declare that this thesis entitled "Porosity and permeability development in evolving fragmental volcanic systems" and the work presented in it are my own. I confirm that:

- This thesis was completed as part of a research degree at the University of Liverpool;
- The material contained in this thesis has not been presented, nor is currently being presented, either wholly or in parts, for any other degree or qualifications;
- Where I have consulted published studies, this has always been clearly referenced;
- Where the work was part of a collaborative effort, I have made clear what others have done and what I have contributed myself;
- Parts of this thesis have been submitted for publication or have been published as:
  - Weaver, J., Eggertsson, G.H., Utley, J.E., Wallace, P.A., Lamur, A., Kendrick, J.E., Tuffen, H., Markússon, S.H. and Lavallée, Y., 2020. Thermal liability of hyaloclastite in the Krafla geothermal reservoir, Iceland: the impact of phyllosilicates on permeability and rock strength. *Geofluids*.
  - Weaver, J., Lavallée, Y., Ashraf, M., Kendrick, J.E., Lamur, A., Schauroth, J., and Wadsworth, F.B., in review. Vesiculation and densification of pyroclasts: a clast-size dependent competition between bubble growth and diffusive outgassing. *Journal of Volcanology and Geothermal Research*.

Signed:

Joshua Weaver

30/03/2022

# Abstract

The capacity for fluid percolation in volcanic environments may be considered a double-edged sword. On the one hand, high permeabilities offer both a pressure release valve to mitigate the explosive potential of a magma, and access to valuable clean energy in geothermal reservoirs. Conversely, low permeabilities are associated with dangerous, highly pressurised magma which have a propensity to violently erupt. In geothermal systems, impervious rocks may prohibit resource utilisation, or provide the necessary cap rock to seal-in and maintain the desired high temperature fluids. In both active volcanic environments and hydrothermal systems, fluid flow is heavily concentrated through fracture networks and fragmental systems, such that they play a central role in determining the style of volcanism and the potential for geothermal energy production.

In this thesis, I investigate how the evolution of several fragmental systems may impact their porosity and permeability development. Specifically, I analyse how dehydration affects juvenile fragmental melts which remain in viscous environments and how altered fragmental deposits respond to thermal stress.

Before exploring the evolution of the aggregate fragmental systems, I first assess individual melt fragments which are dehydrating in an open system, such that volatiles may escape the melt into vesicles, via vesiculation, or into the surrounding atmosphere, via diffusion out of the sample. Where volatiles move into vesicles, the isolated bubble growth expands the fragment volume, whereas volatiles released from the fragment do not directly impart a geometry change. I demonstrate that in pyroclasts, vesiculation will strive towards equilibrium with the closed system conditions, and so it is a fragment-size independent process; volatiles continually diffuse into vesicles until the water content of the melt drops to the melt solubility limit, such that the closed-system vesicularity of fragments can be assessed using bubble growth models. On the other hand, diffusive outgassing equilibrates the melt with the conditions of the open, surrounding gas, and so the effectiveness of diffusive volatile loss is determined by the surface area of the melt-atmosphere interface. I observe that dehydration caused by diffusive outgassing progressively impacts deeper into the fragment, where it causes exsolved volatiles to resorb and the vesicles to shrink and be lost. Accordingly, a dense and dehydrated rind forms at the sample margin, which thickens with the lengthscale of diffusion. I show that where vesiculation and diffusive outgassing occur in a melt fragment concomitantly, the processes compete to expand and densify the fragment. Because the rate

of diffusive outgassing is determined by the melt surface area, the size of pyroclasts controls this competition, such that, as fragment size decreases, the vesicularity moves increasingly away from the closed-system bubble growth models. I find that smaller fragments attain lower vesicularity profiles than larger fragments, and that over time, fragments of all sizes will densify and eventually lose all vesicularity. In fragmental aggregate systems, this evolution in individual melt fragments is likely inversed in the volume of the inter-fragment pore space, leading to implications for the porosity and permeability of the system.

I monitor the evolution of vesicularity, connected porosity, and permeability in open fragmental melts with various grain sizes, to assess how the concurrent processes of vesiculation, diffusive outgassing, and sintering interact. I find that as melt vesiculates, the expansion of fragments causes a commensurate loss in the inter-fragment pore space, which causes a reduction in permeability. However, this process is transient whilst the system remains open to the atmosphere, as diffusive outgassing causes fragment contraction, which reverses the porosity and permeability impact of vesiculation. Overprinting these processes, sintering continues to densify the melt and will ultimately close the permeable network. From the complex fragment size controls for these processes, I establish regimes which determine the general evolution of porosity and permeability during sintering of hydrous melts.

Finally, I assess the impact of dehydration in hydrothermally altered volcaniclastic reservoir rocks. I explore the thermal stability of hydrous minerals in hyaloclastites and investigate how the dehydration and dissolution of matrix constituents influences the porosity, permeability, and mechanical behaviour of the bulk rock. I find that at relatively low temperatures, which are applicable for geothermal resources, smectite dehydrates, causing the mineral lattices to densify and ultimately, collapse. This dissolution creates pore volume, which is increasingly connected, such that thermal stress increases permeability without necessitating the formation of fractures. The increase in porosity reduces the compressive and tensile strength of the hyaloclastites. I show that rocks containing phyllosilicate minerals may be susceptible to thermal fluctuations, and that this enhances porosity and permeability and reduces strength, which may then facilitate mechanical compaction at lower stresses, with significant implications for geothermal reservoir rocks and magmatic host rocks.

Through these studies I highlight that dehydration in fragmental volcanic systems can produce complex porosity and permeability evolution. If these systems are to be well understood, a careful assessment of their compositions (particle size distributions and mineralogies) is

required and their thermal, chemical, and physical environmental conditions should be well constrained.

# Contents

# List of figures

# List of tables

# Acknowledgements

If I have seen anything at all, it is by standing on the shoulders of friends and colleagues. Each fragment of this thesis is the outcome of our collaborations, and many brilliant scientists have left their fingerprints, one way or another, on every word. I could not be more grateful, and here, I offer my effusive thanks.

First and foremost, I must acknowledge the unending support and guidance offered by my supervisory team. Yan, I have learned a great deal from you over the last few years, and I could always count on you as a source of motivation. I have thoroughly enjoyed our discussions (or are they ramblings?), and your often manic excitement for science. No matter how tangled my word spaghetti, you could somehow drill straight to the point, and show me what I was trying to say, only with fewer s's than normal. Jackie, thank you for constant help and advice - in addition to all the scientific insights you shared, your world class ability to to spot spellling and formattings mistakes has improved every piece of my work. Whenever I was struggling, your rapid and detailed emails always helped alleviate the pressure. And finally, the OG matlab guru, Anthony, thank you for patiently answering my endless and daily questions. Your expertise helped me to avoid countless failures and, whenever I was buried under work or feeling tense, you could always offer a volatile night out. I could not have asked for more relaxed supervisors, and I hope we have more opportunities to work together in the future.

In addition, this work could not have advanced without the help of Fabian and Hugh. Their distance from Liverpool did nothing to mitigate the regular help they provided, and, when visiting the lab, my vague ideas could always coalesce and solidify around the wisdom they offered.

Otherwise, many brilliant people have made my time during the PhD enjoyable and rememberable. Any day spent with Amy was filled with strangeness. You could be relied on whenever I was stressed and needed to vent, or if I was looking for a shared collapse into insanity. Jenny, you could always brighten my day foamy twin, and I hope you keep climbing to new heights. Guðjón, thanks for acting as my Icelandic liaison. Your hands-on experience was second to none and the advice you offered could always alter my point of view. Paul, the big man with the teeny tiny graphs, thanks for all the chemistry help, and the laughs that came with it. And, thanks to my long distant PhD brethren, Alastair and Gregor, for being a pair of rheomorphic melts.

Finally, special thanks are owed to Maliha, who intruded violently into my life midway through this project, and quickly showed me that a thick skin can hide a bubbly nature. It is easy to detect which parts of this thesis you contributed towards, and I always feel more intelligent after listening to you talk.

# Chapter 1: Introduction

## 1.1. Background: volcanoes as fragmental systems

Highly evolved volcanic systems - their structure and the activity they exhibit – are, arguably, fragmental. Where magma quickly journeys to the surface of the Earth, stresses may build until the magma breaks into fragments, which if erupted, produce some of the most spectacular volcanic phenomena. Or, where magma is erupted intact, it may subsequently brecciate due to cooling and flow. If magma stalls in the crust, localised fracture and fragmentation may occur, as exhibited by columnar jointing and clastic veins. Ultimately, these effusive and intrusive fragmental products construct volcanic edifices which determine the efficacy of geothermal systems; hence, many volcanic systems may be considered fragmental in nature, and it is the evolution of these systems which controls pressure release or accrual in conduits.

Perhaps of the utmost importance, is how fluids interact with, and transfer through these fragmental environments. In volcanic systems, it is well understood that the efficiency of gas through-flow underpins its explosive potential (e.g., Degruyter et al., 2012; Edmonds et al., 2003). As magma rises through the conduit and depressurises, volatiles exsolve into a buoyant vapour phase which may pressurise inside bubbles (Melnik et al., 2005). Where magma and wall rocks are sufficiently permeable, exsolved volatiles are continuously and quiescently released through fumaroles and venting (Kendrick et al., 2016; Okumura and Sasaki, 2014; Stasiuk et al., 1996), thereby limiting gas pressurisation (Edmonds et al., 2003). However, should a system possess suitably low permeability, the entrapment of volatiles adds to the magmatic overpressure until the tensile strength of magma is exceeded and the pressure is violently released in an explosive eruption (Figure 1-1; Dingwell, 1996; Klug and Cashman, 1996). Monitoring of volcanic vents (e.g., Johnson et al., 2008), textural analysis of products (e.g., Heap et al., 2019; Saubin et al., 2016), and modelling (e.g., Farquharson et al., 2017) all suggest that outgassing is predominantly concentrated in fragment-bearing fracture networks, as are identified in lava domes (Wadge et al., 2009), volcanic plugs, and backfilled conduits (Kolzenburg and Russell, 2014). As such, the permeability of these fracture systems is a key parameter used in the modelling of volcanic systems (Kolzenburg et al., 2019).
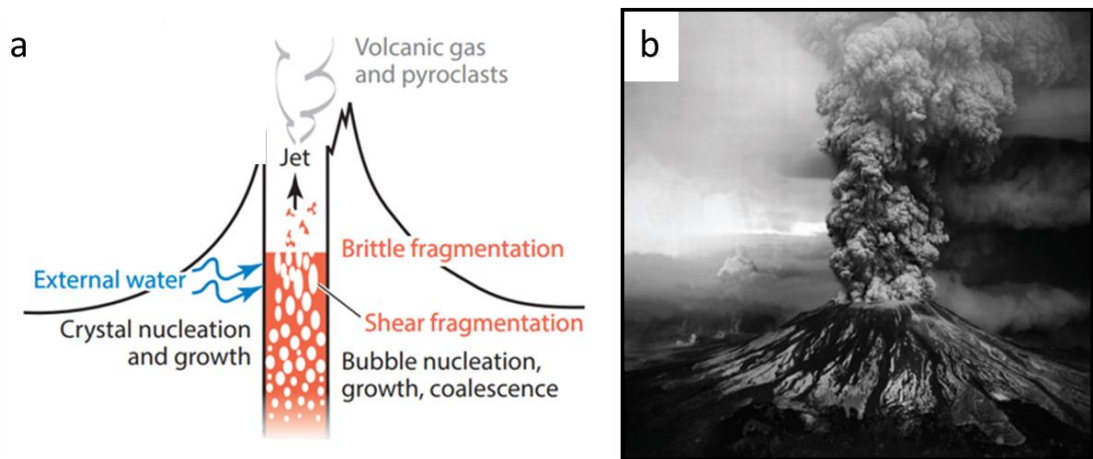
*Figure 1-1: The fragmentation of magma is largely dependent upon the evolution of porosity and its effects on gas pressure. a) sketch of a volcanic conduit, illustrating how the exsolution of volatiles disrupts magma; b) eruption plume from the Mount St Helens 1980 eruption. Ash is produced from the fragmentation of the previously connected magma, which is lofted by the release of volcanic gases. (both images modified from Gonnermann, 2015).*

Alternatively, fragmental products may scatter over wide areas via transport through air, on land, or underwater, and are preserved as volcaniclastic rocks, such as ignimbrites, tuffs, and hyaloclastites (Fisher, 1961; White and Houghton, 2006); they may also be formed in lava flows, which can brecciate during transport (Fisher, 1960) or fracture during cooling (Lamur et al., 2018). In these depositional environments, volcaniclastic lithologies may exhibit substantial fluid storage capacities and as such, are often host to aquifers and hydrothermal reservoirs (Eggertsson et al., 2018), which are used for potable water extraction (Kim et al., 2013), energy production from geothermal reservoirs (e.g., Zakharova and Spichak, 2012), and the long-term fixation of greenhouse gases (Matter et al., 2011). Alongside their potentially high temperatures in active magmatic provinces, the value of these fragmental systems is largely determined by their porosity and permeability, which constrains the rates of fluid extraction, reinjection, and natural recharge (Aqui and Zarrouk, 2011; Gunnarsson, 2011; Rman et al., 2016). The porosity and permeability of these fragmental systems are dependent on the post-depositional processes of lithification, i.e., compaction of the porous network (Eggertsson et al., 2020) and diagenesis, i.e., mineral alteration (Thien et al., 2015) and precipitation (Griffiths et al., 2016). These processes have been well-studied in isolation, but attention is now progressing towards a holistic, integrated view of mineralogical and physical changes in reservoir rock (e.g., Heap et al., 2017).

Evidently, the controls and processes underpinning the generation and subsequent evolution of hot pyroclasts are distinct from those controlling the evolution of cool, fragmental depositional environments. Below, I detail the lifecycles of these systems and describe the

typical developments and complexities of their physical attributes and their permeable porous networks.


## 1.2. Magma rheology and fragmentation

Rheology describes the deformation and flow behaviour of a material, including its propensity to rupture or fragment. The rheology of magma, which is a cornerstone of modern volcanology, is largely determined by the interactions between viscosity and the distribution of stress (Dingwell and Webb, 1989). The ability for magma to viscously dissipate stress is at the heart of the volcanic dilemma: to flow or blow (Dingwell, 1996)?


### 1.2.1. Magma viscosity

Dynamic viscosity is a measure of the resistance of a material to deformation. Determining the apparent viscosity of a multi-phase magma (i.e., liquid melt, exsolved gas bubbles, and solid crystals) is highly complex due to the multitude of variables (intrinsic and extrinsic), which impact shear (Alidibirov and Dingwell, 1996; Lavallée et al., 2008; Lavallée and Kendrick, 2021; Lejeune and Richet, 1995; Truby et al., 2015), and have thus far prevented the formulation of a robust universal rheological model (Kolzenburg et al., 2022; Lavallée and Kendrick, 2021; Mader et al., 2013). Single-phase silicate melts follow Maxwell's (1867) principles of visco-elasticity (Dingwell, 1998) and, if relaxed, exhibit Newtonian rheologies (Dingwell and Webb, 1990). At the fundamental level, the viscosity of a single phase magma is determined by its molecular configuration (i.e., structure), impacted by its chemical composition, as well as temperature, pressure and shear stress (Webb and Dingwell, 1990). The compositional contribution to viscosity is largely a function of silica diffusivity (Dingwell, 2006). Firstly, silica and oxygen form tetrahedral chains (or octahedral chains at great depth), which, as their length and complexity increase, reduce the molecular freedom of motion and inhibit melt flow (Mysen, 1990). Chains of tetrahedra (T) are modified by cations (e.g., Ca, Na, K) which link with non-bridging oxygen (NBO), thereby disrupting the molecular network (Dingwell, 2006). Silica-poor magmas, such as basaltic melts ($\lesssim$52 wt.% $SiO_2$), have a high NBO/T ratio, and thus build shorter order silicate tetrahedral chains and possess lower viscosities than silica-rich rhyolitic magmas ($\gtrsim$68 wt.% $SiO_2$; Figure 1-2a; Dalby and King, 2006; Shaw, 1972). Tetrahedral chains are further disrupted by volatile components (e.g., $H_2O$, $CO_2$, Fl), which essentially depolymerise the tetrahedral chains due to the replacement of bridging oxygens with non-bridging volatile elements (Dingwell and Mysen, 1985). Viscosity is highly

sensitive to volatile concentration, where a few weight percent change in the water content can drastically reduce the viscosity by several orders of magnitude (Figure 1-2b; Hess and Dingwell, 1996), and thus, the rheological impact of volatiles dissolved in melts somewhat overprints that of silica (e.g., Whittington et al., 2009). Importantly, the solubility of volatiles in a melt increases with silica content, such that a rhyolite can cover a greater hydration and hydration-induced viscosity range than a basalt (e.g., Newman and Lowenstern, 2002).
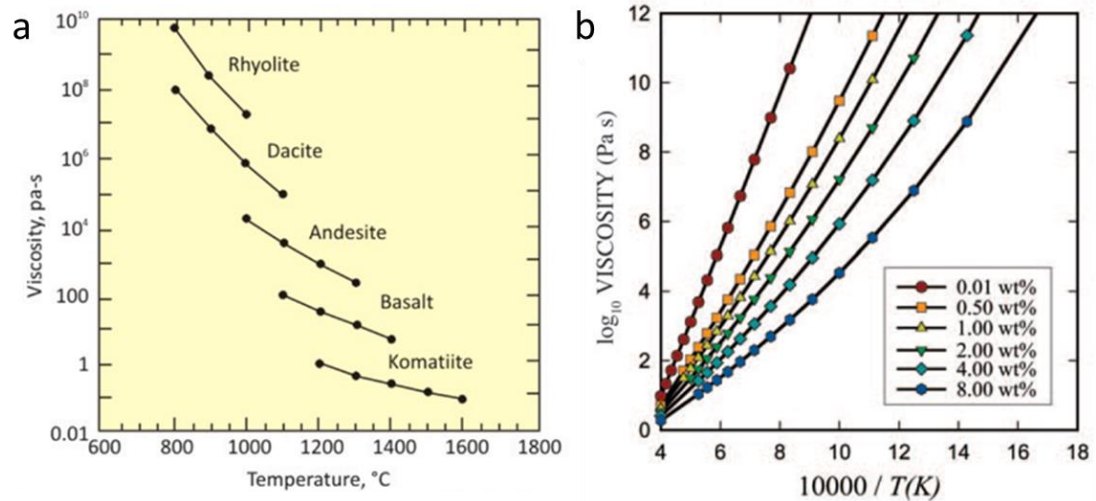


Figure 1-2: *Compositional and temperature controls on silicate melt viscosity. a) The chemical span of common magma promotes a wide range of viscosity, covering several orders of magnitude (modified from Spera, 2000); b) the non-Arrhenian relationship between viscosity and the reciprocal of temperature shows that the presence of dissolved $H_2O$ lowers viscosity drastically and increases the non-linearity of the relationship (modified from Dingwell, 2006).*

The bonds between silicate tetrahedra are said to be in a state of dynamic equilibrium, as they continuously break and reform (Dingwell and Webb, 1989). This propensity of the tetrahedral chains to rearrange their molecular structure is largely a function of the amount of energy in the system, which controls the ability of melt to flow viscously. The viscosity of silicate melts shares a non-Arrhenian relationship with temperature (Dingwell and Webb, 1989), which results from the non-linear increase in the ease of molecular bond exchange with temperature (Figure 1-2a). The temperature conditions experienced by silicate melts in nature typically ranges between 700 and 1300 °C, which equates to several orders of magnitude in viscosity (Giordano et al., 2008). In addition, the solubility of volatiles in silicate melts is also dictated by the magma storage conditions, such that temperature and pressure impart secondary controls on melt viscosity. The most abundant volatile component in shallow magma is water, which comes under two species: molecular ($H_2O$) and hydroxyl ($OH-$). The solubility of water in silicate melts shares a complex relationship with temperature (Figure 1-2b; Liu et al., 2005).

For a given pressure, the solubility of $H_2O$ reduces with increasing temperature, whilst the ratio of OH- to $H_2O$ speciation increases (Zhang, 1999a). At low pressures, water solubility is inversely proportional to temperature, but the opposite is true at high pressure (Figure 1-3; Liu et al., 2005); therefore, the viscosity - temperature relationship of even single phase magma is far more complex than suggested by Figures 1-2 and 1-3 alone, and intricate interplays exist between viscosity and temperature, pressure, melt composition and volatile solubility.
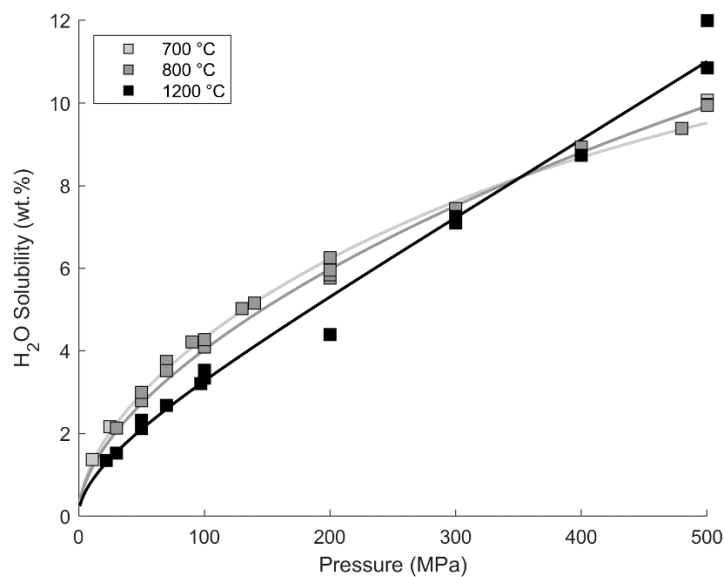


*Figure 1-3: The solubility of H₂O in rhyolitic melts (modified from Liu et al., 2005). The experimental data and modelled solubility curves (Liu et al., 2005) show a pressure dependence which varies as a function of temperature.*

Yet, in nature, magmas are commonly multi-phase, containing gaseous and solid phases, formed via volatile exsolution and crystallisation, respectively. Their presence impacts the rheology and, so too, the viscosity of a magma. Unlike single-phase silicate melts, multiphase magmas are generally non-Newtonian, exhibiting a shear-thinning response (e.g., Caricchi et al., 2007). The exsolution, resorption, and fluxing of volatiles, as well as the physical impacts of bubbles themselves, can impart a complex influence on melt viscosity (Kolzenburg et al., 2022; Mader et al., 2013). As magmas depressurise, they become supersaturated in volatiles, and the nucleation of bubbles alleviates the excess, thereby reducing the local concentration of dissolved volatiles towards the solubility limit (e.g., Figure 1-3; Blower et al., 2001) and increasing the residual melt viscosity (Lensky et al., 2001). Magma can also contain bubbles which have decoupled from deeper melt and have risen as an independent buoyant phase

(e.g., Bachmann and Bergantz, 2006); a melt can therefore co-exist with a distinct gas phase without the melt exceeding the solubility limit.

The impact of bubbles on magma viscosity is not straightforward. Large bubbles have high capillary numbers (i.e., viscous forces vs surface tension forces) and are prone to shear deformation, which may promote an apparent reduction in the viscosity of a bubbly magma as they deform (Llewellin et al., 2002; Manga et al., 1998; Rust and Manga, 2002). On the other hand, small bubbles with low capillary numbers act as non-deformable bodies, like solids, and their accumulation in a magma may promote a viscosity increase (e.g., Manga et al., 1998). The suspension of relatively non-deformable bodies in the melt, such as small bubbles and crystals, can supersede the rheological impacts of chemical composition (e.g., Cordonnier et al., 2009; Lejeune and Richet, 1995) or temperature (Lavallée et al., 2007) on magma viscosity. However, in contrast to the widely held view, crystal-bearing magmas do not exhibit a yield strength and so comprehensive rheological models for magma have moved away from Bingham rheologies (Lavallée et al., 2007). Accordingly, the viscosity of a multiphase magma is determined by the complex interactions between its chemical and physical components, and by the extrinsic conditions of the systems.

### 1.2.2. Magma fragmentation

Silicate melts are viscoelastic bodies; as such, they can behave as liquids or solids, depending on how effectively a melt relaxes an applied stress. Deformation may proceed via either viscous flow or elastic strain, which may further result in brittle rupture or fragmentation at high stresses. This stress relaxation is controlled by the rate at which the melt's molecular bonds change in response to stress, termed 'structural relaxation rate'. The structural relaxation rate is determined by the viscosity of the melt, thus the behaviour of melts under deformation conditions depends on the timescale of deformation [or in other words, how fast they are deformed (Reiner, 1964)]. When the deformation rate imposed by a given applied stress is slower than the relaxation rate, the stress can be relaxed and the melt flows viscously like a liquid (Dingwell and Webb, 1990). However, if the strain rate imparted by a given stress exceeds the structural relaxation rate, the melt may not relax the stress; in such cases, the stress builds up and the melt behaves as a solid (like a glass). If the stress build-up exceeds the strength of this melt in a glassy state, then it may rupture. The divide between the solid and liquid state is known as the glass transition (Figure 1-4); a melt may be forced from a liquid to an elastic behaviour by increasing the deformation rate or by cooling it (Van Otterloo et al.,

2015). Fibre elongation experiments have shown that across the glass transition interval, a melt exhibits a non-Newtonian rheology, showing a reduction in viscosity with strain rate due to progressive breakdown of the melt structure (Webb and Dingwell, 1990).
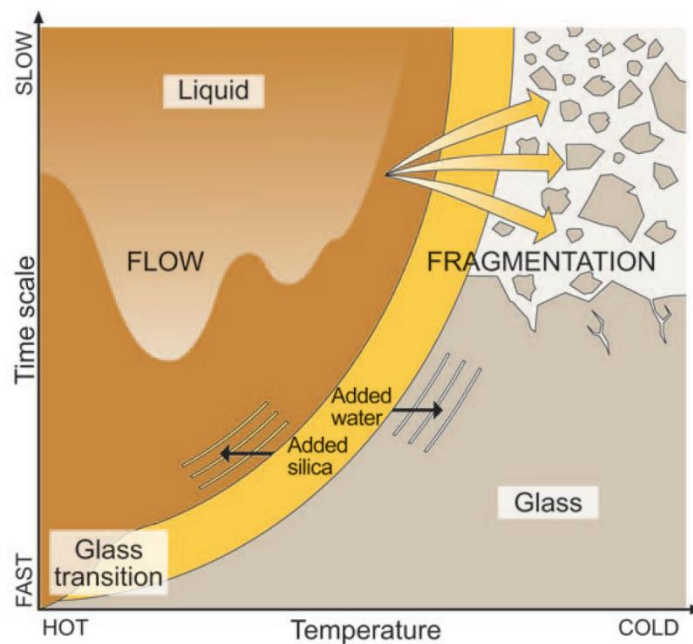


*Figure 1-4: The glass transition, shown using the reciprocal temperature and strain rate (modified from Dingwell, 2006). A melt crossing the glass transition, either through a temperature reduction or an increased strain rate, experiences brittle fragmentation and generates clastic material.*

In high viscosity magma, rupture arises from the nucleation, propagation, and coalescence of micro-cracks, primarily tensile, which form and grow as strain rate exceeds the structural relaxation rate of magma (e.g., Lavallée et al., 2013). In natural settings, a melt may be forced across the glass transition due to either rapid cooling (e.g., during subaqueous and subglacial volcanism) or high strain rates relative to the structural relaxation rate, which may be achieved due to rapid shear, or rapid gas expansion associated with decompression (e.g., if the overburden is removed, such as during sector collapse), or may result from changes to the viscosity (e.g., following crystallisation). During magma transport, strain is generally localised near conduit margins, which can result in magma rupture (Lavallée et al., 2013), and can generate characteristic seismicity (Neuberg et al., 2006). This localised magma failure is responsible for the formation of volcanic fault zones and breccias (e.g., Tuffen et al., 2003). Moreover, in highly vesicular magma, rupture may ensue due to gas overpressure in bubbles – a process commonly termed magmatic fragmentation – and the pressure conditions necessary to rupture such vesicular magma is termed the fragmentation threshold (e.g., Spieler et al., 2004). In this case, there are two important contributing factors: first, volatile

exsolution dehydrates the melt, which rheologically stiffens around bubbles (Lensky et al., 2001; Prousevitch et al., 1993), and second, rapid bubble expansion stretches the dehydrated melt around bubbles, encouraging brittle failure, as strain is localised in the bubble walls (Zhang, 1999b). In all instances, the brittle failure of magma produces fragments of all sizes (e.g., Kennedy and Russell, 2012; Kolzenburg et al., 2013; Kueppers et al., 2006b; Maria and Carey, 2002; Taddeucci et al., 2021), termed pyroclasts, which may evolve physically and chemically in very different manners in intrusive or extrusive environments.

### 1.2.3. Stress relaxation in pyroclasts

Following magma fragmentation and the dissipation of stress via surface area creation, pyroclasts may return to a liquid state, unless a high stress and strain rate persist or they quench (Figure 1-4; e.g., Dingwell and Webb, 1989). In such cases, the fragments will relax stress by viscous deformation and so, brittle failure may be followed by fragment agglutination or fracture healing (e.g., Lamur et al., 2019; Taddeucci et al., 2021; Wadsworth et al., 2016a). Accordingly, the textural evidence of brittle failure in magma may be readily overprinted by viscous processes (Gardner et al., 2019; Tuffen et al., 2003).

Melt surface area is progressively diminished and lost during viscous flow and surface healing within fragmental systems, in order to minimise the Gibb's free energy (Frenkel, 1946). In such systems, surface tension smooths melt surfaces (i.e., melt fragments and bubbles are driven towards a spherical geometry) whilst the re-establishment of contact between melt surfaces encourages healing (e.g., Lamur et al., 2019; Tuffen et al., 2003; Yoshimura and Nakamura, 2010). Healing proceeds first through the wetting of the fracture interface and then by diffusive exchange; a process which can obscure the evidence of pre-existing fractures, although bubble traces are often preserved in the process (Cabrera et al., 2011; Lamur et al., 2019). The rate of healing is predominantly controlled by the relaxation timescale of the melt, which, in turn is largely a function of the melt viscosity (Yoshimura and Nakamura, 2010). Similarly, in irregular fragmental systems, pyroclasts may viscously sinter; melt point contacts begin to heal, leading to the formation of melt 'necks', which extend due to surface tension forces and viscous flow (Frenkel, 1946), and encourage the progressive agglutination (commonly termed welding in pressurised systems or sintering in unpressurised systems) of fragmental products, across the spectrum of melt compositions from basaltic (e.g., Jones et al., 2022) to rhyolitic (Branney et al., 2002; Gardner et al., 2018; Sparks and Wright, 1979; Vasseur et al., 2013a; Wadsworth et al., 2014; Wolff and Wright, 1981). So, in combination,

the relaxation of melt, along with viscous sintering and/ or fracture healing, can erase any trace of fragmentation and may prompt a transition from a fragmental to a coherent magma body. In their lifetimes, magmas may experience multiple episodes of fragmentation and subsequent healing (Cabrera et al., 2011; Tuffen et al., 2003).

## 1.3. Porosity evolution in fragmental systems

Fragmental magmatic systems may experience different processes, largely dependent on their environment and rheology, which impact their porosity. Broadly, where hot fragmental products are deposited in a viscous regime (e.g., in conduits or in rheomorphic flows), fracture healing (e.g., Lamur et al., 2019; Tuffen et al., 2003) and sintering (e.g., Vasseur et al., 2013b) may reduce porosity as the system gains coherence. Conversely, in cold environments, fragments undergo clastic deposition (e.g., Manville et al., 2009), alteration (e.g., Denton et al., 2009), and mechanical compaction (e.g., Eggertsson et al., 2020), which impact their porosity, and hence their fluid storage capacity.

### 1.3.1. Magmatic environments

The most remarkable feature of post-fragmentation viscous systems is their transient nature, as evidenced by the progressive porosity loss in natural materials (Gardner et al., 2018; Heap et al., 2015a; Okumura and Sasaki, 2014), analogue materials (Vasseur et al., 2013b; Wadsworth et al., 2016a), and through the modelling of viscous systems (e.g., Kolzenburg et al., 2019).

In the most-simple failure geometry, a planar fracture devoid of fragments will close if the confining pressure is greater than the pore pressure, and the fracture interface will then proceed to heal (Lamur et al., 2019). However, observations of gas-and-ash explosions released through fractures, indicate that fragmentation, and the subsequent deposition or transport of pyroclasts, is strongly linked to fracture networks (e.g., Angelis et al., 2016). Indeed, preserved fractures in and around volcanic conduits commonly host an assortment of pyroclasts, crystals, and xenoliths (Saubin et al., 2016), which inhibit contact between the fracture walls (Figure 1-5). The presence of solid particles enforces a markedly different evolution to 'clean' fractures, as particles may act as proppants, keeping a fracture open until viscous flow allows the fracture walls to close around these solid particles (e.g., Sakai and Shimizu, 2001). In contrast, where infill is more substantial (such as in tuffisites; Figure 1-5),

the porosity evolution can be predominately controlled by interactions between the infilling fragments (e.g., Farquharson et al., 2017).
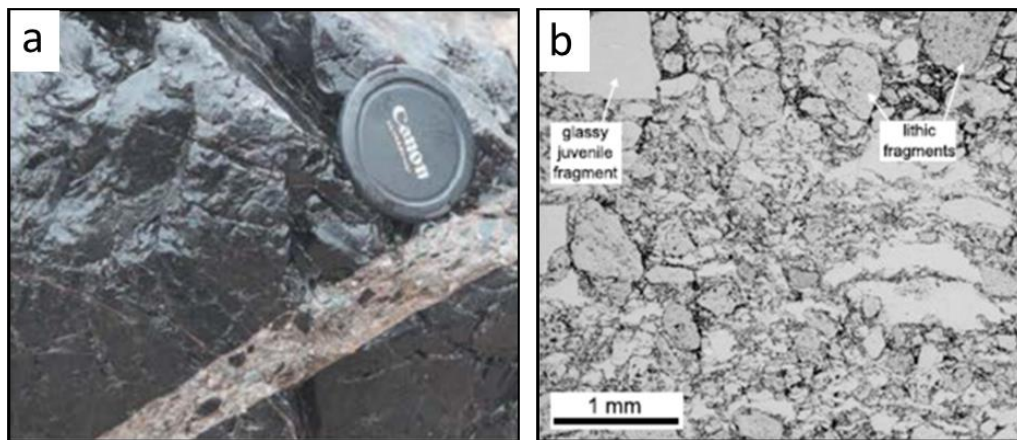


*Figure 1-5: Fragmental infill from a preserved tuffisite vein from Chaiten volcano, Chile (modified from Heap et al., 2019). a) photograph shows a fracture in obsidian, which is held open by polydisperse, welded infill; b) photomicrograph of the same sample highlights the variable nature of the infill and inter-fragment pore space.*

The porosity transience of viscous 'pack' infill is driven by sintering (i.e., classically termed welding in volcanology), which acts to transform a loose fragmental particulate into a cohesive porous body through viscous flow (Figure 1-6a; Gardner et al., 2018; Vasseur et al., 2013b; Wadsworth et al., 2014). Sintering initiates with the formation of particle necks, which then grow as melt flows towards the particle contacts (Frenkel, 1946). As sintering progresses, the density of the bulk infill increases and the fragmental surface area and the connectivity of the intervening pore space decreases until a few isolated bubbles remain (Figure 1-6; Vasseur et al., 2013a; Wadsworth et al., 2016a). Recently contributions have constrained how sintering behaves with fragment polydispersity (Wadsworth et al., 2017a), non-isothermal temperature profiles (Wadsworth et al., 2014), variable crystal content (Colombier et al., 2018), and under confined conditions (Farquharson et al., 2017). The studies have analysed the relative importance of surface tension and compressional forces, whose ratio is dependent on the environment (i.e., depth). This has led to the development of two sintering timescales which define the period of porosity loss from densifying, sintering systems; the surface tension-dominated sintering timescale, $\tau_s = a\mu/\Gamma$ (e.g., Wadsworth et al., 2016a) and the compaction-dominated sintering timescale (Farquharson et al., 2017) $\tau_{s2} = \mu/\sigma\alpha$, where $a$ is the pore radius, $\mu$ is the viscosity of the melt, $\Gamma$ is the melt-vapour surface tension, $\sigma$ is the applied stress, and $\alpha$ is an empirical factor (Quane et al., 2009). These timescales have been applied to tuffisite veins in order to estimate the duration of active outgassing in volcanic

systems with some success [but with a vast range of input values which provide sintering times extending over several orders of magnitude (Heap et al., 2019; Wadsworth et al., 2020a)].
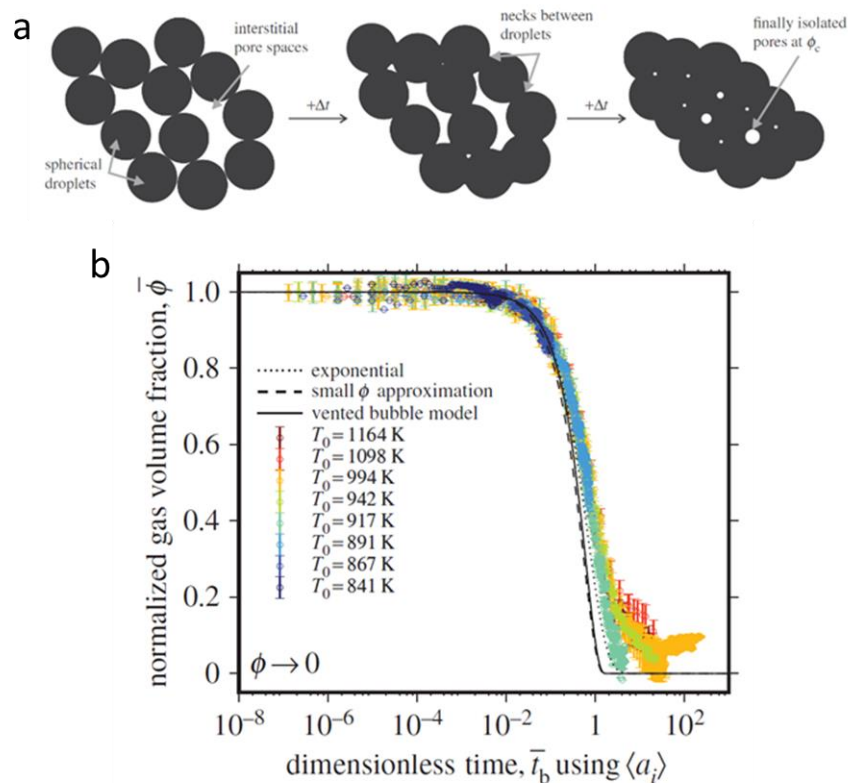


*Figure 1-6: a) Sketches showing how surface tension driven sintering promotes particle neck formation and the isolation of porosity. b) Porosity reduction during sintering; here, the pore volume is normalised to the initial pore volume and the time is normalised to the sintering timescale (modified from Wadsworth et al. (2016a).*

Other studies concede that volcanic outgassing networks can remain active for significantly longer than modelled sintering timescales (e.g., Kolzenburg et al., 2019, and citations therein), which suggests that the current models may be insufficient for constraining the full behaviour of natural fragmental melt systems. In particular, more work is needed to account for the common hydrous nature of volcanic melt fragments, and the impact that volatile redistribution and equilibration may have on the evolution of porous, fragmental systems. For example, where fragments are supersaturated in volatiles, they are liable to exsolve, promoting magma vesiculation. During bubble nucleation and growth, a melt expands (Figure 1-7; e.g., Coumans et al., 2020; Ryan et al., 2015a; von Aulock et al., 2017); thus in a fragmental melt system, vesiculation may encourage a reduction in the inter-fragment pore space in order to accommodate the volume generated by volatile exsolution. Conversely, where conditions remain open and a partial pressure difference exists between the melt fragments and the ambient volatiles in the connected pore space, the diffusive outgassing of volatiles

along fragment margins causes local depletion and subsequently prompts the resorption of volatiles from bubbles present near the edge of fragments. Continued diffusive outgassing leads to the formation of a dense rind which coincides with a volumetric contraction of the fragment (Figure 1-7; von Aulock et al., 2017). This expansive-vesiculation and contractive-outgassing of melt fragments, and their subsequent impacts on inter-granular pore space would influence the development of sintering (Vasseur et al., 2013a), melt fragment indentation and fracture closure (Lamur et al., 2017; Sakai and Shimizu, 2001), and melt contact healing (Lamur et al., 2019; Yoshimura and Nakamura, 2010) in ways which remain untested. As such, the impact of volatiles on the development of porosity-permeability evolution in fragmental melt systems deserves attention.
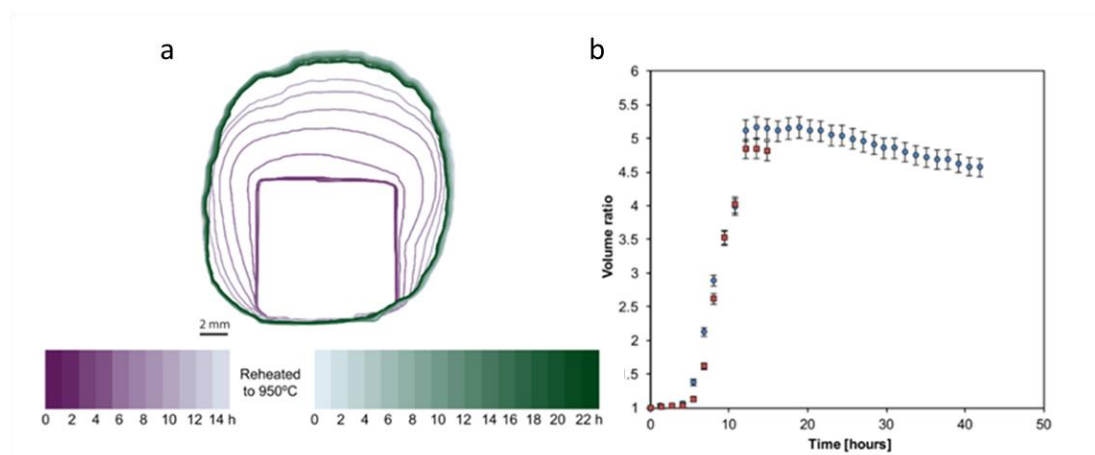


*Figure 1-7: Expansion of a melt fragment during vesiculation, followed by contraction induced through volatile degassing (modified from von Aulock et al., 2017). a) Evolution of the silhouette of an initially cylindrical melt fragment during two periods of dwell at 950 ˚C (purple and green lines). b) Estimation of the fragment volume using the solid of revolution method shows volumetric expansion, followed by a slower contraction for a given sample.*

### 1.3.2. Volcaniclastic deposits

The emplacement of volcaniclastics covers a wide range of lithology types (Fisher, 1961), including primary deposits such as peperites (Skilling et al., 2002; Wohletz, 2002) and autobrecciated lavas (Duraiswami et al., 2014; Hodgetts et al., 2021; Smith, 1996); air transported ash that falls and compacts into tuffs (Bursik et al., 1992); pyroclastic material that deposits as ignimbrites (Branney and Kokelaar, 1992); quench-fragmented hyaloclastites and perlites that form tinder ridges and tuyas (Jakobsson and Gudmundsson, 2008); and volcaniclastic outwash deltas (Duller et al., 2008). When assessing the porosity evolution of these lithologies, there exist important distinctions between the processes which develop in

viscous regimes such as the syn-depositional welding of rhemorphic ignimbrites (Branney and Kokelaar, 1992), as we have just introduced in Section 1.3.1, or in a brittle, clastic, compactional regimes associated with burial and diagenesis (e.g., Eggertsson et al., 2020; Thien et al., 2015). Here I explore how alteration and compaction may impact the architecture of lithologies deposited in the brittle regime.

Following the deposition of brittle volcaniclastics, the porosity of a lithology is determined by the initial vesicularity of the constituent fragments, as well as the fragments' particle size distribution and geometry, which dictate the inter-fragment pore space (e.g., Jia and Williams, 2001). However, over time this distribution of fragments and pore space may be overprinted by additional processes, including glass dissolution, mineral precipitation, alteration, and mechanical compaction. For example, the evolution of hyaloclastite does not end with the quenching of basaltic fragments. Volcanic glasses are metastable, and so, in hydrous depositional environments, silica tetrahedra may be scavenged relatively quickly from surfaces due to the inherent lack of long order molecular structure in glass (Gislason and Oelkers, 2003; Oelkers and Gislason, 2001; Perera et al., 1991). For instance, palagonitisation (which encompasses glass dissolution and subsequent secondary mineralisation) promotes the progressive breakdown of mafic glass margins, first into amorphous gel, and then into crystalline fibrous palagonite (Figure 1-8; Stroncik and Schmincke, 2001) which is composed primarily of clays and zeolites (Drief and Schiffman, 2004). The continued formation of palagonite surrounding and replacing the mafic glass fragments encourages the growth of a matrix, which provides cohesion to fragmental deposits at the expense of the interstitial pore space (Figure 1-8). This is because palagonitic minerals are less dense than the glass from which they are derived (Franzson et al., 2010), particularly under saturated conditions in which phyllosilicate minerals are prone to hydration and swelling (e.g., Boek et al., 1995). The rate of palagonitisation is positively correlated with temperature, and is dependent on the chemistry of the glass and hydrothermal fluids, as well as the available surface of the glass fragments (e.g., Denton et al., 2009; Stroncik and Schmincke, 2001). Thus, local variations in these reservoir properties result in varying proportions of glass and pore-infilling phyllosilicates, which impact the alteration induced porosity loss. Alternatively, the hydration of felsic glasses may cause the crystallisation of spherulites (Castro et al., 2008) as well as the formation of perlite, which becomes host to a rind of intersecting and curved cracks (Denton et al., 2009). Meteoric fluids diffuse into glass at a rate dependent on the system's temperature and chemistry; the subsequent change in the structure of the glass lattice results in tensile stress and fracturing (Anovitz et al., 2008; Denton et al., 2012). Perlite does not

necessarily exhibit cohesion; however it is subject to alteration and smectite crystallisation (Denton et al., 2009; Kawano et al., 1993), similar to palagonitisation, which may infill the pores and weakly connect the fragments.
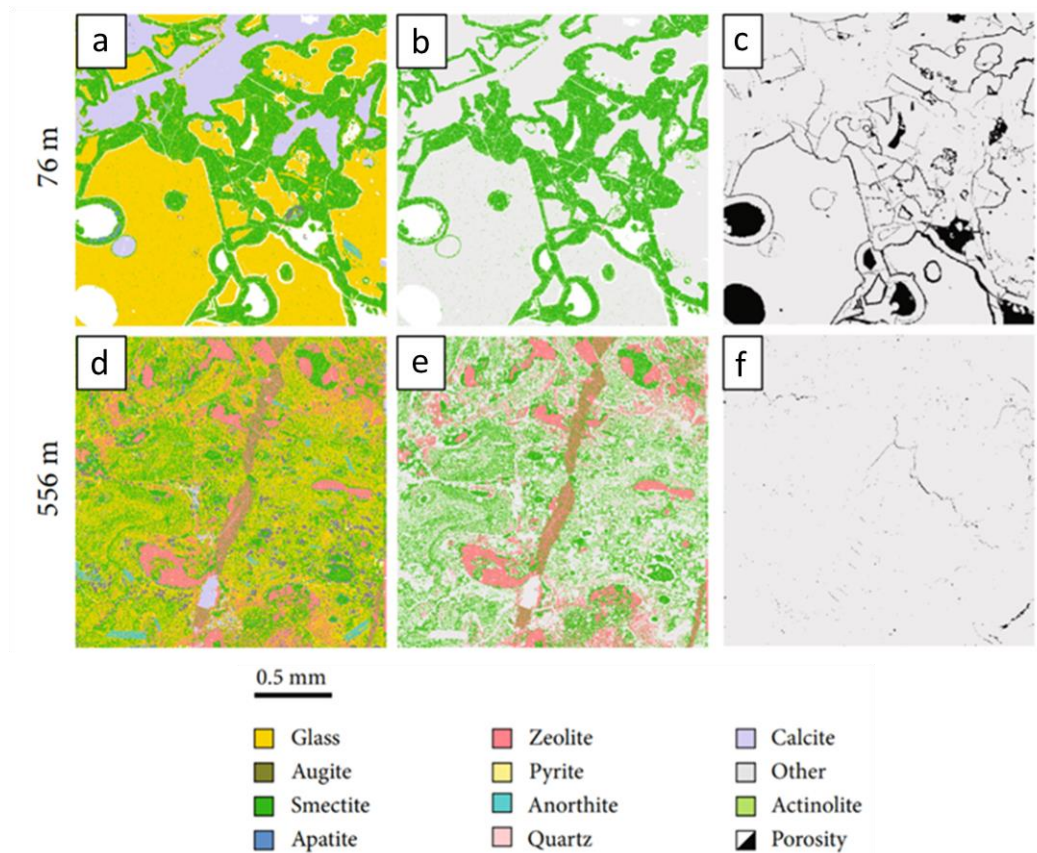


*Figure 1-8: Alteration of hyaloclastites from the Krafla geothermal reservoir, as shown through QEMSCAN analysis (modified from Eggertsson et al., 2020). Glass fragments are altered at their margin and replaced with smectite and zeolite, which impacts on both the connected and isolated porosities of the deposit. The 566 m sample has substantially less porosity than the 76 m sample, indicating that significant compaction has occurred.*

Typically, hydrothermal reservoirs are located in geologically active areas and are host to a plethora of regional and local processes, such as magmatic intrusions and tectonic activity, which can change the temperature, pressure, and chemistry of the system and impact the stability of alteration minerals; therefore, mineral assemblages are dynamic over long time periods. Changes to these aquifer properties can cause the dissolution, alteration, and precipitation of minerals, which may impact the porous network and modify the reservoir storage and fluid flow potential (Mielke et al., 2015). The chemistry and mineralogy of reservoir rocks can be impacted by the dissolution and leaching of minerals or glass (Franzson et al., 2008), and by the secondary precipitation of minerals from meteoric water and sea water, and from connate or magmatic fluids. In concert with fluid chemistry, mineral

assemblages are also dictated by element mobility, where highly mobile elements (e.g., Mg, Ca, Na, and K) may be depleted or accumulated more readily than low mobility elements (e.g., Al and Fe) which tend to enrich at their source (Sturchio et al., 1986). The stability of mineral assemblages is also highly sensitive to the reservoir temperature, which typically increases with depth and can lead to the dehydration and dissolution of alteration minerals. The hydration state of some hydrothermal minerals is reflected in their unit volume, and when subject to temperature increases, devolitisation may densify the crystal lattice and create varying regions of pore infill (Kristmannsdóttir, 1979; Malek et al., 1997). For example, the common alteration of interlayered smectite-chlorite to chlorite typically occurs near 240 °C, and results in dehydration (e.g., Shirozu et al., 1975), leading to disparate mineral swelling (e.g., Rahromostaqim and Sahimi, 2020) and pore infill.

Pore architecture is therefore heavily dependent on the stability of minerals and glasses. However, mineralogy is only half the story, and in addition to dissolution, alteration, and precipitation, porous networks in fragmental systems are affected by physical processes, such as mechanical compaction during burial (Figure 1-8; compare the porosity of the 76 m and 556 m samples). Therefore, to fully describe the porosity evolution in volcaniclastic rocks, an assessment of their mechanical behaviour is also required.

The tolerance of, or resistance to, compaction during loading is largely dependent on the physical properties of a rock (Paterson and Wong, 2005). In particular, porosity is a primary factor in determining rock strength, which impacts the resistance to compaction (Heap and Violay, 2021, and the references therein; Jaeger et al., 2009). High porosity lithologies, such as pyroclastic deposits, are liable to possess low strengths and experience compaction at relatively low effective mean stresses (Eggertsson et al., 2020). This becomes increasingly important for understanding porosity loss in thick fragmental reservoirs which cover a large range of depths, particularly as compaction and densification can lead to the isolation of porosity and the sealing of a porous network to fluid flow (e.g., Heap et al., 2015a).

During loading, volcaniclastic rocks typically develop a strain response which proceeds in the following steps (and is shown in Figure 1-9a); (1) the beginning of stress strain curves are typically convex, as cracks, primarily perpendicular to the applied stress, close; (2) the elasticity of the minerals or glass results in a recoverable, linear elastic stress-strain response, the slope of which defines the Young's modulus; (3) at higher loads, beyond the yield point, stress creates permanent damage, causing a change in the mechanical response, termed inelastic strain hardening. In this latter regime, fracture damage accrues until, (4) the rock

experiences macroscopic failure, at which point the accumulated stress is released (Jaeger et al., 2009). Whether this failure is dilatant or compactional (i.e., if it creates or destroys porosity) is determined by the effective mean stress acting on the rock and is best described through its yield curve (or cap), which is plotted in P-Q space. Here, P is the effective mean stress ($P = \frac{\sigma_1 + \sigma_2 + \sigma_3}{3} - P_f$), where $P_f$ is the pore fluid pressure, and Q is the differential stress ($Q = \sigma_1 - \sigma_3$). Volcanic rocks typically produce a nearly triangular yield curve (Figure 1-9b; Heap et al., 2015a; Paterson and Wong, 2005; Rutter, 1986); at low effective mean stress, rocks exhibit a brittle response and rupture generally results in dilation (porosity increase). With an increase in effective pressure, the differential stress required to fracture a rock increases until the macroscopic deformation mode switches from the brittle field to the ductile field. This transition is dependent on the porosity of the rock being deformed, shifting to lower effective mean stresses for more porous materials (Figure 1-9b). In the ductile field, deformation is generally accompanied by compaction (porosity decrease), associated with cataclastic flow due to grain crushing and pore collapse; it is this mechanism by which initially highly porous volcaniclastics are prone to deform after deposition and burial. With further increases in effective mean stress, the differential stress required to trigger cataclastic flow decreases, down to $P*$, which characterises the effective mean stress for which a rock exhibits no shear strength (Figure 1-9b; Bedford et al., 2018).
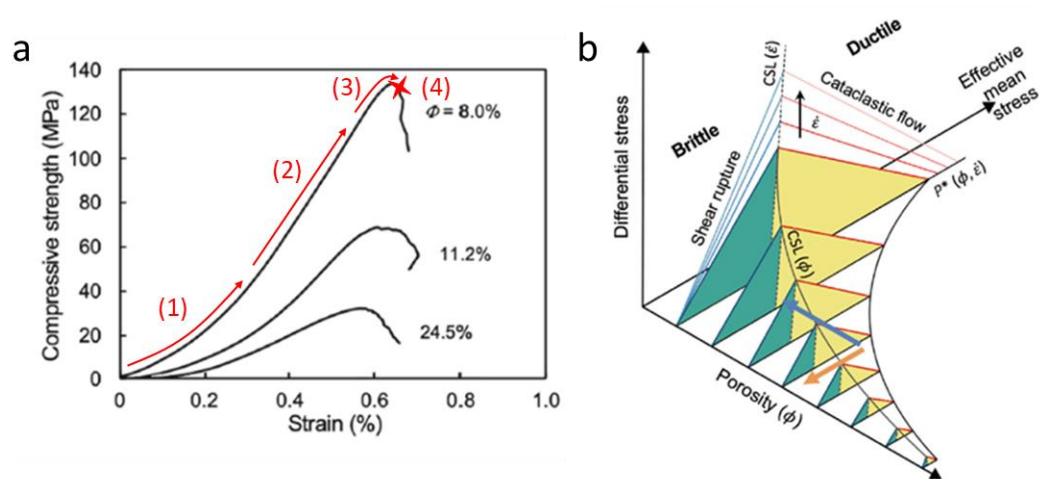


*Figure 1-9: Mechanical response of porous volcanic rocks (modified from Lavallée and Kendrick, 2021). a) example stress – strain curves for rocks showing significant strength reduction with increasing porosity from 8.0, 11.2 and 24.5 %, each curve shows an initial convex inflexion associated with crack closure (1), followed by a near linear stress-strain relationship associated with elastic deformation (2); in the final segment of the loading curve, damage creation results in inelastic strain hardening (3) and, ultimately, failure (4); b) the yield curve of porous volcanic rocks, which is dependent on the stress distribution and the porosity, allows for both a brittle (green) and ductile (yellow) response.*

Characterising the physical and mineralogical processes impacting fragmental volcanic rocks following emplacement, and their interactions, is therefore key to understanding the evolution of porosity in these systems, which impacts fluid flow and geothermal resource utilisation.

## 1.4. Fluid flow in fragmental volcanic environments

Rock permeability is a measure of fluid flow and is predominantly determined by the connected porosity of a rock. The multitude of processes responsible for the evolution of pore space in fragmental volcanic systems, as described above, promotes a porosity range from 0 to >80 % (e.g., Okumura and Sasaki, 2014; Wright and Cashman, 2014); this range results in permeability variations exceeding 10 orders of magnitude (Lavallée and Kendrick, 2021, and references therein), and, for a given porosity, the permeability may range by several log units (Mueller et al., 2005). To explore the underlying reasons for this staggering range, studies have examined the geometry and connectivity of porous networks. Starting with simple hollow cylinder geometries and laminar flow, Darcy's empirical law (Darcy, 1856) has been applied to explore the porosity – permeability relationship in volcanic rocks (e.g., Wright et al. 2009). Expanding on Darcy's law and the Poiseuille formula for a capillary tube, the Kozeny-Carman relationship (Carman, 1937; Kozeny, 1927) incorporates pore structure details into the permeability model, described in terms of the connected porosity, particle size, and particle sphericity. Various advances on the Kozeny-Carman relationship capture additional pore structure details; for example, Costa. (2006) modified it to consider tortuosity and the fractal nature of pore space, whereas, Lucia (1995) applied the model to fracture geometries, which was then expanded to porous and fractured volcanic rocks by Lamur et al. (2017). The Kozeny-Carman relationship also formed the basis for an examination of the role of specific surface (i.e., the ratio of pore surface area and sample volume) by Martys et al. (1994), who provided a universally scaled porosity – permeability model which was later applied to densifying fragmental volcanic environments (Wadsworth et al., 2016b). Most commonly, studies have established various empirical relationships between porosity and permeability in volcanic rocks (e.g., Klug and Cashman, 1996; Mueller et al., 2005; Sparks et al., 1999). The application of these porosity – permeability models (Figure 1-10) have been employed with some success to constrain fragmental volcanic systems (Colombier et al., 2017; Farquharson et al., 2016; Heap et al., 2019, 2015b; Ryan et al., 2020; Wadsworth et al., 2021), and efforts continue in upscaling these relationships for applicability to natural systems (Farquharson and Wadsworth, 2018; Kolzenburg et al., 2019).
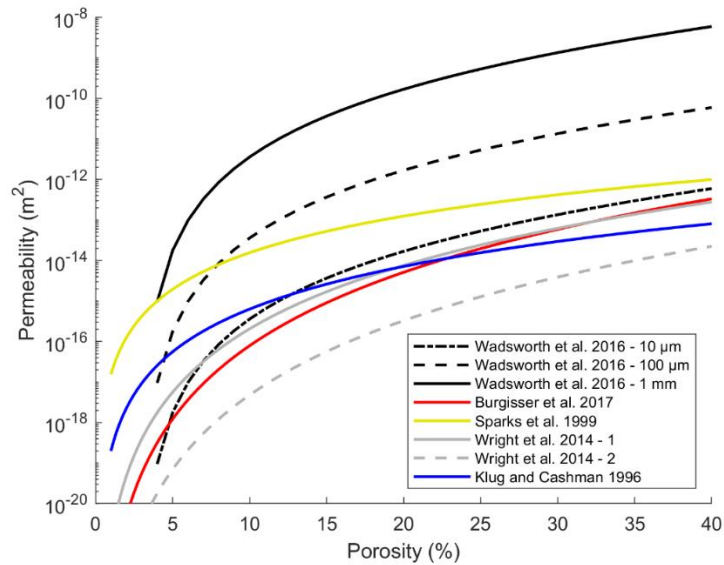
*Figure 1-10: Various porosity and permeability models for densifying granular materials and porous melts* (modified from Kolzenburg et al., 2019)*. Models exhibit a similar, exponential trend despite the different materials constrained.*

In addition to the relationships discussed above for rocks, the permeability of magma is constrained by the percolation threshold, which, for a given material, determines the porosity above which vesicles are connected and provide permeable pathways. Theoretical models derived from monodisperse spherical vesicles suggest permeability is created above 30 % porosity (Sahini and Sahimi, 1994), whereas measurements on natural volcanic samples suggest the percolation threshold varies between ~20-80 % porosity (Burgisser et al., 2017), which, reflects the variable nature of pore structure and connectivity, or lack thereof, in volcanic rocks. A vesicle-dominated magma will have a highly contrasting percolation threshold compared to a magma which has fragmented and partially re-agglutinated, in which it depends upon the initial attributes of the grains (size, geometry) and the degree of sintering. Such differences may be broadly classified in terms of the contrast between effusive and explosive volcanic products, where percolation onset is shifted to higher porosities for explosive products and similar porosities yield lower permeabilities than their effusive counterparts due to pore reduced connectivity (Figure 1-11).
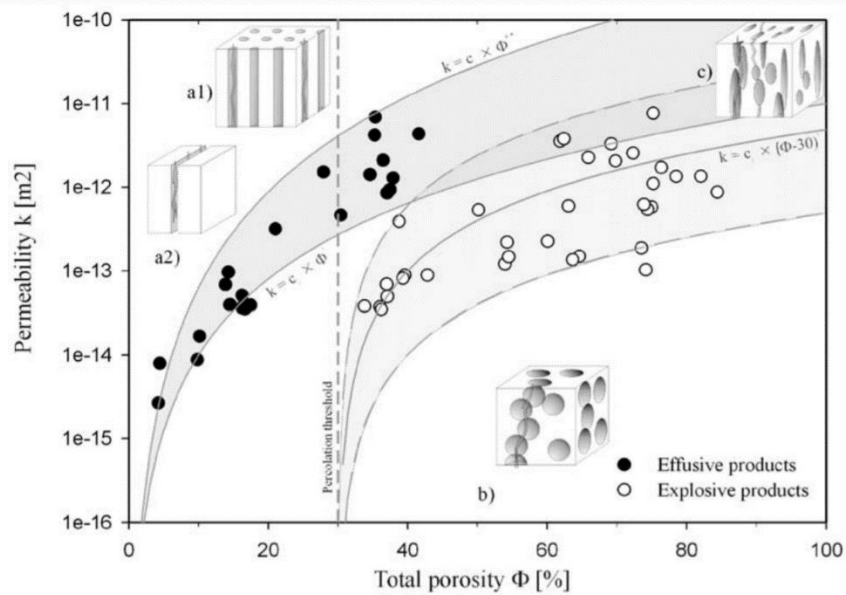
*Figure 1-11: Effusive and explosive volcanic rocks possess distinctly different porosity – permeability relationships, particularly in the value of their percolation threshold (modified from Mueller et al., 2005).*

Permeability evolution in fragmental magma is dynamic due to potential contributions from many processes, including vesiculation, fracturing, healing (i.e., between two planar surfaces), sintering (i.e., between particle accumulations), and shearing, and is impacted by the stress conditions, including both pore pressurisation and depressurisation. Additionally, volcaniclastic deposits exhibit significant spatial heterogeneity in their permeable porous networks due to localised compaction, dissolution, mineral precipitation, and mineral swelling; as these processes create, consume, deform, connect, and isolate pore space, they impact upon the permeability of the system. Evidence of permeability fluctuations in active magmatic systems includes the transience of gas emissions (e.g., Edmonds et al., 2003), and variation in eruptive style (e.g., Cassidy et al., 2018). In preserved systems, the permeability evolution is evident in the dichotomy of the percolation threshold in effusive and explosive products (Figure 1-11; Mueller et al., 2005), and in the variable diffusion length scales in fractured and fragmental volcanic material associated with open system outgassing (Castro et al., 2012; Heap et al., 2019; Saubin et al., 2016; von Aulock et al., 2017). Similarly, the evolution of temperature, pressure, and extracted fluid chemistry in actively exploited geothermal systems (e.g., Bixley et al., 2009; Sanchez-Alfaro et al., 2016) may impact permeable porous networks through dehydration and alteration to the mineral assemblage (e.g., Dobson et al., 2003; Faulkner and Rutter, 2000; Heap et al., 2018; McNamara et al., 2016), and mechanical dilation or compaction at depth (Eggertsson et al., 2020; Siratovich et al., 2016). Ultimately, resolving the evolution of porosity - permeability relationships in transient fragmental

environments, is central to furthering our understanding, and prediction, of volcanic eruption dynamics, and to enhance our utilisation of geothermal resources.

## 1.5. Thesis aims and structure

In this thesis I aim to explore how porosity and permeability evolve in selected fragmental volcanic systems which are of interest to volcanologists and the geothermal industry. Following Chapter 1, in which I introduce the state of the art in our current understanding of fragmental volcanics, Chapter 2 explores the size-dependence of gas loss from hydrous melt fragments, simulating in the laboratory the processes which are observed in natural volcanic systems. Using optical dilatometry, textural analysis, and modelling constraints, the relative importance of vesiculation and diffusive outgassing are investigated for a range of sample sizes. Chapter 3 expands this work on isolated fragments to a range of fragmental, particulate systems, which are intended to imitate shallow or sub-aerial volcanic environments, such as tuffisite infill, pyroclastic deposits, conduit back-fill and any other scenario in which hydrous fragmental particles agglutinate with minimal impact from load. Here, the importance and interaction between vesiculation, diffusive-outgassing, and sintering are explored through changes to the total and connected porosity, and the resultant system permeability. Following this, Chapter 4 focusses on the hydrothermally altered volcaniclastic deposits found in the Krafla geothermal reservoir. Here, hyaloclastites sampled from a range of reservoir depths are thermally stressed in the laboratory and changes to their porosity, permeability, strength, and mineralogy are systematically monitored to assess the role of thermal fluctuations on fluid flow pathways in volcaniclastic reservoir rocks. Finally, Chapter 5 summarises the findings of this doctoral study, places each piece of work in the context of the others, and explores their implications through other published studies. I then suggest further research which could follow from the findings of the studies included here.

## 1.6. Status of manuscripts

### Chapter 2

**Manuscript Title:** Vesiculation and densification of pyroclasts: a clast-size dependent competition between bubble growth and diffusive outgassing

**Authors:** Joshua Weaver[1], Yan Lavallée[1], Maliha Ashraf[2], Jackie E. Kendrick[1], Anthony Lamur[1], Jenny Schauroth[1], Fabian B. Wadsworth[3]

Affiliations:

[1] Department of Earth, Ocean and Ecological Sciences, University of Liverpool, L69 3GP, U.K

[2] Department of Electrical and Electronic Engineering, University of Liverpool, L69 3GJ, U.K

[3] Earth Sciences, Durham University, Science Labs, DH1 3LE, U.K

Author Contributions: JW performed all vesiculation experiments and the associated data processing, and the textural analysis and rind thickness data collection. JS performed the FTIR analysis and assessed the sample water content. MA wrote the solid of revolution code used to estimate sample volume evolution. JW led the project and was the main contributor to the manuscript preparation. All other co-authors contributed to the manuscript writing and offered advice and feedback throughout the project.


Chapter 3

Manuscript Title: Sintering of vesiculating and outgassing hydrous pyroclasts

Authors: Joshua Weaver[1], Yan Lavallée[1], Thomas Lea[1], Jackie E. Kendrick[1], Anthony Lamur[1], Fabian B. Wadsworth[2]

Affiliations:

[1] Department of Earth, Ocean and Ecological Sciences, University of Liverpool, L69 3GP, U.K

[2] Earth Sciences, Durham University, Science Labs, DH1 3LE, U.K

Author Contributions: All sintering and volume quantification was performed by JW and TL. JW performed all permeability measurements and textural analysis. The modelling was led by JW, with substantial support from FW. JW was the main contributor to the manuscript preparation, with contributions from all the co-authors.

**Manuscript Title:** Thermal Liability of Hyaloclastite in the Krafla Geothermal Reservoir, Iceland: The Impact of Phyllosilicates on Permeability and Rock Strength

**Authors:** Joshua Weaver[1], Guðjón H. Eggertsson[1], James E. P. Utley[1], Paul A. Wallace[1], Anthony Lamur[1], Jackie E. Kendrick[1], Hugh Tuffen[2], Sigurður H. Markússon[3], and Yan Lavallée[1]

**Affiliations:**

[1] Department of Earth, Ocean and Ecological Sciences, University of Liverpool, L69 3GP, U.K

[2] Lancaster Environment Centre, Lancaster University, LA1 4YQ, UK

[3] Landsvirkjun, Háaleitisbraut 68, 110 Reykjavík, Iceland

**Journal:** Geofluids

**Status:** Published

**Author Contributions:** GE and YL carried out the fieldwork and sample collection, including the selection of subsurface samples from Landsvirkjun drill cores. JW performed all thermal treatment of the samples, simultaneous thermal analysis, thermomechanical analysis, optical microscopy analysis, and porosity, permeability, and strength measurements, including the associated data processing. JU performed the X-ray diffraction and QEMSCAN analysis and data processing. JW led the project and was the main contributor to the manuscript preparation. All other co-authors contributed to the manuscript writing and offered advice and feedback throughout the project.

# Chapter 2: Vesiculation and densification of pyroclasts: a clast-size dependent competition between bubble growth and diffusive outgassing

## Abstract

During volcanic eruptions, bubble growth and outgassing determine the porosity, buoyancy, and rheological evolution of magmas, which in turn, dictates the potential for explosive eruption. The processes which lead to magmatic fragmentation have received substantial attention, whereas the subsequent modification of fragmented pyroclasts remains poorly constrained. Here, we present the results of experimentation using obsidian cylinders in the ash to lapilli size range (1-12 mm diameter), for which we find that closed system bubble growth is progressively suppressed by fragment size-dependent, diffusive outgassing. We find that when the volatile partial pressure is lower in the ambient exterior gas than in the melt-hosted bubbles, the volatiles diffusively outgas. This volatile loss produces a bubble-free dehydrated rind, which thickens proportional to the diffusion lengthscale. We show that more outgassing is possible from fragments with higher surface area to volume ratios, and therefore, pyroclasts with a smaller initial radius develop a higher proportion of dehydrated rind, densify faster, and attain more subdued vesicularities. We find that this diffusive outgassing process can produce fully dense, non-vesicular pyroclasts, effectively erasing the textural evidence of the vesiculation event altogether. Using an analytical approximate approach to the evolving clast geometry, we show that current closed system bubble growth models and diffusion models can be combined to estimate vesicularity in pyroclasts surrounded by a free gas of relatively low partial pressure of $H_2O$. Our analyses highlight that a single explosive eruptive episode with disequilibrium volatile partial pressures may produce both dense and vesicular pyroclasts depending on their grain size.

Keywords: transient porosity, open system, degassing, dehydration, resorption, rhyolite

## 2.1. Introduction

The ability of magmas to lose volatiles imposes a first-order control on eruption dynamics (Cassidy et al., 2018). Volatile loss from melts occurs through degassing by vesiculation and outgassing (i.e., segregation of the magma and gas) and together these processes play a

central role in magma pore network evolution, which controls buoyancy, permeability, pressure accumulation, and ultimately, eruptive style (e.g., Sparks, 2003). Vesiculation occurs when volatiles dissolved in magmas become supersaturated due to changes in pressure, temperature, or chemical composition (e.g., Sparks, 1978), and undergo exsolution through the nucleation and growth of gas bubbles (e.g., Prousevitch et al., 1993). The majority of models and experimental work pertaining to degassing-driven bubble growth focus on closed systems of isolated bubbles (e.g., Coumans et al., 2020). However, in nature, most shallow magmas are open-system and gas-permeable as vesiculation progresses, producing a complex system in which vesiculation and outgassing compete (e.g., Degruyter et al., 2012).

Vesiculation in closed-system conditions (i.e. when volatiles remain confined by the melt in isolated bubbles) is strongly dependent on bubble number density and the size of bubbles (Bagdassarov et al., 1996; Coumans et al., 2020; Proussevitch and Sahagian, 1998; Ryan et al., 2015a; Stevenson et al., 1997). In a closed system of bubbles in high-viscosity magmas, the gas remains coupled to the surrounding melt (Degruyter et al., 2012). By contrast, in open-system magma containing connected porous networks, the exsolved volatiles may percolate through, and escape magma due to permeable flow, resulting in gas pressure changes and densification of the magma (Ashwell et al., 2015; Degruyter et al., 2012; Gonnermann, 2015; Gonnermann et al., 2017). A key but under-explored phenomenon is that open, permeable, magma systems may experience a change in volatile partial pressure while outgassing (e.g., von Aulock et al., 2017). This can occur if the gas composition in the permeable pore network changes via vapour fluxing (Rust et al., 2004) or shallow mixing with atmospheric air. A change in volatile partial pressure in a pore network may locally change supersaturation, induce saturation gradients, and result in less bubble growth or bubble shrinkage in the adjacent magma (von Aulock et al., 2017; Yoshimura and Nakamura, 2008). Therefore, we propose that complexities associated with open-system degassing require further work.

Following magma fragmentation (by shear-brecciation or explosive eruption), the portion of the open volcanic conduit above the fragmentation interval but below the Earth's surface is a key part of the volcanic system subject to both open-system decoupled gas-magma dynamics, and partial pressure changes in the gas phase. In this region, magma fragmentation forms a mixture of gas and variably vesicular pyroclasts; volatiles in these clasts may exsolve, progressively increasing the vesicularity, but they may also diffuse through the free surface created by fragmentation (e.g., von Aulock et al., 2017). This additional diffusive process - which we term *diffusive outgassing* - is sensitive to the pyroclast size and to the surface area to volume ratio, which can be large in the fine pyroclasts formed by fragmentation (Liu et al.,

2015). In particular, von Aulock et al. (2017) showed that dense pyroclasts with a low partial pressure of volatiles on the outside of the magma clast may vesiculate due to supersaturated conditions, but then, near the margin of clasts, the vesicles may shrink and be lost (Figure 2-1). Here, continued diffusive outgassing from the fragment surface dehydrates the melt along the fragment margin, locally forcing exsolved volatiles to resorb before being purged to the open, surrounding atmosphere; so, diffusive outgassing may effectively negate the vesiculation event, forming a bubble-free dehydrated rind, which thickens over time with the evolving diffusion lengthscale (von Aulock et al., 2017). Although rarely analysed, dense rinds can be observed in natural pyroclasts presented in many studies (Castro et al., 2014, 2012; Heap et al., 2019; Saubin et al., 2016). In the laboratory, experiments have shown that the gradual thickening of this bubble-free rind suppresses the bulk porosity of pyroclasts (von Aulock et al., 2017; Yoshimura and Nakamura, 2008). The implication may be that some degassed dense pyroclasts – such as obsidian fragments common in silicic explosive eruptions (e.g., Gardner et al., 2019; Watkins et al., 2017) and tuffisites (Heap et al., 2019) – could result from vesiculation and subsequent densification, leaving no textural trace of these processes.
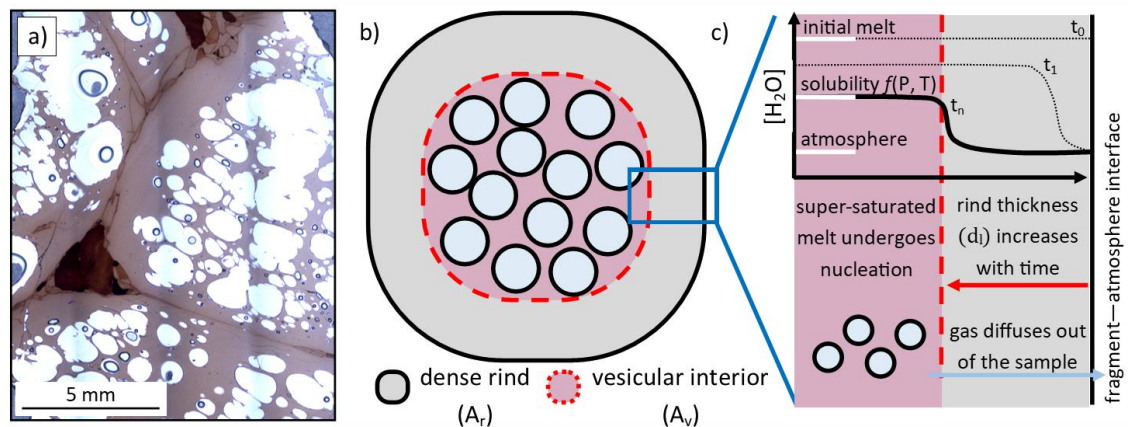


*Figure 2-1: (a) Photomicrograph of a fragmental, vesicular rhyolite from Hrafntinnuhryggur, Iceland. The fragments are agglutinated together and exhibit a dense rind which is surrounded by an isolated, vesicular interior. (b-c) Simplified, annotated sketches of (b) a vesicular fragment and (c) the rind-interior boundary, highlighting the active processes and conditions which result from vesiculation and the associated development of a marginal dense rind. Note that the $H_2O$ concentration across the rind reduces from the initial melt water content at time $t_0$, to between the values determined by the solubilities at the total melt pressure, and the atmospheric partial pressure, at any time $t_n$.*

We therefore suggest that in shallow volcanic eruptive systems, the evolution of vesicularity within pyroclasts can be complex and may not be predictable using existing models for bubble formation and growth in response to supersaturation (cf. Coumans et al., 2020). As a starting point for this contribution, we posit that diffusive outgassing would impact the evolution of

pyroclast vesicularity in the following ways: (1) small pyroclasts may lose all supersaturated volatiles by diffusive outgassing before any bubbles form [as assumed by Wadsworth et al. (2020)]; (2) volatiles in larger pyroclasts may vesiculate but then resorb and diffusively outgas, causing the initial bubble growth to be followed by densification (von Aulock et al., 2017); and (3) these larger pyroclasts may cool prior to the completion of diffusive outgassing and preserve vesicular cores surrounded by dense rinds, texturally akin to breadcrust bombs (Benage et al., 2014). It is the densification which has received the least attention, and in particular, here we aim to constrain the effect of particle size in controlling the competition between bubble growth and diffusive outgassing.

## 2.2. Methods

### 2.2.1.  Material

A natural, rhyolitic obsidian block was collected from Hrafntinnuhryggur, Iceland. It was selected for use in this experimental study as the glass is homogenous and devoid of bubbles, crystals, and fractures, and has been used extensively for analyses and experimentation (Casas et al., 2019; Coumans et al., 2020; Ryan et al., 2015a; Tuffen and Castro, 2009; Wadsworth et al., 2021, 2019). The bulk-rock major element composition was determined by X-ray fluorescence (XRF) using a PANalytical Axios Advanced XRF spectrometer. Major elements were measured on glass beads fused from ignited powders using a sample to flux ratio of 1:5 (80 % Li metaborate: 20 % Li tetraborate). The XRF results (Table 2-1) have been recalculated to include loss on ignition (LOI). The water content was determined by Fourier-transform infrared spectroscopy (Table 2-1) using a Thermo Nicolet 380 FT-IR and Nicolet Centaurus microscope. The spectra of two $100 \ \mu m^2$ spots were analysed using a polished $216 \pm 1 \ \mu m$ thick sample wafer. $H_2O$ concentrations were calculated by measuring the height (absorbance) of the ~3500 $cm^{-1}$ peak above a linear background using the Beer-Lambert law, a molar absorptivity coefficient of 90 $mol^{-1}cm^{-1}$ (Hauri et al., 2002), and a density of 2.40 $g.cm^{-3}$ (dry powder density measured by helium pycnometry). The XRF data are broadly comparable to the microprobe analysis of Tuffen and Castro, (2009), whilst the water content measured here ($0.10 \pm 0.005$ wt.% $H_2O$ for both analysed spots) is slightly lower than their minimum value ($0.11$-$0.20$ wt.% $H_2O$).

*Table 2-1: Rhyolite composition attained from XRF and water content from FTIR analysis.*

| Oxide | (wt.%) |
|---|---|
| $SiO_2$ | 75.43 |
| $TiO_2$ | 0.24 |
| $Al_2O_3$ | 12.33 |
| $Fe_2O_3$ | 3.64 |
| MnO | 0.10 |
| MgO | 0.10 |
| CaO | 1.67 |
| $Na_2O$ | 4.29 |
| $K_2O$ | 2.49 |
| $P_2O_5$ | 0.03 |
| $SO_3$ | 0.01 |
| LOI | 0.11 |
| Total | 100.44 |
| $H_2O_t$ | 0.10 |

### 2.2.2. Experiments and data collection

In this study, we investigated the volumetric expansion of obsidian specimens of different sizes subjected to magmatic temperatures. To this end, we created samples by coring obsidian into cylinders with diameters of 1, 3, 5, 6, 7.5, 10, and 12 mm, and with lengths approximately equal to the diameter. The samples were sat on a holocrystalline basalt plate (non-reactive, with petrography described in Lamur et al., 2018) and placed in a furnace. For the experiments with the 1 mm and 3 mm samples, we used a tube furnace, whilst for the experiments with the 5 - 12 mm samples, we used a box furnace. In both set-ups, samples were carefully placed equidistant from the heating elements to minimise the effect of any thermal gradients in the furnaces. Prior to heating, the initial volumes of the sample and sub-plate (to which they weld after heating) were measured independently, in a Micromeritics AccuPyc 1340 helium pycnometer (accurate to ±0.1 % of the measured volume).

Two separate series of experiments were conducted for vesicularity quantification and for textural analysis. In the first set of experiments, the samples were heated individually to 1006 °C at 10 °C.min$^{-1}$, left to dwell for 48 hours, and then cooled to room temperature at 10 °C.min$^{-1}$ (not accounting for thermal lag of the furnace in the later stages of cooling). Throughout each experiment, the geometrical evolution of the sample's 2-dimensional vertical cross-section silhouette was recorded every 60 seconds. Due to size and pixel resolution constraints,

the tube furnace experiments were recorded using a Nikon D800 optical camera (with a AF-S NIKKOR 105mm f/1.4E ED lens), whilst the box furnace experiments were recorded through a sapphire window in the furnace using a FLIR X6540sc thermographic camera (with a 50 mm F/2 lens). The optical and thermal images have spatial resolutions of $12,450 \pm 1,750$ pixels.mm$^{-2}$ and $31.9 \pm 4.2$ pixels.mm$^{-2}$, respectively.

For the second series of experiments, textural analysis was conducted for the 1, 3, 5, and 12 mm sample sizes after 3, 6, 12, 24, 36, and 48 hour dwell durations at 1006 °C (the 48 hour samples are taken from the first set of experiments). Again, the samples were heated, and subsequently cooled to room temperature, at a rate of 10 °C.min$^{-1}$. Using samples vertically cut through their centre, backscattered electron images were captured at >80x magnification via a Hitachi TM3000 scanning electron microscope operating at 15 kV. The outer margin of each sample in cross-section was imaged in order to quantify the thicknesses of the dense rinds developed through time. We estimate the thickness of the rind by manually measuring the minimum distance between the outermost layer of bubbles (i.e., the bubble walls adjacent to the rind) and the outer surface of the sample; herein we report the average rind thickness for each experiment duration, along with the standard error.


### 2.2.3.  Sample volume and vesicularity

The thermographic and photographic images of the samples' silhouettes were used to compute the volume and surface area change of the samples during the heating and isothermal dwell periods. For each recording, the frames were segmented into binary images to isolate the vertical-plane cross-sectional area of the sample from the background; frames which did not reveal a clearly distinguishable sample silhouette for segmentation were discarded. The height $h$ and diameter $d$ of the sample in the first frame were quantified for each sample. To scale these measurements and convert pixel units into millimetres, the image-based estimates of initial sample geometry were compared to the initial sample dimensions measured with a calliper.

While the initial volume can be computed by $V_{(0)} = \pi r^2 h$ where $r = d/2$, during heating, dwell, and cooling, the geometry of the sample deviates from cylindrical. Therefore, we use the solid of revolution approach (e.g., Wadsworth et al., 2016a) to find the time-dependent volume $V(t)$, which can be applied to any axisymmetric shape for which the cross section can be observed, such as is the case here. The local radius $r_j$ at vertical position $y_j$ from the base

can be measured from the images and the volume is then $V(t) = \int_{y_j=0}^{y_j=h} \pi r_j^2 dy$. This integral

becomes a discrete sum when the pixel resolution is taken to be $dy$. Surface area was then

estimated using $\int_{y_j=0}^{y_j=h} 2\pi r_j dy + \pi r_{j=0}^2 + \pi r_{j=h}^2$, where subscript $j = 0$ and $j = h$ refer to the

first slice (sample base) and final slice (sample top), respectively. For each sample, the initial

volume estimated from the first frame was within 10 % of the initial sample volume

determined by helium pycnometry, which we use solely to assess the accuracy of the solid of

revolution result. Following Ryan et al. (2015a), we do not account for the volumetric impact

of the thermal expansivity of the melt during heating because the linear thermal expansion

coefficient of rhyolitic glass is estimated at $6 \times 10$ °C$^{-1}$ (Bagdassarov and Dingwell, 1992) and

therefore any volume change associated with heating to our isothermal temperature is well

within the uncertainty of our volume estimation through the solid of revolution.

The evolution of bulk sample vesicularity $\phi(t)$ was estimated by equating the sample volume

change to a change in gas volume by assuming the initial sample was a single-phase melt (i.e.,

vesicle-free) prior to heating. Vesicularity is then given by

$$\phi(t) = 1 - \frac{V_{(0)}}{V_{(t)}}$$
Equation 2-1.

## 2.3. Results and analysis

### 2.3.1. Raw data: the evolution of sample cross-sectional area

We continuously recorded ten experiments for 48 hours, covering the full sample size range

(see Table 2-2 for details). The two-dimensional silhouette of every sample experienced a

comparable qualitative shape evolution (Figure 2-2a). Once at experimental temperature

conditions, the sample silhouettes initially remained rectangular (representing the initial

cylindrical geometries; Figure 2-2b and f) and expanded slowly, before expansion accelerated

and the geometries progressively and smoothly morphed toward circular (i.e., representing

quasi-spherical shapes in 3D; Figure 2-2c, d, g, and h). The time between the start of the

isotherm and the onset of rapid expansion ranged between 720 and 1500 seconds and was

independent of the initial sample size. The rate of samples' expansion reduced as the

experiment progressed, until the samples reached their maximum size. Following this peak in

size, the sample areas began to decrease, during which anisotropy increased as the sample

height decreased relatively more than the diameter (Figure 2-2d-e and h-i). For the smallest

1 mm samples, the geometrical evolution revealed that the rate of contraction eventually

slowed until finally, the sample shape reached an equilibrium and stopped changing; for larger samples, the experiment duration appeared insufficient to yield this observation.
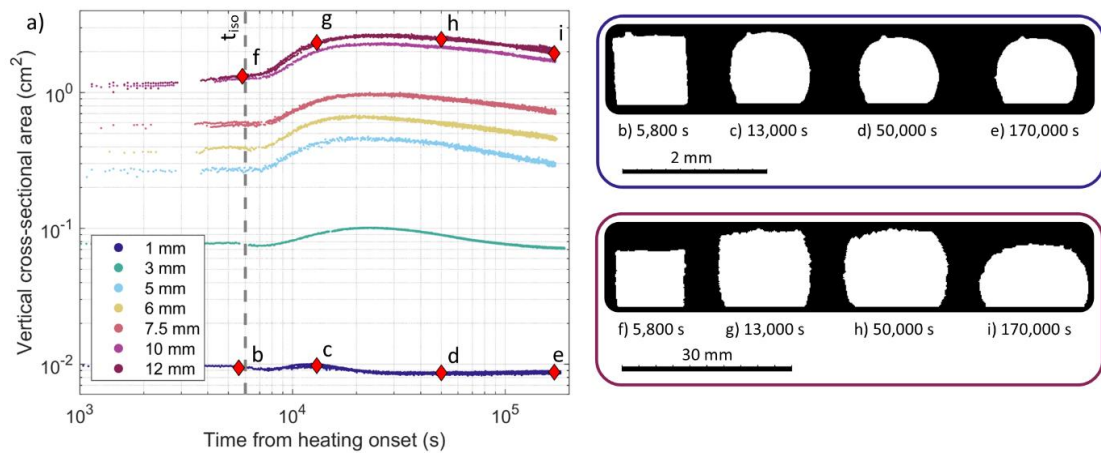


*Figure 2-2: The raw experimental data acquired in this study for the change in cross-sectional area of samples subjected to furnace conditions. (a) The cross-sectional area of segmented images shows that samples experience an expansion dominated regime, followed by a relatively slower contraction dominated regime. Each sample is plotted individually in Supplementary Figure A.I-1. (b-i) Selected images are presented for an initial 1 mm sample (b-e) and a 12 mm sample (f-i). The start of the isothermal heating period ($t_{iso}$) is denoted by the dashed grey line in (a).*

The sample area evolution and the initial sample area are closely related; at their peak cross-sectional area, larger samples have increased from their initial size relatively more than smaller samples (e.g., 115-130 % for the 12 mm samples compared to 13-17 % for the 1 mm samples). Additionally, both the expansion and contraction rates are correlated to the initial size, with larger samples experiencing faster expansion and slower contraction than smaller samples. These sample size dependencies result in larger samples experiencing greater, and more lasting excursions from their initial size.

Table 2-2: Initial sample dimensions and rind thickness measurements follow heating. The timescale for diffusive outgassing to complete, $\tau_d$, and the ratio of the diffusive outgassing and bubble growth timescales $Pe$, are estimated following details in Section 2.4.1.

| Height (mm) | Diameter (mm) | Pycnometer volume (mm³) | Isothermal time (hrs) | No. of rind thickness measurements | Average rind thickness (mm) | Standard error (mm) | $\tau_d$ (s) | $Pe$ |
|---|---|---|---|---|---|---|---|---|
| 1.00 | 0.99 | - | 3 | 13 | 0.248 | 0.020 | $9.92 \times 10^4$ | 4.8 - 7.9 |
| 1.04 | 1.03 | - | 3 | 6 | 0.267 | 0.023 | $1.07 \times 10^5$ | 5.2 - 8.6 |
| 3.15 | 2.92 | - | 3 | 19 | 0.275 | 0.023 | $8.63 \times 10^5$ | 42.1 - 69 |
| 5.11 | 4.95 | - | 3 | 37 | 0.211 | 0.010 | $2.48 \times 10^6$ | 121 - 198.4 |
| 12.40 | 12.06 | - | 3 | 75 | 0.180 | 0.008 | $1.47 \times 10^7$ | 718 - 1177.4 |
| 1.12 | 1.10 | - | 6 | 2 | 0.285 | 0.065 | $1.22 \times 10^5$ | 6 - 9.8 |
| 1.02 | 0.98 | - | 6 | 7 | 0.332 | 0.030 | $9.72 \times 10^4$ | 4.7 - 7.8 |
| 0.97 | 0.99 | - | 6 | 6 | 0.348 | 0.023 | $9.92 \times 10^4$ | 4.8 - 7.9 |
| 1.08 | 1.05 | - | 6 | 0 | 0.390* | - | $1.12 \times 10^5$ | 5.4 - 8.9 |
| 2.96 | 2.92 | - | 6 | 26 | 0.300 | 0.017 | $8.63 \times 10^5$ | 42.1 - 69 |
| 2.91 | 2.92 | - | 6 | 27 | 0.331 | 0.019 | $8.63 \times 10^5$ | 42.1 - 69 |
| 3.03 | 2.92 | - | 6 | 18 | 0.274 | 0.017 | $8.63 \times 10^5$ | 42.1 - 69 |
| 5.02 | 4.95 | - | 6 | 36 | 0.259 | 0.016 | $2.48 \times 10^6$ | 121 - 198.4 |
| 11.78 | 12.06 | - | 6 | 42 | 0.250 | 0.018 | $1.47 \times 10^7$ | 718 - 1177.4 |
| 0.98 | 0.98 | - | 12 | 0 | 0.515* | - | $9.72 \times 10^4$ | 4.7 - 7.8 |
| 3.07 | 2.92 | - | 12 | 21 | 0.469 | 0.034 | $8.63 \times 10^5$ | 42.1 - 69 |
| 5.04 | 4.92 | - | 12 | 17 | 0.420 | 0.052 | $2.45 \times 10^6$ | 119.5 - 196 |
| 12.10 | 12.06 | - | 12 | 105 | 0.386 | 0.012 | $1.47 \times 10^7$ | 718 - 1177.4 |
| 1.19 | 1.13 | - | 24 | 0 | 0.460* | - | $1.29 \times 10^5$ | 6.3 - 10.3 |
| 3.16 | 2.92 | - | 24 | 14 | 0.525 | 0.035 | $8.63 \times 10^5$ | 42.1 - 69 |
| 5.32 | 4.93 | - | 24 | 32 | 0.582 | 0.029 | $2.46 \times 10^6$ | 120 - 196.8 |

*Table 2-2: continued.*

| Height (mm) | Diameter (mm) | Pycnometer volume (mm$^3$) | Isothermal time (hrs) | No. of rind thickness measurements | Average rind thickness (mm) | Standard error (mm) | $\tau_d$ (s) | Pe |
|---|---|---|---|---|---|---|---|---|
| 11.82 | 12.06 | - | 24 | 43 | 0.489 | 0.032 | $1.47 \times 10^7$ | 718 - 1177.4 |
| 0.80 | 1.00 | - | 36 | 0 | 0.545* | - | $1.01 \times 10^5$ | 4.9 - 8.1 |
| 3.11 | 2.92 | - | 36 | 6 | 0.538 | 0.082 | $8.63 \times 10^5$ | 42.1 - 69 |
| 5.05 | 4.93 | - | 36 | 22 | 0.639 | 0.040 | $2.46 \times 10^6$ | 120 - 196.8 |
| 11.90 | 12.06 | - | 36 | 51 | 0.626 | 0.040 | $1.47 \times 10^7$ | 718 - 1177.4 |
| 1.03 | 1.03 | 0.8$^x$ | 48 | 0 | 0.520* | - | $1.08 \times 10^5$ | 5.3 - 8.7 |
| 1.03 | 1.02 | 0.8$^x$ | 48 | 0 | 0.510* | - | $1.05 \times 10^5$ | 5.1 - 8.4 |
| 2.82 | 2.92 | 18.7 | 48 | 7 | 0.587 | 0.077 | $8.63 \times 10^5$ | 42.1 - 69 |
| 5.58 | 4.95 | 106.9 | 48 | 44 | 0.742 | 0.036 | $2.48 \times 10^6$ | 121 - 198.4 |
| 6.52 | 5.94 | 179.9 | 48 | - | - | - | $3.57 \times 10^6$ | 174.2 - 285.6 |
| 7.97 | 7.55 | 355.9 | 48 | - | - | - | $5.77 \times 10^6$ | 281.4 - 461.5 |
| 7.60 | 7.55 | 335.7 | 48 | - | - | - | $5.77 \times 10^6$ | 281.4 - 461.5 |
| 11.27 | 10.10 | 895.9 | 48 | - | - | - | $1.03 \times 10^7$ | 503.6 - 825.8 |
| 10.64 | 12.06 | 1212.8 | 48 | - | - | - | $1.47 \times 10^7$ | 718 - 1177.4 |
| 10.31 | 12.06 | 1166.5 | 48 | 109 | 0.726 | 0.018 | $1.47 \times 10^7$ | 718 - 1177.4 |

$^x$ Value nearing measurement precision

* Fully dense sample. Measurement taken from the minimum sample radius, post-experiment

### 2.3.2. Rind thickness scaling

Examination of the 2-dimensional backscattered electron images, captured from 36 dissected experimental products, revealed a vesicular core surrounded by a dense rind (Figure 2-3). Texturally, the rind is predominantly homogeneous (made of dense glass devoid of fractures), is identical across all samples and times, and is indistinguishable from the featureless, pre-vesiculated obsidian; however, it does contain rare, isolated bubbles which are generally much smaller than the bubbles in the vesicular interior (see red arrow in Figure 2-3f).

The thickness $d_l$ of the dense rind was negligible for short experiments (e.g. Figure 2-3a) and, while spatially variable, increased, on average, with experiment duration (Figure 2-3a-f; Table 2-2). For the first ~50,000 s, the rate of the rind growth was generally negatively correlated to the initial sample size, after which, no significant sample size correlation remained. For the 1 mm samples with experimental durations longer than 27,600 s, the rind thickness appears limited by the sample size (i.e., $d_l(t)$ equals the initial sample radius; Figure 2-3g inset). We found a significant degree of rind thickness variability both within single samples and between repeated samples at the same conditions (see Table 2-2). Note that the smaller samples contain substantially fewer bubbles than the larger samples, which limited the number of rind thickness measurements available per sample.

In order to test the hypothesis that this rind grows by diffusion of volatiles from the bubbly region of the vesiculating sample, through the sample edge and to the exterior surrounding gas atmosphere (see von Aulock et al., 2017), we compare our determinations of $d_l$ with a scaling for diffusion length

$$d_l(t) = K\sqrt{Dt} \hspace{4cm} \text{Equation 2-2,}$$

where $D$ is the diffusivity of the volatile species in question, $t$ is the time for which diffusion operates (i.e., considered to initiate from the onset of the isotherm, unlike in the figures, where $t$ is reported from the beginning of the experiment), and $K$ is a factor related to the geometry of the interface through which the diffusion is occurring. In our case, the dominant volatile remnant in the experimental material is $H_2O$ for which Zhang and Ni. (2010) provide an empirical estimate of $D$ as a function of temperature and local dissolved water concentration. We calculate a constant $D$ using the experimental isothermal temperature and the solubility of water in the melt at the isothermal conditions [where solubility is found using Liu et al. (2005)]. Using these assumptions, we show results for Equation 2-2 for different values of $K$ and find that $K = 2$ provides a reasonable description of our data within uncertainty and that therefore $d_l \propto \sqrt{t}$ (Figure 2-3g).
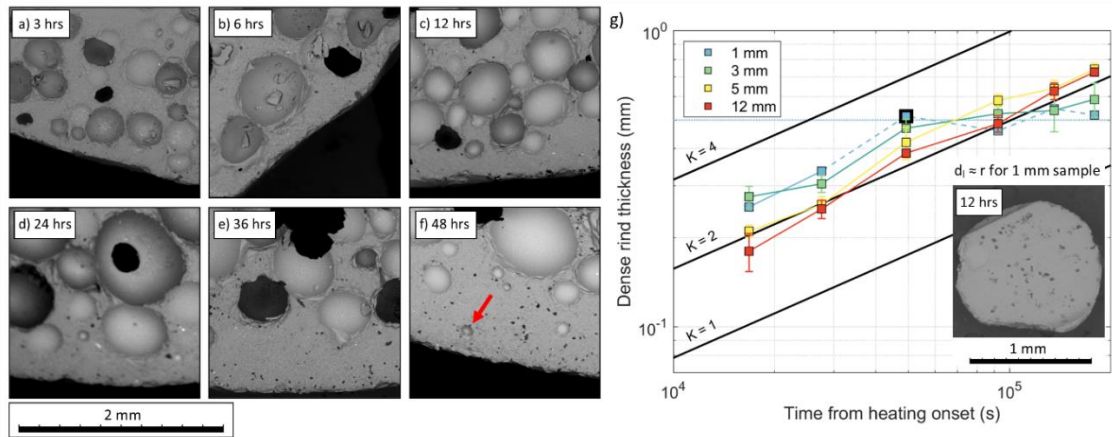
*Figure 2-3: Development of the dense rind. (a-f) Selected backscatter electron images from a suite of dissected 12 mm samples which were subjected to a range of isothermal periods. (f) The red arrow highlights a small, isolated bubble in the dense rind after 48 hrs. (g) Average thickness of the dense rind $d_l(t)$ measured after isothermal dwells using a range of initial sample sizes. The error bars show the standard error for the full set of measurements taken at each time and sample size condition. The 1 mm samples heated for longer than 6 hours are vesicle-free (see inset image, corresponding to the data point with a thick black outline); in place of the rind thickness, the 1 mm values connected by the dashed lines represent the minimum sample radii, which limits the diffusion length, as indicated by the horizontal line at 0.5 mm. The observed rind thicknesses are compared to the scaled thickness attained from Equation 2-2 for different values of $K$ (black lines).*

We propose that this agreement between our data and the diffusion scaling (Equation 2-2) confirms that diffusive mass transport is the mechanism for rind formation and that $H_2O$ loss from the sample edge drives this process at the expense of the bubbles adjacent to the growing rind. We note that the agreement between the measured $d_l(t)$ and the scaling given by Equation 2-2 with a constant $K = 2$ is systematically less good for smaller samples, which appear to be better scaled with $K > 2$ (e.g., $K = 2.8$ provides the best fit for the 1 mm samples, where $d_l(t)$ is less than the sample radius). We suggest that this deviation from a constant $K$ is due to subtly different trajectories of sample shape from cylindrical to sub-spherical, which occur at different rates in samples of different initial cylinder sizes.

Using the rind thickness evolution scaling $d_l(t)$ given by Equation 2-2, we reanalysed the cross-sectional areas of the sample silhouettes to separate the 2-dimensional sample images into two regions with distinct areas. First, a rind region with area $A_r(t)$ and a vesicular inner region with area $A_v(t)$. In order to compute $A_r(t)$, we use morphological image processing to erode a rim with thickness $d_l(t)$ inward from the edge of the segmented sample image. The computed $A_r(t)$ ratioed with the total sample cross-sectional area $A_s(t)$ increases non-linearly with time, as predicted by Equation 2-2. $A_r(t)/A_s(t)$ is larger for smaller samples and,

for the 1 mm samples, approaches one (fully dense) at finite time (Figure 2-4). This is consistent with the observation that the cross-sectional area stops changing toward the end of the experiment (Figure 2-2).

As noted, the $K$ value in Equation 2-2 has a small apparent dependence on sample size, which we do not account for here; as such, the calculated rind growth rate may slightly over or underestimate the rind growth and cross-sectional area change for each sample; for instance, Figure 2-4d suggests that the rind in the smallest 1 mm sample is still thickening at 50,000 s, whilst textural observation in Figure 2-3g indicates that the sample had fully densified by 12 hrs (43,200 s).
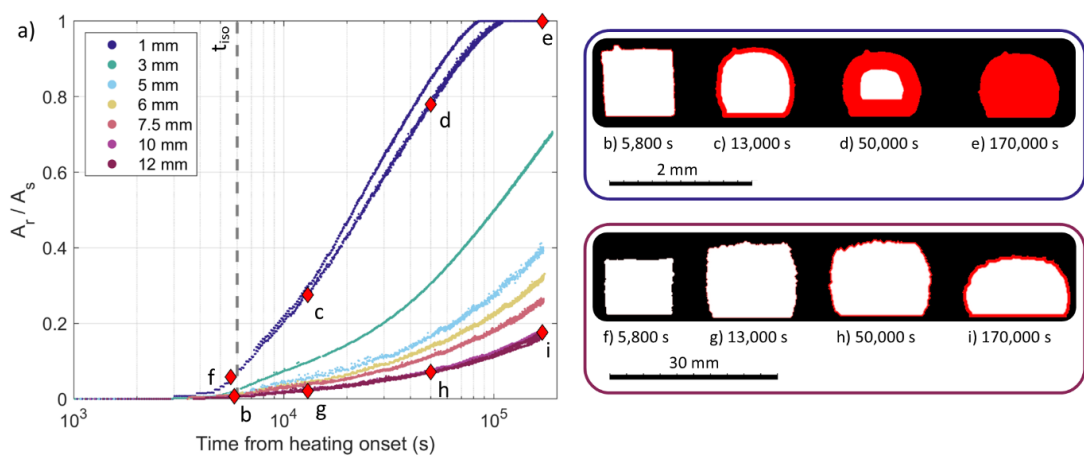


*Figure 2-4: Dense rind growth through time found using image processing. (a) Ratio of the calculated dense rind area $A_r(t)$ to sample area $A_s(t)$ though time. $A_r(t)/A_s(t)$ shows scale dependence, as smaller samples (1 mm; b-e) are more dominated by the rind growth (rind shown in red) than larger samples (12 mm; f-i), for a given time. However, for all samples a rind forms and the samples contract as a result. Each sample is plotted individually in Supplementary Figure A.I-2.*

In detail, the relatively simple scaling given by Equation 2-2 breaks down when the diffusive growth of the rind fully consumes the sample. This break-down can be seen as the data for $d_l(t)$ appear to deviate from the scaling given by Equation 2-2 and instead approach the sample size limit of $d_l \rightarrow r$ for the 1 mm, smallest sample size (see Figure 2-3g). Nevertheless, for larger samples in our sample suite, and particularly for short experiment durations, we expect Equation 2-2 and our image processing technique for rind area quantification to be valid (as supported by Figure 2-3g).

### 2.3.3. Bulk vs internal vesicularity

To constrain the evolution of vesicularity, we based our analysis on the observation that sample volume changes are associated with vesiculation and the diffusive outgassing flux described in the introduction. Therefore, we use the same solid of revolution method (see Section 2.2.3) to convert $A_v(t)$ to a volume representing the volume of the vesicular interior of the samples $V_v(t)$. The rind volume $V_r(t)$ is then the difference between the whole sample volume $V(t)$ and $V_v(t)$ [i.e. $V_r(t) = V(t) - V_v(t)$]. Given that the rind is vesicle free, we can compute the vesicularity of the interior region $V_v(t)$ as $\phi_v(t) = 1 - \big(V_{(0)} - V_r(t)\big)/V_v(t)$. Importantly, this allows us to separately assess the bulk sample vesicularity evolution from that of the interior of the sample. This is useful because while the bulk sample vesicularity is controlled by a combination of internal vesiculation and the diffusive loss of $H_2O$ during rind formation, the region of interior vesicularity is beyond the diffusion front and has not been overprinted by the rind formation.

The estimated bulk sample vesicularities $\phi$ show rapid increases up to peaks of 12-67 % depending on the initial sample volume, with larger samples attaining greater vesicularities (Figure 2-5a). The vesiculation rate (i.e., expansion) increases with the initial sample size, whereas the rate of contraction is faster for smaller samples. The data show that the 1 mm and 3 mm samples proceeded to expand and then fully contract, ultimately returning to their vesicle-free origin, whereas the larger samples exhibited slower contraction rates and thus, longer observation periods would have been required for the contraction process to complete. For instance, due to the non-linear rate of rind growth, our largest 12 mm samples would require ~5 months to fully densify under our experimental conditions (Equation 2-2).

The evolution of the calculated internal sample vesicularity $\phi_v$ for the 1 mm and 3 mm samples was similar to that of their bulk sample vesicularities, albeit with slightly higher peaks (Figure 2-5b). For the intermediate 5-7.5 mm samples, the peak vesicularity was followed by a minor loss in vesicularity after long observation times. The internal sample vesicularities for the larger 10-12 mm samples showed a rapid increase up to 60-70 %, at which point expansion slowed down, and the vesicularity was maintained. Because the bulk volumes of these larger samples decrease at long timescales (Figure 2-2a and Figure *2-5*a) but their internal vesicularities do not decrease (Figure 2-5b), the sample contraction must result from the thickening of the dense rind and the volume reduction associated bubble loss near the sample margin.
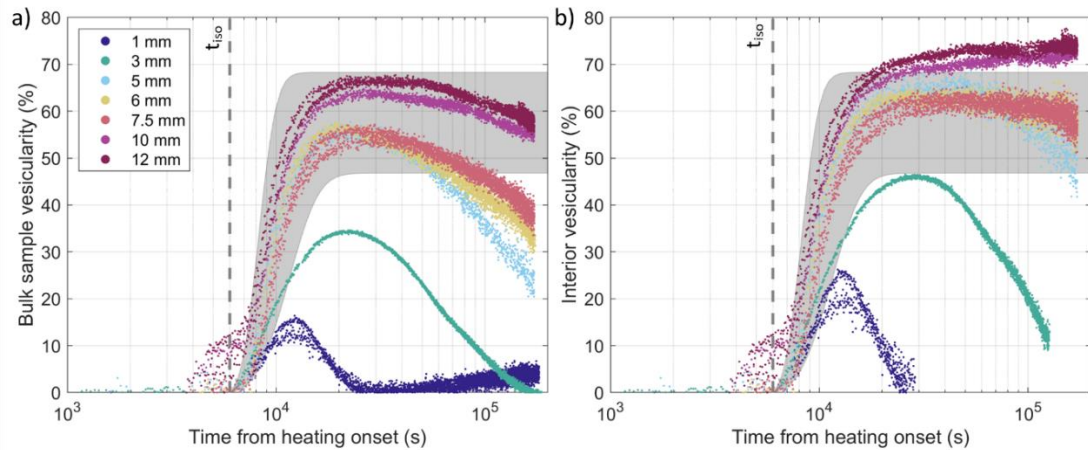
*Figure 2-5: (a) Bulk sample vesicularities and (b) calculated internal vesicularities (i.e., omitting the volume of the rind) for the different initial sample sizes through time. The grey shaded areas present the modelled vesicularity range from an isobaric solution to the numerical bubble growth model of Coumans et al. (2020), using initial water contents ranging between 0.095 wt.% and 0.105 wt.% and an initial bubble number density of $4.63 \times 10^{10}$ $m^{-3}$. Each sample is plotted individually in Supplementary Figure A.I-3.*

In order to analyse the evolution of the internal vesicularity, we modelled bubble growth using the model by Coumans et al. (2020). The model predicts vesiculation of a volatile-supersaturated magmatic melt in a closed system and is based on earlier shell model geometries (e.g., Blower et al., 2001). To apply the model to our system, we use starting conditions of initial water content in the range 0.095-0.105 wt.%, a surface tension $\Gamma$ of 0.3 $N.m^{-1}$ and an initial bubble number density of $4.63 \times 10^{10}$ $m^{-3}$, which we assess by manual segmentation of the backscatter images (see Supplementary Figure A.I-4), and extrapolate to three dimensions following (Sahagian and Proussevitch, 1998). The model inputs include the temperature path applied to our samples at atmospheric pressure, and constitutive models for the volatile solubility and diffusivity, and the melt viscosity. For these, we choose the models developed by Ryan et al. (2015b), Zhang and Ni. (2010), and Hess and Dingwell. (1996). The equation of state for the gas phase is predicted using Pitzer and Sterner (1994). The model predicts higher vesicularities than those observed for the smallest samples but provides a good agreement with values constrained for the larger sample vesicular interiors (Figure 2-5b). This suggests that the internal vesicularity follows standard, closed-system bubble growth.

## 2.4. Discussion

### 2.4.1. Diffusive growth of a dense rind in a vesiculating pyroclast

To understand our experimental observations – namely, how the thickening of bubble-free rinds results in sample-size dependent densification of vesiculating samples – we need to consider the processes, summarized here. 1) The rind grows by diffusion of $H_2O$ toward the sample exterior edge (Figure 2-3; von Aulock et al. 2017); 2) the bubbly interior of the sample vesiculates according to closed-system isolated bubble growth (Figure 2-5b); 3) the rind growth, relative to the bulk sample volume, is sample size dependent (Figure 2-4). Following von Aulock et al. (2017), we argue that these processes are explained by the partial pressure difference between the sample interior and the sample exterior exposed to our laboratory atmosphere. Specifically, the partial pressure of $H_2O$ in a laboratory furnace is estimated to be around 20 % of the total atmospheric pressure at these high temperatures (von Aulock et al., 2017; Wadsworth et al., 2019). The solubility of volatiles dictates the concentration at equilibrium and is dependent on the partial pressure (e.g., Liu et al., 2005; Ryan et al., 2015b), such that the exterior of the sample can have a lower equilibrium solubility than the interior. The result is a partial pressure difference to drive diffusion at the sample edge, which in turn drives rind formation and growth. Volatiles move in response to this partial pressure difference because the solubility at the sample margin effectively drops, leading to gas loss from the sample margin into the surrounding gas, depleting the volatile concentration in the melt. As this diffusion front advances into the sample and approaches bubbles that have already grown, volatiles are scavenged from those bubbles (i.e., volatiles resorb into the melt), causing the bubbles to shrink, which progressively reverses vesiculation in a region proximal to the sample edge. This is a process that is in the category of bubble resorption processes (e.g., McIntosh et al., 2014) albeit driven by changes in partial pressure rather than changes in temperature or total pressure. Thus, as the sample progressively dehydrates, bubble resorption and diffusive outgassing creates a thickening dense rind at the expense of the vesicular interior.

The relative importance of vesiculation and diffusive outgassing is captured by their characteristic timescales. At a given set of conditions, vesiculation occurs to completion (i.e., to equilibrium) over a time $\tau_b$. In detail, models such as that presented by Coumans et al. (2020) demonstrate that $\tau_b$ is controlled by changes in equation of state of the gas in the bubbles, the diffusive flux of volatiles from the melt into the bubbles, and by viscous processes and surface tension. Therefore, there are a range of nested regimes which may control $\tau_b$. But here, we take $\tau_b$ as an output of full models such as the Coumans et al. (2020) formulation

and rely on these to predict $\tau_b$ for a given set of conditions. For example, for our sample and temperature pathway, $\tau_b$ can be estimated from the Coumans et al. (2020) outputs at 12,500 - 20,500 s, which we choose as where the first time derivative of vesicularity evolution falls to $1 \times 10^{-8}$ s$^{-1}$ (see vesicularity asymptotes in Figure 2-5). Similarly, the diffusive flux out of the sample is associated with a timescale found by rearranging Equation 2-2: $\tau_d = r^2/(K^2D)$. The diffusive outgassing timescale required for a sample to complete rind formation and fully densify is determined by its radius. For this reason, it is clear that $\tau_d$ is sample size dependent, while $\tau_b$ is not.

The competition between the vesiculation timescale $\tau_b$ and the diffusive rind formation timescale $\tau_d$ is a Péclet number $Pe = \tau_d/\tau_b = r^2/(\tau_b K^2D)$. The first-order prediction would be therefore that at $Pe \ll 1$, the rind formation can be rapid compared with vesiculation, and so a melt sample or pyroclast would lose gas outwardly by diffusion and not necessarily vesiculate; a regime typical of small fragments where $r$ is small (Wadsworth et al., 2020a). Whereas at $Pe \gg 1$, rind formation is sluggish and vesiculation will complete first. Indeed, as $Pe$ becomes very large (i.e., for large fragments), bubble growth will occur without the development of a volumetrically substantial rind. However, if the partial pressure of the relevant volatile continues to be low outside the fragment, then the rind will progressively thicken after vesiculation has completed to equilibrium $\phi$, such that the end-state can be a dense fragment regardless of $Pe$ if other processes such as cooling do not intervene. This implies the key distinction made by $Pe$ is that while at low $Pe$, outgassing by diffusion dominates and effectively no vesiculation will occur, whereas at high $Pe$, vesiculation will occur, and will be overprinted by diffusive outgassing if the total time available exceeds $\tau_d$. Given the output from Coumans et al. (2020) defining $\tau_b$, we estimate that for our sample size range $4 \leq Pe \leq 1177$ for our experiments (see Table 2-2). Because the lowest $Pe$ value ($Pe = 4.7$) is close to our first order estimate for the regime boundary around $Pe = 1$, we suggest this $Pe$ range is consistent with the variable densification observed in our samples, resulting from coincident vesiculation and rind growth (e.g. Figure 2-3).

The principle finding from our experimental and analytical work is that melt fragments may diffusively lose volatiles at their edges, and not simply vesiculate. This diffusive loss will occur if the partial pressure of the volatile is lower outside the pyroclast than it is in the melt as well as in the bubbles that form by vesiculation. If this is the case, then the Péclet number, and so the size of pyroclasts, determines whether vesiculation can occur or not before diffusion overprints it or before cooling 'locks in' the vesicularity (the effects of cooling will be discussed

later). This analysis helps to position our discussion and ask where in the volcanic system these processes may be relevant.

### 2.4.2. Does the dense rind rheologically impede fragment expansion?

The 1 mm, 3 mm, and to an extent, 5 mm samples, achieve lower internal vesicularities than expected for closed system vesiculation (Figure 2-5b). These smaller samples develop a greater proportion of dense, dehydrated rind more quickly (Figure 2-4), and so they may experience a greater influence from this higher viscosity melt (e.g., Hess and Dingwell, 1996). To resolve the viscosity of the melt across the dense rind, we first estimate the water concentration range during our experiments using the water solubility model for rhyolitic melts of Liu et al. (2005). For the fragment interior, beyond the diffusion front (experiencing a temperature of 1006 °C and pressure of 0.1 MPa) we estimate that 0.088 wt.% of water is soluble in the melt, but in the dehydrated rind we estimate a minimum water concentration of 0.039 wt.%, considering an equivalent 20 % partial pressure of water in the surrounding atmosphere (e.g., von Aulock et al., 2017). Thus we calculate melt viscosities of $5.1 \times 10^6$ Pa s and $7.2 \times 10^6$ Pa s, respectively (Hess and Dingwell, 1996). Here, we suggest that as $\mathrm{Pe}$ decreases with sample size, the greater proportion of high viscosity, dehydrated melt in the smaller samples limits the sample expansion and could result in bubble overpressure. Our results indicate that the internal vesicularities of melt fragments deviate from the closed system bubble growth model when $\mathrm{Pe}$ is less than approximately 100 to 200. Hence, as $\mathrm{Pe}$ and the ratio of dense rind volume to sample volume are inversely proportional to sample size (Figure 2-4a), the 5 mm, 3 mm, and 1 mm samples progressively deviate further from the modelled closed system vesicularity, having progressively lower bulk vesicularities (Figure 2-5b). This deviation from the modelled vesicularity defines an intermediate Péclet regime, between $\mathrm{Pe} \ll 1$, where outgassing completely prevents vesiculation, and $\mathrm{Pe} \gtrsim 200$, where vesicles in the hydrous sample interior follow closed system bubble growth models. Although we acknowledge that $\mathrm{Pe}$ is not strictly a universal scaling for the effect of rind thickness on internal pyroclast pressurisation (which would also depend on the rate of bubble growth), it offers an ideal regime-discriminator to constrain whether bubbles can grow in a pyroclast before all supersaturated volatiles are outgassed by diffusion.

### 2.4.3. An analytical approximation for the scale dependency of bulk vesicularity

Bubble growth models for magma, such as the Coumans et al. (2020) model presented in Figure 2-5, replicate closed-system conditions, and thus, do not account for diffusive outgassing from the system (i.e., pyroclasts) and densification of the rind. Therefore, current models do not resolve the scale-dependent sample evolution presented herein (Figure 2-2, Figure *2-4*, Figure *2-5*a). Here, we integrate the output from the bubble growth model of Coumans et al., (2020) with the semi-empirical constraints obtained for the development of the rind (Equation 2-2), alongside simple geometric relationships, to resolve how vesicularity develops in vesiculating and outgassing melt fragments. To do this, we have to assume a pyroclast geometry. To begin with, we consider dense oblate ellipsoidal samples with a range of initial short and long radii ($r_{01}$ and $r_{02}$). The solid volumes (i.e., not accounting for pore volume) of the vesicular interior $V_v(t)$ and the dense rind $V_r(t)$ are calculated as follows,

$$V_v(t) = \left(\frac{4}{3}\pi(r_{01} - d_l(t))(r_{02} - d_l(t))^2\right) \qquad \text{Equation 2-3.}$$

$$V_r(t) = \left(\frac{4}{3}\pi r_{01} r_{02}^2\right) - V_v \qquad \text{Equation 2-4.}$$

As presented in Figure 2-5b, the internal volumes (i.e., beyond the diffusion front) of the larger fragments are initially unaffected by diffusive outgassing and thus follow closed-system expansion. As such, we calculate the volume of the vesicular interior, using $V_v$ and the vesicularity $\phi(t)$ derived from the bubble growth model (Coumans et al., 2020), via $V_v(t)/(\phi(t) - 1)$. When doing this, we do not account for the observed deviation from the closed bubble growth model for intermediate $Pe$ samples. In Equation 2-5, the dense rind volume $V_r(t)$ is combined with the vesicular interior volume, to provide an estimate for the final bulk volume $V(t)$ of a sample which has experienced both vesiculation-induced expansion and outgassing-induced contraction.

$$V(t) = V_r(t) + \frac{V_v(t)}{(\phi(t) - 1)} \qquad \text{Equation 2-5.}$$

Finally, the initial sample volume and the bulk sample volume $V(t)$ are used to calculate the bulk sample vesicularity (Equation 2-1). In Figure 2-6 we explore how the geometrical relationships outlined in Equation 2-3 - 2-5 impact the evolution of the vesicularity of samples with different initial sizes.
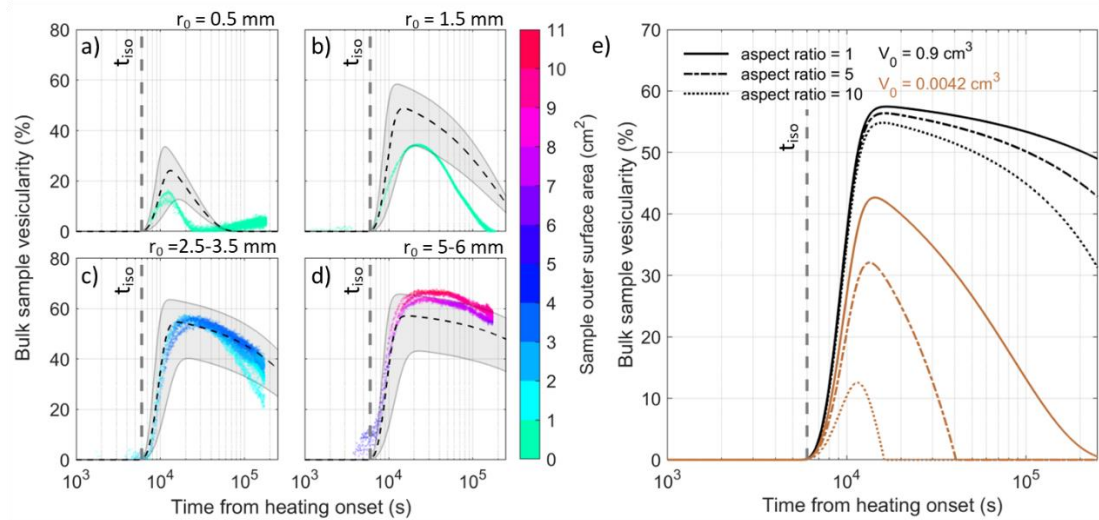
*Figure 2-6: (a-d) Modelled vesicularity for a range of initial fragment sizes, with surface area and volume equivalent to spheres with varying $r_0$, equal to 0.5 mm (a), 1.5 mm (b), 3 mm (c), and 5.5 mm (d). The dashed black lines denote the vesicularity calculated using the average water content (0.1 wt.%), whilst the shaded areas reflect the water content range (±0.005 wt.%). The modelled results are compared to similar sized experimental vesicularity results (see $r_0$ range labels). (e) Modelled vesicularity for two initial sample volumes (equivalent to spheres with $r_0$ equal to 6 mm, coloured black, and 1 mm, coloured brown) using the average water content (0.1 wt.%), to show the impact of varying aspect ratios of 1 (spherical), 5, and 10 (oblate ellipsoids). In both plots, higher surface area to volume ratios (i.e. smaller, and lower aspect ratio) result in more dominant diffusive outgassing-induced contraction.*

Our modelled vesicularities clearly show the scale dependence of the diffusion process acting along fragment margins (Figure 2-6a-d); smaller samples attain slower rates of expansion, faster rates of contraction, lower peak vesicularities, and thus, experience smaller and shorter excursions from their original dense state. The modelled results generally match the trend of the experimental data; however, our analytical approximation deviates from the experimental results for the 1 mm and 3 mm samples (Figure 2-6a-b), which have lower peak vesicularities and faster rates of contraction than the equivalent modelled curves. We suggest this is due to our approximation not accounting for the vesicularity deviation from the bubble growth model in the vesicular interior for intermediate $Pe$ samples. For the high $Pe$ samples ($r \geq 3$ mm), our approximation provides a reasonably accurate constraint (Figure 2-6c-d). The model also deviates from the experimental data because it is based on a spherical geometry, which we compare to our relatively irregular shaped samples; irregular shapes possess higher surface area to volume ratios, which causes greater diffusive outgassing and so results in faster sample densification (i.e., comparatively lower $Pe$ values). It is therefore more appropriate to compare the vesicularity evolution of the modelled curves and experimental data by matching their surface area to volume ratios. To further understand the surface area

to volume control, we explore the vesicularity evolution of vesiculating and outgassing pyroclasts of oblate ellipsoid geometries with aspect ratios of 1, 5, and 10 (Figure 2-6e). Samples with higher aspect ratios achieve greater surface area to volume ratios and are thus more readily impacted by diffusional gas loss and so, reach lower peak vesicularities at slower rates of expansion and faster rates of late-stage contraction. The combined impact of sample size and aspect ratio on the expansive and contractional regimes is clear when comparing the vesicularity evolution of a large and small fragment (Figure 2-6e).

### 2.4.4. Application to volcanic environments

Understanding the relative contribution of vesiculation and diffusive outgassing in shallow and surficial volcanic systems is central to understanding eruptive style (e.g., Degruyter et al., 2012). As magma ascends through the crust, it vesiculates, first with closed bubbles isolated from one another, and then as an inter-connected permeable bubble network that is variably open-system (e.g., Cassidy et al., 2018; Degruyter et al., 2012; Giachetti et al., 2019; Vasseur et al., 2020). While it is possible that the gas in interconnected permeable magma is segregating from the magma itself (e.g., Diller et al., 2006), the propensity for large gradients in gas composition and partial pressures within confined pore spaces is limited by the permeability of the magma, and the gas pressure gradient. However, by contrast, fragmentation in the uppermost conduit can fundamentally change this picture of magma degassing, changing the geometry to discrete particles surrounded by free gas (e.g., Gonnermann, 2015). In this case, the gas and magma are generally highly separated, the flow may be turbulent, and it is possible that gas mixing, gas fluxing from depth, and air incorporation can occur. We propose that in some shallow or surficial fragmental environments, such as tuffisites (cf. Castro et al., 2012; Tuffen and Dingwell, 2005), breccias and ignimbrites (Lavallée et al., 2015), and more broadly, the upper conduits of silicic systems, the partial pressure of gas species such as $H_2O$ can be different between the inside and the outside of vesiculating fragmental pyroclasts, setting the conditions for the processes we explore herein.

The scale-dependence of diffusive outgassing in melt fragments exhibits a clear control on the extent and dynamics of vesiculation within pyroclasts and can result in fragment densification. We posit that pyroclasts with high surface area to volume ratios in complex gas environments, such as fine fragments produced in high energy fragmentation (Kueppers et al., 2006a) or high aspect ratio fragments, can densify by diffusive outgassing. Therefore, where the processes

are not interrupted by cooling, we find that diffusive outgassing completes early in the finest pyroclast fraction, whilst the trivial impact of gas loss from large fragments promotes bubble formation and the maintenance of vesicularity.

As a direct application of the process of diffusive outgassing, we model the evolution of pyroclast vesicularity for a closed system, and for diffusively outgassing spherical pyroclasts (following Section 2.4.3; Figure 2-7). In this analysis we assume conditions in which the total pressure on the pyroclast drops (i.e., in a fragmentation event) and in which the partial $H_2O$ pressure in the gas surrounding the pyroclasts is lower than in the bubbles which form within the pyroclast. Our process of diffusive outgassing requires that the gas species can mix or change on the timescales of eruptions. This may be the case in shallow conduits during pulsatory shallow-seated hybrid explosive-effusive eruptions such as the post-Plinian phase of the 2011-2012 eruption of Cordón Caulle (Schipper et al., 2013); when obsidian pyroclasts form and/ or erupt (e.g., Gardner et al., 2019); in tuffisites forming in shallow conduit wall and plugs (e.g., Heap et al., 2019); and in pyroclastic deposits such as rheomorphic flow (e.g., Wadsworth et al., 2020a).

To set up this model, we envisage a situation following fragmentation in which an initially dense (non-vesicular) pyroclast, with a temperature of 900 °C, is produced at a given depth below the surface $H$, and is initially at a pressure equivalent to a magmastatic pressure $P_o = \rho g H$ where $g$ is the gravitational acceleration and $\rho = 2390 \, \mathrm{kg. m^{-3}}$ is the melt density. Using the solubility model of Liu et al. (2005), the initial $H_2O$ concentration of the melt is calculated to be in equilibrium with the magmastatic and bubble surface pressure, given by $P_o + (2\Gamma/R_{B0})$, where $R_{B0}$ is the initial bubble radius. As the model runs, two things change: (1) the pressure on the pyroclast decreases to 0.1 MPa, inducing bubble growth which is computed using Coumans et al. (2020), and (2) the diffusion at the rim of the pyroclast begins, using our method described in Section 2.4.3. We use two indicative pressure drop rates: (1) the instantaneous end-member of an infinite decompression rate, and (2) a pressure drop rate of 0.003 MPa.s⁻¹, which is in the typical range for more slowly ascending rhyolitic explosive eruptions (Cassidy et al., 2018).
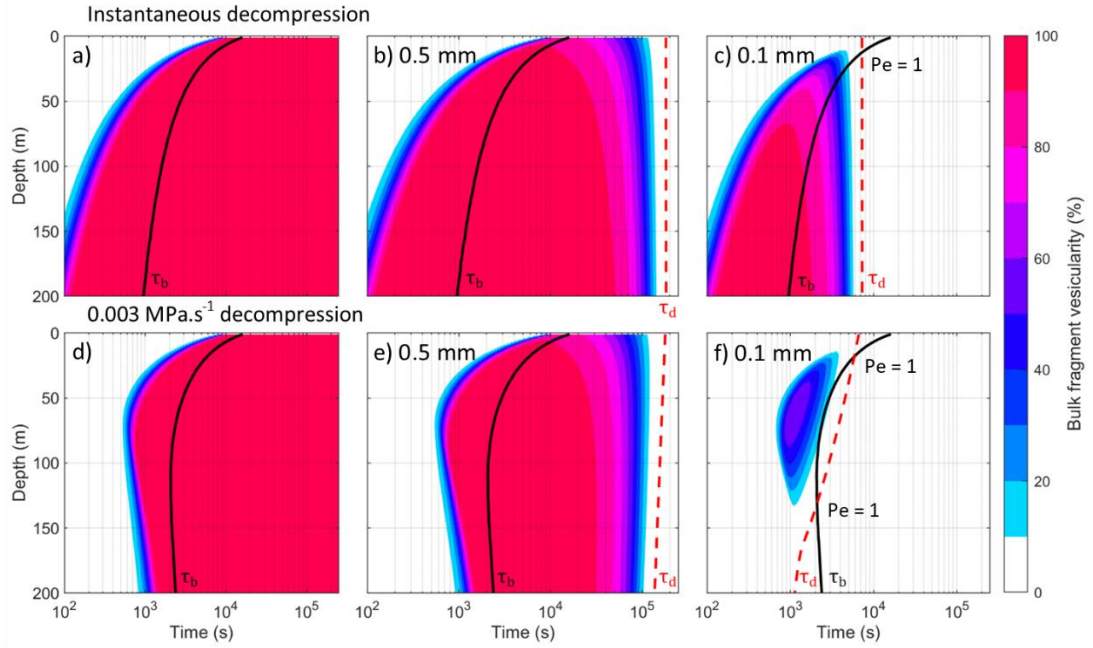
*Figure 2-7: Modelled vesicularity evolution (colour coded) in melt fragments which have isothermally decompressed to atmospheric pressure from different depths and at different rates in a volcanic conduit. (a) vesicularity evolution in a rapidly decompressed, closed system with no diffusive outgassing. The data shows that melt fragments reach a maximum vesicularity more rapidly at greater depth in the system. (b-c) Suppressed vesicularity evolution for fragments with radius of (b) 0.5 mm and (c) 0.1 mm as a function of depth in a volcanic system. (d) In a slowly decompressing conduit (0.003 MPa.s⁻¹), the closed system vesiculation rate is a complex function of depth. Slower vesiculation is suppressed further by diffusive outgassing (e) and may be fully prevented where $Pe < 1$ (f). The solid black lines represent the closed-system vesiculation timescale, picked where the vesicularity gradient falls below $1 \times 10^{-8}$ $s^{-1}$. The red dashed lines represent the size-dependent diffusive outgassing timescale (see text).*

To compute these two processes – bubble and rind growth – we set an initial bubble size of $1.7 \times 10^{-6}$ m (i.e. vanishingly small, as recommended by Coumans et al. (2020), we use the pressure dependent solubility model of Liu et al. (2005) and the same viscosity and diffusivity models as used with our experiments (i.e. appropriate for rhyolites), and we use a few indicative pyroclast sizes (see Figure 2-7). In the computation of bubble growth, both the diffusivity and the viscosity in the shells around the bubbles are updated and integrated across the bubble shells to give average values, accounting for the changing conditions and properties. By contrast, because the law for dense rind growth is a scaling approach, we instead simply iterate the input diffusivity for each pressure and equilibrium solubility value of $H_2O$. This means we compute the rind growth by $d_l(t) = \Delta t^{-1} \int_0^{\Delta t} K\sqrt{D_e t}\, dt$, where $D_e$ is the diffusivity computed using the equilibrium $H_2O$ and pressure at each timestep and $\Delta t$ is the interval of time up to the point of interest. The result is that for instantaneous

decompression to low pressure, $d_l(t)$ relates to a constant $\tau_d = r^2/(K^2 D_e)$ because $D_e$ is a constant value. By contrast, in the case of the slow decompression, there is no single $\tau_d$ for a given initial pressure (and therefore initial depth) because $\tau_d$ evolves as $D_e$ evolves. For this reason, we instead track the iterated $d_l(t)$ at each timestep and output the time when $d_l(t) = r$, which is the condition for when the pyroclast rind has grown to the full pyroclast radius, and diffusive outgassing is complete.

Using the framework described above, we track the change in vesicularity of the pyroclasts as they evolve with time for the case of (1) no diffusive outgassing (Figure 2-7a and d), (2) diffusive outgassing for a 0.5 mm radius pyroclast (Figure 2-7b and e), and (3) diffusive outgassing for a 0.1 mm radius pyroclast (Figure 2-7c and f). We repeat these simulations for particles of different $P_o$ equivalent to $H$ between 1 and 200 m (Figure 2-7). In all runs we assume that the bubble number density (set at $4.63 \times 10^{10}$ m$^{-3}$) is depth-independent. Because our analysis is isothermal, thermal quenching is not considered and so, melt fragments completely degas to reach equilibrium.

Firstly, the results of the model described above show the striking difference between the case where the vesicularity evolution is scale-independent and restricted to melt forming closed bubbles (Figure 2-7a and d), and that in pyroclastic, size-dependent, diffusively outgassing systems (Figure 2-7b-c, e-f). In closed systems, gas exsolution reaches and remains at finite vesicularities, which are a function of the initial sample depth and corresponding initial H$_2$O content (Figure 2-7a, d), whereas gas loss from fragments in an open system counteracts vesiculation. As such, in the pyroclastic case, we note that vesiculation may be prevented, or where it does develop, a rapid increase is followed by a decrease in vesicularity through time. This fragment densification is more pronounced where the vesiculation rate is slow (e.g., shallow, rapidly decompressing melt; Figure 2-7b-c) and in fragments with higher surface area to volume ratios (Figure 2-7c, f). Secondly, we find that higher decompression rates result in both faster vesiculation (Figure 2-7a vs d) and slower rind growth; therefore, vesiculation in rapidly decompressing pyroclasts is able to outcompete the diffusive outgassing more significantly, and so, they attain higher vesicularities than slowly decompressing pyroclasts, which densify faster (Figure 2-7b-c vs e-f). The control of this vesicularity transience is well described by $Pe$. Here, we see that coarse fragments (i.e., high $Pe$) are more dominated by vesiculation, and thus achieve higher and more enduring vesicularities (Figure 2-7b, e) than fine fragments with relatively low $Pe$ (Figure 2-7c, f), as predicted on the grounds of the earlier scaling. The findings clearly show that small pyroclasts may not significantly or persistently develop vesicularity in openly outgassing scenarios,

indicating that a scale- and fragmentation depth-dependent threshold exists beyond which pyroclasts outgas faster than vesiculation can occur, and no intra-clast isolated porosity develops (i.e., $Pe \ll 1$). This is most notable in the model for slowly decompressing, fine pyroclasts (Figure 2-7f), which shows that pyroclasts of a given size may only develop vesicularity (i.e., $Pe \geq 1$) when originating from a particular depth range. So, it follows that the competition between vesiculation and diffusive outgassing during a single volcanic episode may be responsible for the generation of fragments which are dense and hydrous, vesicular, or dense and dehydrated, depending on their depth of origin, decompression rate, size dependent Péclet number, and their time before quenching at the glass transition. Further textural complexity likely arises from surface cooling and fracturing, as displayed in the rinds of breadcrust bombs (e.g., Benage et al., 2014), which we do not consider here. Through this analysis, we find that the degree and rate of decompression and, importantly, the size of magma fragments, can influence the development of vesicularity and gas loss in fragmental volcanic systems.

Our analyses show that pyroclasts in gas-mixed environments can variably experience both, vesiculation and diffusive outgassing. However, our model is flexible, to the extent that it can be applied to a wide range of pyroclast scales and environmental conditions (albeit it would require consideration of cooling rate; see below). Therefore, this competition could have implications for the formation of obsidian pyroclasts (Gardner et al., 2019) or dense rhyolite lava by viscous sintering of pyroclasts (Wadsworth et al., 2020a), or the decompression, emplacement, and sintering of particles in tuffisites, lavas, ignimbrites and ash-fall deposits (e.g., Castro et al., 2014, 2012; Giachetti et al., 2021; Lavallée et al., 2015; Wadsworth et al., 2021). Wadsworth et al. (2021) showed that gas-fluxing through sintering particulate systems occurs in conduits, which is a mechanism by which the partial pressures could be different between clasts and their surrounding gas phase. In these sintering scenarios (e.g., tuffisites, ignimbrites, and conduit backfill), the complex relationships between pyroclast size, vesiculation, and gas loss discussed herein would further influence rheologically-sensitive processes, such as viscous sintering (e.g., Wadsworth et al., 2017a) or fracture healing (Lamur et al., 2019), which may shut inter-pyroclast porosity and permeability (e.g., Wadsworth et al., 2021), thus causing additional physico-chemical feedbacks that further affect these processes (see Chapter 3:). In steps, we envisage the following implications. First, volatile loss by diffusive outgassing decreases the diffusivity in, and increases the viscosity of, silicate melts (Lensky et al., 2001), which would hinder sintering or healing. Second, fragment contraction, associated with gas loss by diffusive outgassing, could generate inter-clast space for the

accumulation of gas, thus counteracting the development of sintering and fracture healing. Third, continued pyroclast size evolution (during vesiculation-triggered expansion and late-stage contraction) would affect the sintering dynamics (Wadsworth et al., 2017a). We suggest that in fragments with efficient diffusive outgassing (i.e., high surface area to volume ratios; moderate to low Pe), the more subdued vesicularity profile will cause fragment expansion to impede less on the surrounding inter-clast, connected porosity and so, permeability will be less impacted (cf. Heap et al., 2019; Kolzenburg et al., 2019; Wadsworth et al., 2016b). This scale and time dependence of porous network evolution, permeability, and diffusive outgassing from in-conduit fragmental melts may translate to a control on volcanic outgassing rates and gas emissions (e.g., Edmonds et al., 2003), pressure accumulation (e.g., Kendrick et al., 2016), and eruption dynamics (e.g., Degruyter et al., 2012; Edmonds and Herd, 2007).

In our experiments, the time required for cooling is always long compared with the processes involved in the experimental investigation; i.e., the cooling timescales $\tau_q$ exceeds $\tau_d$ and $\tau_b$. Therefore, in our experimental work, the cooling pathway is not relevant. However, in volcanic environments, pyroclast cooling may be important, and as such we can speculate that the characteristic cooling timescale $\tau_q = (T_o - T_f)/q$ (Wadsworth et al., 2021) is a relevant timescale for addressing the effects of cooling pathways. Here, $T_o$ is the initial (magmatic) temperature, $T_f$ is a final temperature where the relevant processes can be assumed to cease, and $q$ is the average cooling rate for the fragment. We suggest that if $\tau_q < \tau_d$ or if $\tau_q < \tau_b$, then samples will quench before the completion of diffusive outgassing or bubble growth, respectively. In what follows, we model some volcanic scenarios, and then discuss the cooling effect. Cooling rates of eruptive products are highly variable and span orders of magnitude, from $10^6$ to $10^{-2}$ K s$^{-1}$ (Helo et al., 2013; Nichols et al., 2009; Potuzak et al., 2008; Wilding et al., 2000), controlling $\tau_q$. Pyroclasts in Plinian eruptions may have $\tau_q$ on the order of $10^2$ s (e.g., Gardner et al., 1996); using the modelling parameters from Figure 2-7, this quench time would limit diffusion lengthscales to ~10 μm, which is far below the scales investigated here, but does compare well with rind thicknesses and dense fragment sizes from sintering Plinian ash (cf. Giachetti et al., 2021). Accordingly, for pyroclasts ejected from a conduit, we expect that only very fine material would fully outgas and densify (consistent with Wadsworth et al., 2020a), and for coarse fragments, the relatively thin rind would have a negligible impact on the bulk vesicularity (e.g., Figure 2-4 and Figure *2-5*). Conversely, in environments where $\tau_q$ is long, the pyroclast size range over which diffusive outgassing may be important could be larger. Indeed, the repeated sticking and sintering of pyroclasts at conduit walls or in tuffisites involves an extended period of time in the high-temperature conduit (Gardner et al., 2019,

2018; Heap et al., 2019; Kendrick et al., 2016) compared with standard predictions for Plinian eruption pyroclast cooling timescales. Additionally, transport of pyroclasts in high temperature insulated pyroclastic density currents, from which welded ignimbrites may be deposited, provides a sub-aerial context in which high temperatures may be sustained for longer times, effectively increasing $\tau_q$ (Lavallée et al., 2015). It is in these environments where $\tau_q$ is longer than or comparable with $\tau_d$ and $\tau_b$, that diffusive outgassing may be important. It is also exactly these same scenarios in which gas-mixing or movement from magmatic conditions to conditions of different gas partial pressure are most likely (e.g., during air entrainment in pyroclastic density currents).

Finally, we highlight that the fragment-size dependence of diffusive outgassing has important implications for the textural development of pyroclastic materials. Textural and chemical evidence of vesiculation may be erased if a sample loses its volatiles entirely, to the extent that all bubbles are resorbed as volatiles are transferred out of the pyroclast (Figure 2-3g) and the volatile content reaches equilibrium with the local atmosphere. It may, therefore, be challenging to reconstruct the physical history of pyroclasts in gas-mixed systems. We show here that dense and dehydrated glass fragments are attainable from initially hydrous melts following diffusive outgassing. Also, in cases where dense obsidian clasts are observed in volcaniclastic deposits containing highly vesicular clasts, their presence may not strictly indicate the pre-existence of a dense plug in the conduit before an explosion (e.g., Ross et al., 2017). Instead, they may be the product of initially vesicular clasts with moderate to high Péclet numbers and sufficiently long cooling times, as influenced by their initial sizes, depths of origin, and post-fragmentation environment. We surmise that the fragment-size dependence of diffusive outgassing is key when resolving the post-fragmentation history of pyroclasts which have experienced mixed gas atmospheres, as their texture may result from a hysteretic cycle of vesiculation and densification.

## 2.5. Conclusions

Through the exploration of pyroclast-size dependent vesicularity evolution during vesiculation and diffusive outgassing, we highlight the potential importance of gas loss from the melt as fragments transition from closed to open systems. Whilst in a closed system, decompression causes the exsolution of excess volatiles from a supersaturated melt in order to reach equilibrium at its new, magmatic, pressure condition; in a fragmental open system, diffusive volatile loss from the pyroclast can continue until the melt reaches equilibrium with the

volatile partial pressure of its surrounding atmosphere. In a situation where the volatile partial pressure in the surrounding gas is different from that in the growing bubbles, diffusive outgassing from fragments can occur. In such an environment, vesiculation is concurrent with the diffusive volatile loss from a fragment's surface, which acts to dehydrate the melt along its margin and prompts volatile resorption from bubbles into the melt and the diffusion of those volatiles out of the pyroclast altogether. This leads to the development of a bubble-free rind; as diffusive outgassing proceeds, the rind thickens and acts as a boundary which regulates gas loss from the vesicular interior and so controls the resultant intra-fragment vesicularity. We find that in contrast to closed-system bubble growth, openly outgassing fragments exhibit size-dependent vesicularity evolution, as the effective rate of diffusion is controlled by the surface area to volume ratio of the melt. We show that fine to medium fragmental products in the ash to lapilli range (1 mm to 12 mm) are increasingly impacted by diffusive outgassing at smaller sizes as the surface area to volume ratio increases. The findings indicate that the transience of pyroclast vesicularity, as a function of their size and depth of origin, can substantially impact their resultant physico-chemical properties. This has direct implications for sintering, healing, and densification processes in shallow volcanic environments, which controls gas-magma coupling, volcanic activity, and the associated hazards. We conclude that future work should aim to better understand the evolution of volatile partial pressure changes in shallow conduits, including the propensity for gas mixing, air incorporation, and gas-fluxing, all of which would serve to activate diffusive outgassing from pyroclasts, thus modifying their resultant vesicular texture.

# Chapter 3: Sintering of vesiculating and outgassing hydrous pyroclasts

## Abstract

Hot pyroclastic deposits in volcanic conduits can play a central role in determining the efficiency and longevity of shallow, gas-venting porous networks, which impact gas emissions and the explosive potential of volcanic systems. They can sinter, vesiculate, and outgas in concert – a combination which remains unconstrained. Here we experimentally and theoretically investigate the evolution of the permeable porous network during sintering of vesiculating and diffusively outgassing melt fragments of different grain sizes. We observe that during sintering in oversaturated and coarse-grained hydrous fragmental systems, the intergranular porous network can both shut and open due to concomitant vesiculation and diffusive outgassing, i.e., the process by which volatiles are lost via diffusion from fragment surfaces. We find that bubble growth during vesiculation and bubble resorption during diffusive outgassing compete to determine the intra-fragment isolated vesicularity. The development of intra-fragment vesicularity directly impacts the inter-fragment pore space and its connectivity, which decreases during vesiculation and subsequently increases during diffusive outgassing, prompting complex, non-linear permeability evolution during sintering of these hydrous pyroclasts. We show that the evolution of the porous network is strongly influenced by fragment size – coarse fragments attain greater vesicularities than finer ones – and therefore, the coarse fragmental pyroclasts experience a greater, yet transient, reduction in connected porosity and permeability. We suggest that where vesiculation is sufficient, it can lead to the complete loss of connected porosity and the sealing of permeable pathways much earlier than in a sintering-only system. Our results suggest that classical sintering models are modified by these vesiculation and diffusive degassing processes, and that only an integrated sintering, vesiculation, and diffusion model is able to resolve the evolution of fragmental volcanic systems.

## 3.1. Introduction

Pyroclasts are a principal product of explosive volcanism. Upon eruption, pyroclasts are variably supersaturated in volatiles, and can therefore continue to degas as long as they remain sufficiently hot (e.g., Giachetti and Gonnermann, 2013). Similarly, if deposited hot,

they can sinter and weld to form ignimbrites on the Earth's surface, or tuffisites and vent-filling welded breccias in the volcanic conduit itself (Branney et al., 2002; Kolzenburg and Russell, 2014; Tuffen and Dingwell, 2005). It is the latter – vent-filling deposits and tuffisites – where sintering of hot pyroclasts can essentially clog the volcanic system and inhibit outgassing pathways (Castro et al., 2012), with implications for gas pressure build-up and subsequent eruption triggering. Constraining the porosity and permeability evolution of these in-conduit welding systems is key for understanding volcanic activity and eruption cycles.

Hot pyroclasts – or melt fragments – may deposit (Saubin et al., 2016; Unwin et al., 2021), agglutinate due to sintering (Vasseur et al., 2013a) or fracture healing (Lamur et al., 2019), chemically evolve due to dehydration or rehydration (McIntosh et al., 2014; von Aulock et al., 2017) and physically deform due to shear, vesiculation, and densification (Ryan et al., 2015a; von Aulock et al., 2017). It is clear that all of these processes are relevant in natural volcanic settings, and yet, they are typically investigated in isolation, such that the competition between each process is not well understood. Here, we investigate how the interactions between sintering, vesiculation, and diffusive outgassing impact the evolution of permeable porous networks and consider the implications for fragmental volcanic systems.

Sintering describes the densification of a loose particulate aggregate into a cohesive, variably porous material through diffusional and viscous processes (e.g., Wadsworth et al., 2017a). The evolution and timescales of sintering silicate melt fragments [synthetic; e.g., Wadsworth et al. (2016a) and fine ash; e.g., Gardner et al. (2018)] can be modelled using empirically-validated theory (Wadsworth et al., 2016a). This theory shows that at low pressures, sintering is controlled by the viscosity of the melt, the size of the pore spaces between the grains (which is related to the grain size), and the melt-gas interfacial tension (Wadsworth et al., 2019, 2016a). The resultant permeability of sintering and densifying networks is determined by the connectivity and surface area of the inter-fragment pore space (e.g., Wadsworth et al., 2016b); direct observation and modelling indicate that permeability reduction is non-linear, as the fragmental system undergoes topological inversion (Wadsworth et al., 2017b). However, the previous work in which this theory is tested has focussed on systems in which the melt fragments are not vesiculating during sintering.

Vesiculation occurs in melt fragments when they are supersaturated in volatiles, leading to bubble nucleation and growth (Bagdassarov et al., 1996; Coumans et al., 2020; Giachetti et al., 2010; Navon and Lyakhovsky, 1998; Sparks, 1978). Quenched volcanic products demonstrate that vesiculation occurs inside sintered pyroclasts (Figure 3-1a). Under closed-

system conditions, the porosity of a vesiculating melt fragment is captured by bubble growth models (Bagdassarov et al., 1996; Coumans et al., 2020), which show that bubble growth leads to a bulk volume increase until equilibrium (e.g., Blower et al., 2001). In molten particulate and fragmental systems, we anticipate that vesiculation and the volumetric expansion of pyroclasts would occur at the expense of the connected pore volume between fragments (Figure 3-1b-e).
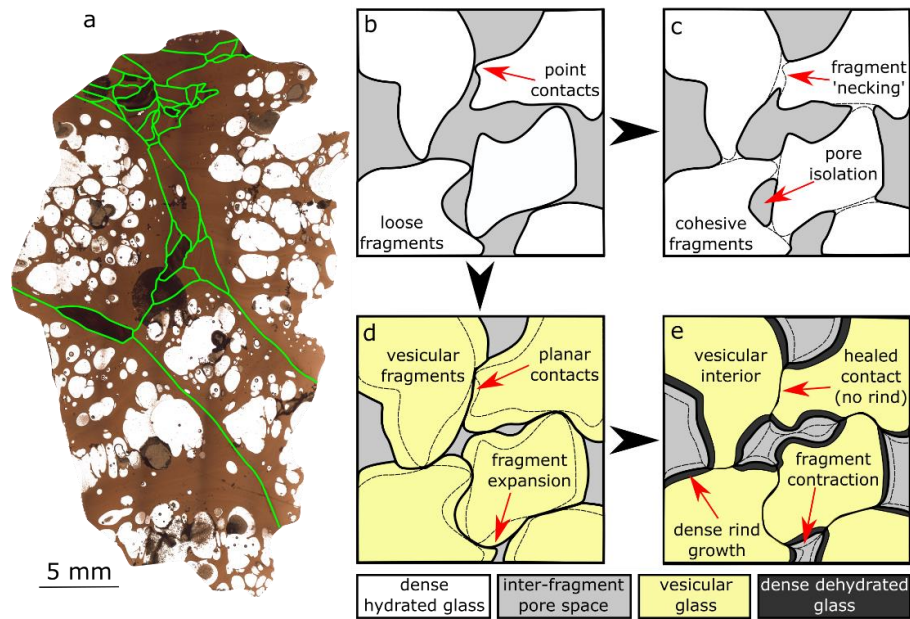


*Figure 3-1: Volumetric changes associated with vesiculation, diffusive outgassing, and sintering, from (a) photomicrograph of naturally sintered glass fragments from Krafla, showing dense rinds, vesicular interiors (white), and fragment interfaces (green). The photomicrograph is available without annotation in Appendix II: Chapter 3; (b) a sketch of an initially cohesionless fragmental melt; (c) sintered, fragmental melt which is anhydrous or has a $Pe \ll 1$; (d) hydrous fragmental melt which develops vesicularity ($Pe \gtrsim 1$) at the expense of the interstitial pore space, followed by (e) diffusive outgassing which creates a dense, bubble-free rind which progressively densifies the vesicular melt fragments. Where $Pe \gtrsim 1$, vesiculation, diffusive outgassing and sintering synchronously impact porosity.*

In open-system conditions, volatile equilibrium in the melt may be modified by the entrainment, mixing, or fluxing of atmospheric and volcanic gases (Rust et al., 2004). This can create partial pressure differences between the melt and the connected pore space, prompting chemical exchange (von Aulock et al., 2017). Experiments have shown that diffusive volatile loss through the surface of vesiculating melt fragments – termed diffusive outgassing - causes marginal volatile resorption and bubble shrinkage, promoting the development of a dense, dehydrated rind, which thickens at a rate predicted by the diffusion length scale (Otsuki et al., 2015; von Aulock et al., 2017; Yoshimura and Nakamura, 2008;

Chapter 2). This resorption reduces vesicularity and causes fragments to densify (Chapter 2). The effective rate of diffusive outgassing is sensitive to the surface area of melt fragments (Otsuki et al., 2015), such that the size of fragments controls the efficacy of diffusive outgassing and the vesicularity evolution.

When occurring together, vesiculation and diffusive outgassing may compete to expand and contract melt fragments, at different rates, depending on the sizes of fragments present in the aggregate material (Chapter 2). Textual analysis commonly captures this competition in sintering fragmental environments, where dense rinds commonly surround parcels of vesiculated melt (cf. Cabrera et al., 2011; Castro et al., 2012; Giachetti et al., 2021; Heap et al., 2019; Saubin et al., 2016; Figure 3-1). For a first order approximation, this competition can be assessed through a fragment size dependent Peclét number $Pe$, which is determined by the ratio of the timescales required for diffusive outgassing and vesiculation to complete (see Section 2.4.1 for further details). Where $Pe \ll 1$, vesiculation may be inhibited by the complete diffusive outgassing of supersaturated volatiles and sintering may proceed following anhydrous melt dynamics (Gardner et al., 2018); whereas, if $Pe \gtrsim 1$, vesicles form and are subsequently resorbed until all bubbles are lost or the densification is otherwise interrupted (e.g., by cooling). Therefore, sintering fragmental systems with $Pe > 1$ will be variably impacted by vesiculation and diffusive outgassing, which may play a decisive role in the evolution of permeable porous networks, and possibly influence the transition between open and closed gas-venting systems. Here, we experimentally investigate and monitor the porosity and permeability development during sintering of vesiculating and outgassing melt fragments of various sizes (i.e., various $Pe$), and assess the power of an integrated sintering, vesiculation, and diffusion model in capturing this complex evolution.

## 3.2. Material and methods

### 3.2.1. Material and experiment setup

For our experiments, we selected a well-studied aphyric, vesicle free, calc-alkaline rhyolitic glass from Hrafntinnuhryggur, Iceland (Ryan et al., 2015a, 2015b; Tuffen and Castro, 2009; Wadsworth et al., 2021). We used the same sample material as in Chapter 2, wherein, the geochemical composition of the glass was determined by X-ray fluorescence and the water content was measured using FTIR at 0.1±0.005 wt.%. The block was manually crushed into irregular-shaped fragments which were sieved to four size ranges to provide a range of $Pe$ conditions (see Section 3.4.1). The fragment size ranges, 0.50–1.00 mm, 1.00-1.40 mm, 1.40–

2.00 mm and 2.00-2.36 mm, are attained through sieving and are henceforth referred to by their average diameters of 0.75 mm, 1.20 mm, 1.70 mm, and 2.18 mm, respectively. The crushed glass was cleaned in an ultrasonic water bath and oven dried at 50 ˚C to remove any adsorbed water. Crucibles were fashioned out of dense holocrystalline basalt from Seljavellir, Iceland (rock described in Lamur et al., 2018) by coring 50 mm-long cylinders with internal and external diameters of 18.6 mm and 26 mm, respectively. The base of each tube was closed using a detachable base of the same basalt. Prior to testing, the crucible assemblies were thermally treated to 1006 °C for 6 hours to ensure no physico-chemical alteration would occur during the experiments. A 13 g aliquot of loose fragments of a single size range were placed into a crucible, which was gently shaken to encourage a uniform packing density. Each glass-filled crucible was heated individually to 1006 °C at 10 °C.min$^{-1}$ in a Carbolite® box furnace. The assemblies were left to dwell at this isotherm for 0.5 to 24 hours, before being cooled at 10 °C.min$^{-1}$. The resultant products were then subjected to porosity and permeability measurements, and select samples were embedded in epoxy, sliced, and imaged using a Hitachi TM3000 scanning electron microscope operating at 15 kV.

### 3.2.2. Volume and porosity determination

The pore space evolution is complex in these experiments. Isolated porosity is fully enclosed within the melt (i.e., as vesicles), between extensively sintered fragments, or trapped by melt fragments agglutinated against the crucible, and cannot contribute to permeable flow through the assembly. Conversely, connected porosity retains system-wide permeable pathways. The inter-fragment porosity can be either isolated or connected, depending on the degree of sintering and pore closure. To quantify the development of porosity the volumetric evolution of the samples and pore space was measured for each experimental product (conducted with different fragment sizes over various dwell times) using an AccuPyc 1340 helium pycnometer from Micromeritics, accurate to ±0.1% of the measured volume. Prior to an experiment the skeletal volume of each thermally stressed crucible $V_B$ was measured. After being filled with crushed glass, the skeletal volume of the pre-experimental sample assembly $V_{BGo}$ were measured, and, following an experiment, the skeletal volume of each sample and crucible $V_{BGp}$ was measured again. The skeletal volume of the experimental glass products $V_{Gp}$ is then given by $V_{Gp} = V_{BGp} - V_B$. Then, the isolated porosity of the sample $\phi_i$ was calculated using Equation 3-1:

$$\phi_i = 1 - \frac{V_{BGo} - V_B}{V_{Gp}}$$

Equation 3-1.

This method assumes that the pre-experimental glass fragments did not contain vesicles (see Supplementary Figure A.II-2:).

The original height of the glass fragment aggregate was measured, which along with the crucible inner diameter, was used to constrain the initial bulk cylindrical volume of the crushed glass and pores $V_{To}$. The post-experimental height of the sintered aggregate was also measured, which was used to obtain the bulk cylindrical volume of the sintered sample $V_{Tp}$. These allowed us to calculate the connected porosity of the glass particulate before $\phi_{co}$ and after $\phi_{cp}$ the experiments, via:

$$\phi_{c(n)} = 1 - \frac{(V_{BG(n)} - V_B)}{(V_{T(n)})} \qquad \text{Equation 3-2,}$$

where the subscripts $(n)$ maybe be replaced with $o$ or $p$ for pre- or post-experiment samples, respectively.

Finally, the total porosities of the pre- and post-experiment sample aggregate (i.e., the combined isolated and connected pore space), $\phi_{to}$ and $\phi_{tp}$, respectively, were determined for each sample using:

$$\phi_{t(n)} = 1 - \frac{V_{BGo} - V_B}{V_{T(n)}} \qquad \text{Equation 3-3.}$$

### 3.2.3. Permeability measurements

To evaluate the permeability of the experimental products, steady state measurements were conducted using a synthetic oil with a density of 862.4 kg.m$^{-3}$. For these measurements, the base of the sample assembly was removed (leaving the basalt tube and sintered fragments), and the assembly was saturated in oil overnight using a vacuum chamber at 0.1 bar. Following Wadsworth et al. (2020), the saturated assembly was placed upright into a tight-fitting Viton® sleeve with a 25 mm inner diameter and extending 26 cm above the sample. The sleeve was then filled with oil, which applied 2.2 kPa of hydraulic head pressure to the sample. As oil percolated through the sample, the pressure was maintained for 10 minutes by continuously refilling the top of the sleeve. We measured the amount of oil passing through the sample and determined the flow rate and permeability using Darcy's law, considering an oil viscosity of 381 mPa.s. To ensure no oil flowed through the basalt tube or between the sleeve and the tube, we assessed the oil permeability of a solid 26 mm diameter by 50 mm core of Seljavellir basalt [with a known gas permeability of $5 \times 10^{-20}$ m$^2$ (Lamur et al., 2018)] and found it to be impervious to oil on the experimental timeframe, under the conditions tested here.

## 3.3. Results

In this study we conducted 59 experiments, the details of which are reported in Table 1. Within the evolving particulate systems, we observe changes to the porous network, including the isolated, connected, and total porosities. The time-dependence of these properties depends on the fragment size. Through textural analysis, we find that each melt fragment grows bubbles and develops an encompassing dense rind which thickens with time. The melt fragments begin to agglutinate and fragment necks form, as sintering ensues, which reduces the connectivity of pore space. Phenomenologically, the volume and connectivity of the inter-fragment pore space also decreases with bubble growth, and subsequently increases through fragment densification, the latter of which occurs faster in finer fragments relative to coarser fragments (Figure 3-2).
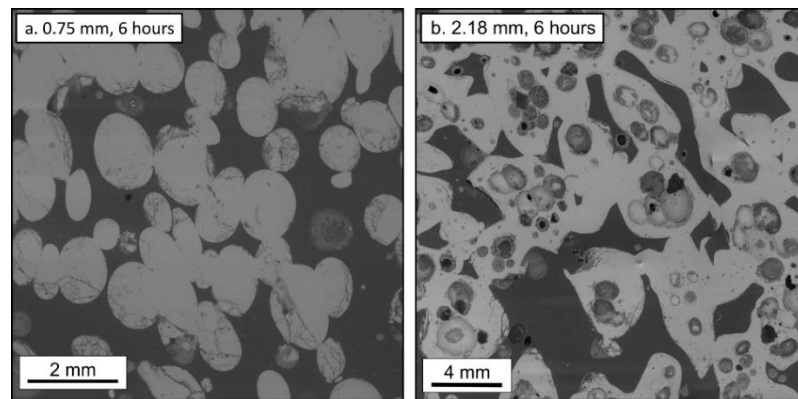


*Figure 3-2: Selected backscatter electron images of the experimental products. Melt fragments (pale grey) vesiculate and are subsequently densified by diffusive outgassing. Finer fragments with low $Pe$ (a) lose vesicularity faster than coarse, high $Pe$ fragments (b) – note the different scale of the images. High vesicularity is associated with lower and less connected inter-fragment pore space (dark grey).*

These processes are captured quantitatively through volume and permeability measurements from the time-series products. The pre-experimental melt is vesicle free and so initially no pore space is isolated. Upon dwelling at the experimental temperature, each samples' isolated porosity rapidly increases to a peak as they vesiculate, before more slowly reducing and returning to zero (Figure 3-3a). The peaks and durations of the porosity curves positively correlate with the fragment size; the 0.75 mm samples increase in the first 3,600 s to a peak of ~5 vol.%, and then return to, and remain at ~0 vol.% after 21,600 s of heating; the 1.20, 1.70, and 2.18 mm samples increase for the first 7,200 s to maximum values of ~10, 25, and 33 vol.%, respectively. Subsequently, the isolated porosities decrease, with the 1.20 mm samples returning to near zero values after 43,200 s of heating, whilst the 1.70 mm and 2.18 mm samples required heating times between 43,200 s and 86,400 s to approach 0 vol.%.

Table 3-1: Experimental sample parameters and results. For each sieve size range $R$, the original, pre-experiment volumes are measured for the empty crucible $V_B$, filled crucible $V_{BGo}$, and cylindrical aggregate $V_{To}$, to calculate the initial connected $\phi_{co}$ and total $\phi_{to}$ sample porosities. Following heating, the permeability $k$ is measured, and the volumes for the filled crucible $V_{BGp}$ and cylindrical aggregate $V_{Tp}$ are remeasured, to calculate the post-experiment isolated $\phi_i$, connected $\phi_{cp}$, and total porosities $\phi_{tp}$.

| R (mm) | t (s) | $V_B$ (mm³) | $V_{BGo}$ (mm³) | $V_{To}$ (mm³) | $\phi_{co}$ & $\phi_{to}$ | $V_{BGp}$ (mm³) | $V_{Tp}$ (mm³) | $\phi_i$ | $\phi_{cp}$ | $\phi_{tp}$ | k (m²) |
|---|---|---|---|---|---|---|---|---|---|---|---|
| | 1800 | 14720.3 | 20158.3 | 10447.5 | 0.48 | 20294.7 | 9912.2 | 0.02 | 0.44 | 0.45 | $6.49^{-10}$ |
| | | 15018.1 | 20451.1 | 10808.9 | 0.50 | 20785.8 | 10254.6 | 0.06 | 0.44 | 0.47 | $1.11^{-9}$ |
| | 3600 | 21112.3 | 26560.7 | 10675.7 | 0.49 | 26773.9 | 10208.4 | 0.04 | 0.45 | 0.47 | $1.34^{-9}$ |
| | | 13510.8 | 18974.2 | 10249.1 | 0.47 | 19325.3 | 9708.4 | 0.06 | 0.40 | 0.44 | $3.13^{-9}$ |
| | 7200 | 17081.3 | 22525.9 | 10118.7 | 0.46 | 22704.9 | 9556.3 | 0.03 | 0.41 | 0.43 | $9.69^{-10}$ |
| | | 14228.7 | 19691.5 | 10789.9 | 0.49 | 19942.2 | 10145.9 | 0.04 | 0.44 | 0.46 | $1.51^{-9}$ |
| 0.50 - 1.00 | 14400 | 17126.9 | 22574.3 | 10716.5 | 0.49 | 22593.3 | 9874.2 | 0.00 | 0.45 | 0.45 | $1.45^{-9}$ |
| | | 14964.7 | 20405.8 | 10338.8 | 0.47 | 20495.1 | 9836.1 | 0.02 | 0.44 | 0.45 | $1.69^{-9}$ |
| | 21600 | 17087.5 | 22531.0 | 11556.1 | 0.53 | 22540.0 | 10787.1 | 0.00 | 0.49 | 0.50 | - |
| | | 14492.2 | 19944.6 | 10664.9 | 0.49 | 19923.0 | 9882.3 | 0.00 | 0.45 | 0.45 | $1.89^{-9}$ |
| | 43200 | 14849.4 | 20313.0 | 10491.0 | 0.48 | 20277.1 | 9548.1 | -0.01 | 0.43 | 0.43 | $1.48^{-9}$ |
| | | 14923.2 | 20366.2 | 10849.6 | 0.50 | 20358.3 | 9811.7 | 0.00 | 0.45 | 0.45 | $3.72^{-9}$ |
| | 86400 | 15012.3 | 20465.0 | 10444.8 | 0.48 | 20499.8 | 9616.0 | 0.01 | 0.43 | 0.43 | $2.08^{-9}$ |
| | | 14624.2 | 20087.2 | 10643.1 | 0.49 | 20078.1 | 9526.4 | 0.00 | 0.43 | 0.43 | $2.06^{-9}$ |

*Table 3-1: Continued.*

| R (mm) | t (s) | $V_B$ (mm³) | $V_{BGo}$ (mm³) | $V_{To}$ (mm³) | $\phi_{co}$ & $\phi_{to}$ | $V_{BGp}$ (mm³) | $V_{Tp}$ (mm³) | $\phi_i$ | $\phi_{cp}$ | $\phi_{tp}$ | $k$ (m²) |
|---|---|---|---|---|---|---|---|---|---|---|---|
| | 1800 | 13453.3 | 18906.6 | 11072.4 | 0.51 | 19258.3 | 10466.5 | 0.06 | 0.46 | 0.48 | - |
| | | 14906.7 | 20346.1 | 11105.0 | 0.51 | 21371.5 | 10463.8 | 0.16 | 0.38 | 0.48 | $2.20^{-9}$ |
| | 3600 | 14312.6 | 19768.2 | 10645.8 | 0.49 | 20458.9 | 10162.2 | 0.11 | 0.40 | 0.46 | $1.63^{-9}$ |
| | | 14990.3 | 20440.0 | 11186.6 | 0.51 | 21131.5 | 10298.0 | 0.11 | 0.40 | 0.47 | $2.54^{-9}$ |
| | 7200 | 21581.2 | 27042.2 | 10789.9 | 0.49 | 27823.9 | 10192.1 | 0.13 | 0.39 | 0.46 | $2.00^{-9}$ |
| | | 14704.8 | 20172.3 | 10833.3 | 0.50 | 20807.9 | 10151.3 | 0.10 | 0.40 | 0.46 | $3.08^{-9}$ |
| | 14400 | 17785.5 | 23227.5 | 10667.6 | 0.49 | 23621.3 | 10080.7 | 0.07 | 0.42 | 0.46 | $2.43^{-9}$ |
| 1.00 - 1.40 | | 14813.1 | 20244.1 | 10776.3 | 0.50 | 20611.2 | 9914.9 | 0.06 | 0.42 | 0.45 | $3.68^{-9}$ |
| | 21600 | 16090.8 | 21536.8 | 10961.0 | 0.50 | 21657.0 | 9933.9 | 0.02 | 0.44 | 0.45 | $3.37^{-9}$ |
| | | 16916.9 | 22261.8 | 10455.6 | 0.49 | 22584.7 | 9531.8 | 0.06 | 0.41 | 0.44 | $3.66^{-9}$ |
| | | 17220.5 | 22683.4 | 10366.0 | 0.47 | 22788.4 | 9738.3 | 0.02 | 0.43 | 0.44 | $2.87^{-9}$ |
| | | 13575.5 | 19033.7 | 10705.6 | 0.49 | 19120.6 | 9828.0 | 0.02 | 0.44 | 0.44 | $2.89^{-9}$ |
| | 43200 | 14175.1 | 19625.9 | 10618.7 | 0.49 | 19660.0 | 9667.7 | 0.01 | 0.43 | 0.44 | $2.92^{-9}$ |
| | | 15048.2 | 20483.2 | 10944.7 | 0.50 | 20545.9 | 9746.5 | 0.01 | 0.44 | 0.44 | $4.03^{-9}$ |
| | 86400 | 14874.8 | 20322.2 | 10971.9 | 0.50 | 20355.2 | 9684.0 | 0.01 | 0.43 | 0.44 | $4.34^{-9}$ |
| | | 14787.8 | 20234.7 | 11034.4 | 0.51 | 20465.5 | 9607.9 | 0.04 | 0.41 | 0.43 | $4.91^{-9}$ |
| | 1800 | 14564.7 | 20021.4 | 10917.6 | 0.50 | 20603.5 | 10455.6 | 0.10 | 0.42 | 0.48 | $3.26^{-9}$ |
| | | 14363.8 | 19793.7 | 10863.2 | 0.50 | 21044.6 | 10295.3 | 0.19 | 0.35 | 0.47 | $2.66^{-9}$ |
| | 3600 | 14543 | 19996.1 | 10412.2 | 0.48 | 21413.3 | 10129.6 | 0.21 | 0.32 | 0.46 | $1.50^{-9}$ |
| 1.40 - 2.00 | | 12641.1 | 18104.6 | 10450.2 | 0.48 | 20067.9 | 9953.0 | 0.26 | 0.25 | 0.45 | $1.80^{-9}$ |
| | 7200 | 17858.6 | 23305.3 | 10602.4 | 0.49 | 25120.0 | 10298.0 | 0.25 | 0.29 | 0.47 | $1.24^{-9}$ |
| | | 13473.3 | 18906.4 | 10512.7 | 0.48 | 20926.5 | 10075.2 | 0.27 | 0.26 | 0.46 | $1.43^{-9}$ |
| | 14400 | 16677.5 | 22124.7 | 11197.4 | 0.51 | 23290.6 | 10553.5 | 0.18 | 0.37 | 0.48 | $3.03^{-9}$ |
| | | 14315.5 | 19772.9 | 10433.9 | 0.48 | 20981.9 | 9852.4 | 0.18 | 0.32 | 0.45 | $1.56^{-9}$ |

*Table 3-1: Continued.*

| R (mm) | t (s) | $V_B$ (mm³) | $V_{BGo}$ (mm³) | $V_{To}$ (mm³) | $\phi_{co}$ & $\phi_{to}$ | $V_{BGp}$ (mm³) | $V_{Tp}$ (mm³) | $\phi_i$ | $\phi_{cp}$ | $\phi_{tp}$ | k (m²) |
|---|---|---|---|---|---|---|---|---|---|---|---|
| | 21600 | 17641.7 | 23090.2 | 10912.1 | 0.50 | 23893.7 | 10004.6 | 0.13 | 0.38 | 0.46 | $2.74^{-9}$ |
| | | 17372.2 | 22813.2 | 10692.0 | 0.49 | 23515.0 | 10398.6 | 0.11 | 0.41 | 0.48 | $2.86^{-9}$ |
| | | 15118.4 | 20568.1 | 11029.0 | 0.51 | 21445.5 | 10249.1 | 0.14 | 0.38 | 0.47 | $3.64^{-9}$ |
| 1.40 - 2.00 | 43200 | 14497.3 | 19937.5 | 10629.5 | 0.49 | 20138.5 | 9781.8 | 0.04 | 0.42 | 0.44 | $3.47^{-9}$ |
| | | 14684.9 | 20143.4 | 10849.6 | 0.50 | 20281.0 | 9800.8 | 0.02 | 0.43 | 0.44 | $4.18^{-9}$ |
| | 86400 | 14609.9 | 20053.2 | 10512.7 | 0.48 | 20138.4 | 9260.1 | 0.02 | 0.40 | 0.41 | $3.42^{-9}$ |
| | | 14837.5 | 20273.9 | 10768.1 | 0.50 | 20351.3 | 9333.5 | 0.01 | 0.41 | 0.42 | $5.37^{-9}$ |
| | 1800 | 14936.3 | 20381.6 | 10599.7 | 0.49 | 21392.9 | 10238.3 | 0.16 | 0.37 | 0.47 | $3.03^{-9}$ |
| | | 13343.7 | 18776.3 | 9662.2 | 0.44 | 19679.8 | 9154.1 | 0.14 | 0.31 | 0.41 | $2.99^{-9}$ |
| | 3600 | 17390.9 | 22853.7 | 11091.5 | 0.51 | 24872.0 | 10898.5 | 0.27 | 0.31 | 0.50 | $1.47^{-9}$ |
| | | 15041.7 | 20478.6 | 11042.6 | 0.51 | 22164.9 | 10273.6 | 0.24 | 0.31 | 0.47 | $2.15^{-9}$ |
| | 7200 | 17125.8 | 22560.1 | 10341.5 | 0.47 | 25123.7 | 10129.6 | 0.32 | 0.21 | 0.46 | $1.01^{-9}$ |
| | | 14894.5 | 20360.9 | 10751.8 | 0.49 | 23055.4 | 10539.9 | 0.33 | 0.23 | 0.48 | $1.05^{-9}$ |
| 2.00 - 2.36 | 14400 | 15307 | 20764.0 | 10113.3 | 0.46 | 22649.1 | 9697.6 | 0.26 | 0.24 | 0.44 | $1.07^{-9}$ |
| | | 14085.2 | 19543.8 | 10523.6 | 0.48 | 21981.7 | 10140.5 | 0.31 | 0.22 | 0.46 | - |
| | 21600 | 16868.3 | 22314.3 | 10789.9 | 0.50 | 24100.5 | 9822.5 | 0.25 | 0.26 | 0.45 | - |
| | | 16824.8 | 22252.4 | 9904.1 | 0.45 | 24115.8 | 9257.4 | 0.26 | 0.21 | 0.41 | $1.10^{-9}$ |
| | 43200 | 13877.4 | 19327.6 | 10654.0 | 0.49 | 19982.1 | 9670.4 | 0.11 | 0.37 | 0.44 | $1.71^{-9}$ |
| | | 14368.7 | 19814.4 | 10890.4 | 0.50 | 20685.4 | 9624.2 | 0.14 | 0.34 | 0.43 | $3.28^{-9}$ |
| | 86400 | 14924.7 | 20368.3 | 10912.1 | 0.50 | 20522.6 | 9485.6 | 0.03 | 0.41 | 0.43 | $3.99^{-9}$ |
| | | 14793 | 20244.6 | 10708.3 | 0.49 | 20319.7 | 9246.5 | 0.01 | 0.40 | 0.41 | $2.69^{-9}$ |

The initial connected porosities average 49±2.8 vol.% across all samples and show no fragment size control. However, the evolution of connected porosity is dependent on fragment size and mirrors the isolated porosity evolution; the connected porosities decrease to a minimum, before increasing and returning to values approaching their pre-experimental porosities (Figure 3-3b). The connected porosities of the 0.75 mm, 1.20 mm, 1.70 mm, and 2.18 mm samples decrease for the first 7,200 s to ~42, 40, 28, and 20 vol.%, respectively. Following this, the connected porosities increase until 21,600 s for the 0.75 mm samples, 43,200 s for the 1.20 mm and 1.70 mm samples, and 86,400 s for the 2.18 mm samples. For the three finer populations, the connected porosities then slightly decrease until the end of observation. Due to the initial absence of vesicles, the total porosities are initially equal to the connected porosities. The total porosities show that the fragmental systems generally densify over the timescale of our observations, yet the paths taken contrast markedly and show subtle fragment-size dependencies (Figure 3-3c). The 0.75 mm and 1.20 mm samples experience relatively constant total porosities for 21,600 s before porosity loss accelerates; in contrast, the 1.70 mm and 2.18 mm samples experience a total porosity increase between 1,800 s and 7,200 s, followed by porosity loss for longer heating durations. After the longest dwell period of 86,400 s the final total porosity reduction appears dependent on fragment size, with the coarser fragments showing more significant densification (Figure 3-3c).

The observed non-linear changes in connected porosity result in a complex temporal evolution in permeability, the values of which develop as a function of fragment size (Figure 3-3d). The first measurements after 1,800 s reveal higher permeabilities for coarser fragment sizes. There is however, less than one log unit in variability across the entire sample suite. Subsequently, the permeabilities of the 0.75 mm samples increase briefly before stabilising. In contrast, the permeabilities of the 1.20 mm samples decrease for the first 3,600 s, before subsequently increasing over longer timescales to values comparable with the 1,800 s measurement. The coarser 1.70 mm and 2.18 mm samples experience a greater permeability decrease for the first 7,200 s, before also subsequently increasing. The extent of permeability reduction, and the time required to reach the lowest value, increase with fragment size.
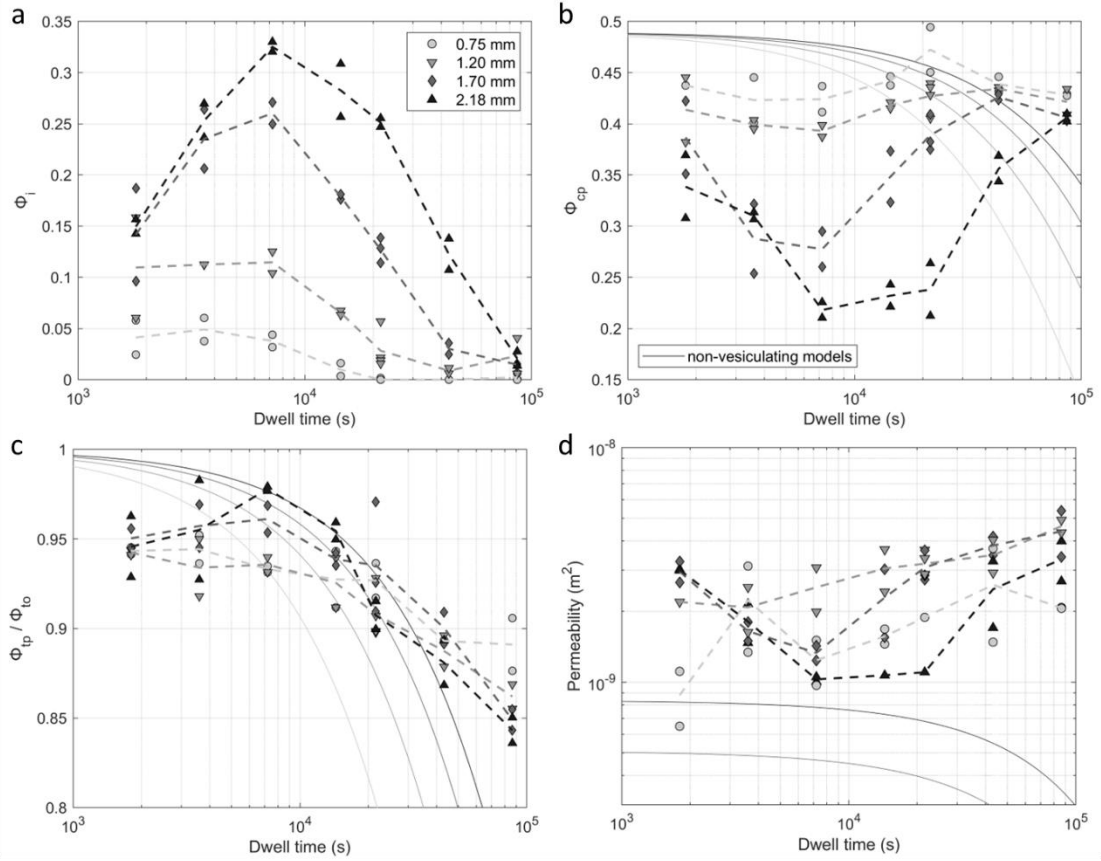
*Figure 3-3: Evolution of the porous permeable network during sintering of vesiculating and diffusively outgassing pyroclasts. The systems experience fragment-size dependent evolution in (a) isolated porosity $\phi_i$, (b) connected porosity $\phi_c$, (c) normalised total porosity, and (d) permeability (see Figure 3-6 for individual pyroclast size plots). For each fragment size, a dashed line connects the average value for each time increment. The sample data are compared to non-vesiculating models (i.e., no dehydration) for densification during sintering* (Wadsworth et al., 2016a)*, the results of which are used in the presented permeability models (Wadsworth et al., 2016b).*

We observe the porosity evolution of our samples is substantially different than would be anticipated for the densification of non-vesiculating systems during sintering (Figure 3-3). We illustrate this deviation by comparing our sample porosity data to the sintering model of Wadsworth et al. (2016a), using the average sieve grain size for each population to estimate the average pore size (following Wadsworth et al., 2016a), a melt-vapour surface tension $\Gamma$ equal to 0.3 N.m$^{-1}$ (Parikh, 1958), a melt viscosity $\mu$ equal to $3.47 \times 10^7$ Pa.s, as modelled using our initial sample water content and the experimental temperature (Hess and Dingwell, 1996), and a monodisperse particle size correction (Wadsworth et al., 2017a). Likewise, we illustrate the permeability deviation using the outputs of the non-vesiculating porosity modelling, in conjunction with a universally scaled permeability model (Wadsworth et al., 2016b). Therein, we estimate the specific surface area $S$ of our fragments using the average grain size for that

population, and include a factor of 1.2 to account for the irregular fragment shape, as defined by Wadsworth et al. (2021). The marked differences between our data and these relatively simple models, which only account for sintering under isochemical conditions, suggests that an approximate estimate for permeability evolution in hydrous fragmental systems demands an understanding of inter- and intra-granular porosity development during simultaneous sintering, vesiculation, diffusive outgassing.

## 3.4. Discussion

As magma rises through a volcanic system, the melt often fragments due to rapid depressurisation (e.g., Spieler et al., 2004), bubble-wall tearing (Sparks, 1978), and strain localisation (e.g., Lavallée and Kendrick, 2022). Concurrently, the melt may become saturated in volatiles as the pressure decreases, leading to vesiculation (e.g., Sparks, 1978). Through the combination of these processes, vesicular pyroclasts may be produced, as found in volcanic ejecta and the shallow conduit (cf. Cabrera et al., 2011; Castro et al., 2012; Giachetti et al., 2021; Figure 3-1). These sub-aerial and near-surface environments may also be subjected to diffusive outgassing if a disequilibrium exists between the volatile partial pressure of the melt fragments and surrounding gas, as would occur following the entrainment of atmospheric air (e.g., Ohsawa et al., 2000). Under these conditions, we may expect vesiculation, diffusive outgassing, and sintering to occur in concert.

In our experiments, the pyroclasts are oversaturated in volatiles (primarily $H_2O$) whilst exposed to the laboratory atmosphere, such that a partial pressure difference exists between the concentration of volatiles in and out of fragments. Therefore, we propose that the evolution of pore space within our hydrous, fragmental melts is determined by the processes affecting volatile redistribution (i.e., vesiculation and diffusive outgassing) and the dynamics of viscous sintering. Our experiments show that a sintering model which does not account for vesiculation cannot be used to resolve the evolution of the permeable, porous networks in these systems, as they exhibit transient and fragment size dependent porosity and permeability excursions (Figure 3-3). As such, here we first set out to evaluate the relative timescales of vesiculation, diffusive outgassing, and sintering, in order to constrain when they operate and dominate during the evolution of pyroclasts in our experiments.

### 3.4.1. <u>Timescales of vesiculation, diffusive outgassing, and sintering</u>

The vesiculation timescale $\tau_b$ gives the time required for bubble growth to fully exsolve the fraction of volatiles in excess of saturation at equilibrium (i.e., when a parcel of magma reaches its maximum vesicularity without diffusive outgassing). We estimate the vesicularity evolution for our samples using the bubble growth model by Coumans et al. (2020), and select $\tau_b$ where the vesicularity asymptote is reached. We run the bubble growth model using our initial sample water content (0.1 wt.% $H_2O$) and experimental temperature and pressure conditions, as well as a bubble number density of $4.63 \times 10^{10}$ $m^{-3}$, following Chapter 2. Within the bubble growth model, we employed the models for the equation of state of gas, volatile solubility, diffusivity, and melt viscosity developed by Pitzer and Sterner (1994), Ryan et al (2015b), Zhang and Ni (2010), and Hess and Dingwell (1996), respectively.

The diffusive outgassing timescale $\tau_d$ gives the duration of volatile loss out of the sample, which is equivalent to the dense rind consuming the full fragment. We calculate the rind thickness $d_l$ over time $t$, where $d_l(t) = K\sqrt{Dt}$ (von Aulock et al., 2017). Here, $K$ is a scaling factor, which for our sample size populations, was empirically constrained at 2.7 (Section 2.3.2). $D$ is the diffusion coefficient of $H_2O$ in the melt. We estimate $D$ using the model provided by Zhang and Ni, (2010), considering the pressure and temperature conditions in our experiments, and the initial $H_2O$ concentration in the melt. As the melt vesiculates in a closed system, the $H_2O$ concentration drops from the initial water content (0.1 wt.%) to the solubility limit of the melt for our experimental conditions (0.088 wt.%), estimated using the model of Liu et al. (2005) at 1 bar pressure. Diffusive outgassing completes when $d_l$ equals the minimum radius of the sample. However, the fragment sizes for each of our populations are determined by a sieve opening range (e.g., 0.5–1 mm), which poorly constrains the radii of our irregular fragments, and so we have some uncertainty on $\tau_d$. To account for this, we calculate apparent fragment radii, $r = 3S^{-1}$, which, as the specific surface area $S$ is determined by an irregular fragment approximation (Wadsworth et al., 2021), would correlate to their equivalent spherical surface area to volume ratios. For our four fragment size populations, we calculate $r$ ranges equal to 0.21–0.42, 0.42–0.58, 0.58–0.83, and 0.83–0.98 mm. We then calculate $\tau_d$ when the diffusion length scale equals $r$, such that $\tau_d = r^2/K^2D$, following Chapter 2. The Peclét number $Pe$, is determined by the ratio of the diffusive outgassing and vesiculation timescales, such that $Pe = \tau_d/\tau_b = r^2/(\tau_b DK^2)$.

Finally, the sintering timescale for shallow, surface tension-dominated melt fragments is given by $\tau_s = a_o\mu C/\Gamma$ (Wadsworth et al., 2019), where $a_o$ is the initial radius of the pores between the packet particles [computed using the model provided in Wadsworth et al. (2016b)], $C$ is a

correction factor, accounting for the fact that we use a monodisperse particle size (computed using Wadsworth et al. 2017a), and $\mu$ is the viscosity. Here, as we consider a chemically evolving system, we anticipate that the viscosity will be transient (Hess and Dingwell, 1996) which will impact the sintering timescale. As such, we consider that the sintering timescale may vary between that predicted for the initially hydrated sample ($\tau_{s(wet)}$), and for the late, dehydrated sample ($\tau_{s(dry)}$), which, following von Aulock et al. (2017), experience 20% partial pressure of water in the furnace compared to the atmosphere, which provides an open system equilibrium for the $H_2O$ concentration in the melt equal to 0.039 wt.%.

*Table 3-2: The timescales for the completion of vesiculation $\tau_b$ (closed system), diffusive outgassing $\tau_d$, and sintering $\tau_s$ (wet and dry) for each of our sieved fragment size $R$, and for the initial, and the two end-state degassed conditions. The Peclét number $Pe$ normalises the diffusive outgassing timescale to vesiculation timescale to assess the dominant mode of volatile redistribution.*

| R (mm) | $\tau_b$ (s) | $\tau_d$ (s) | $\tau_s$ (s) | $Pe = \tau_d/\tau_b$ |
|---|---|---|---|---|
| Initial sample conditions, - 0.1 wt.% $H_2O$, D= $7.01 \times 10^{-13}$, $\mu$= $3.47 \times 10^7$ (wet) | | | | |
| 0.50 | $9 \times 10^3$ | $8.48 \times 10^3$ | $1.05 \times 10^5$ | 0.94 |
| 1.00 | $9 \times 10^3$ | $3.39 \times 10^4$ | $2.10 \times 10^5$ | 3.77 |
| 1.40 | $9 \times 10^3$ | $6.65 \times 10^4$ | $2.94 \times 10^5$ | 7.39 |
| 2.00 | $9 \times 10^3$ | $1.36 \times 10^5$ | $4.13 \times 10^5$ | 15.08 |
| 2.36 | $9 \times 10^3$ | $1.89 \times 10^5$ | $4.96 \times 10^5$ | 21.00 |
| Closed-system equilibrium, - 0.088 wt.% $H_2O$, D= $6.18 \times 10^{-13}$, $\mu$= $4.44 \times 10^7$ (intermediate) | | | | |
| 0.50 | $9 \times 10^3$ | $9.64 \times 10^3$ | $1.35 \times 10^5$ | 1.07 |
| 1.00 | $9 \times 10^3$ | $3.86 \times 10^4$ | $2.70 \times 10^5$ | 4.28 |
| 1.40 | $9 \times 10^3$ | $7.56 \times 10^4$ | $3.78 \times 10^5$ | 8.40 |
| 2.00 | $9 \times 10^3$ | $1.54 \times 10^5$ | $5.30 \times 10^5$ | 17.14 |
| 2.36 | $9 \times 10^3$ | $2.15 \times 10^5$ | $6.36 \times 10^5$ | 23.86 |
| Open-system equilibrium, - 0.039 wt.% $H_2O$, D= $6.18 \times 10^{-13}$, $\mu$= $1.99 \times 10^8$ (dry) | | | | |
| 0.50 | $9 \times 10^3$ | $9.64 \times 10^3$ | $6.05 \times 10^5$ | 1.07 |
| 1.00 | $9 \times 10^3$ | $3.86 \times 10^4$ | $1.21 \times 10^6$ | 4.28 |
| 1.40 | $9 \times 10^3$ | $7.56 \times 10^4$ | $1.69 \times 10^6$ | 8.40 |
| 2.00 | $9 \times 10^3$ | $1.54 \times 10^5$ | $2.38 \times 10^6$ | 17.14 |
| 2.36 | $9 \times 10^3$ | $2.15 \times 10^5$ | $2.86 \times 10^6$ | 23.86 |

Comparing the timescales for the completion of sintering, vesiculation, and diffusive outgassing (Table 3-2; Figure 3-4a) constrains which processes complete and/ or dominate in our experiments. We note that sintering and diffusive outgassing are size dependent

processes and occur from start of the experiment until their completion time; conversely, vesiculation is not fragment size dependent, but requires an incubation period, delaying its onset ($\tau_{b(0)}$). Therefore, the relative position of these timescales establish different scenarios relevant for our experimental conditions, as defined by pyroclast size: (I) $\tau_d < \tau_{b(0)}$ (i.e., $Pe \ll 1$) and $\tau_d \ll \tau_s$ – very fine pyroclasts fully outgas before bubbles nucleate, followed by the sintering of the dehydrated melt; (II) intermediate sized fragments, where $\tau_d < \tau_b$ (i.e. $Pe < 1$) and $\tau_d < \tau_s$, – vesiculation and diffusive outgassing compete concurrently to expand and densify the melt fragments, respectively. Because $\tau_d < \tau_b$, the fragment fully outgasses before vesiculation could complete. Once $\tau_d$ is reached all vesicularity is lost and the dehydrated melt continues to sinter; (III) intermediate sized fragments, $\tau_d > \tau_b$ (i.e., $Pe > 1$) and $\tau_d < \tau_s$, – similar to scenario II, vesiculation and diffusive outgassing occur concurrently, however here, vesiculation reaches its closed system equilibrium prior to losing all vesicularity through diffusive outgassing. Again, sintering of the dry melt completes last; (IV) coarse fragments, where $\tau_d \gg \tau_b$ (i.e., $Pe \gg 1$) and $\tau_d > \tau_s$, – vesiculation reaches equilibrium with little impact from diffusive outgassing. Sintering also dominates over diffusive outgassing and the associated rind growth, leading to sintered melt aggregates which are variably vesiculated and hydrous.
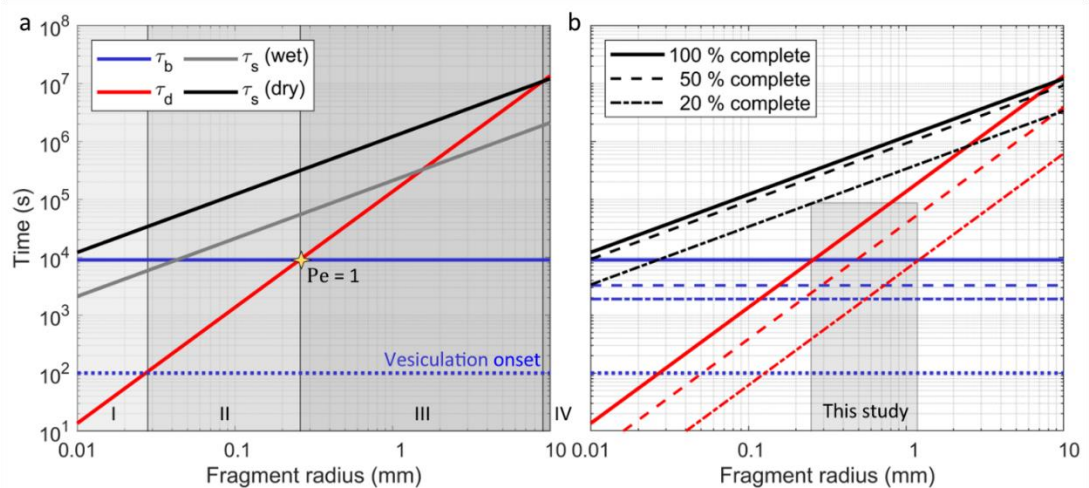


Figure 3-4: Timescales of vesiculation $\tau_b$, diffusive outgassing $\tau_d$, and sintering $\tau_s$ (wet and dry). (a) melt fragments may reach the time required for each process to complete in different orders, depending on the fragment size of the aggregates. In scenario I, fragments outgas before the onset of vesiculation (blue dotted line), followed by sintering of dehydrated fragments $\tau_{s(dry)}$; in scenario II, vesiculation and diffusive outgassing occur concurrently, but the fragment fully outgasses before vesiculation and sintering complete ($Pe < 1$), and sintering is the final processes to complete; similarly, in scenario III, vesiculation and diffusive outgassing occur concurrently, but here, vesiculation completes before diffusive outgassing ($Pe > 1$), and sintering is the final processes to complete; in scenario IV, fragments vesiculate

*to their fullest extent and seal through sintering before completion of diffusive outgassing. (b) Progression of vesiculation (blue lines), diffusive outgassing (red lines), and sintering (black lines). These processes progress to completion in a non-linear fashion; the progress of vesiculation is based on vesicularity (e.g., 20 % complete is equivalent to 20 % of the final, closed-system vesicularity), the progress for diffusive outgassing is based on the closed-system water solubility and is predicted by the model for rind growth (e.g., 20 % denotes where the rind thickness equals 20 % of the fragment radius), and the progress of sintering is taken from the modelled results for our samples, using Wadsworth et al. (2019), when the initial connected porosity is reduced by one fifth (i.e., 20 %) and by half (i.e., 50 %).*

We suggest that for all four scenarios, a dense rind will form which, even when thin relative to the fragment radius, will influence the inter-fragment dynamics and so, these openly outgassing sintering pyroclasts should be assessed using $\tau_{s(dry)}$, which increases the fragment size range where scenarios II and III are applicable (Figure 3-4b). We note that $\tau_d$ is largely unaffected by dehydration for our samples which originally contained only 0.1 % water (Table 2), but, for more hydrous samples, $\tau_d$ may vary significantly (Section 2.4.4). We stress that the timescales outlined in Figure 3-4a provide the approximate, characteristic time required for the completion of each process. Vesiculation, diffusive outgassing, and sintering progress non-linearly, and remain active from their onset until reaching their respective completion timescale (Figure 3-4b). In the next sections, we invoke these scenarios to resolve the processes responsible for the observations made in our experiments.

### 3.4.2. Porosity and permeability hysteresis

Our experiments are contained by the intermediate scenarios II and III defined above (Figure 3-4a), whereby we expect vesiculation and fragment size dependent diffusive outgassing to compete, before the system densifies substantially through sintering. In our samples, bubble growth during vesiculation rapidly creates isolated porosity, which increases the skeletal melt volume at the expense of inter-fragment pore space (Figure 3-5); conversely, marginal bubble resorption during diffusive outgassing slowly densifies the skeletal volume and increases the inter-fragment pore space. We find that this competition is controlled by fragment size, where a systematic shift in the vesicularity evolution of our samples creates non-unique, fragment size dependent hysteresis in porosity and permeability (Figure 3-5).

Diffusive outgassing is less effective for systems of coarser fragments compared with systems of finer fragments. This means that for relatively coarser fragment sizes, vesiculation is increasingly dominant, which results in greater isolated and connected porosity changes before experiencing densification due to diffusive outgassing (Figure 3-5a v 3-5d). The more

substantial reduction in connected porosity due to vesiculation develops increasingly clear permeability relationships in coarser fragmental melts (Figure 3-5e v 3-5h). However, diffusive outgassing continues to occur after vesiculation has completed, causing continual fragment densification due to volatile resorption until the time $\tau_d$ is reached (see Figure 3-2a); this enhances connected porosity and permeability (e.g., Figure 3-5h).
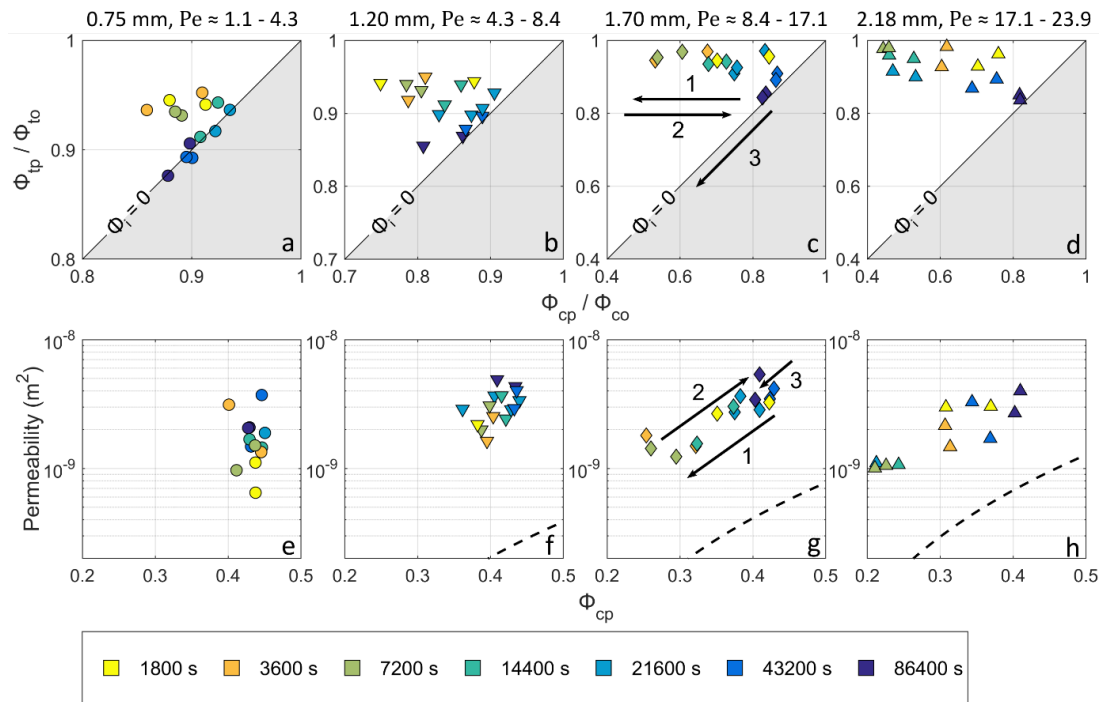


*Figure 3-5: Porosity and permeability hysteresis is dependent on fragment size (and therefore Pe). Here, $\phi_c$ and $\phi_t$ are the connected and total porosities, where o denotes the value prior to heating and p is the value following heating. In steps (as shown by the numbered arrows); (1) coarser fragments develop more vesicularity [porosity is isolated, as the data move away from the $\phi_i = 0$ line (a-d)], at the expense of connected porosity and permeability (e-h). (2) diffusive outgassing densifies melt fragments until the isolated porosity is lost, which increases the connected porosity and permeability; and (3) sintering densifies the full system, reducing the total and connected porosities, which are approximately equal. The densification through sintering is minor at these timescales, and so permeability shows little effect. The permeability model of Wadsworth et al. (2016b) is presented as a dashed line.*

The behaviour described here is complicated by the observation that sintering acts to progressively densify the system (e.g., Figure 3-3c) and close the connected porosity, thereby reducing permeability and increasing $\tau_d$. At short timescales relative to the sintering timescale (where vesiculation and diffusive outgassing operate), the resultant expansion and densification of hydrous fragments modify the total porosity evolution from the expected sintering curve (Figure 3-3c). Yet, densification is evident in the total porosity reduction

observed for the longer duration experiments, particularly in the fine-fragment systems which would experience faster sintering rates (e.g., Figure 3-5a).

Previous studies have suggested that densification through sintering may have a limited impact on permeability until $\sim 0.25\tau_s$ (Wadsworth et al., 2017b), which is beyond the experiment duration for our samples. This is consistent with our observation that permeability is not substantially impacted by sintering in our experiments. We expect that longer durations at high temperature would cause further densification and result in more substantial permeability reduction. For hydrous systems, we may therefore expect that aggregates of fine fragments at $Pe \ll 1$ will rapidly expel their volatiles through diffusive outgassing and closely follow anhydrous porosity and permeability models (scenario I, Figure 3-4a). For aggregates of intermediate fragments (including our full fragment size range), connected porosity and permeability may reduce whilst dominated by vesiculation, and then subsequently increase again during diffusive outgassing, and finally, experience a second reduction during sintering (scenarios II and III, Figure 3-4a). For aggregates of coarse fragments at $Pe \gg 1$, connected porosity and permeability decrease first during vesiculation and then further during sintering, whilst the impacts of diffusive outgassing are increasingly muted as the fragment size increases (scenario IV, Figure 3-4a).

### 3.4.3.   Analytical approximation of porosity in hydrous fragmental systems

To approximate the impact of sintering, vesiculation, and diffusive outgassing on the isolated and connected porosity of hydrous fragmental systems, we employ previously established models for densification through sintering (Wadsworth et al., 2019), closed system bubble growth (Coumans et al., 2020), and one-dimensional diffusion scaling (von Aulock et al., 2017). However, as sintering is the last process to complete for our experimental conditions (Figure 3-4b), we first opt to disregard sintering and only estimate the volumetric impact of vesiculation and diffusive outgassing on the isolated pore space. Following Section 2.4.3, we consider individual spherical particles with initial volume $V_{I(0)} = \frac{4}{3}\pi r^3$, subject to the following steps; 1) the evolution of vesicularity $\phi(t)$ is estimated for a closed system using the bubble growth model from Coumans et al., (2020), as described in Section 3.4.1; 2) the rind thickness $d_l(t)$ is subtracted from the initial apparent fragment radius $r$ to partition the spherical volume into a shrinking hydrous interior $V_{int(0)} = \frac{4}{3}\pi(r - d_l(t))^3$ and a thickening dehydrated rind; 3) the interior volume $V_{int(0)}$ is expanded by the vesicularity $\phi(t)$; 4) the evolving vesicular interior $V_{int}$ and dense rind volumes are summed to provide the bulk

skeletal fragment volume $V_I(t)$ throughout vesiculation and diffusive outgassing (Equation 3-4);

$$V_I(t) = -\frac{V_{int}}{(\phi(t)-1)} + V_{I(0)} - V_{int}$$
<div align="right">Equation 3-4.</div>

The bulk, open-system vesicularity for a fragment is then given by $\phi_i(t) = 1 - V_{I(0)}/V_I(t)$. For a monodisperse fragmental system which has not isolated any pore space through sintering, the development of any isolated porosity would be attributed (and so equal) to the vesicularity.

Given that the isolated and connected pore volumes are inversely proportional whilst $t < \tau_d$ (Figure 3-5), we can approximate the connected porosity of a monodisperse fragmental system by first estimating the skeletal volume evolution of the system $V_{I*}(t)$, in which sintering does not isolate any pore space (Equation 3-5),

$$V_{I*}(t) = \frac{-\rho_f V_T}{\phi_i - 1}$$
<div align="right">Equation 3-5,</div>

where $\rho_f$ is the fragment packing fraction and $V_T$ is the total volume of the system. The evolving connected porosity $\phi_c(t)$ is then calculated using $\phi_c(t) = 1 - V_{I*}(t)/V_T$.

To incorporate the impact of sintering on the connected porosities, we first consider the resultant densification in isolation using the non-vesiculating sintering model of Wadsworth et al. (2016a). The change in connected porosity is given by,

$$\frac{d\phi_{cp}}{dt} = -\frac{3\Gamma}{2\mu a_o}\left(\frac{\phi_{co}}{1-\phi_{co}}\right)^{1/3} \phi_{cp}^{2/3}\left(1 - \phi_{cp}\right)^{1/3}$$
<div align="right">Equation 3-6,</div>

where the viscosity $\mu$ is estimated using the water content of the dehydrated, outgassed rind (Hess and Dingwell, 1996), and the initial pore size $a_o$ accounts for the approximately monodisperse particle size distribution of our experiments, following Wadsworth et al. (2017a). The pore volume evolution through sintering is then calculated by $V_s(t) = V_T \phi_{cp}(t)$.

To assess how concurrent sintering, vesiculation and diffusive outgassing impacts the connected porosity, we combine the results from Equation 3-5 and Equation 3-6, assuming, for simplicity, that the two equations (and the underlying processes) do not interfere with one another. With this caveat, we estimate the connected pore volume evolution of monodisperse, vesiculating, diffusively outgassing, and sintering fragmental systems $V_{C*}(t)$, where $V_{C*}(t) = V_T - V_{I*}(t) - (V_{S(0)} - V_S(t))$. The estimated connected porosity evolution $\phi_{c*}(t)$ is then calculated using $\phi_{c*}(t) = 1 - (V_T - V_{C*}(t))/V_T$.

By assuming that densification during sintering progresses independently from the physical impacts of vesiculation and diffusive outgassing, we do not account for complex interactions and feedback mechanisms, such as; fragment expansion increasing the melt contact area and thereby increasing the healing surface (e.g., Lamur et al., 2019) and fragment agglutination rate; sintering reducing the surface area of the aggregate (e.g., Wadsworth et al., 2021) and thus hindering the effectiveness of diffusive outgassing; and vesicular fragments being subject to intra-fragment interfacial forces acting between the vesicles and surrounding melt films (e.g., Mangan and Sisson, 2005), thereby disrupting the surface tension driven contraction of the particulate. Despite this simplification, we find that the model outlined here for a monodisperse system provides a close approximation to the evolution of the isolated and connected porosities of our samples (Figure 3-6).
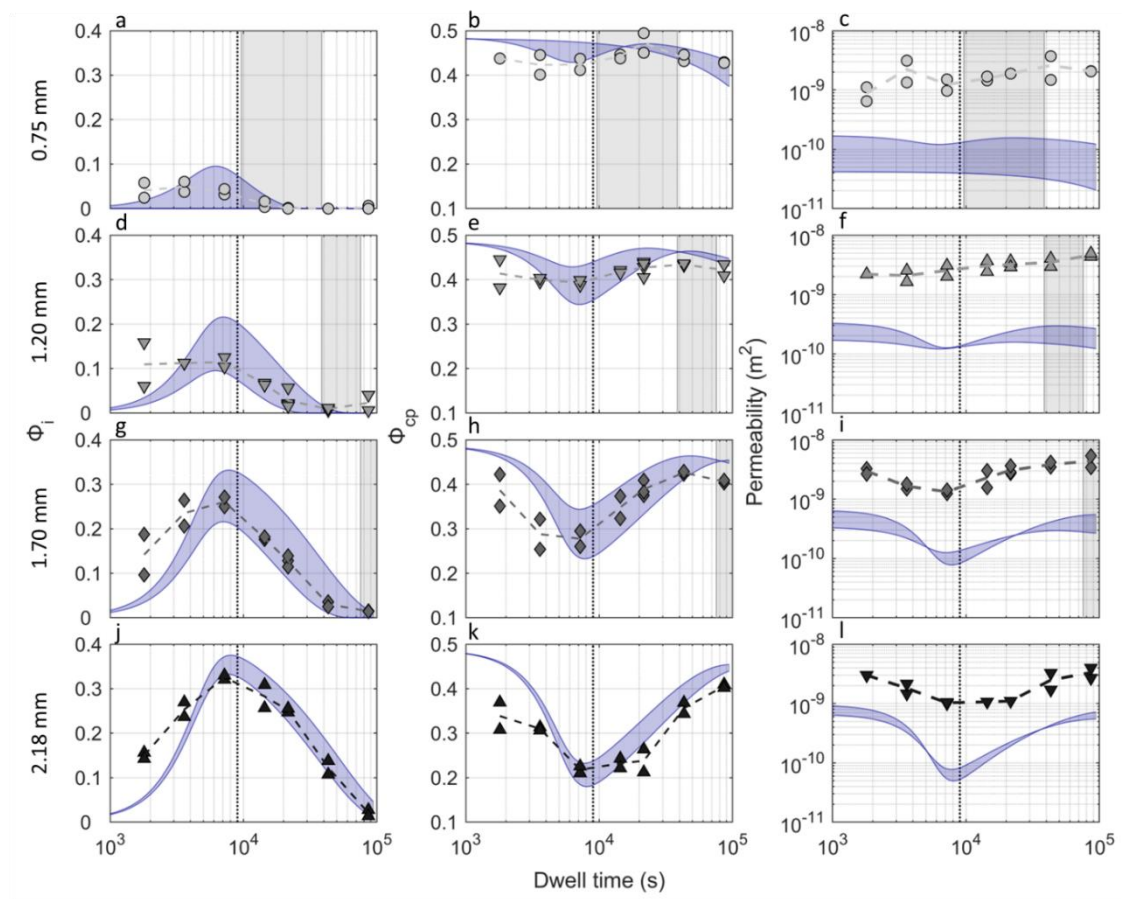


*Figure 3-6: The isolated sample porosities $\phi_i$ (column 1) and connected sample porosities $\phi_{cp}$ (column 2) are compared to a fragment size-dependent geometrical approximation for vesiculation, diffusive outgassing, and sintering (blue shading). The sample permeabilities (column 3) are compared to modelled values using the modelled connected porosities and a permeability model (Wadsworth et al., 2016b). The vesiculation timescale is displayed as a dotted black line, whilst the range in diffusive outgassing timescales is shown by the grey shaded vertical region.*

The impact of fragment size on the porosity distribution is captured to a reasonable extent, and we find that $\tau_d$ is a useful measure for determining the time required to fully densify fragments (see $\tau_d$ range in Figure 3-6). Furthermore, when the approximation for the connected porosity is input into the porosity-permeability model of Wadsworth et al. (2016b), following the details in Section 3.3, we obtain an estimate for the permeability evolution in sintering, hydrous fragmental melts, which shares similar attitudes to our data (Figure 3-6). We therefore suggest that our approach is appropriate when $\tau_b$ and $\tau_d$ are much shorter than $\tau_s$, such that sintering can be considered to progress unimpeded.
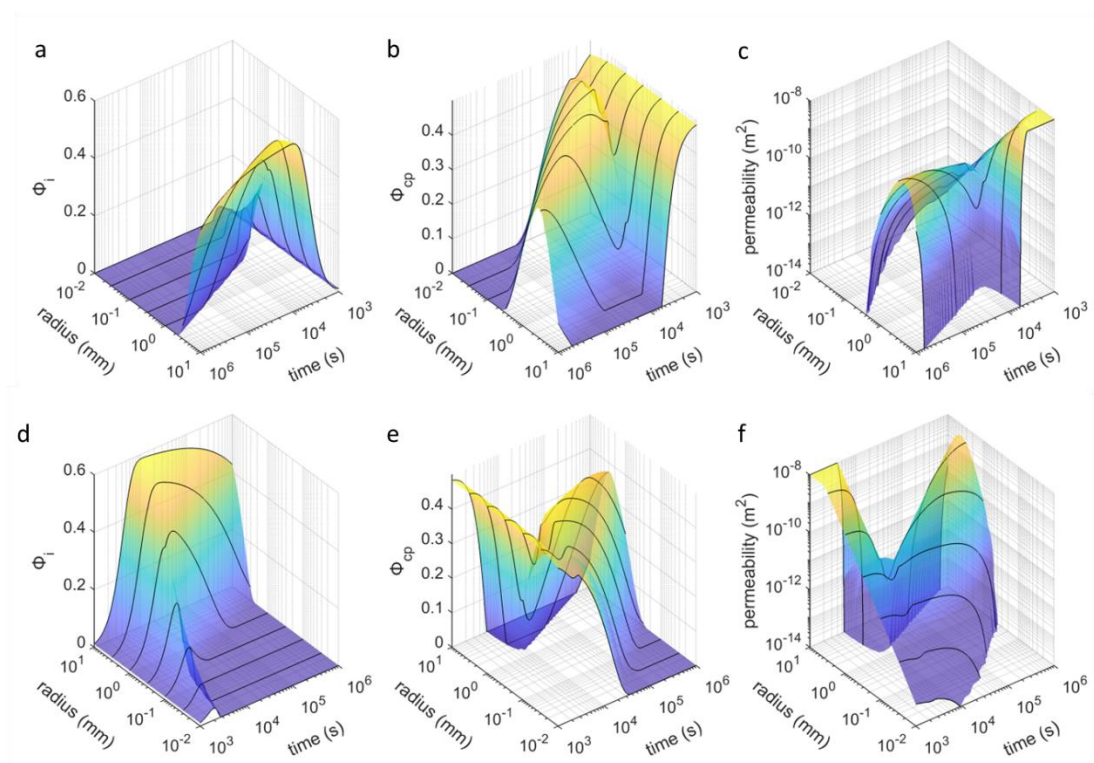


Figure 3-7: Modelled (a) isolated porosity $\phi_i$, (b) connected porosity $\phi_{cp}$, and (c) permeability due to vesiculation, diffusive outgassing, and sintering of hydrous melt fragments in open-system conditions. (d-f) alternate view of the top row. Note that vesiculation causes a drop in connected porosity and permeability, which is reversed by diffusive outgassing. Densification via sintering overlays this transient behaviour and causes a progressive loss in connected porosity and permeability.

This modelling reinforces the importance of fragment size when considering the evolution of porosity and permeability in hydrous fragmental melts (see Figure 3-7), which maintain an open system and a partial pressure differential with the surrounding gas. Extrapolating the relationship between fragment size and the minimum connected porosity, we suggest that, under certain conditions, the connected porosity may reach zero (Figure 3-7b, e) and so, the system could momentarily seal due to the sole action of vesiculation (Figure 3-7). This scenario

occurs when the skeletal melt volume equals the total system volume ($V_{I*}(t) \approx V_T$), such that all inter-fragment pore space is lost, which marks the limit of the open systems studied here. This may be achieved by the considerable vesiculation of monodisperse fragments (i.e., coarse and significantly oversaturated) or by less substantial vesiculation in densely packed fragmental systems, as might occur with high polydispersity. We thus anticipate that sealing by vesiculation may be applicable for a wider range of particle size distributions and occur much earlier than via sintering-induced densification.

### 3.4.4. Implications for natural fragmental melts

Understanding the evolution, distribution, and connectivity of porosity in fragmental melts, and the resulting permeability, is key for resolving the development of preserved systems through textural analysis (e.g., Colombier et al., 2017) and for constraining gas emission volcanic activity (e.g., Heap et al., 2019; Kolzenburg et al., 2019). Our analyses highlight that coarse oversaturated fragmental melts which experience a partial pressure differential with their surrounding gas may evolve in a complex manner compared with very fine particles that do not vesiculate (e.g., Wadsworth et al., 2021). Careful assessment of particle size distributions is required to determine the fragment size dependent porosity and permeability evolution during sintering of dehydrating systems; fine melt fragments may diffusively outgas without vesiculating and closely follow anhydrous porosity–permeability relationships, as shown in Wadsworth et al. (2021); coarser fragments attain higher and more long-lived vesicularities, which lead to substantial but transient losses in connected porosity and permeability.

For certain conditions (e.g., fragments are sufficiently hydrous, coarse, or densely packed) vesiculation can shut all intergranular void space, and the system may seal permeable pathways more rapidly than sintering alone, potentially inhibiting gas emission and promoting gas accumulation and pressurisation. Sealing through vesiculation accounts for the textures present in fragmental infill (Figure 3-1a), where vesicular melt parcels are separated by agglutinated dense rinds (cf. Cabrera et al., 2011; Castro et al., 2012; Giachetti et al., 2019; Heap et al., 2019; Saubin et al., 2016; Schipper et al., 2021). Where systems do not seal, the transience of vesicularity suggests that dense melt fragments should not necessarily be taken at face value as they may have vesiculated and subsequently resorbed and densified (see Figure 3-2). Therefore, in volcanic conduits where localised fragmentation is prevalent (e.g., Schipper et al., 2021), diffusive outgassing from pyroclasts provides an effective means of

dehydrating magma, which, following further sintering, may produce dense and dry melts (as suggested by Wadsworth et al., 2020a).

The new Insights we have made into porosity and permeability evolution in complex sintering systems relevant to natural volcanic systems may be applied to shallow conduits (e.g., Schipper et al., 2021), tuffisite infill (e.g., Saubin et al., 2016), in-conduit sintering during pyroclast transport (e.g., Giachetti et al., 2021), and ignimbrites (e.g., Lavallée et al., 2015), and the simple models we provide may prove useful for determining the longevity and efficiency of open gas venting networks.

## 3.5. Conclusions

Through the use of novel experiments, we highlight that the evolution of coarse hydrous fragmental melts is not captured by classical sintering models and instead, their porosity and permeability evolution is partly controlled by vesiculation and diffusive outgassing. The nucleation and growth of bubbles progressively expands melt fragments into the inter-fragment pore space, which loses connectivity and permeability. However, when fragments are in an open system, vesiculation acts in competition with diffusive outgassing, during which, volatile resorption densifies melt fragments' margins, increases the inter-fragment pore space, and enhances permeability. We highlight that the effectiveness of diffusive outgassing is determined by the surface area of pyroclasts, such that finer fragments attain lower vesicularities and lose vesicles faster than those of coarse fragments. Very fine pyroclasts may diffusively outgas all supersaturated volatiles prior to the onset of vesiculation, and therefore essentially follow non-vesiculating sintering models for dehydrated fragments. These processes induce complex porosity and permeability hysteresis. We show that this behaviour can be described using the timescales for the completion of sintering, vesiculation, and diffusive outgassing, and that the porosity-permeability development can be assessed through the integration of existing models for bubble growth, diffusion lengthscale, and surface tension driven densification. Our data and analyses may help to illuminate the textural history of glassy pyroclastic systems and constrain the porosity-permeability evolution of natural melt systems as well as their densification efficiency during shallow volcanic venting.

# Chapter 4: Thermal liability of hyaloclastite in the Krafla geothermal reservoir, Iceland: the impact of phyllosilicates on permeability and rock strength

## Abstract

Geothermal fields are prone to temperature fluctuations from natural hydrothermal activity, anthropogenic drilling practices, and magmatic intrusions. These fluctuations may elicit a response from the rocks in terms of their mineralogical, physical (i.e., porosity and permeability), and mechanical properties. Hyaloclastites are a highly variable volcaniclastic rock predominantly formed of glass clasts that are produced during nonexplosive quench-induced fragmentation, in both subaqueous and subglacial eruptive environments. They are common in high-latitude geothermal fields as both weak, highly permeable reservoir rocks and compacted impermeable cap rocks. Basaltic glass is altered through interactions with external water into a clay-dominated matrix, termed palagonite, which acts to cement the bulk rock. The abundant, hydrous phyllosilicate minerals within the palagonite can dehydrate at elevated temperatures, potentially resulting in thermal liability of the bulk rock. Using surficial samples collected from Krafla, northeast Iceland, and a range of petrographic, mineralogical, and mechanical analyses, we find that smectite dehydration occurs at temperatures commonly experienced within geothermal fields. Dehydration events at 130, 185, and 600 °C result in progressive mass loss and contraction. This evolution results in a positive correlation between treatment temperature, porosity gain, and permeability increase. Gas permeability measured at 1 mPa confining pressure shows a 3-fold increase following thermal treatment at 600 °C. Furthermore, strength measurements show that brittle failure is dependent on porosity and therefore the degree of thermal treatment. Following thermal treatment at 600 °C, the indirect tensile strength, uniaxial compressive strength, and triaxial compressive strength (at 5 mPa confining pressure) decrease by up to 68 % (1.1 mPa), 63 % (7.3 mPa), and 25 % (7.9 mPa), respectively. These results are compared with hyaloclastite taken from several depths within the Krafla reservoir, through which the palagonite transitions from smectite- to chlorite-dominated. We discuss how temperature-induced changes to the geomechanical properties of hyaloclastite may impact fluid flow in hydrothermal reservoirs and consider the potential implications for hyaloclastite-hosted

intrusions. Ultimately, we show that phyllosilicate-bearing rocks are susceptible to temperature fluctuations in geothermal fields.

## 4.1. Introduction

Reservoir rocks in geothermal fields are exposed to thermal fluctuations from natural (Ármannsson et al., 2013) and anthropogenic temperature sources (De Simone et al., 2013). These fluctuations range from ~250 °C of cooling during thermal stimulation practices (Tulinius et al., 2000) to heating of up to 400 °C during flow testing (Axelsson and others, 2012) and up to ~1200 °C during basaltic magma intrusions (Schauroth et al., 2016). Importantly, for the sustainability of hydrothermal systems, temperature variations cause volumetric changes that may impart damage (Browning et al., 2016; Coats et al., 2018; Eggertsson et al., 2018; Heap et al., 2013b; Kendrick et al., 2013; Schaefer et al., 2015; Siratovich et al., 2014) and have the potential to trigger mineral reactions, prompting precipitation or breakdown (Ghassemi and Kumar, 2007) in altered reservoir rocks (Bird et al., 1984). These reactions can affect key reservoir rock properties, such as porosity, permeability, and strength (Heap et al., 2013a), which may influence the capacity for fluid circulation (Kumar and Ghassemi, 2005; Siratovich et al., 2015) and thus dictate energy production potential (Clearwater et al., 2015). Understanding the lithology-specific development of these properties in response to temperature is important for improved fluid flow modelling in geothermal fields.

Hyaloclastite is a rock type prevalent in subaqueous and high-latitude, glaciated regions such as Iceland, where it forms a major reservoir constituent in several geothermal fields (Kristmannsdóttir, 1979; Marks et al., 2010; Mortensen et al., 2014). It is often highly porous and permeable, such that it is frequently targeted for geothermal production, shallow freshwater aquifers, or carbon reinjection and mineralisation (Kim et al., 2009; Matter et al., 2011; Zakharova and Spichak, 2012), but it is also weak and can collapse to form a mechanically sealed, impermeable caprock (Nielson and Stiger, 1996). Hyaloclastites are highly variable, altered volcaniclastic breccias that form explicitly by severe quench-induced fragmentation of magma interacting with a large volume of external water or ice (Wohletz, 1986). However, the term is often applied ambiguously in the literature to any lava fragmented by interaction with water (Honnorez and Kirst, 1975); consequently, it is commonly identified in a wide range of water-rich environments, such as mid-ocean ridges (Hekinian et al., 2000), seamounts (Davis and Clague, 2003; Mitchell, 2003), submarine volcanic flanks (Ferrer et al., 2010; Schiffman et al., 2006), subglacial tuyas (Jakobsson and

Gudmundsson, 2008),80trengr ridges (Jarosch et al., 2008; Schopka et al., 2006), nearshore waters (Bergh and Sigvaldason, 1991), and emergent islands (Kokelaar, 1986; Wohletz and Sheridan, 1983). Therefore, hyaloclastite is more appropriately considered a non-genetic term (Cas and Wright, 2012) that is more accurately defined by the descriptive lithological criteria, used herein, of quench-fragmented sideromelane (i.e., basaltic glass) supported by a palagonite matrix (Van Otterloo et al., 2015). This is in contrast to the largely cohesionless perlite, which is produced following the hydration-induced alteration of the dacitic and rhyolitic glasses (Denton et al., 2009).

The abundance of palagonite in hyaloclastites arises from the inherent metastable nature of basaltic volcanic glass exposed to fluids (Oelkers and Gislason, 2001), especially at moderate to high temperatures (Cerling et al., 1985; Von Aulock et al., 2013). Palagonite is considered the first alteration product of mafic glass; it forms initially as an amorphous phase during the complex, concurrent processes of glass hydration and devitrification (Berger et al., 1987; Stroncik and Schmincke, 2001). The crystallographic character of palagonite is time-dependent, transitioning from a clear amorphous phase displayed in concentric bands of gel-palagonite to a highly variable assortment of crystal habits (e.g., fibrous, lath-like, or granular structure) termed fibro-palagonite. Fibro-palagonite is commonly dominated by clays, namely smectite, and zeolites (Drief and Schiffman, 2004; Franzson et al., 2010).

Rocks composed of clay and zeolite minerals tend to be highly sensitive to moderate thermal fluctuations on the order of a few hundred degrees Celsius (Heap et al., 2012). In particular, high temperatures may trigger devolatilisation reactions that prompt the breakdown of these minerals. This occurrence leads to a loss of material that results in the creation of porosity, thereby affecting the strength and permeability of the rock (Bedford et al., 2018; Bernabé et al., 2003; Heap et al., 2012). This is also true for incomplete reactions in rocks experiencing short excursions to high temperature (Mordensky et al., 2019). In the case of palagonite undergoing a temperature increase, dehydration can begin below 200 °C and result in greater mass loss than in many other clays (Milliken and Mustard, 2005). This suggests hyaloclastite may be particularly susceptible to thermally induced devolatilisation reactions that are likely to affect geomechanical properties (Heap et al., 2012).

Here, we investigate the impact of thermal treatment on hyaloclastite, constraining the mineralogical, mechanical, and physical evolution at a range of temperatures up to 600 °C.

## 4.2. Material and methods

### 4.2.1. Overview

Samples were initially characterised using a suite of thermal analysis equipment in order to select a series of treatment temperatures at which the hyaloclastite would be analysed in further detail. After fully characterising the mineralogical, physical, and mechanical properties of the as-collected material, cores were dwelled at the selected treatment temperature and cooled to room temperature; petrographic observations were made; and the impact on mineralogy, mass, porosity, permeability, and strength was determined.

### 4.2.2. Materials

Krafla caldera, located in northeast Iceland (Figure 4-1), hosts a well-developed geothermal field operated by Landsvirkjun, the national power company of Iceland. The caldera infill is dominated by hyaloclastite and basaltic intrusions to a depth of 1300 m (Mortensen et al., 2014), which comprise the reservoir rock hosting hydrothermal fluids harnessed for heating and energy production (Gudmundsson and Arnórsson, 2002). The surficial sample block was collected from the south-eastern caldera edge (65° N 41.067; -16° W 43.089) in August 2015, where the outcrops protrude from the surface and are isolated from the hydrothermal reservoir, thus undergoing trivial debilitation from exposure to the high-temperature reservoir fluids. However, the youngest and shallowest hyaloclastites at Krafla formed during the last glacial period (Ármannsson et al., 1987) and have possibly been buried and then subsequently exhumed due to glacial erosion (Tuffen and Castro, 2009). To complement these''fres'' samples, a limited suite of subsurface samples was retrieved during the coring of boreholes KH-4 (70 m) and KH-6 (556 m and 732 m) by Landsvirkjun. The in situ sample temperatures were recorded during and after drilling of the wells; the 70 m sample from KH-4 was measured at 41 °C during drilling, whilst after leaving borehole KH-6 to thermally equilibrate for one week, the 556 m and 732 m depths were measured at 145 and 125 °C, respectively (Gautason et al., 2007). Note that the sample collected from 556 m depth may have interacted with a basaltic dyke, located approximately 1 m below. The surficial sample was chosen to ensure it was texturally representative of the local geology and similar to the subsurface samples in terms of clast size and abundance. Upon visual inspection, the selected sample was relatively homogenous and lacked large features such as fractures or clasts greater than 1 cm in diameter. For all the mechanical and permeability measurements, heterogeneities were limited to less than 10 % of the sample size of 26 mm by 52 mm for

cores and 26 mm by 13 mm for discs. Following sample preparation and prior to all testing, samples were oven-dried at 70 °C for 4 hours and subsequently stored in a desiccator at room temperature. All samples were prepared, characterised, and tested at the University of Liverpool.
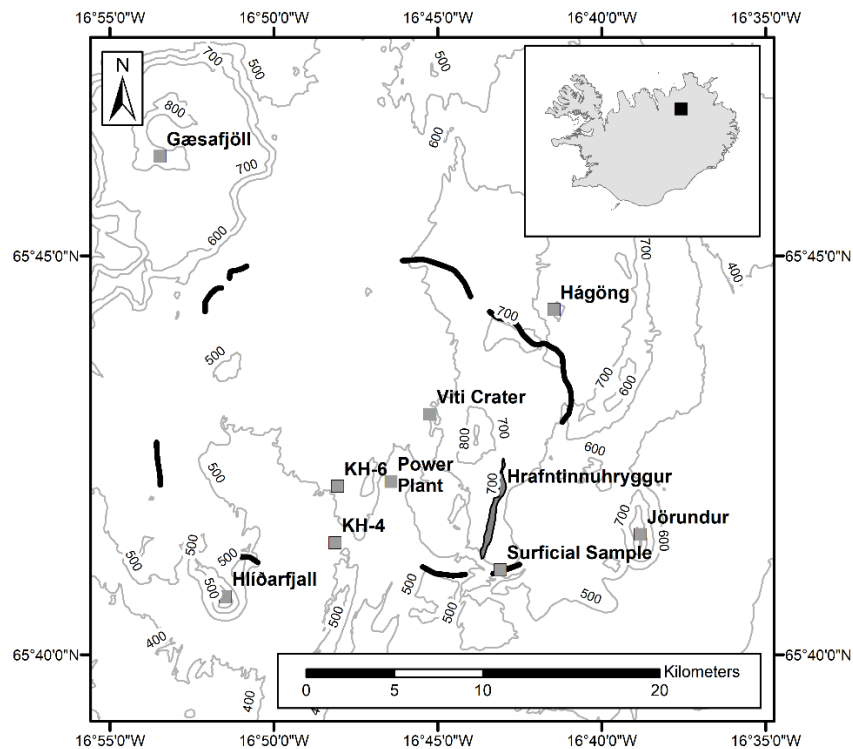


*Figure 4-1: A map of the Krafla geothermal field showing the location of the surficial sampling site, subsurface sampling sites (boreholes KH-4 and KH-6), the Krafla power plant and local geomorphological features. Faults associated with the Krafla caldera complex are marked in black.*

### 4.2.3. Simultaneous thermal analysis (STA)

Mass loss and heat capacity were measured against temperature concurrently in a Netzsch STA 449 F1 Jupiter using a simultaneous thermal analyser (STA), which combines thermogravimetric analysis and differential scanning calorimetry (TGA-DSC). Samples were cored to 6 mm by 1 mm discs and loaded into a platinum crucible. Prior to each test run, the sample chamber was purged with argon gas and exhausted to vacuum conditions. Each test was initially conducted with an empty crucible to provide a correction baseline, a second time containing a sapphire standard with the same sample dimensions, to correlate the DSC data, and a final time containing the hyaloclastite sample. All temperature profiles were initially heated to 50 °C at 2 °C.min$^{-1}$ for a 10-minute isothermal period. For surficial samples,

constant-rate temperature profiles, heated to 700 °C at 5, 10, and 20 °C.min$^{-1}$, as well as stepped isothermal profiles, consecutively heated to each treatment temperature at 5 °C.min$^{-1}$ and dwelled for 12 hours, were conducted. For subsurface samples, constant-rate temperature profiles were heated to 700 °C at a rate of 10 °C.min$^{-1}$ only. Data was collected from 50 °C at a 0.1-minute resolution, with mass accurate to 0.025 µg and heat capacity to ±2 %.

### 4.2.4. Thermomechanical analysis (TMA)

Absolute thermal expansion coefficients were recorded using a Netzsch TMA 402 F1 Hyperion. Samples were cored in to cylinders measuring 6 mm in diameter by 5 mm in height. A core sample was loaded between the piston of the TMA, and the furnace was sealed shut around the sample assembly. Prior to each test, the sample chamber was purged with argon gas and exhausted to vacuum conditions. For each test, the temperature and load profiles were completed twice; initially, a ceramic cylinder, matching the sample proportions to within 5 %, was used to supply a correction baseline that was removed from the second test run containing the hyaloclastite sample; this allowed an accurate determination of the sample length changes. All temperature profiles were initially heated to 40 °C at 2 °C.min$^{-1}$ for a 10-minute isothermal period. Constant-rate temperature profiles, heated to 700 °C at 5, 10, and 20 °C.min$^{-1}$, were completed using a 1 N load. Subsurface samples were heated to 700 °C at a constant rate of 5 °C.min$^{-1}$. Data was collected at a 0.01-minute resolution, with height change accurate to 1.25 nm and load to 0.01 mN.

### 4.2.5. Thermal treatment

Thermal treatment temperatures of 130 °C, 185 °C, 400 °C, and 600 °C were selected following the TGA-DSC and TMA measurements. Sample cores, 26 mm in diameter by 52mm in height, and Brazilian discs, 26 mm in diameter by 13 mm in height, were thermally treated in a Carbolite CWF 1300 box furnace, to be compared against the as-collected samples. Samples were heated at 5 °C.min$^{-1}$ and, once at target temperature, were left to dwell for 12 hours before being cooled to room temperature at a rate of 5 °C.min$^{-1}$.

### 4.2.6. Mineralogical analysis

The mineralogical and textural changes at each treatment temperature were investigated using a combination of X-ray diffraction (XRD) analysis, optical microscopy, and quantitative evaluation of minerals by scanning electron microscopy (QEMSCAN). Adjacent samples were cored and subjected to the temperature profile for each of the treatment temperatures discussed above in order to prepare samples for mineralogical analysis; parts of these rocks were cut for thin section preparation, and the rest was crushed to powder (see below). Adjacent samples were selected to minimise potential mineralogical differences from within the hyaloclastite, which are petrogenetically heterogeneous.

XRD analysis was completed on the dried, glycolated, and clay-separated samples using a Panalytical X'Pert Pro MPD diffractometer fitted with an X'Celerator detector. Texturally representative rocks were crushed, in distilled water, to a powder <10 µm using an agate McCrone micronizing mill, and subsequently dried at 60 °C before being further crushed into a loose powder using an agate pestle and mortar. Clay-separated samples were partially crushed in a ceramic pestle and mortar and then prepared with ultrasonication in distilled water, with the equivalent spherical particle size selected for by standard centrifugation methods. Clay separated samples were then dried at 60 °C and recrushed into a light random powder. For glycolated samples, saturation of a random powder was achieved by using ethylene glycol by vapour pressure at 60 °C, for 24 hours. Samples were backloaded into cavity holders as random powders. A copper X-ray tube was used, with a Ni filter to select for Cu K-$\alpha$ radiation. Scans covered the 2 theta range of 4-70°. Data was analysed using the Relative Intensity Ratio (RIR) method within the HighScore Plus® software, alongside reference patterns from the International Centre for Diffraction Data, Powder Diffraction File 2 Release 2008.

Mineral distribution was imaged at 20 µm resolution for each thin section and at 4 µm resolution for selected sites, using Scanning Electron Microscope Energy-Dispersive Xray Spectroscopy (SEM-EDS) on uncovered, carbon-coated thin sections imbedded with luminescent dye. Using a QEMSCAN developed by FEI, elemental chemistry was mapped and quantified using two Bruker EDS detectors and matched to known compositions of minerals and glasses. Crystallographic features are not recorded, preventing the differentiation of polymorphs and mineral dissociation (in the case where chemical transport is limited). Mineral and glass abundance was quantified at 20 µm resolution by comparing the relative proportions of pixels in each image, normalised against the pore space.

### 4.2.7. Porosity determination

Prior to and following thermal treatment, the skeletal volume of each sample (i.e., the volume of solid rock, including isolated pore space) was measured using a Micromeritics AccuPyc II 1340 Helium Pycnometer, accurate to ±0.1 % of the measured volume. The connected porosity $\phi_c$, into which fluids are able to flow, was then determined by the ratio of the connected pore volume (equivalent to the difference between the core volume $V_T$ and the measured skeletal volume $V_G$) to the core volume $V_T$, such that:

$$\phi_c = \frac{V_T - V_G}{V_T}$$  Equation 4-1.

### 4.2.8. Permeability measurements

Gas permeability was measured for each sample core, prior to and following thermal treatment, using a Vinci Technologies gas permeameter with nitrogen gas. The 26 mm by 52 mm sample cores were inserted into a compressible Viton jacket and loaded to 1 mPa confining pressure using a manual valve. Gas flow was automatically set to a constant rate through the sample, which increased by a factor of 2 until a differential pressure of >0.5 psi was achieved between the inlet and the outlet. The flow rate values ranged from 33 to 190 cm$^3$/min. The sample permeability $k$ was calculated using Darcy's law:

$$W = \frac{-kA\Delta P}{\mu h}$$  Equation 4-2,

where $W$ is the flow rate; $A$ is the cross-sectional surface area of the sample; $\Delta P$ is the pressure differential, accurate to 1 % full scale, measured across the sample; $\mu$ is the viscosity of the liquid (in this case nitrogen); and $h$ is the sample length.

For selected cores, steady-state water permeability was also measured in a hydrostatic loading cell from Sanchez Technologies. Within the load cell, the 26 mm by 52 mm sample cores were inserted into an impermeable Viton jacket and loaded to the desired effective pressure (confining pressure–– pore pressure). Confining pressure was applied using low-viscosity silicone oil, and pore pressure was applied using demineralised water. Permeability was measured by maintaining 2 mPa of pore pressure at one side of the sample and 1 mPa of pore pressure at the other, such that a constant 1 mPa pressure differential was upheld with a85trengtge pore pressure of 1.5 MPa, and the flow rate was measured, accurate to 0.01 ml.min$^{-1}$. For each sample, the permeability was measured at 5 mPa confining pressure increments consecutively, up to 30 mPa, to simulate depths up to and in excess of the deepest hyaloclastite units at Krafla. To ensure that permeability was measured under steady-state

conditions and that no gas slippage was occurring, the need for the Klinkenberg, (1941) and Forchheimer, (1901) corrections was assessed for each sample and found to not be required for any of the samples in both the gas and water permeameters.

Porosity change associated with fracture closure during loading was also recorded in the hydrostatic cell, prior to each permeability measurement (Eggertsson et al., 2018), using the monitored volume of water that was expelled from the sample. However, absolute porosity variations are not reported as volume change is not monitored during the first loading step; instead, the porosity reduction (in %) is calculated from the initial porosity measured by helium pycnometry. Note that due to potential damage inflicted during loading, samples measured in the hydrostatic load cell were not used for subsequent strength testing.

### 4.2.9.   Strength measurements

The uniaxial and triaxial compressive strength tests and indirect tensile strength tests were performed on the as-collected and thermally treated (TT) samples at dry, ambient room temperature conditions. The uniaxial compressive strength (UCS) of the rocks was determined using an 8800 Instron uniaxial press. Cylindrical rock cores, for which porosity and gas permeability had been measured, were loaded at a constant strain rate of $10^{-5}\,s^{-1}$ until failure. Load was recorded with a resolution of 0.1 N at 10 Hz.

The compressive triaxial strength (TXL) of cores subjected to various confining pressures was measured using a Sanchez Technologies TRIAX100 press. Here again, cylindrical rock cores for which porosity and permeability had been determined were placed between the pistons and jacketed using an impermeable Viton sleeve. The sample assembly was subjected to confining pressure $\rho_c$ by introducing argon gas in the pressure vessel; 5 mPa confining pressure was applied to each sample whilst a constant 1 mPa differential stress was maintained by controlling the axial load. Note that no pore pressure was applied, so that the confining pressure is equivalent to the effective pressure. Upon reaching the confining pressure, the sample was axially deformed at a strain rate of $10^{-5}\,s^{-1}$ until rupture, denoted by a stress drop in the mechanical data, or until a stress plateau was reached. The confining pressure, pore pressure, axial stress, and sample deformation were recorded at 1 Hz.

Young's modulus, calculated by dividing stress over strain, was derived using the gradient of the manually defined, elastic linear loading section of each uniaxial and triaxial strength curve.

The indirect tensile strength (UTS) of the samples was measured by employing the Brazilian disc method using a 5969 Instron uniaxial press. Here, cylindrical discs, 26 mm diameter by 13 mm thickness, were radially loaded at a constant deformation rate of 26 $\mu m.s^{-1}$ until a stress drop was recorded, associated with failure. Sample deformation, accurate to ±0.1 µm, and load were recorded with a resolution of 0.05 s, and the tensile strength $\sigma_t$, was calculated following the ASTM 2008 standard:

$$\sigma_t = \frac{2P_m}{\pi h d}$$
Equation 4-3,

where $P_m$ is the maximum applied load (in N) and $h$ and $d$ are the thickness and diameter of the specimen (in m), respectively. Note that the mechanical data was corrected for compliance of the loading frame of each press in accordance with the ASTM D7070-16 standard procedure.

## 4.3. Results

### 4.3.1. Simultaneous thermal analysis (STA)

Thermogravimetric analysis (TGA) reveals progressive, nonlinear mass loss upon heating above 50 °C (Figure 4-2a). For the surficial samples (referred to as 0 m), mass loss is initially negatively correlated with the heating rate, whereby mass is lost more rapidly at low heating rates; however, beyond 250 °C, there is no correlation and the mass loss at 700 °C ranges from 7 to 10 %, reflecting sample heterogeneity. In contrast, the subsurface samples (referred to by their sampling depths of 70 m, 556 m, and 732 m) have distinct multistep mass loss shoulders around 100-200 °C and 475-600 °C; yet, the magnitude of mass loss in each of these temperature ranges varies with depth. Ultimately, the fraction of mass lost is higher in surficial samples than in subsurface samples.

Differential scanning calorimetry measurements associated with the above thermogravimetric analysis reveal further details associated with the mass loss events (Figure 4-2b). The surface samples show double-shouldered endothermic peaks at 130 °C and 185 °C (Figure 4-2b), consistent with the 100 – 200 °C mass loss event recorded by the TGA (Figure 4-2a). With the increased heating rate, the endothermic peaks are pushed to slightly higher temperatures (up to ~150 °C and 220 °C at 20 °C.min$^{-1}$). At a higher temperature, a faint shoulder develops around 300 °C and a broad, low-magnitude peak is evident around 650 °C; yet, neither corresponds to distinct mass loss events in Figure 4-2a. In contrast, the subsurface samples exhibit a less substantial double-shouldered peak at 130 °C and 185 °C than the

surficial samples and faint, broad peaks around 300 °C; however, they display strong endothermic peaks at high temperatures: for the 70 m sample, a wide peak develops between 550 °C and 660 °C; for the sample from 556 m, the data show a peak at 525 °C; and for the sample from 732 m, the data show a peak at 560 °C.

Based on the simultaneous thermal analysis (Figure 4-2a and b), four temperatures were selected as thermal treatment targets: 130, 185, 400, and 600 °C. Results from the 12-hour isothermal TGA measurements at these temperatures show that mass reaches a new stable value over long time periods, resulting in mass loss of 5 %, 5.8 %, 7.1 %, and 7.5 %, respectively (Figure 4-2c).

### 4.3.2. Thermomechanical analysis (TMA)

Thermomechanical analysis was employed to constrain the length changes associated with the mass loss events observed in Figure 4-2a. Surface samples initially exhibit limited thermal expansion, followed by minor contraction between 110 °C and 290 °C (Figure 4-2d). A return to limited thermal expansion ends at 500 °C, after which significant contraction occurs. The temperature of the maximum extent of contraction between 110 °C and 290 °C and the rate of collapse beyond 500 °C are positively correlated with the heating rate. Subsurface samples from 70 m depth show moderate expansion up to 475 °C, at which point expansion ceases, before rapidly accelerating beyond 640 °C. Note that a visual inspection of the two 70 m samples, following the TMA analysis, indicated the occurrence of vesiculation of the glass phase; we do not study this further as no surficial samples underwent such a process. The 556 m sample is entirely dominated by thermal expansion up to 700 °C, whilst the 732 m sample expands rapidly up to 185 °C and collapses beyond ~575 °C.
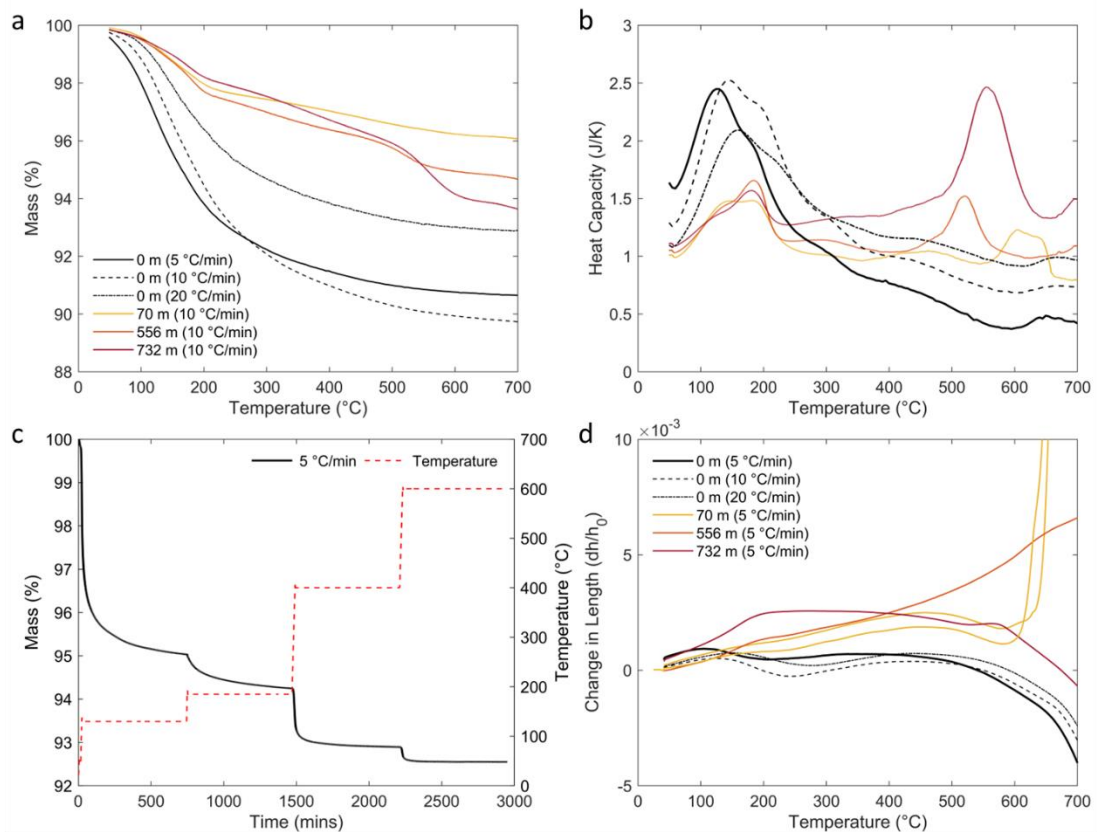
*Figure 4-2: Thermal analysis using TGA-DSC and TMA. a) Fixed-rate TGA showing thermally induced mass loss for the surficial and subsurface hyaloclastites. b) Fixed-rate DSC showing low-temperature heat capacity peaks against temperature for surficial samples and high-temperature peaks for subsurface samples. c) TGA showing mass loss during the sequential 12-hour isothermal dwells, for surficial hyaloclastite. d) Fixed-rate TMA for the surficial and subsurface samples, showing volumetric collapse for surficial material and a range of depth-dependent responses for subsurface material.*

### 4.3.3. Mineralogical analysis

A range of mineralogical and petrographic techniques were applied to further investigate the crystallographic and textural impact of suspected reactions. XRD analysis (Table 4-1) shows that the surficial hyaloclastite is primarily composed of the common mafic igneous minerals, anorthite, augite, and quartz, along with secondary minerals chabazite (i.e., zeolite group) and smectite (i.e., clay group). The analysis indicates that, other than small fluctuations in the anorthite and augite proportions, the mineralogical assemblage remains essentially stable up to 130 °C. The fraction of smectite identified in the samples decreases by ~6 % following treatment to 185 °C and is mostly absent beyond 400 °C (Table 4-1). Analysis of the X-ray diffractograms show that the d(060) peak for unaltered surficial material is at 1.535 Å, whist the d(001) peak expands from 15 Å to 16.2 Å upon glycolation and collapses to 10 Å after

dwelling at 400 °C for 12 hours, typical of saponite (Supplementary Figure A.III-1). XRD analysis of the subsurface hyaloclastite from Lévy et al., (2018) highlights that the smectite transitions from saponite in the surficial and shallow hyaloclastites to interlayered saponite-chlorite in the deeper (556 m and 732 m) hyaloclastites.

*Table 4-1: Primary mineralogy identified by X-ray diffraction analysis of hyaloclastite that has experienced different thermal treatment temperatures. Note that the reduction in the smectite proportion causes the relative proportions of the other components to increase and that the presence of sideromelane is not quantified nor included in this analysis.*

| Temperature experienced: | 20 °C | 130 °C | 185 °C | 400 °C | 600 °C |
|---|---|---|---|---|---|
| Anorthite (%) | 52 | 59 | 60 | 63 | 73 |
| Augite (%) | 17 | 13 | 18 | 25 | 17 |
| Chabazite (%) | 8 | 8 | 7 | 5 | 7 |
| Quartz (%) | 3 | 2 | 2 | 6 | 3 |
| Smectite (%) | 19 | 18 | 13 | Trace | Trace |
| Total (%) | 99 | 100 | 100 | 99 | 100 |

Petrographic analysis provides a textural counterpart to the quantitative mineralogical XRD. Thin section analysis, using both optical microscopy and scanning electron microscopy, reveals the highly variable nature of hyaloclastite (Figure 4-3). In particular, we note significant textural heterogeneity in terms of glass distribution and geometry, crystal fraction and size, and pore space distribution (Figure 4-3). The pore space is shown to be predominantly hosted in the matrix in both the as-collected and TT samples (Figure 4-3b and r), with additional, isolated porosity hosted within the highly variable vesicular glass clasts (Figure 4-3j). Textural examination of the thin sections for the as-collected material shows a low quantity of intra-mineral microfractures within the phenocrysts and glass (Figure 4-3b). A qualitative inspection of the TT sample thin sections found a comparable number of intra-mineral microfractures. Given the material heterogeneity, we do not quantify this further, finding that material characterisation which examines porosity and permeability before and after TT on the same sample to be a more robust measure of sample evolution with TT. Thin section analysis also offers no evidence of reaction rims around crystals or of sintering textures, such as particle necking during agglutination occurring during TT (Figure 4-3).
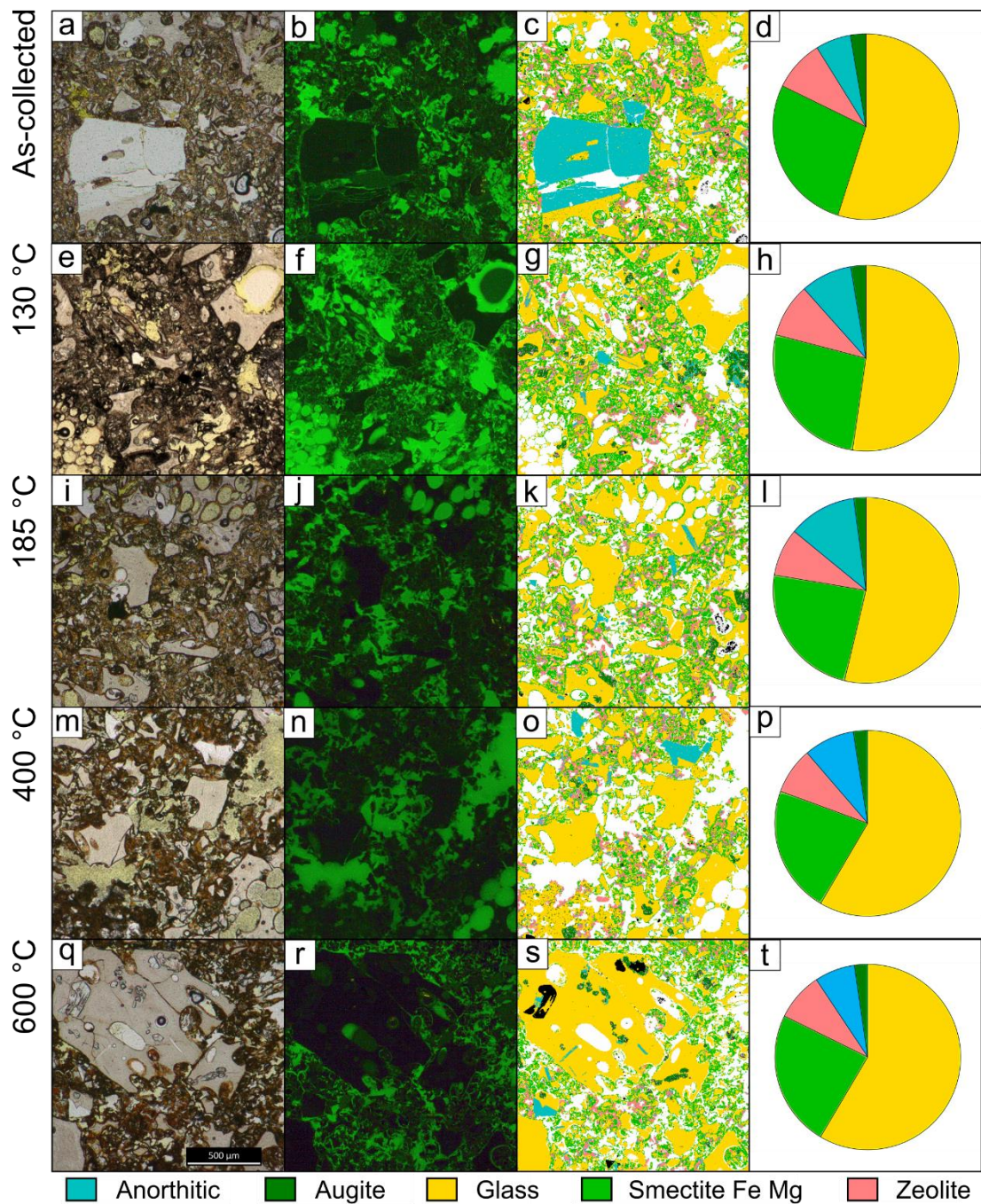
Figure 4-3: Petrographic analysis for the as-collected and TT samples. The as-collected images are presented in a–d, 130 °C TT images in e–h, 185 °C TT images in i–l, 400 °C TT images in m–p, and 600 °C TT images in q–t; each image shows 1.5 mm². Plane polarised light images are displayed in column 1 (Supplementary Figure A.III-2 shows an annotated example of the petrographic images); ultraviolet images in reflected light of samples impregnated by fluorescent epoxy highlight porosity in column 2; QEMSCAN mineralogy maps at 4 μm resolution in column 3 highlight mineral distribution; and quantified mineralogy pie charts from 20 μm resolution QEMSCAN maps in column 4 (images are shown in Supplementary Figure A.III-3–- A.III-6).

Changes in the abundance of constituent phases as a result of TT are revealed by QEMSCAN (Table 4-2, Figure 4-3). Changes in crystallinity are not recorded in the QEMSCAN maps, and so the dissociation of smectite is not quantified; however, the textural evolution highlights that the porosity increase is dominated by changes in the matrix, which we associate with a reduction in smectite revealed by XRD (from ~19 % to trace content at TT > 400 °C, Table 4-1). Loss of smectite with temperature results in an irregular desiccated texture, distinct from a fractured surface due to its smoother edges and globular distribution (Figure 4-3b and r), causing the matrix to transition from a continuous, pervasive network (Figure 4-3c and g) to discrete patches with increasing TT temperature, particularly in the 400 °C and 600 °C samples (Figure 4-3o and s).

*Table 4-2: Mineralogy for the as-collected material and for each treatment temperature quantified from the QEMSCAN image analysis at 20 μm resolution (see Supplementary Figure A.III-2–- A.III-7). Note that changes to mineral structure, such as dissolution, are not captured by QEMSCAN. Values are normalised by the background (pore space) of each image.*

| Temperature experienced: | 20 °C | 130 °C | 185 °C | 400 °C | 600 °C |
|---|---|---|---|---|---|
| Glass (%) | 53.8 | 51.4 | 53.0 | 57.9 | 57.6 |
| Smectite (Fe Mg) (%) | 26.8 | 26.3 | 23.6 | 22.0 | 23.4 |
| Zeolite (%) | 8.8 | 9.2 | 8.2 | 8.0 | 8.3 |
| Anorthite (%) | 6.0 | 8.8 | 11.8 | 8.7 | 6.9 |
| Augite (%) | 2.6 | 2.6 | 2.1 | 2.5 | 2.3 |
| Quartz (%) | 0.3 | 0.3 | 0.3 | 0.3 | 0.4 |
| Actinolite (%) | 0.3 | 0.3 | 0.2 | 0.2 | 0.1 |
| Others (%) | 1.2 | 1.0 | 0.7 | 0.2 | 0.6 |
| Unclassified (%) | 0.2 | 0.1 | 0.2 | 0.2 | 0.4 |
| Total (%) | 100 | 100 | 100 | 100 | 100 |

### 4.3.4.  Thermally induced changes in porosity and permeability

The evolution of mass during thermal treatment is reported for the 26 mm by 52 mm samples in order to explore the impact of material heterogeneity, discussed in Section 4.3.3, on mass loss (indicated by thermal analysis in Section 4.3.1). Sample mass change in the surface cores is positively correlated with the TT (Figure 4-4a).
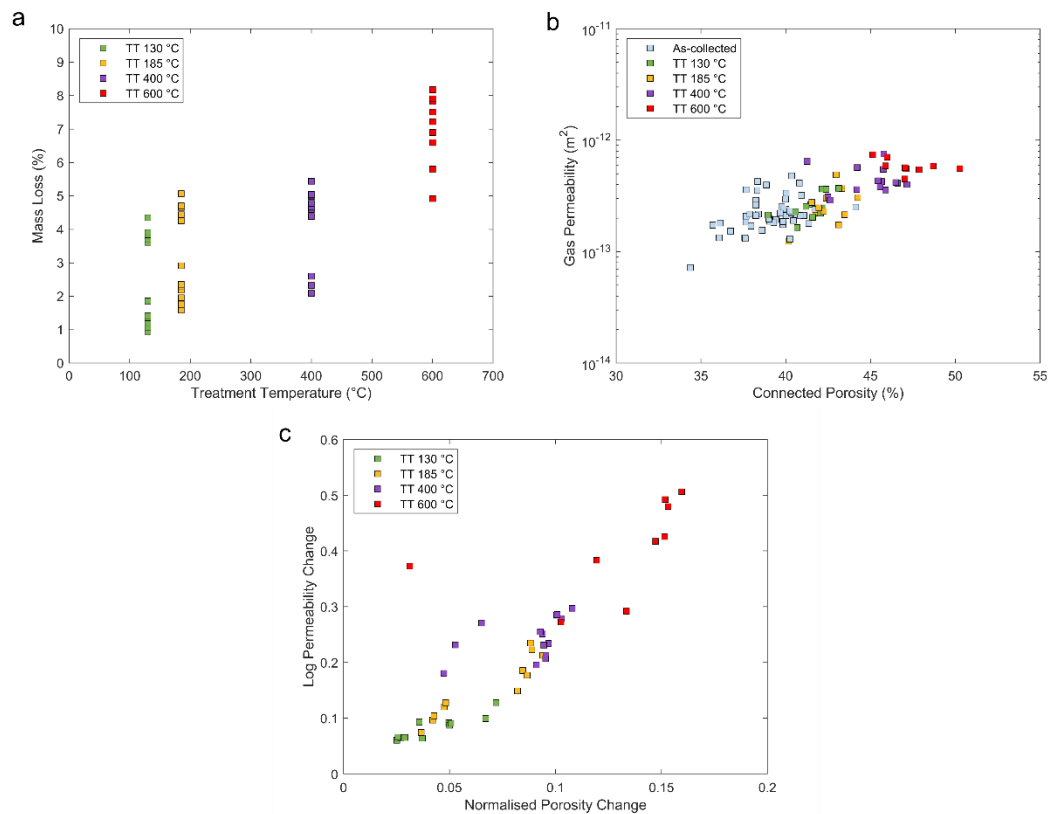
*Figure 4-4: Influence of TT on mass, porosity, and permeability. a) Percentage mass change induced by thermal treatment for each 26 mm by 52 mm core, showing increasing mass reduction up to temperatures of 600 °C. b) Increasing porosity-gas permeability of the as-collected and post-treatment samples as the treatment temperature is increased. c) Normalised porosity and gas permeability change from the as-collected materials, showing a linear permeability change with increased normalised porosity change.*

The samples cored from the as-collected material show a large degree of heterogeneity in the material properties despite being sourced from a single block ~40 cm in length. This hyaloclastite heterogeneity corresponds to substantial scatter in the porosity-gas permeability relationship (Figure 4-4b). However, the effect of this scatter can be accounted for and removed from the TT data by normalising the pore volume fraction change against the initial skeletal volume fraction of the corresponding core prior to TT, $\phi_{ci}$:

$$\overline{\phi}_c = \frac{\phi_{ci} - \phi_{cp}}{1 - \phi_{ci}}$$    Equation 4-4,

where $\phi_{cp}$ is the post-thermal treatment porosity; similarly, the resultant permeability changes are normalised by dividing the post-thermal treatment sample permeability with the original sample permeability (Figure 4-4c). The normalised plot shows that the permeability and porosity changes of all samples increase with TT (Figure 4-4c).

The water permeability of the hyaloclastite measured in the hydrostatic cell shows a negative correlation with effective pressure (Figure 4-5a; Supplementary Table A.III-1) as the permeable pathways are constricted by pore space closure (Figure 4-5b). Again, the samples exhibit a large degree of scatter in permeability for all TTs, which is independent of the mass change induced by TT. The as-collected samples as well as those TT to 130 °C, and to an extent 185 °C, show a moderate-to-large drop in permeability above 17.5 mPa that is not observed in the 400 and 600 °C TT samples. These effective pressure thresholds are also observed in the porosity evolution plot (Figure 4-5b), which shows a transition from low to high densification with effective pressure across these values. The samples that have been TT to higher temperatures exhibit contrasting evolution of permeability and porosity with effective pressure. In these cases, the permeability of samples does not change significantly with effective pressure (Figure 4-5a), whilst the porosity shuts linearly with effective pressure (Figure 4-5b); the exception to this behaviour is for one sample (thermally treated to 400 °C) which shows an increase in permeability between 7.5 and 17.5 mPa (Figure 4-5a); interestingly, this sample was accompanied by almost no porosity decrease between 17.5 and 23.5 mPa (Figure 4-5b).
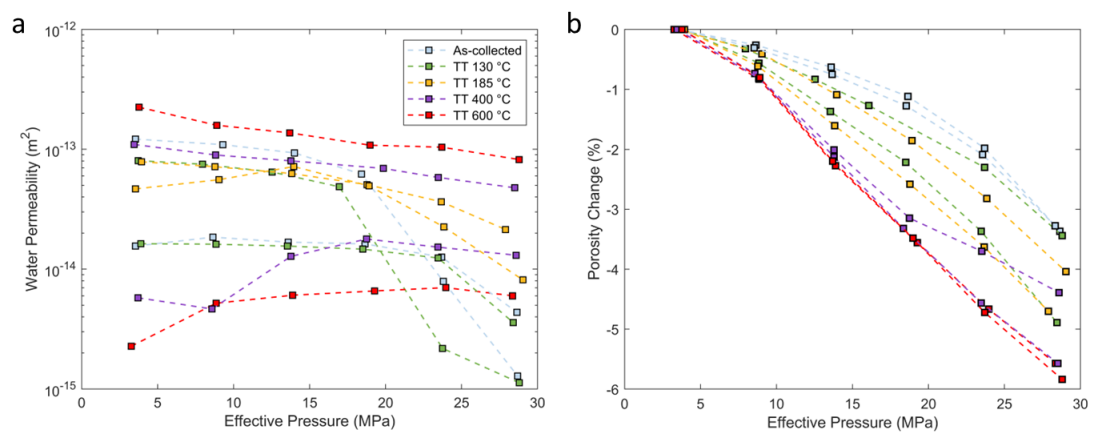


*Figure 4-5: The effect of loading on permeability and porosity. a) Water permeability evolution against effective pressure. Samples exhibit a large range of responses and degree of scatter for a given TT. b) Pore space collapse associated with increased effective pressure. Change in porosity is measured from ~3.5 effective pressure.*

### 4.3.5. Thermally induced impacts on strength

Uniaxial testing was used to constrain the behaviour of samples under compressive loading (Figure 4-6a). The data show typical stress-strain relationships, such as documented in Heap et al., (2014), transitioning from an initial concave-upward segment to being quasilinear, followed by a concave-downward segment. In terms of absolute strain, the beginning and end

of the quasilinear segments are not correlated with treatment temperature; however, the average strain of the linear portion decreases from 0.0034-0.0037 in the as-collected 130 and 185 °C samples to 0.0021-0.0023 in the 400 and 600 °C samples. As the 400 and 600 °C samples experience more strain prior to failure than the as-collected and lower temperature samples, the shortening of the linear portion also corresponds to a significantly smaller proportion of the total stress-strain curve. The average gradient of the linear segment, which is associated with rock elasticity and is used to calculate Young's modulus (Figure 4-7d), also decreases with temperature beyond 400 °C, from between ~1.3 gPa and 1.56 gPa for the as-collected 130 and 185 °C samples, to between ~0.7 gPa and 1.07 gPa for the 400 and 600 °C samples. The data show that the as-collected, surficial hyaloclastites exhibit a range of compressive strength from 8 to 10 mPa (Figure 4-6a). Upon thermal treatment to 130 and 185 °C, we observe no systematic changes in the sample strength, although the data show wider scatter (Figure 4-6a), whilst samples thermally treated to 400 and 600 °C weaken to between 4.2 and 6.8 mPa (Figure 4-6a).

Triaxial testing was used to constrain the behaviour of the hyaloclastite at a confining pressure of 5 mPa (Figure 4-6b), which is representative of ~300 m depth in the geothermal reservoir, assuming nominal rock and water densities of 2500 kg.m$^{-3}$ and 800 kg.m$^{-3}$, respectively (Scott et al., 2019). Under such a confinement, the compressive strength of the as-collected hyaloclastite is ~30 mPa, exhibiting a small stress drop upon rupture. Following thermal treatment at 130 and 185 °C, hyaloclastite exhibits a moderate strength decrease of up to 3.3 and 7.2 mPa, respectively; yet, the stress-strain curves show systematic reductions in the stress drop upon rupture. Hyaloclastites subjected to higher temperatures of 400 or 600 °C reveal contrasting behaviour in which samples tend to yield at lower differential stress, beginning to flow upon strain (Figure 4-6b); the one exception to this is the strongest sample, treated at 400 °C, which was texturally comparable to the other TT samples and yet shows mechanical behaviour similar to samples subjected to lower temperatures. Thus, thermal debilitation slightly weakens hyaloclastite and promotes a shift towards a ductile regime (Figure 4-6b; Supplementary Table A.III-2).

Brazilian tests were used to quantify the UTS of hyaloclastite (Figure 4-6c; Supplementary Table A.III-3). The as-collected hyaloclastite shows a near-linear stress loading curve and a UTS of 1.5 mPa. Upon thermal treatment to 130, 185, and 400 °C, we note a systematic weakening trend down to 0.6 mPa. Hyaloclastites subjected to the higher 600 °C temperature do not weaken further but rather undergo more compaction prior to failure.
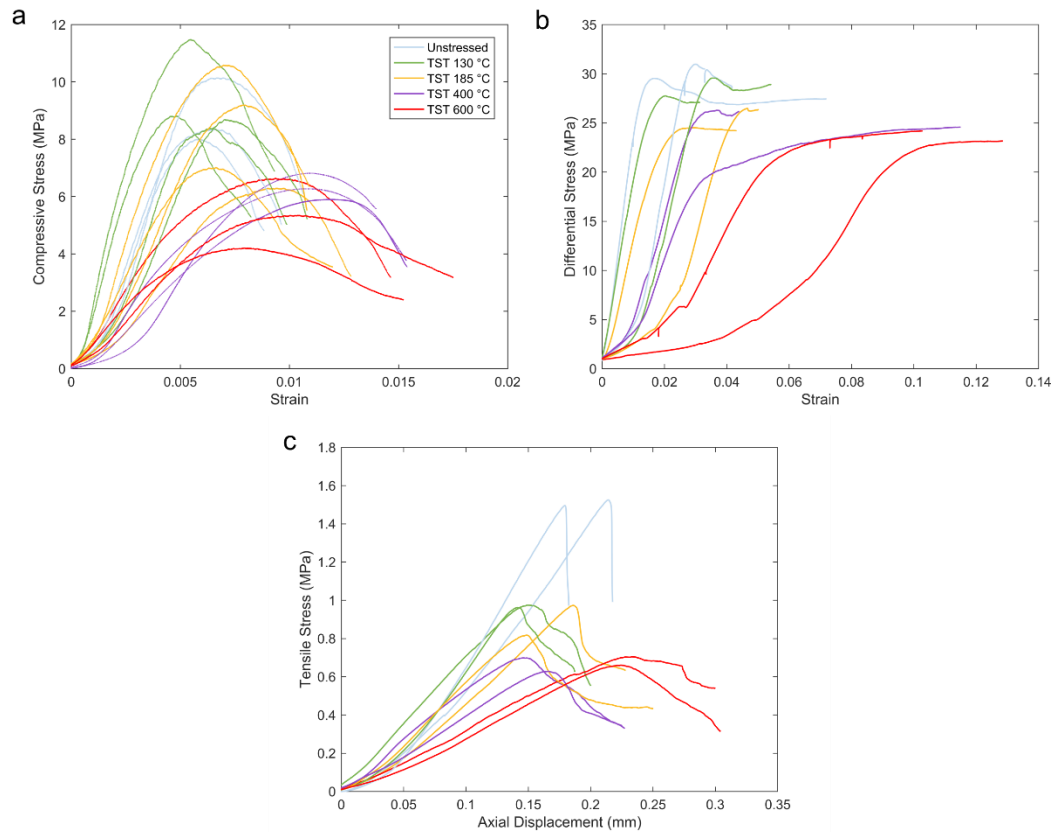
*Figure 4-6: The impact of TT on strength. a) UCS curves at $10^{-5}$ $s^{-1}$ strain rate. b) TXL curves at $10^{-5}$ $s^{-1}$ strain rate. c) UTS curves, using the Brazilian disc method, at $10^{-4}$ $s^{-1}$ diametric equivalent strain rate. For increased TT, all strength test types display a weakening trend and an increased accommodation of strain prior to failure (additional tensile strength curves are shown in Supplementary Figure A.III-8).*

The peak strengths from the UCS, TXL, and UTS curves show a decreasing trend with porosity and TT (Figure 4-7a). Analysis of the UCS (Figure 4-7b), UTS (Figure 4-7c), and Young's modulus data (Figure 4-7d) shows they follow trends published for igneous rocks. Young's moduli obtained from the uniaxial (Figure 4-6a) and triaxial (Figure 4-6b) strength tests reveal a negative correlation with the connected porosity of samples, imparted by thermal treatment. Young's moduli obtained during uniaxial tests are generally lower than the equivalent triaxial results for a given porosity (Figure 4-7d). The data presented here highlights the substantial impact of thermal treatment on the mineralogical, physical, and mechanical properties of altered reservoir rocks as present in active geothermal systems. Notably, increasing temperature results in lower smectite contents, higher porosity and permeability, and lower compressive and tensile strengths.
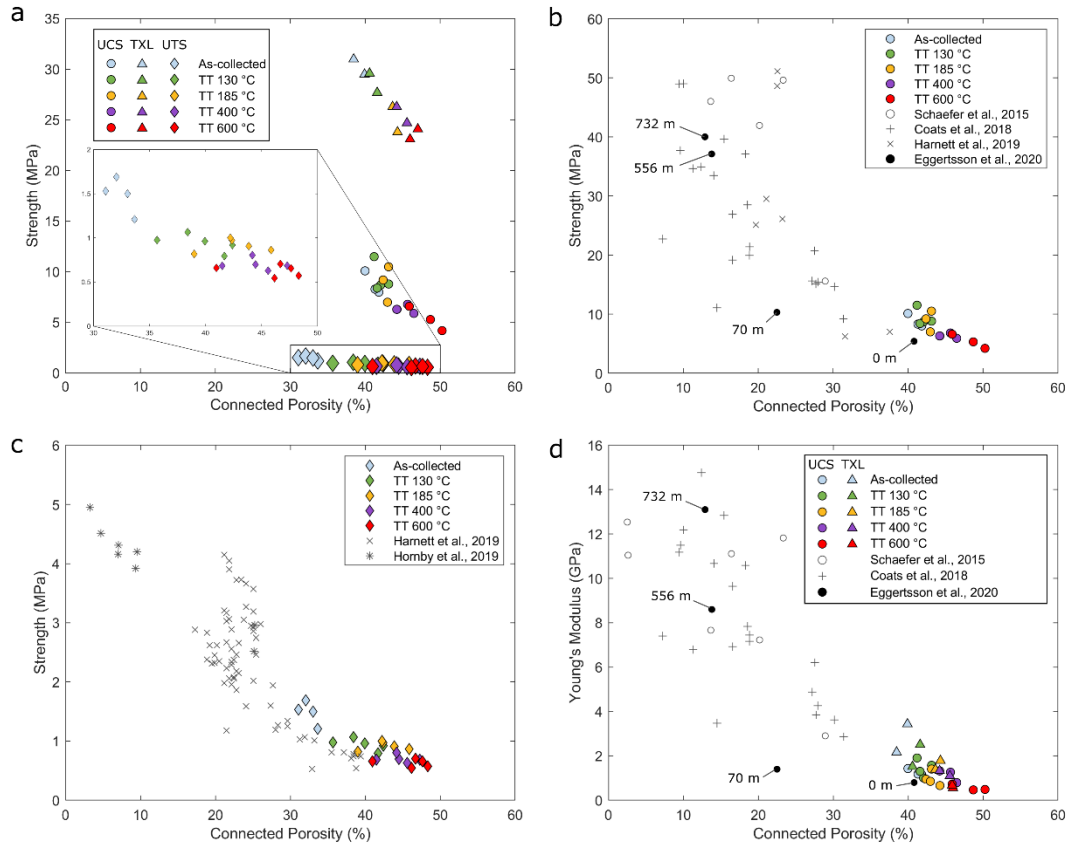
*Figure 4-7: Porosity control on UCS, TXL, UTS, and Young's modulus. a) Comparison of UCS, TXL, and UTS peak strength of hyaloclastite for each treatment temperature. All strength test types show weakening associated with increased TT and porosity. b) UCS results follow the general trend for igneous rocks, with TT decreasing strength proportional to the porosity increase. However, TT increases porosity, whilst hyaloclastite densifies and strengthens with depth [values show depth of sampling; Eggertsson et al. (2020)]. c) UTS results, regardless of TT, also fall within the general trend for igneous rocks. d) Young's modulus from the UCS and TXL tests follow the general trend for igneous rocks [values show depth of sampling; Eggertsson et al. (2020)].*

## 4.4. Interpretation and discussion

### 4.4.1. Application of laboratory results to the field

The investigation on the thermal stability of hyaloclastite present up to 1300 m depth in the shallow geothermal reservoir within the Krafla caldera provides important constraints on the properties of a common reservoir rock. However, due to the physically and mineralogically heterogeneous nature of hyaloclastite, studies at a laboratory scale (Eggertsson et al., 2018; Franzson et al., 2010) are challenging to apply to field scales. The variations noted in the mineralogical assemblage of the surficial hyaloclastite studied here (Table 4-1 and Table 4-2) are likely due to the physically and mineralogically variable source volcaniclastic components,

despite being prepared from a single 40 cm block. Influence of this heterogeneity continuously transpires in the physical and mechanical characterisation of both the as-collected and TT samples, particularly highlighted by the contrasting permeability behaviour in Figure 4-5a. Heterogeneity at the field scale may be markedly greater due to sorting and componentry (Schopka et al., 2006) and the degree of alteration, particularly between hyaloclastites exposed to different fluid chemistry (Kristmannsdóttir, 1979). Therefore, the data and trends of thermal treatment are most applicable to smectite-bearing hyaloclastite exposed to meteoric-sourced fluids, such as at Krafla. Here, we interpret the influence of thermal treatment on the physical and mechanical properties of surficial hyaloclastite and compare the resultant properties with those obtained from cores sampled from depth.

### 4.4.2.  Impact of temperature on the mineralogical assemblage of hyaloclastite

Thermally treating hyaloclastite results in mass loss (Figure 4-2a), which can be used as a proxy for water loss in hydrous clays (Bishop et al., 1994; Milliken and Mustard, 2005; Yen et al., 1998). However, it is important to note that phyllosilicates, such as smectite, comprise a group of highly variable minerals that have distinct dehydration and dehydroxylation temperatures (Yariv et al., 1992). The reduction in the d(001) spacing in the XRD data (Supplementary Figure A.III-1) is linked to the dissociation of the palagonite matrix resulting from smectite dehydration (Table 4-1). In detail, gylcolation firstly causes the d(001) peak to increase to 16.2 Å, as ethylene glycol replaces water in the interlayer space (Mosser-Ruck et al., 2005); subsequent heating to 400 °C for 12 hours drives ethylene glycol and water out of the interlayer space, decreasing the d(001) peak to 10 Å (Shirozu et al., 1975). Therefore, the reduction in smectite quantity with temperature is more accurately a case of progressive alteration (dehydration), which ultimately damages the crystal structure and reduces the effectiveness of the diffraction process. This produces smaller peaks in the diffractogram, which are interpreted as a lower mineral quantity; a similar reduction in smectite is not observed in the QEMSCAN data (Table 4-2) as only chemistry is monitored, not crystal structure. The low temperature (<200 °C) devolatilisation reactions identified in the TGA-DSC data (Figure 4-2a and b) correlate well with the clay-separated XRD results (Supplementary Figure A.III-1). The endothermic DSC peaks at 130 °C and 185 °C (Figure 4-2b) are encompassed within the 100–200 °C dehydration window expected for saponite (Malek et al., 1997) and are likely due to the loss of sorbed water and interlayer water (Shirozu et al., 1975). Saponite commonly precipitates from hydrothermal fluids found at depth (Alfredsson et al., 2013; Gysi and Stefánsson, 2012) and has been previously identified in cores from the Krafla

geothermal reservoir (Kristmannsdóttir, 1979). The subsurface samples have less prominent saponite dehydration peaks due to a combination of lower saponite-chlorite ratios and the higher in situ temperatures potentially causing partial dehydration prior to measurement (Lévy et al., 2018). The ability of smectite to rehydrate is dependent upon temperature, cation size, and saturation state (Kawano and Tomita, 1991). Under many conditions, saponite is able to fully or partially rehydrate (Russell and Farmer, 1964), suggesting the impacts discussed here may be partially reversible.

The 525–560 °C endothermic peaks identified in the 556 m and 732 m samples (Figure 4-2b) are indicative of chlorite dehydroxylation from interstratified saponite-chlorite (Shirozu et al., 1975), resulting in a second higher temperature mass loss response (Figure 4-2a). The endothermic peak and associated mass loss are greater within the 732 m sample, suggesting it has a lower saponite-chlorite ratio than the 556 m sample. The combined saponite-chlorite content at Krafla increases erratically from 19 % at the surface to ~50 % at depth, not including glass content (Lévy et al., 2018), suggesting thermally induced devolatilisation reactions at depth may be more impactful. However, note that all of the TGA-DSC measurements were performed under near-atmospheric pressure conditions and that increased pressure from the subsurface may suppress dehydration and dehydroxylation to higher temperatures (Vidal and Dubacq, 2009), such that the temperatures for reactions presented here are potentially conservative compared to those occurring in situ. Following the devolatilisation of the phyllosilicates, the bulk rock density increases due to the residual minerals emitting light elements; upon compaction, this may impact the physical and mechanical rock properties.

### 4.4.3. Impact of temperature on the thermal expansivity of hyaloclastite

In addition to mass loss, the thermal treatment of hyaloclastite also results in direct volume change as the palagonite phyllosilicate phases are prone to swelling at low temperatures and subsequently collapse following thermally induced dehydration and dehydroxylation (e.g., >500 °C; Figure 4-2d). However, identifying the swelling properties of individual components in a porous polymineralic rock is challenging due to the potential for overlapping responses and the possibility of accommodating expansion into the pore space (Cooper and Simmons, 1977). In the surface samples, the impact of saponite dehydration in the thermomechanical data (Figure 4-2d) is subtle, causing a minor compaction of the bulk rock, followed by significant compaction correlating with the chlorite dehydroxylation temperature. This suggests that hyaloclastite retains structural integrity throughout saponite dehydration whilst

a higher temperature reaction correlated to chlorite dehydroxylation causes a partial loss of cohesion between the palagonite matrix and the supported clasts. The similar, more distinct collapse in the relatively chlorite-rich 732 m sample at 575 °C correlates well with the endothermic peak at 560 °C and the mass loss identified between 515 °C and 615 °C (Figure 4-2a and b). However, the 556 m subsurface sample has lower saponite-chlorite ratios and does not exhibit this collapse; instead, the response shows limited thermal expansion throughout the heating profile. Thus, we find that hyaloclastites with thermally stable mineralogical assemblage expand with temperature, whereas unstable assemblages may breakdown and cause contraction, as exemplified by the thermal treatment of surficial hyaloclastites (Figure 4-2d). The thermal expansion responses measured under near-atmospheric pressure conditions, and any damage attributed to them, may be pushed to higher temperatures under the increased pressure conditions associated with burial, as dehydration is suppressed (Vidal and Dubacq, 2009). However, without a change in temperature, an increase in pressure alone does not result in smectite dehydration (Carniel et al., 2014).

The occurrence of substantial acceleration in thermal expansion above 640 °C from the 70 m samples (Figure 4-2d) coincided with vesiculation of glass clasts in the experimental products; this was not reproduced in samples from other depths, despite the abundance of glass in all samples (Figure 4-3). In detail, thermal expansivity started to accelerate around 600 °C, following a moderate endothermic peak (Figure 4-2b), associated with crossing of the glass transition for hydrated basaltic glass (Giordano et al., 2008; Robert et al., 2014), expected in shallow, water-rich environments (Cerling et al., 1985). Beyond this temperature, structural relaxation of the stress enabled water exsolution and increased vesiculation that sustained the heat absorption leading to a prolonged endothermic plateau (Figure 4-2d), as the samples rapidly expanded (Figure 4-2b).

### 4.4.4.  Impact of temperature on the porosity and permeability of hyaloclastite

The mass loss associated with the dehydration/dehydroxylation of the phyllosilicate phases during thermal treatment of hyaloclastite is also responsible for the increase in porosity and permeability displayed in Figure 4-4. A temperature increase can strongly impact the physical attributes for fluid storage capacity and flow, as the basal spacing of palagonite decreases upon devolatilisation, causing densification and generating intrinsically connected micropores (Kolaříková et al., 2005). In detail, the amount and ratio of saponite-chlorite available for

reaction provides a first-order control on the maximum extent of porosity possibly created by excursion to high temperature. As such, the time-dependent crystallisation of sideromelane to palagonite (Drief and Schiffman, 2004) suggests that older hyaloclastite units, which can contain more phyllosilicates, are more susceptible to temperature increases and the resultant enhancements to the porous permeable network. Thus, the lithology-specific initial glass chemistry, hydrothermal fluid chemistry, and pressure-temperature conditions will therefore impact the potential for the temperature-induced mineralogical and physical alterations that regulate the evolution of the storage capacity and permeability of a reservoir subjected to thermal fluctuations. In addition, the reservoir fluid properties will impact the hydration state of the phyllosilicate minerals; the increased scatter from water permeability (Figure 4-5a) to gas permeability (Figure 4-4b) is likely a result of interaction between the pore fluid and the minerals (especially clays) lining the permeable network.

At the sample scale, the lack of additional fractures in the TT samples suggests that dehydration/dehydroxylation is the primary mechanism responsible for porosity and permeability gain. Whilst cracking due to thermal stresses during heating and cooling has been shown to impart changes in the physical properties of some rocks, we advance that thermally generated cracks may not necessarily accumulate in hyaloclastite. Thermal cracking has been ascribed to the generation of stresses resulting from (1) a mismatch in thermal expansion or contraction between minerals, (2) thermal expansion anisotropy within a mineral, and (3) thermal gradients across a sample (Richter and Simmons, 1974; Yong and Wang, 1980). Hyaloclastites are fragmental rocks with variable degrees of cohesion arising from the presence of palagonite, so thermal stressing is expected to cause minimal damage in hyaloclastite as mineral expansion is in part buffered by palagonite, which is weaker than typical volcanic minerals, and due to the abundant and ubiquitous pore space that accommodates expansion without stress development. Eggertsson et al. (2018) showed that thermal stimulation may avoid fracture genesis and result in negligible permeability change, independent of the cooling rate, if the thermal stress associated with expansion is alleviated by preferential closure of the existing porous network, such as present in these samples (Figure 4-2b). We also note no evidence of intra-mineral thermal cracking induced by anisotropic expansion. However, it is possible that inter-phenocryst/glass fragment micro-fracturing occurred, as noted in hyaloclastite quenched from 350 °C (Siratovich et al., 2011), but that textural evidence was subsequently overprinted by phyllosilicate dissolution. Thermal microfractures are often non-pervasive in nature (Browning et al., 2016; Heap et al., 2012), suggesting the limited contribution they provide to permeability is unable to account for the

permeability evolution revealed in this study. Deformation-induced macro-fractures may induce a more substantial permeability increase (Heap and Kennedy, 2016; Lamur et al., 2017), yet such damage is not imparted by thermal treatment alone. However, the impact of thermal fracturing on the broad range of volcanic lithologies is yet to be well constrained, as discussed in Heap et al., (2014), and very few studies focus on highly altered material and the impact of pressure on thermal stimulation (Mordensky et al., 2019).

A further measure of changing material properties as a response to TT can be the sensitivity of materials to effective pressure; water permeability shows a negative correlation with effective pressure as porosity is isolated (Figure 4-5). The as-collected samples as well as those TT to 130 °C, and to 185 °C, show a significant drop in porosity and permeability during confinement to effective pressures above 17.5 mPa that is not observed in the 400 and 600 °C TT samples. The samples that have been TT to higher temperatures exhibit contrasting evolution of permeability and porosity with effective pressure, where porosity decreases linearly and more significantly than the lower TT samples, but permeability is not as sensitive to increasing effective pressure, suggesting that the porous network remains highly connected even as effective pressure is increased. There is one exception (thermally treated to 400 °C) which shows an increase in permeability with increasing effective pressure, and a less significant reduction in porosity; this could be a result of irreversible compaction in the sample whereby connected pore space was generated, yet we observed no textural evidence for this.

### 4.4.5.  Impact of temperature on the mechanical properties of hyaloclastite

The addition of thermal stress can also impact the resultant mechanical properties of hyaloclastite. In particular, a pressure increase causes a relatively abrupt reduction in pore space and permeability within the as-collected hyaloclastite and the samples thermally treated to 130 °C (Figure 4-5). This transition from elastic to inelastic compaction upon loading is termed $P*$ (Zhang et al., 1990). Beyond $P*$, compaction and grain crushing lead to a loss of pore space available for fluid flow (Bedford et al., 2018; Eggertsson et al., 2018; Heap et al., 2015a). Figure 4-5b indicates that $P*$ shifts to lower effective pressure with thermal treatment. The samples thermally treated up to 185 °C exhibit poorly defined changes in permeability associated with $P*$, and samples treated to higher temperatures develop no distinct changes with $P*$. This suggests that thermal treatment promotes a style of

compaction that has limited impact on permeability, despite higher rates of porosity loss (Figure 4-5b).

The devolatilisation of the palagonite matrix results in a weakening of the rock, both in tension and in compression, where the UCS is 6–10 times greater than the UTS (Figure 4-7a). The UTS of hyaloclastite decreased with TT and, following treatment at 600 °C, lost coherence and underwent more deformation before rupture (Figure 4-6c). The mode of deformation evolves similarly in compression, as noted by the onset of dilation occurring at lower stress and the accommodation of more substantial strain hardening prior to failure (Figure 4-6a), concordant with the lower Young's modulus upon increasing treatment temperature (Figure 4-7d). Deformation under an effective pressure of 5 mPa accentuated the distinction between the low TT (≤185 °C) and high TT (≥400 °C) hyaloclastites as they macroscopically behaved in a brittle and ductile manner, respectively (Figure 4-6b).

The resultant strengths measured in all test types display a porosity control, irrespective of the stress field experienced (Figure 4-7a), which follows the common porosity-strength trend (Figure 4-7b and c) for a range of igneous rock types, regardless of TT (Coats et al., 2018; Eggertsson et al., 2020; Harnett et al., 2019; Hornby et al., 2019; Schaefer et al., 2015). The treatment temperature has a strong impact on porosity (Figure 4-4c), thereby further influencing mechanical compaction; however, comparison with strength and Young's modulus data collected from subsurface samples (Eggertsson et al., 2020) shows that temperature alone cannot explain the mechanical changes occurring within the reservoir, instilling the roles of compaction and alteration on strength changes. In part, this is due to the opposing influences of temperature and compaction on porosity; however, in concert, increased temperature will create additional pore space that may enable more complete compaction and densification to occur at depth (Eggertsson et al., 2020). The change in style, from a dominantly brittle to ductile failure, may be explained by a change in geometry of the pore space (e.g., Figure 4-3b and r), as dehydration increases the connectivity and irregularity of the desiccated pore network (Bubeck et al., 2017). The influence of porosity in controlling sample strength can be further assessed using micromechanical modelling such as the pore-emanated crack model developed by Sammis and Ashby, (1986) and analytically modified by Zhu et al., (2010) to derive the UCS $\sigma_{UCS}$:

$$\sigma_{UCS} = \frac{1.325 K_{IC}}{\phi^{0.414}\sqrt{\pi a}}$$
Equation 4-5.

The strength is dependent upon the fracture toughness (or critical stress intensity factor) $K_{IC}$, the porosity $\phi$, and pore size $a$. This model was demonstrated to successfully approximate the

UCS of limestone (Zhu et al., 2010) and porous glass sintered in the laboratory (Vasseur et al., 2013b) but show arguable efficiency to approximate the strength of heterogeneous, coherent volcanic rocks, owing to their common abundance of microfractures (Coats et al., 2018; Heap et al., 2014). Here, the UCS values decrease as porosity increases with TT (Figure 4-8), suggesting that $K_{IC}/\sqrt{\pi a}$ would decrease from ~5 mPa down to ~3 mPa. Assuming $K_{IC}$ remains constant within a single lithology (even upon smectite hydration), the analysis would suggest that the reduction in strength and $K_{IC}/\sqrt{\pi a}$ may be the result of pore creation and widening, as suggested by Heap et al. (2014) when evaluating the mechanisms underlying thermally induced rock weakening. However, the applicability of the pore-emanated crack model to hyaloclastite is questionable as the pore space is highly irregular and rock failure is promoted by increasingly more pervasive fracture architecture in thermally treated hyaloclastites.
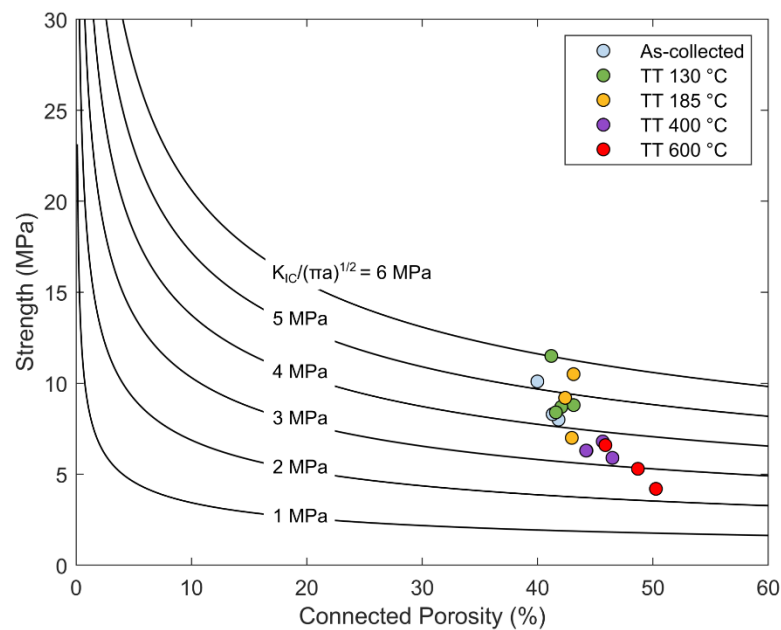


*Figure 4-8: UCS measurements compared against the pore-emanated crack model suggest an increase in porosity and pore-widening results in weakening.*

4.4.6.  Implications for hyaloclastite-bearing geothermal reservoirs

The temperatures investigated here cover the range of conditions hyaloclastite generally encounters in the shallow geothermal reservoir at Krafla (Bodvarsson et al., 1984) and encompass several important mineral transitions within the palagonite matrix. The transition from smectite to chlorite is common in hyaloclastite-bearing geothermal regions and is predominately controlled by temperature, assuming similar fluid chemistry (Kristmannsdóttir,

1979). Saponite is dominant below 200 °C, transitions to saponite-chlorite interlayers between 200 and 240 °C, and is fully replaced with chlorite beyond 240 °C (Kristmannsdóttir, 1979). Therefore, these results provide a first-order approximation of the changes occurring in hyaloclastite during burial and regional heating. Well and core logging at Krafla suggests that the deepest hyaloclastite units at 1300 m naturally experience temperatures of approximately 320 °C (Fridleifsson et al., 2006) and thus would have been subjected to the full range of transitions. However, as the temperature profile is spatially variable across the field, the depth of mineral transitions range over several hundred meters (Fridleifsson et al., 2006).

Some geothermal regions, such as Krafla, are also host to magmatic intrusions that can transfer heat to their host rock, inducing much greater localised temperature changes (Schauroth et al., 2016). Similarly, harnessing of very hot fluids, as experienced during flow testing of a 2100 m deep, near-magma borehole during IDDP-1 (Mortensen et al., 2014), resulted in fluids up to 550 °C reaching the wellhead. Thus, a shallow magmatic intrusion or superheated/supercritical fluid ingress during flow testing can alter the mineralogical, physical, and mechanical properties of shallow hyaloclastite, common in conventional geothermal reservoirs. This may promote more efficient fluid flow in geothermal fields; yet, fluid flow in clay-bearing rocks is partially controlled by the chemistry of the fluids which can interact with the host (Kwon et al., 2004); thus, the impact of fluid chemistry on fluid flow is expected to decrease upon palagonite dissociation. Here, comparing the surficial hyaloclastite with the hyaloclastites sampled from the reservoir, we find that the thermally induced mass loss and mineralogical distribution of the deep hyaloclastites cannot be explained by simple heating events, as those performed in our experiments, but rather evoke the importance of pressure-temperature history and chemistry in the hydrothermal system. For instance, the onset of saponite dehydration may increase by several hundred degrees by increasing pressure to 30 mPa (Vidal and Dubacq, 2009), such as through rock burial or glaciation, suggesting the physical and mechanical changes detailed here may be shifted to higher temperatures for buried samples. Additionally, the impact of pore fluid pressure may suppress dehydration reactions to higher temperatures than recorded in the dry measurements presented here (de Siqueira et al., 1999). As such, the interplay between temperature and pressure produces a complex relationship with the resultant mineralogical, physical, and mechanical properties. Geothermal regimes with low effective pressure and high temperature, such as the shallow subsurface, may exhibit a positive correlation between the temperature experienced and the resultant porosity and permeability, whilst in a deeper high-

pressure environment, the breakdown from thermal fluctuations, if any, may promote compaction.

Anthropogenic-induced compaction may possibly occur due to the extraction of geothermal fluids inducing a reduction in the reservoir pore pressure (Segall and Fitzgerald, 1998); this would increase the effective pressure and subsequently raise the depth threshold of compaction (Farquharson et al., 2016), locally altering the dominant permeability regime. Porosity change associated with temperature fluctuations may also influence the depth threshold of compaction. Similarly, a temperature reduction caused by fluid extraction may result in rehydration and swelling due to the potentially reversible nature of smectite dehydration, thereby clogging fluid pathways.


### 4.4.7. Implications for magma intrusions in hyaloclastite

The intrusion of magma into hyaloclastite may result in complex intrusion-host rock interaction, evolution, and feedback, owing to variable degrees of devolatilisation and compaction. Initially, an intrusion would bake the margin, promoting phyllosilicate devolatilisation that improves the porous permeable network, allowing for efficient fluid flow; however, this may be accompanied by changes in strength and a transition from brittle to ductile deformation, which may instead favour compaction of the hyaloclastite along the magma boundary, causing a decrease in permeability (Farquharson et al., 2017) and compartmentalisation of fluid flow (Senger et al., 2012). The construction versus destruction of a permeable porous network may have crucial impacts for the evolution of shallow magmatic systems. Firstly, the liberation of fluids from smectite and chlorite may, if trapped, locally increase pore pressure and generate induced seismicity akin to hydraulic fracturing (Wang and Wong, 2003) and, in extreme cases, cause phreatic explosions, as seen at Viti crater, Krafla (Mayer et al., 2015). Secondly, the volatiles liberated may promote magma hydration and increase the likelihood of explosive activity (Zhang, 1999b) or result in cooling and quenching of the magma. Thirdly, and similarly, margin compaction and shutting of the permeable network may limit magma outgassing, which again increases the likelihood of explosive volcanism. And finally, magma intrusion may result in viscous relaxation of sideromelane or melting of hyaloclastite, thus generating new magma, which may mix and interact with the intrusion. Thus, the evolution and feedback between magma and hyaloclastite are likely to be very complex depending on the nature (e.g., chemistry, temperature) and size of an intrusion and on the state and properties of hyaloclastites. We

suggest that further research should be undertaken to better understand these complex feedback systems and the implications for the volcanic and geothermal processes.

## 4.5. Conclusion

In this study, we show that rock heterogeneity impacts the mineralogical, physical, and mechanical properties of hyaloclastite, which are susceptible to thermal fluctuations experienced within geothermal fields. This is due to the devolatisation of the palagonite matrix, composed of varying phyllosilicate minerals which are sourced from the tendency of metastable basaltic glass to crystallise and produce a smectite-dominant (i.e., saponite) palagonite matrix in cool settings (<200 °C) and a chlorite-dominant matrix in hotter settings.

Thermal treatment of surficial hyaloclastite indicates that smectite dehydrates upon heating, with increased treatment temperature causing up to 10 wt.% mass loss at 700 °C. This dehydration, quantified at 130, 185, 400, and 600 °C, results in an enhanced porous permeable network, a decreased compressive and tensile strength, a decreased Young's modulus, and a shift from brittle to ductile mode of deformation upon thermal treatment (≥400 °C), even at a moderate effective pressure of 5 mPa (as experienced at shallow depths in a geothermal system). We assess the impact of temperature on hyaloclastite sampled from boreholes at 70, 556, and 732 m depth in the reservoir, finding that the glass in the shallow rock may have been hydrated whereas the deeper rocks contain abundant chlorite, which dehydroxylates at ~560 °C.

The increased temperatures and pressures experienced in geothermal fields will reduce the hydration state of phyllosilicate minerals, causing weakening and potentially lowering the depth threshold for compaction. Such deformation in geothermal systems and areas surrounding magmatic bodies may result in the construction/destruction of fluid pathways and the compartmentalisation of reservoirs, possibly impacting the progression of volcanic activity.

# Chapter 5: Implications and future work

## 5.1. Summary of results

In this project, I have investigated how selected109trengto-physico-chemical properties develop in complex and evolving fragmental volcanics, ranging from juvenile melt systems to altered, geothermal lithologies. Chapter 2 and Chapter 3 relate to melt systems in active volcanic environments whereas Chapter 4 concerns the impact of thermal fluctuations on hydrothermally altered volcaniclastic rocks. The scope of the studies progressively increases, as I move from considering the development of vesicularity in isolated melt fragments in Chapter 2, to vesicularity, connected porosity, and permeability evolution of pyroclast assemblages in Chapter 3, and finally to mineralogy, porosity, permeability, and strength development of agglutinated fragmental rocks in Chapter 4.

In detail, Chapter 2 offers new insights on the development of vesicularity within openly outgassing melt fragments. I subject obsidian cylinders in the ash to lapilli size range to magmatic temperatures and continuously record their cross-sectional areas for 48 hours in order to track their vesicularity evolutions. I find that, in contrast to closed system melts, the full time series of vesicularity in openly outgassing melt fragments is dependent on the initial size of the melt fragment; for a given condition, the rate of expansion during vesiculation and the maximum vesicularity achieved increases with fragment size. I find that my smallest samples, 1 mm in diameter, reach a maximum vesicularity of ~15 % whereas, my 12 mm diameter samples attain a peak vesicularity of ~65 %, which is in the range expected by closed-system bubble growth (e.g., Coumans et al., 2020). Importantly, I observe that vesicularity reduces after reaching the peak, and the rate of contraction is also dependent on fragment size, where larger samples densify more slowly. Where the observation time is sufficient, samples may lose all vesicularity and fully re-densify. These transient and sample size dependent vesicularity profiles stand in stark contrast to closed system bubble growth models, where a size independent vesicularity equilibrium is reached upon exhausting the supply of supersaturated volatiles (e.g., Coumans et al., 2020; Ryan et al., 2015a). Through textural analysis, I reveal that a dense rind is growing around the samples, creating an isolated and progressively shrinking parcel of vesiculated melt. Following the work of von Aulock et al. (2017), I show that the thickness of this rind scales with the diffusion lengthscale, which indicates that diffusion causes volatile loss at the sample margin, leading to volatile

resorption, bubble shrinkage, and densification as the rind thickens. The diffusion lengthscale is comparable across all sample sizes, whereas the diffusion timescale (i.e., the time required for outgassing to complete) is not; therefore, in a given timeframe, the dense rind grows to the same thickness for all samples and thus, the rind accounts for a greater proportion of the melt in smaller samples. I describe how this increased effectiveness of outgassing in smaller samples, with larger surface areas, causes more substantial densification and produces the sample size dependent vesicularity profiles described above.

The results throughout this study highlight that melt fragments in open systems behave in a distinctly different manor to fragments in closed systems (e.g., Bagdassarov et al., 1996; Coumans et al., 2020; Ryan et al., 2015a). To explore these results further, I develop simple geometrical constraints, in conjunction with an established diffusion lengthscale model (von Aulock et al., 2017) and a closed system vesiculation model (Coumans et al., 2020). My modelling results show that for large, rapidly decompressing fragments, where the observation time is short, diffusive outgassing is inconsequential and fragments follow closed-system bubble growth; in finer fragments, diffusive outgassing may complete before bubble nucleation occurs, such that bubble growth is completely obstructed, as suggested by Wadsworth et al. (2020). Importantly, this work shows that dense obsidian fragments may not necessarily represent fragmented lava dome or plug materials and may reflect the complex physico-chemical history of a melt fragment which could have been vesicular at the outset and subsequently densified; thus, this study advises caution when interpreting post-eruption materials in volcanic systems.

In Chapter 3, I expand on the single melt fragment physico-chemical dynamics explored in Chapter 2 by monitoring porosity change in particulate, hydrous fragmental melt systems. I investigate how concurrent vesiculation, diffusive outgassing, and sintering interact to control the development of isolated and connected porosity and explore how this impacts the permeability of these pyroclast assemblages. In these experiments, I crush and sieve natural, hydrous obsidian to a range of fragment sizes and then heat filled crucibles to magmatically relevant temperature for various durations. I find that porosity evolution in hydrous fragmental melt systems can be far more complex than suggested by non-vesiculating sintering models, which apply to systems of typically anhydrous melt particles (Vasseur et al., 2013b; Wadsworth et al., 2017a, 2017b, 2016a, 2014) and fine, rapidly outgassed melt fragments (Gardner et al., 2019, 2018; Wadsworth et al., 2021, 2019). Since the development of vesicularity is fragment-size dependent (as determined in Chapter 2), I find that coarser fragment populations attain higher isolated porosities and densify more slowly during

diffusive outgassing, such that they remain vesicular for longer. The fragment populations sieved between 2.00 mm and 2.36 mm diameter reached a maximum vesicularity (isolated porosity) of ~33 %, whereas the 0.50–- 1.00 mm diameter populations only reached ~6 %. These values are substantially lower than expected for vesicularity of a melt under closed-system conditions, which reaches ~60-80 % vesicularity (e.g., Bagdassarov et al., 1996; Coumans et al., 2020; Ryan et al., 2015a). The change in inter-granular connected pore space largely shows the inverse trend to that of vesicularity, primarily due to the skeletal melt volume impinging on the inter-fragment pore space during expansion of pyroclasts. The connected porosity then increases once diffusive outgassing dominates and the fragments contract and decreases again upon sintering. This porosity change is strongly determined by the fragment size, such that the 0.50 - 1.00 mm fragment assemblages reach a minimum connected porosity of ~42 %, whereas the 2.00–- 2.18 mm fragment populations reach ~22 %. In our samples, this drop is transient and the subsequent recovery in the connected porosity highlights the important distinction between the hydrous phenomenon which I explore in Chapters 2 and 3, and the typical densifying behaviour of chemically stable fragmental melts during sintering (e.g., Vasseur et al., 2013b). However, I note that this complex porosity behaviour is limit to the timescales of vesiculation and diffusive outgassing, after which, densification continues as expected by non-vesiculating sintering models. I find that permeability changes are commensurate with the evolution of the connected porosity, as previously explored for clastic lithologies (Heap et al., 2019; Klug and Cashman, 1996; Wadsworth et al., 2021, 2016b). However, given the complex evolution of connected porosity in my hydrous samples, I find that permeability may not progressively decrease in fragmental systems over time, as discussed in classical sintering studies (e.g., Farquharson et al., 2017; Heap et al., 2019, 2015b; Kendrick et al., 2016; Kolzenburg et al., 2019; Wadsworth et al., 2021), but in fact, may momentarily increase as the melt diffusively outgasses. To my knowledge, this transient and fragment size dependent behaviour has not been previously described in other studies.

By building on the modelling applied in Chapter 2, I show that the porosity and permeability hysteresis of my samples can be assessed through a combination of models for bubble growth (Coumans et al., 2020), diffusive outgassing (von Aulock et al., 2017), and sintering (Vasseur et al., 2013a). Importantly, the relative timescales of these processes define behavioural regimes which control the evolution of shallow melt fragments when a partial pressure differential exists between the melt and atmosphere; very fine fragments can rapidly outgas their volatiles and evolve as predicted from sintering models for anhydrous samples [as shown

by Gardner et al. (2018)]; intermediate sized fragments develop vesicularity that is transient due to concurrent vesiculation and diffusive outgassing, which is lost prior to the completion of sintering; and very coarse fragments will vesiculate first, then sinter before outgassing completes, preserving vesicular melt pockets and dense rinds (cf. Cabrera et al., 2011; Castro et al., 2012; Giachetti et al., 2019; Heap et al., 2019; Saubin et al., 2016; Schipper et al., 2021). I suggest these regimes can explain the wide range of vesicular textures found in fragmental melts and provide clues as to the scope of volcanic venting timescales of such systems.

In Chapter 4, I investigate the physico-chemical and mechanical response of altered volcaniclastic materials to thermal stress. Hyaloclastite samples, collected from the geothermal field at Krafla volcano, Iceland, were selected from the surface (0 m), and the subsurface (70 m, 556 m, and 732 m depth), in order to assess the mechanical properties of hyaloclastites with a range of palagonite mineralogies. Then, to assess the impact of thermal fluctuations that may have influenced these rocks I thermally stress near-pristine, surficial hyaloclastite samples and analyse changes in their properties, including the mineralogy, porosity, permeability, and strength. Differential scanning calorimetry analyses helped identify the temperatures at which mineral alterations occurred; for the surficial material, I observe endothermic reactions at 130 and 185 °C which are typical for the dehydration of smectite (Malek et al., 1997; Shirozu et al., 1975). In the subsurface samples, these dehydration events are also observable, in addition to further endothermic peaks between 525 °C and 660 °C, which correlate with the temperature of chlorite dehydroxylation (Shirozu et al., 1975). The mass loss associated with the dehydration events is greater in the surficial samples, but the dehydroxylation mass loss in the subsurface samples suggests that the chlorite content increases with depth. Using X-ray diffraction to quantify the resultant mineralogy of samples following 12 hours at high temperature confirmed that smectite progressively loses volatiles and breaks down. The percentage of smectite decreases from 19 % in the unstressed samples, to 13 % after 185 °C, and is absent in the 400 °C and 600 °C samples. Textual analysis shows the dehydration and breakdown of smectite damages the palagonite matrix, opening pore space which promotes fluid flow.

The impact of the mineralogical and textural changes associated with thermal stressing are reflected in the evolution of the physical properties (porosity, permeability, and strength) of the surficial samples. Porosity values typically increase from the as-collected values of 35–- 42 %, to 45–- 50 % after being subject to 600 °C, due to breakdown of the palagonite matrix. I find that thermal stressing to 600 °C can produce a three-fold increase in permeability measured at 1 mPa confining pressure, increasing from ~2 × 10$^{-13}$ m$^2$ to ~6 × 10$^{-13}$ m$^2$. These

physical impacts from thermal stress are similar in other hydrothermally altered reservoir rocks (Heap et al., 2017; Mordensky et al., 2019). I also assess the rock strength using room temperature uniaxial compression tests, triaxial tests, and brazil (tensile) tests, which all capture a progressive strength reduction as the stressing temperature and porosity increase, correlating well with other studies (Eggertsson et al., 2020; Harnett et al., 2019; Heap and Violay, 2021; Sammis and Ashby, 1986; Schaefer et al., 2015). I find that after thermal treatment to 600 °C th113trengthth is reduced by 63 % when measured in uniaxial compression, 25 % when measured in triaxial compression (at 5 mPa effective pressure), and 68 % when measured by brazil tensile measurements. Similarly, at high pressure, I observe that compaction (both densification and shutting of permeability) occurs at lower stresses for the samples which had experienced higher temperatures, and which had higher porosities. This correlates well to other descriptions of the compaction behaviour of these hyaloclastites, which shows a strong porosity control (Eggertsson et al., 2020). In concert, I find that the palagonite matrix of hyaloclastite is susceptible to dehydration reactions during excursions to high temperatures, which results in an increase in rock porosity that increases permeability, reduces strength, and enhance the likelihood of compaction. These findings, which are applicable to phyllosilicate-bearing rocks in geothermal regions, may help to illuminate and model how reservoir rocks respond to thermal fluctuations associated with magmatic and/ or anthropogenic, geothermal activities.

## 5.2. Implications for porosity and permeability in fragmental volcanics

The evolution of porosity and permeability in volcanic environments has wide ranging consequences for active volcanism and for fluid flow in geothermal reservoirs. As I discuss in Chapters 2 and 3, the evolution of fragmental lithologies, such as tuffisite veins and clastic conduits, are essential regulators of gas release and pressure dissipation for magmas (e.g., Kendrick et al., 2016; Schipper et al., 2021). The evolution of porosity in these systems has been heavily studied (e.g., Colombier et al., 2017; Farquharson et al., 2017; Heap et al., 2019; Kolzenburg et al., 2019) in order to constrain the behaviour of gas release from magma and resolve the extant conditions associated with different eruptive styles (Castro et al., 2014, 2012; Schipper et al., 2013). The phenomena explored in Chapters 2 and 3 highlight that hydrous melt fragments which experience a partial pressure differential between their interior and the surrounding atmosphere, can develop complex porosity and permeability behaviour which is not captured by existing sintering models (e.g., Vasseur et al., 2013a). The conditions in which this behaviour develops may be achieved in shallow or sub-aerial volcanic

environments, where gas flux (e.g., Rust et al., 2004) or the entrainment of air is common. In fragmental assemblages, the rapid loss in permeability during pyroclast vesiculation may impede the ability to quiescently release gas (cf. Cassidy et al., 2018) potentially resulting in fluid pressure accumulation (e.g., Farquharson et al., 2017), which can drive fragmentation (e.g., Spieler et al., 2004). However, such behaviour is transient and may be short-lived; could sufficient pore pressure accumulate to trigger wholesale fragmentation and an explosive eruption? Potentially, as we show that the fragment size determines how effectively volatiles can escape melt fragments, and so, controls the short-term evolution of the permeable, porous network of pyroclast assemblages. Coarse melt fragments are prone to higher total vesicularity and more effective closure of permeable pathways, whereas predominantly fine melt fragments may experience little vesiculation, suggesting that diffusive outgassing may help to retain degassing pathways and negate pressure accumulation in magma. As such, where diffusive outgassing is prevalent, it may provide an effective mechanism for the removal of volatiles from larger magmatic bodies which contain networks of fragmental pyroclasts (e.g., Castro et al., 2012; Wadsworth et al., 2020a). Studies suggest that tuffisite vein networks may densely permeate throughout magmatic systems (e.g., Castro et al., 2012; Farquharson et al., 2017; Kendrick et al., 2016; McGowan, 2016), and that they may repeatedly form during cycles of failure (fracture and fragmentation) and healing (densification due to diffusive outgassing and sintering; Lamur et al., 2019; Tuffen et al., 2003) and so, are likely associated with hybrid volcanic activity (e.g., Schipper et al., 2013).

The fragment size dependence of volatile redistribution and porosity development is also important for assessing the textural history of a melt. I propose that the variable densification of melt fragments may partly or fully overprint vesiculation, especially at depth (e.g., Kolzenburg et al., 2012), and that textural analyses must consider the transient processes outlined here. This is especially true when comparing fragments of different sizes and determining their densification and vesiculation history. Very fine materials may forgo vesiculation and densify following simple sintering models for non-vesiculating fragments (Gardner et al., 2018). More coarse fragments will deviate from these models as vesiculation increasingly approaches closed-system bubble growth. An assessment of diffusion outgassing timescales may therefore need to be considered when analysing dense melt fragments, or vesicular fragments surrounded by a dense rind (cf. Cabrera et al., 2011; Castro et al., 2012; Giachetti et al., 2021; Heap et al., 2019; Saubin et al., 2016; Schipper et al., 2021). However, it is important to note that the processes I explore here may be limited by higher loads or by rapid cooling. The application of load to a sintering system is captured by the compaction

timescale (Quane et al., 2009), which can vastly outpace surface tension induced sintering at even moderate depths (cf. Heap et al., 2019). Tuffisites and thick ignimbrite deposits may therefore seal before outgassing completes. Similarly, in a rapidly cooling environment, such as might be experienced by ejecta , volumetric changes associated with sintering and volatile redistribution cease below the glass transition, potentially 'locking in' the porosity of pyroclasts and fragmental bodies.

The importance of particle size and surface area on physico-chemical processes explored in Chapter 2 and Chapter 3 are also relevant to the case of altered hyaloclastite in Chapter 4. Here, following deposition, the alteration of basaltic glass to palagonite occurs through elemental diffusion at the margin of glass fragments (e.g., Sturchio et al., 1986), such that the surface area partly determines the extent of palagonitisation. I find that glass is largely immune to the relatively low temperature thermal fluctuations, whereas the palagonite matrix is highly susceptible, and therefore, the physical changes associated with altered hyaloclastite are impacted by the rate of palagonitisation and so, by their fragment size distribution.

I find that temperatures reached in high enthalpy geothermal reservoirs, such as at Krafla (Bodvarsson et al., 1984; Mortensen et al., 2014), cross the stability threshold for some common phyllosilicate minerals (e.g., Kristmannsdóttir, 1979), the dissolution of which induces changes to their host rocks. Temperature in geothermal fields typically increases with depth (e.g., Mortensen et al., 2014), which in part, controls palagonite alteration, alongside the associated pressure increases (Vidal and Dubacq, 2009) and the exposure to various fluid chemistries (e.g., Gislason and Oelkers, 2003). Where the conditions result in the dehydration or dehydroxylation of phyllosilicate minerals in the matrix, as I show in Chapter 4, the fluid storage potential and extraction rate may improve. However, the porosity increase may weaken the rock to the extent that the rocks are forced to compact due to the local stress conditions (Eggertsson et al., 2020). In such cases, fluid flow is compartmentalised, and the permeability and value of the reservoir is greatly reduced (e.g., Nielson and Stiger, 1996). An understanding of the relationships between porosity, permeability, and mechanical characteristics as a function of temperature may help to model reservoir properties with depth (Mortensen et al., 2014; Scott et al., 2022) and around heat sources, such as magma (Saubin et al., 2019). It may also be useful as a constraint during geothermal well stimulation procedures (e.g., Eggertsson et al., 2018; Siratovich et al., 2011), and may need to be considered when assessing ideal fluid extraction and reinjection rates, which have been shown to impact reservoir temperature, porosity, and permeability (e.g., Gunnarsson, 2011).

Where hyaloclastite is host to magmatic intrusions, which impart very high temperatures, the complex suite of feedback mechanisms aforementioned may arise in both the rocks and magma. The baking of hyaloclastite host rock may liberate fluid during dehydration, equivalent to more than 10% of the dry rock mass, which as a vapour would be volumetrically even more substantial. This may cause the magma to quench or phreatomagmatically fragment (e.g., Mayer et al., 2015). If an intrusion dehydrates the host rock and enhances its permeability, then magma outgassing may proceed quiescently; however, if the host rock weakens and then compacts, permeability may be lost, and outgassing may be hindered, causing pressure accumulation that can trigger fragmentation. Where magma intrudes into geothermal reservoirs, the alteration of the host rock may therefore change the hydrothermal system, possibly channelising fluid flow (Kennedy et al., 2022).

The findings from Chapters 2, 3, and 4 highlight that care must be taken when considering and quantifying the properties of fragmental lithologies which are susceptible to chemically- or thermally-activated physical changes. The chemistry, particularly the volatile content, mineralogy, clast size distribution, and pressure conditions can fundamentally change the evolution of porosity and permeability of fragmental systems, with implications for both the development of volcanic eruptions and hazards, and the utilisation of geothermal resources.

## 5.3. Outlook and future work

In Chapter 2, I explore how fragments densify through the formation of a dense rind, which, as I show in Chapter 3, plays an important role in the porosity and permeability evolution of fragmental melts. I show in Chapter 2 that the rind thickness can be modelled by a scaling of the diffusion length and a factor $\mathrm{K}$. Whilst I experimentally constrained that $\mathrm{K} = 2$ to $2.7$ for the range of sample size and experiment conditions I tested, it likely varies slightly as a function of sample geometry and may vary at other conditions. Future studies may be warranted to accurately constrain the rind thickness for a range of melt chemistries, temperatures, partial pressures, and fragment shapes. This would allow for a more accurate assessment of vesicular melt fragment densification in a wider range of environments, and lead to more robust modelling of permeability evolution in hydrous fragmental systems.

In Chapter 3 I highlight that the connected porosity of fragmental melts may decrease as a result of vesiculation. Through the extrapolation of this trend and the application of modelling outlined in Chapter 3, I suggest that vesiculation may remove all connected porosity from a system, and the permeable network may be rapidly shut, especially if the fragmental system

is confined. Further experiments, similar to those in Chapter 3, could assess this vesiculation induced sealing using melt fragments which will vesiculate more or otherwise reach a lower connected porosity; this may be achieved with more coarse fragments, fragments with a higher water content, or potentially, by using more polydisperse fragment populations with higher packing densities. Similarly, experiments in restricted volumes and under confining pressure and load would help resolve the wider range of conditions which can apply to natural systems. I have briefly explored the impact of crystal fragments amongst the hydrous melt particles and found that the systems generally developed poor cohesion and were unable to sinter at crystal fractions above 30 % (data not presented here); in the coming year, I intend to expand on this preliminary observation to widen applicability of the findings to more complex scenarios.

Chapter 4 highlights the complexity associated with thermally driven mineralogical breakdown of altered rocks. The results and the associated interpretations apply to the hyaloclastite samples studied here, and yet, hyaloclastites and other hydrothermally altered rocks comprise a group of highly variable lithologies which are comprised of differing hydrous mineral assemblages, and so, likely share similarity in response to high temperature excursions. To assess the extent to which the findings presented in Chapter 4 can be applied to other lithologies, detailed study is required to determine the dehydration potential of individual minerals, and to assess how rocks comprised of assemblages of these minerals physically respond to the dissolution of their constituents. Furthermore, to accurately determine the thermo-physico-mechanical properties of reservoir rocks, holistic experimental approaches should integrate temperature, pressure, and chemical controls, as the stability of minerals, and their subsequent impact on rock physics, will likely prove complex.

The work presented in this thesis highlights the dynamism of fragmental systems. The experiments provide idealised and controlled recreations of complex volcanic processes in order to constrain the evolution of different volcanic, magmatic, and hydrothermal environments; and yet, even these simple reconstructions offer new insights into inaccessible locales, which were unanticipated at the onset of the projects. Future experimentation, and their integration with in-situ observations, will provide further insights, and I enthusiastically await the discoveries to come.

*"…and thus by sleeping little, and reading much, the moisture of his brain was exhausted to that degree, that at last he lost the use of his reason"*

Don Quixote

# Bibliography

Alfredsson, H.A., Oelkers, E.H., Hardarsson, B.S., Franzson, H., Gunnlaugsson, E., Gislason, S.R., 2013. The geology and water chemistry of the Hellisheidi, SW-Iceland carbon storage site. Int. J. Greenh. Gas Control 12, 399–418. https://doi.org/10.1016/J.IJGGC.2012.11.019

Alidibirov, M., Dingwell, D.B., 1996. Magma fragmentation by rapid decompression. Nature 380, 146–148.

Angelis, S. De, Lamb, O.D., Lamur, A., Hornby, A.J., Von Aulock, F.W., Chigna, G., Lavallée, Y., Rietbrock, A., 2016. Characterization of moderate ash-and-gas explosions at Santiaguito volcano, Guatemala, from infrasound waveform inversion and thermal infrared measurements. Geophys. Res. Lett. 43, 6220–6227.

Anovitz, L.M., Cole, D.R., Fayek, M., 2008. Mechanisms of rhyolitic glass hydration below the glass transition. Am. Mineral. 93, 1166–1178.

Aqui, A.R., Zarrouk, S., 2011. Permeability enhancement of conventional geothermal wells, in: New Zealand Geothermal Workshop. p. 1.

Ármannsson, H., Fridriksson, T., Benjamínsson, J., Hauksson, T., 2013. History of Gas in Geothermal Fluids, Krafla, Northeast Iceland. Procedia Earth Planet. Sci. 7, 23–26. https://doi.org/10.1016/J.PROEPS.2013.03.192

Ármannsson, H., Gudmundsson, A., Steingr\'\imsson, B., 1987. Exploration and development of the Krafla geothermal area. Jökull 37, 13–30.

Ashwell, P.A., Kendrick, J.E., Lavallée, Y., Kennedy, B.M., Hess, K.-U., von Aulock, F.W., Wadsworth, F.B., Vasseur, J., Dingwell, D.B., 2015. Permeability of compacting porous lavas. J. Geophys. Res. Solid Earth 120, 1605–1622.

Axelsson, G., others, 2012. Temperature condition modelling for well IDDP-1 in Krafla, N-Iceland. 001251218.

Bachmann, O., Bergantz, G.W., 2006. Gas percolation in upper-crustal silicic crystal mushes as a mechanism for upward heat advection and rejuvenation of near-solidus magma bodies. J. Volcanol. Geotherm. Res. 149, 85–102.

Bagdassarov, N.S., Dingwell, D.B., 1992. A rheological investigation of vesicular rhyolite. J. Volcanol. Geotherm. Res. 50, 307–322.

Bagdassarov, N.S., Dingwell, D.B., Wilding, M.C., 1996. Rhyolite magma degassing: an experimental study of melt vesiculation. Bull. Volcanol. 57, 587–601.

Bedford, J.D., Faulkner, D.R., Leclère, H., Wheeler, J., 2018. High-resolution mapping of yield curve shape and evolution for porous rock: The effect of inelastic compaction on porous bassanite. J. Geophys. Res. Solid Earth 123, 1217–1234.

Benage, M.C., Dufek, J., Degruyter, W., Geist, D., Harpp, K., Rader, E., 2014. Tying textures of breadcrust bombs to their transport regime and cooling history. J. Volcanol. Geotherm. Res. 274, 92–107.

Berger, G., Schott, J., Loubet, M., 1987. Fundamental processes controlling the first stage of alteration of a basalt glass by seawater: an experimental study between 200° and 320°C. Earth Planet. Sci. Lett. 84, 431–445. https://doi.org/10.1016/0012-821X(87)90008-2

Bergh, S.G., Sigvaldason, G.E., 1991. Pleistocene mass-flow deposits of basaltic hyaloclastite on a shallow submarine shelf, South Iceland. Bull. Volcanol. 53, 597–611.

Bernabé, Y., Mok, U., Evans, B., 2003. Permeability-porosity relationships in rocks subjected to various evolution processes. Pure Appl. Geophys. 160, 937–960.

Bird, D.K., Schiffman, P., Elders, W.A., Williams, A.E., McDowell, S.D., 1984. Calc-silicate mineralization in active geothermal systems. Econ. Geol. 79, 671–695.

Bishop, J.L., Pieters, C.M., Edwards, J.O., 1994. Infrared spectroscopic analyses on the nature of water in montmorillonite. Clays Clay Miner. 42, 702–716.

Bixley, P.F., Clotworthy, A.W., Mannington, W.I., 2009. Evolution of the Wairakei geothermal reservoir during 50 years of production. Geothermics 38, 145–154.

Blower, J.D., Mader, H.M., Wilson, S.D.R., 2001. Coupling of viscous and diffusive controls on bubble growth during explosive volcanic eruptions. Earth Planet. Sci. Lett. 193, 47–56.

Bodvarsson, G.S., Benson, S.M., Sigurdsson, O., Stefansson, V., Eliasson, E.T., 1984. The Krafla geothermal field, Iceland: 1. Analysis of well test data. Water Resour. Res. 20, 1515–1530.

Boek, E.S., Coveney, P. V, Skipper, N.T., 1995. Molecular modeling of clay hydration: A study of hysteresis loops in the swelling curves of sodium montmorillonites. Langmuir 11, 4629–4631.

Branney, M.J., Kokelaar, P., 1992. A reappraisal of ignimbrite emplacement: progressive aggradation and changes from particulate to non-particulate flow during emplacement of high-grade ignimbrite. Bull. Volcanol. 54, 504–520.

Branney, M.J., Kokelaar, P., Kokelaar, B.P., 2002. Pyroclastic density currents and the sedimentation of ignimbrites.

Browning, J., Meredith, P., Gudmundsson, A., 2016. Cooling-dominated cracking in thermally stressed volcanic rocks. Geophys. Res. Lett. 43, 8417–8425.

Bubeck, A., Walker, R.J., Healy, D., Dobbs, M., Holwell, D.A., 2017. Pore geometry as a control on rock strength. Earth Planet. Sci. Lett. 457, 38–48.

Burgisser, A., Chevalier, L., Gardner, J.E., Castro, J.M., 2017. The percolation threshold and permeability evolution of ascending magmas. Earth Planet. Sci. Lett. 470, 37–47.

Bursik, M.I., Sparks, R.S.J., Gilbert, J.S., Carey, S.N., 1992. Sedimentation of tephra by volcanic plumes: I. Theory and its comparison with a study of the Fogo A plinian deposit, Sao Miguel (Azores). Bull. Volcanol. 54, 329–344.

Cabrera, A., Weinberg, R.F., Wright, H.M.N., Zlotnik, S., Cas, R.A.F., 2011. Melt fracturing and healing: A mechanism for degassing and origin of silicic obsidian. Geology 39, 67–70.

Caricchi, L., Burlini, L., Ulmer, P., Gerya, T., Vassalli, M., Papale, P., 2007. Non-Newtonian rheology of crystal-bearing magmas and implications for magma ascent dynamics. Earth Planet. Sci. Lett. 264, 402–419.

Carman, P.C., 1937. Fluid flow through granular beds. Trans. Inst. Chem. Eng. 15, 150–166.

Carniel, L.C., Conceição, R.V., Dani, N., Stefani, V.F., Balzaretti, N.M., dos Reis, R., 2014. Structural changes of potassium-saturated smectite at high pressures and high temperatures: Application for subduction zones. Appl. Clay Sci. 102, 164–171.

Cas, R., Wright, J., 2012. Volcanic successions modern and ancient: A geological approach to processes, products and successions. Springer Science & Business Media.

Casas, A.S., Wadsworth, F.B., Ayris, P.M., Delmelle, P., Vasseur, J., Cimarelli, C., Dingwell, D.B., 2019. SO2 scrubbing during percolation through rhyolitic volcanic domes. Geochim. Cosmochim. Acta 257, 150–162.

Cassidy, M., Manga, M., Cashman, K., Bachmann, O., 2018. Controls on explosive-effusive volcanic eruption styles. Nat. Commun. 9, 1–16.

Castro, J.M., Beck, P., Tuffen, H., Nichols, A.R.L., Dingwell, D.B., Martin, M.C., 2008. Timescales of spherulite crystallization in obsidian inferred from water concentration profiles. Am. Mineral. 93, 1816–1822.

Castro, J.M., Bindeman, I.N., Tuffen, H., Schipper, C.I., 2014. Explosive origin of silicic lava: textural and $\delta$D--H2O evidence for pyroclastic degassing during rhyolite effusion. Earth Planet. Sci. Lett. 405, 52–61.

Castro, J.M., Cordonnier, B., Tuffen, H., Tobin, M.J., Puskar, L., Martin, M.C., Bechtel, H.A., 2012. The role of melt-fracture degassing in defusing explosive rhyolite eruptions at volcán Chaitén. Earth Planet. Sci. Lett. 333, 63–69.

Cerling, T.E., Brown, F.H., Bowman, J.R., 1985. Low-temperature alteration of volcanic glass: hydration, Na, K, 18O and Ar mobility. Chem. Geol. Isot. Geosci. Sect. 52, 281–293.

Clearwater, J., Azwar, L., Barnes, M., Wallis, I., Holt, R., 2015. Changes in injection well capacity during testing and plant start-up at Ngatamariki. Changes 19, 25.

Coats, R., Kendrick, J.E., Wallace, P.A., Miwa, T., Hornby, A.J., Ashworth, J.D., Matsushima, T., Lavallée, Y., 2018. Failure criteria for porous dome rocks and lavas: a study of Mt. Unzen, Japan. Solid Earth 9, 1299–1328.

Colombier, M., Wadsworth, F., Scheu, B., Dobson, K., Caceres, F., Vasseur, J., Allabar, A., Llewellin, E., Marone, F., Schlepuetz, C., others, 2018. The role of crystals on vesiculation and outgassing during volcanic eruptions: insights from 4D synchrotron experiments, in: EGU General Assembly Conference Abstracts. p. 639.

Colombier, M., Wadsworth, F.B., Gurioli, L., Scheu, B., Kueppers, U., Di Muro, A., Dingwell, D.B., 2017. The evolution of pore connectivity in volcanic rocks. Earth Planet. Sci. Lett. 462, 99–109.

Cooper, H.W., Simmons, G., 1977. The effect of cracks on the thermal expansion of rocks. Earth Planet. Sci. Lett. 36, 404–412.

Cordonnier, B., Hess, K.-U., Lavallee, Y., Dingwell, D.B., 2009. Rheological properties of dome lavas: Case study of Unzen volcano. Earth Planet. Sci. Lett. 279, 263–272.

Costa, A., 2006. Permeability-porosity relationship: A reexamination of the Kozeny-Carman equation based on a fractal pore-space geometry assumption. Geophys. Res. Lett. 33.

Coumans, J.P., Llewellin, E.W., Wadsworth, F.B., Humphreys, M.C.S., Mathias, S.A., Yelverton, B.M., Gardner, J.E., 2020. An experimentally validated numerical model for bubble growth in magma. J. Volcanol. Geotherm. Res. 402, 107002.

Dalby, K.N., King, P.L., 2006. A new approach to determine and quantify structural units in silicate glasses using micro-reflectance Fourier-Transform infrared spectroscopy. Am. Mineral. 91, 1783–1793.

Darcy, H., 1856. Les fontaines publiques de la ville de Dijon: exposition et application... Victor Dalmont.

Davis, A.S., Clague, D.A., 2003. Hyaloclastite from Miocene seamounts offshore central California: compositions, eruption styles, and depositional processes. Washingt. DC Am. Geophys. Union Geophys. Monogr. Ser. 140, 129–142.

De Simone, S., Vilarrasa, V., Carrera, J., Alcolea, A., Meier, P., 2013. Thermal coupling may control mechanical stability of geothermal reservoirs during cold water injection. Phys. Chem. Earth, Parts A/B/C 64, 117–126.

de Siqueira, A. V, Lobban, C., Skipper, N.T., Williams, G.D., Soper, A.K., Done, R., Dreyer, J.W., Humphreys, R.J., Bones, J.A.R., 1999. The structure of pore fluids in swelling clays at elevated pressures and temperatures. J. Phys. Condens. Matter 11, 9179.

Degruyter, W., Bachmann, O., Burgisser, A., Manga, M., 2012. The effects of outgassing on the transition between effusive and explosive silicic eruptions. Earth Planet. Sci. Lett. 349–350, 161–170. https://doi.org/10.1016/j.epsl.2012.06.056

Denton, J.S., Tuffen, H., Gilbert, J.S., 2012. Variations in hydration within perlitised rhyolitic lavas—evidence from Torfajökull, Iceland. J. Volcanol. Geotherm. Res. 223, 64–73.

Denton, J.S., Tuffen, H., Gilbert, J.S., Odling, N., 2009. The hydration and alteration of perlite and rhyolite. J. Geol. Soc. London. 166, 895–904.

Diller, K., Clarke, A.B., Voight, B., Neri, A., 2006. Mechanisms of conduit plug formation: Implications for vulcanian explosions. Geophys. Res. Lett. 33.

Dingwell, D.B., 2006. Transport properties of magmas: diffusion and rheology. Elements 2, 281–286.

Dingwell, D.B., 1998. The glass transition in hydrous granitic melts. Phys. Earth Planet. Inter. 107, 1–8.

Dingwell, D.B., 1996. Volcanic Dilemma--Flow or Blow? Science (80-. ). 273, 1054–1055.

Dingwell, D.B., Mysen, B.O., 1985. Effects of water and fluorine on the viscosity of albite melt at high pressure: a preliminary investigation. Earth Planet. Sci. Lett. 74, 266–274.

Dingwell, D.B., Webb, S.L., 1990. Relaxation in silicate melts. Eur. J. Mineral. 427–449.

Dingwell, D.B., Webb, S.L., 1989. Structural relaxation in silicate melts and non-Newtonian melt rheology in geologic processes. Phys. Chem. Miner. 16, 508–516.

Dobson, P.F., Kneafsey, T.J., Hulen, J., Simmons, A., 2003. Porosity, permeability, and fluid flow in the Yellowstone geothermal system, Wyoming. J. Volcanol. Geotherm. Res. 123, 313–324.

Drief, A., Schiffman, P., 2004. Very low-temperature alteration of sideromelane in hyaloclastites and hyalotuffs from Kilauea and Mauna Kea volcanoes: implications for the mechanism of palagonite formation. Clays Clay Miner. 52, 622–634.

Duller, R.A., Mountney, N.P., Russell, A.J., Cassidy, N.C., 2008. Architectural analysis of a volcaniclastic jökulhlaup deposit, southern Iceland: sedimentary evidence for supercritical flow. Sedimentology 55, 939–964.

Duraiswami, R.A., Gadpallu, P., Shaikh, T.N., Cardin, N., 2014. Pahoehoe--a' a transitions in the lava flow fields of the western Deccan Traps, India-implications for emplacement

dynamics, flood basalt architecture and volcanic stratigraphy. J. Asian Earth Sci. 84, 146–166.

Edmonds, M., Herd, R.A., 2007. A volcanic degassing event at the explosive-effusive transition. Geophys. Res. Lett. 34.

Edmonds, M., Oppenheimer, C., Pyle, D.M., Herd, R.A., Thompson, G., 2003. SO2 emissions from Soufrière Hills Volcano and their relationship to conduit permeability, hydrothermal interaction and degassing regime. J. Volcanol. Geotherm. Res. 124, 23–43.

Eggertsson, G.H., Kendrick, J.E., Weaver, J., Wallace, P.A., Utley, J.E.P., Bedford, J.D., Allen, M.J., Markússon, S.H., Worden, R.H., Faulkner, D.R., others, 2020. Compaction of hyaloclastite from the active geothermal system at Krafla volcano, Iceland. Geofluids 2020.

Eggertsson, G.H., Lavallée, Y., Kendrick, J.E., Markússon, S.H., 2018. Improving fluid flow in geothermal reservoirs by thermal and mechanical stimulation: The case of Krafla volcano, Iceland. J. Volcanol. Geotherm. Res.

Farquharson, J., Heap, M.J., Baud, P., Reuschlé, T., Varley, N.R., 2016. Pore pressure embrittlement in a volcanic edifice. Bull. Volcanol. 78, 6.

Farquharson, J.I., Heap, M.J., Lavallee, Y., Varley, N.R., Baud, P., 2016. Evidence for the development of permeability anisotropy in lava domes and volcanic conduits. J. Volcanol. Geotherm. Res. 323, 163–185.

Farquharson, J.I., Wadsworth, F.B., 2018. Upscaling permeability in anisotropic volcanic systems. J. Volcanol. Geotherm. Res. 364, 35–47.

Farquharson, J.I., Wadsworth, F.B., Heap, M.J., Baud, P., 2017. Time-dependent permeability evolution in compacting volcanic fracture systems and implications for gas overpressure. J. Volcanol. Geotherm. Res. 339, 81–97.

Faulkner, D.R., Rutter, E.H., 2000. Comparisons of water and argon permeability in natural clay-bearing fault gouge under high pressure at 20° C. J. Geophys. Res. Solid Earth 105, 16415–16426.

Ferrer, M., Seisdedos, J., de Vallejo, L.I., others, 2010. The role of hyaloclastite rocks in the stability of the volcanic island flank of Tenerife. Volcan. Rock Mech. Taylor Fr. Group, London 167–170.

Fisher, R. V, 1961. Proposed classification of volcaniclastic sediments and rocks. Geol. Soc. Am. Bull. 72, 1409–1414.

Fisher, R. V, 1960. Classification of volcanic breccias. Geol. Soc. Am. Bull. 71, 973–982.

Forchheimer, P., 1901. Wasserbewegung durch boden. Z. Ver. Deutsch, Ing. 45, 1782–1788.

Franzson, H., Gu\dhfinnsson, G.H., Helgadóttir, H.M., Frolova, J., 2010. Porosity, density and chemical composition relationships in altered Icelandic hyaloclastites. CRC Press Inc.

Franzson, H., Zierenberg, R., Schiffman, P., 2008. Chemical transport in geothermal systems in Iceland: evidence from hydrothermal alteration. J. Volcanol. Geotherm. Res. 173, 217–229.

Frenkel, J., 1946. Viscous flow of crystalline bodies. Zhurnal Eksp. i Teor. Fiz. 16, 29–38.

Fridleifsson, G., Ármannsson, H., Mortensen, A.K., 2006. Geothermal conditions in the Krafla

caldera with focus on well KG-26. Icel. Geosurvey Reykjavik, Icel.

Gardner, J.E., Thomas, R.M.E., Jaupart, C., Tait, S., 1996. Fragmentation of magma during Plinian volcanic eruptions. Bull. Volcanol. 58, 144–162.

Gardner, J.E., Wadsworth, F.B., Llewellin, E.W., Watkins, J.M., Coumans, J.P., 2019. Experimental constraints on the textures and origin of obsidian pyroclasts. Bull. Volcanol. 81, 1–15.

Gardner, J.E., Wadsworth, F.B., Llewellin, E.W., Watkins, J.M., Coumans, J.P., 2018. Experimental sintering of ash at conduit conditions and implications for the longevity of tuffisites. Bull. Volcanol. 80, 23.

Gautason, E., Blischke, A., Danielsen, P.E., 2007. Krafla: Borun tveggjakjarnaholna, KH-5 og KH-6 veturinn 2006–2007. ÍSOR technical report 07075,Reykjavik 22.

Ghassemi, A., Kumar, G.S., 2007. Changes in fracture aperture and fluid pressure due to thermal stress and silica dissolution/precipitation induced by heat extraction from subsurface rocks. Geothermics 36, 115–140.

Giachetti, T., Druitt, T.H., Burgisser, A., Arbaret, L., Galven, C., 2010. Bubble nucleation, growth and coalescence during the 1997 Vulcanian explosions of Soufrière Hills Volcano, Montserrat. J. Volcanol. Geotherm. Res. 193, 215–231.

Giachetti, T., Gonnermann, H.M., 2013. Water in volcanic pyroclast: Rehydration or incomplete degassing? Earth Planet. Sci. Lett. 369, 317–332.

Giachetti, T., Gonnermann, H.M., Gardner, J.E., Burgisser, A., Hajimirza, S., Earley, T.C., Truong, N., Toledo, P., 2019. Bubble coalescence and percolation threshold in expanding rhyolitic magma. Geochemistry, Geophys. Geosystems 20, 1054–1074.

Giachetti, T., Trafton, K.R., Wiejaczka, J., Gardner, J.E., Watkins, J.M., Shea, T., Wright, H.M.N., 2021. The products of primary magma fragmentation finally revealed by pumice agglomerates. Geology 49, 1307–1311.

Giordano, D., Russell, J.K., Dingwell, D.B., 2008. Viscosity of magmatic liquids: a model. Earth Planet. Sci. Lett. 271, 123–134.

Gislason, S.R., Oelkers, E.H., 2003. Mechanism, rates, and consequences of basaltic glass dissolution: II. An experimental study of the dissolution rates of basaltic glass as a function of pH and temperature. Geochim. Cosmochim. Acta 67, 3817–3832.

Gonnermann, H.M., 2015. Magma fragmentation. Annu. Rev. Earth Planet. Sci. 43, 431–458.

Gonnermann, H.M., Giachetti, T., Fliedner, C., Nguyen, C.T., Houghton, B.F., Crozier, J.A., Carey, R.J., 2017. Permeability during magma expansion and compaction. J. Geophys. Res. Solid Earth 122, 9825–9848.

Griffiths, L., Heap, M.J., Wang, F., Daval, D., Gilg, H.A., Baud, P., Schmittbuhl, J., Genter, A., 2016. Geothermal implications for fracture-filling hydrothermal precipitation. Geothermics 64, 235–245.

Gudmundsson, B.T., Arnórsson, S., 2002. Geochemical monitoring of the Krafla and Námafjall geothermal areas, N-Iceland. Geothermics 31, 195–243.

Gunnarsson, G., 2011. Mastering reinjection in the Hellisheidi Field, SW-Iceland: a story of successes and failures, in: Proc., 36th Workshop on Geothermal Reservoir Engineering, Stanford University.

Gysi, A.P., Stefánsson, A., 2012. Mineralogical aspects of CO2 sequestration during hydrothermal basalt alteration—An experimental study at 75 to 250 C and elevated pCO2. Chem. Geol. 306, 146–159.

Harnett, C.E., Kendrick, J.E., Lamur, A., Thomas, M.E., Stinton, A., Wallace, P.A., Utley, J.E.P., Murphy, W., Neuberg, J., Lavallée, Y., 2019. Evolution of Mechanical Properties of Lava Dome Rocks Across the 1995--2010 Eruption of Soufrière Hills Volcano, Montserrat. Front. Earth Sci. 7.

Hauri, E., Wang, J., Dixon, J.E., King, P.L., Mandeville, C., Newman, S., 2002. SIMS analysis of volatiles in silicate glasses: 1. Calibration, matrix effects and comparisons with FTIR. Chem. Geol. 183, 99–114.

Heap, Lavallée, Y., Petrakova, L., Baud, P., Reuschle, T., Varley, N.R., Dingwell, D.B., 2014. Microstructural controls on the physical and mechanical properties of edifice-forming andesites at Volcán de Colima, Mexico. J. Geophys. Res. Solid Earth 119, 2925–2963.

Heap, M.J., Farquharson, J.I., Baud, P., Lavallée, Y., Reuschlé, T., 2015a. Fracture and compaction of andesite in a volcanic edifice. Bull. Volcanol. 77, 55.

Heap, M.J., Farquharson, J.I., Wadsworth, F.B., Kolzenburg, S., Russell, J.K., 2015b. Timescales for permeability reduction and strength recovery in densifying magma. Earth Planet. Sci. Lett. 429, 223–233.

Heap, M.J., Kennedy, B.M., 2016. Exploring the scale-dependent permeability of fractured andesite. Earth Planet. Sci. Lett. 447, 139–150.

Heap, M.J., Kennedy, B.M., Farquharson, J.I., Ashworth, J., Mayer, K., Letham-Brake, M., Reuschle, T., Gilg, H.A., Scheu, B., Lavallée, Y., others, 2017. A multidisciplinary approach to quantify the permeability of the Whakaari/White Island volcanic hydrothermal system (Taupo Volcanic Zone, New Zealand). J. Volcanol. Geotherm. Res. 332, 88–108.

Heap, M.J., Lavallée, Y., Laumann, A., Hess, K.-U., Meredith, P.G., Dingwell, D.B., 2012. How tough is tuff in the event of fire? Geology 40, 311–314.

Heap, M.J., Lavallée, Y., Laumann, A., Hess, K.-U., Meredith, P.G., Dingwell, D.B., Huismann, S., Weise, F., 2013a. The influence of thermal-stressing (up to 1000 C) on the physical, mechanical, and chemical properties of siliceous-aggregate, high-strength concrete. Constr. Build. Mater. 42, 248–265.

Heap, M.J., Mollo, S., Vinciguerra, S., Lavallée, Y., Hess, K.-U., Dingwell, D.B., Baud, P., Iezzi, G., 2013b. Thermal weakening of the carbonate basement under Mt. Etna volcano (Italy): implications for volcano instability. J. Volcanol. Geotherm. Res. 250, 42–60.

Heap, M.J., Reuschlé, T., Farquharson, J.I., Baud, P., 2018. Permeability of volcanic rocks to gas and water. J. Volcanol. Geotherm. Res. 354, 29–38.

Heap, M.J., Tuffen, H., Wadsworth, F.B., Reuschlé, T., Castro, J.M., Schipper, C.I., 2019. The permeability evolution of tuffisites and implications for outgassing through dense rhyolitic magma. J. Geophys. Res. Solid Earth 124, 8281–8299.

Heap, M.J., Violay, M.E.S., 2021. The mechanical behaviour and failure modes of volcanic rocks: a review. Bull. Volcanol. 83, 1–47.

Hekinian, R., Pineau, F., Shilobreeva, S., Bideau, D., Gracia, E., Javoy, M., 2000. Deep sea explosive activity on the Mid-Atlantic Ridge near 34 50' N: Magma composition, vesicularity and volatile content. J. Volcanol. Geotherm. Res. 98, 49–77.

Helo, C., Clague, D.A., Dingwell, D.B., Stix, J., 2013. High and highly variable cooling rates during pyroclastic eruptions on Axial Seamount, Juan de Fuca Ridge. J. Volcanol. Geotherm. Res. 253, 54–64.

Hess, K.U., Dingwell, D.B., 1996. Viscosities of hydrous leucogranitic melts: A non-Arrhenian model. Am. Mineral. J. Earth Planet. Mater. 81, 1297–1300.

Hodgetts, A.G.E., McGarvie, D., Tuffen, H., Simmons, I.C., 2021. The Thórólfsfell tuya, South Iceland--A new type of basaltic glaciovolcano. J. Volcanol. Geotherm. Res. 411, 107175.

Honnorez, J., Kirst, P., 1975. Submarine basaltic volcanism: morphometric parameters for discriminating hyaloclastites from hyalotuffs. Bull. Volcanol. 39, 441.

Hornby, A., Lavallée, Y., Kendrick, J.E., De Angelis, S., Lamur, A., Lamb, O.D., Rietbrock, A., Chigna, G., 2019. Brittle-ductile deformation and tensile rupture of dome lava during inflation at Santiaguito, Guatemala. J. Geophys. Res. Solid Earth.

Jaeger, J.C., Cook, N.G.W., Zimmerman, R., 2009. Fundamentals of rock mechanics. John Wiley \& Sons.

Jakobsson, S.P., Gudmundsson, M.T., 2008. Subglacial and intraglacial volcanic formations in Iceland. Jökull 58, 179–196.

Jarosch, A., Gudmundsson, M.T., Högnadóttir, T., Axelsson, G., 2008. Progressive cooling of the hyaloclastite ridge at Gjálp, Iceland, 1996--2005. J. Volcanol. Geotherm. Res. 170, 218–229.

Jia, X., Williams, R.A., 2001. A packing algorithm for particles of arbitrary shapes. Powder Technol. 120, 175–186.

Johnson, J.B., Lees, J.M., Gerst, A., Sahagian, D., Varley, N., 2008. Long-period earthquakes and co-eruptive dome inflation seen with particle image velocimetry. Nature 456, 377–381.

Jones, T.J., Russell, J.K., Brown, R.J., Hollendonner, L., 2022. Melt stripping and agglutination of pyroclasts during the explosive eruption of low viscosity magmas. Nat. Commun. 13, 1–11.

Kawano, M., Tomita, K., 1991. Dehydration and rehydration of saponite and vermiculite. Clays Clay Miner. 39, 174–183.

Kawano, M., Tomita, K., Kamino, Y., 1993. Formation of clay minerals during low temperature experimental alteration of obsidian. Clays Clay Miner. 41, 431–441.

Kendrick, J.E., Lavallée, Y., Varley, N.R., Wadsworth, F.B., Lamb, O.D., Vasseur, J., 2016. Blowing off steam: tuffisite formation as a regulator for lava dome eruptions. Front. Earth Sci. 4, 41.

Kendrick, J.E., Smith, R., Sammonds, P., Meredith, P.G., Dainty, M., Pallister, J.S., 2013. The influence of thermal and cyclic stressing on the strength of rocks from Mount St. Helens, Washington. Bull. Volcanol. 75, 728.

Kennedy, B., Heap, M., Burchardt, S., Villeneuve, M., Tuffen, H., Gilg, H.A., Davidson, J., Duncan, N., Saubin, E., Gestsson, E.B., others, 2022. Thermal impact of dykes on ignimbrite and implications for fluid flow channelisation in a caldera. Volcanica 5, 75–93.

Kennedy, L.A., Russell, J.K., 2012. Cataclastic production of volcanic ash at Mount Saint Helens. Phys. Chem. Earth, Parts A/B/C 45, 40–49.

Kim, K.-Y., Han, W.S., Park, E., 2013. The impact of highly permeable layer on hydraulic system in a coastal aquifer. Hydrol. Process. 27, 3128–3138.

Kim, K.-Y., Park, Y.-S., Kim, G.-P., Park, K.-H., 2009. Dynamic freshwater--saline water interaction in the coastal zone of Jeju Island, South Korea. Hydrogeol. J. 17, 617–629.

Klinkenberg, L.J., others, 1941. The permeability of porous media to liquids and gases, in: Drilling and Production Practice.

Klug, C., Cashman, K. V, 1996. Permeability development in vesiculating magmas: implications for fragmentation. Bull. Volcanol. 58, 87–100.

Kokelaar, P., 1986. Magma-water interactions in subaqueous and emergent basaltic. Bull. Volcanol. 48, 275–289.

Kolaříková, I., Přikryl, R., Hanus, R., Jelínek, E., 2005. Thermal loading of smectite-rich rocks: natural processes vs. laboratory experiments. Appl. Clay Sci. 29, 215–223.

Kolzenburg, S., Chevrel, M.O., Dingwell, D.B., 2022. Magma/suspension rheology. Rev. Mineral. Geochemistry 87, 639–720.

Kolzenburg, S., Russell, J.K., 2014. Welding of pyroclastic conduit infill: A mechanism for cyclical explosive eruptions. J. Geophys. Res. Solid Earth 119, 5305–5323.

Kolzenburg, S., Russell, J.K., Kennedy, L.A., 2013. Energetics of glass fragmentation: Experiments on synthetic and natural glasses. Geochemistry, Geophys. Geosystems 14, 4936–4951.

Kolzenburg, S., Ryan, A.G., Russell, J.K., 2019. Permeability evolution during non-isothermal compaction in volcanic conduits and tuffisite veins: Implications for pressure monitoring of volcanic edifices. Earth Planet. Sci. Lett. 527, 115783.

Kozeny, J., 1927. Uber kapillare leitung der wasser in boden. R. Acad. Sci. Vienna, Proc. Cl. I 136, 271–306.

Kristmannsdóttir, H., 1979. Alteration of Basaltic Rocks by Hydrothermal-Activity at 100-300 C, in: Developments in Sedimentology. Elsevier, pp. 359–367.

Kueppers, U., Perugini, D., Dingwell, D.B., 2006a. "Explosive energy" during volcanic eruptions from fractal analysis of pyroclasts. Earth Planet. Sci. Lett. 248, 800–807.

Kueppers, U., Scheu, B., Spieler, O., Dingwell, D.B., 2006b. Fragmentation efficiency of explosive volcanic eruptions: A study of experimentally generated pyroclasts. J. Volcanol. Geotherm. Res. 153, 125–135.

Kumar, G.S., Ghassemi, A., 2005. Numerical modeling of non-isothermal quartz dissolution/precipitation in a coupled fracture--matrix system. Geothermics 34, 411–439.

Kwon, O., Herbert, B.E., Kronenberg, A.K., 2004. Permeability of illite-bearing shale: 2. Influence of fluid chemistry on flow and functionally connected pores. J. Geophys. Res. Solid Earth 109.

Lamur, A., Kendrick, J.E., Eggertsson, G.H., Wall, R.J., Ashworth, J.D., Lavallée, Y., 2017. The permeability of fractured rocks in pressurised volcanic and geothermal systems. Sci. Rep. 7, 1–9.

Lamur, A., Kendrick, J.E., Wadsworth, F.B., Lavallée, Y., 2019. Fracture healing and strength

recovery in magmatic liquids. Geology 47, 195–198.

Lamur, A., Lavallée, Y., Iddon, F.E., Hornby, A.J., Kendrick, J.E., von Aulock, F.W., Wadsworth, F.B., 2018. Disclosing the temperature of columnar jointing in lavas. Nat. Commun. 9, 1–7.

Lavallée, Y., Benson, P.M., Heap, M.J., Hess, K.-U., Flaws, A., Schillinger, B., Meredith, P.G., Dingwell, D.B., 2013. Reconstructing magma failure and the degassing network of dome-building eruptions. Geology 41, 515–518.

Lavallée, Y., Hess, K.-U., Cordonnier, B., Bruce Dingwell, D., 2007. Non-Newtonian rheological law for highly crystalline dome lavas. Geology 35, 843–846.

Lavallée, Y., Kendrick, J.E., 2022. Strain localization in magmas. Rev. Mineral. Geochemistry 87, 721–765.

Lavallée, Y., Kendrick, J.E., 2021. A review of the physical and mechanical properties of volcanic rocks and magmas in the brittle and ductile regimes. Forecast. Plan. Volcan. hazards, risks, disasters 153–238.

Lavallée, Y., Meredith, P.G., Dingwell, D.B., Hess, K.-U., Wassermann, J., Cordonnier, B., Gerik, A., Kruhl, J.H., 2008. Seismogenic lavas and explosive eruption forecasting. Nature 453, 507–510.

Lavallée, Y., Wadsworth, F.B., Vasseur, J., Russell, J.K., Andrews, G.D.M., Hess, K.-U., von Aulock, F.W., Kendrick, J.E., Tuffen, H., Biggin, A.J., others, 2015. Eruption and emplacement timescales of ignimbrite super-eruptions from thermo-kinetics of glass shards. Front. Earth Sci. 3, 2.

Lejeune, A.-M., Richet, P., 1995. Rheology of crystal-bearing silicate melts: An experimental study at high viscosities. J. Geophys. Res. Solid Earth 100, 4215–4229.

Lensky, N.G., Lyakhovsky, V., Navon, O., 2001. Radial variations of melt viscosity around growing bubbles and gas overpressure in vesiculating magmas. Earth Planet. Sci. Lett. 186, 1–6.

Lévy, L., Gibert, B., Sigmundsson, F., Flóvenz, Ó.G., Hersir, G.P., Briole, P., Pezard, P.A., 2018. The role of smectites in the electrical conductivity of active hydrothermal systems: electrical properties of core samples from Krafla volcano, Iceland. Geophys. J. Int. 215, 1558–1582.

Liu, E.J., Cashman, K. V, Rust, A.C., Gislason, S.R., 2015. The role of bubbles in generating fine ash during hydromagmatic eruptions. Geology 43, 239–242.

Liu, Y., Zhang, Y., Behrens, H., 2005. Solubility of H2O in rhyolitic melts at low pressures and a new empirical model for mixed H2O--CO2 solubility in rhyolitic melts. J. Volcanol. Geotherm. Res. 143, 219–235.

Llewellin, E.W., Mader, H.M., Wilson, S.D.R., 2002. The rheology of a bubbly liquid. Proc. R. Soc. London. Ser. A Math. Phys. Eng. Sci. 458, 987–1016.

Lucia, F.J., 1995. Rock-fabric/petrophysical classification of carbonate pore space for reservoir characterization. Am. Assoc. Pet. Geol. Bull. 79, 1275–1300.

Mader, H.M., Llewellin, E.W., Mueller, S.P., 2013. The rheology of two-phase magmas: A review and analysis. J. Volcanol. Geotherm. Res. 257, 135–158.

Malek, Z., Balek, V., Garfinkel-Shweky, D., Yariv, S., 1997. The study of the dehydration and

dehydroxylation of smectites by emanation thermal analysis. J. Therm. Anal. 48, 83–92.

Manga, M., Castro, J., Cashman, K. V, Loewenberg, M., 1998. Rheology of bubble-bearing magmas. J. Volcanol. Geotherm. Res. 87, 15–28.

Mangan, M., Sisson, T., 2005. Evolution of melt-vapor surface tension in silicic volcanic systems: Experiments with hydrous melts. J. Geophys. Res. Solid Earth 110.

Manville, V., Németh, K., Kano, K., 2009. Source to sink: a review of three decades of progress in the understanding of volcaniclastic processes, deposits, and hazards. Sediment. Geol. 220, 136–161.

Maria, A., Carey, S., 2002. Using fractal analysis to quantitatively characterize the shapes of volcanic particles. J. Geophys. Res. Solid Earth 107, ECV--7.

Marks, N., Schiffman, P., Zierenberg, R.A., Franzson, H., Fridleifsson, G.Ó., 2010. Hydrothermal alteration in the Reykjanes geothermal system: Insights from Iceland deep drilling program well RN-17. J. Volcanol. Geotherm. Res. 189, 172–190.

Martys, N.S., Torquato, S., Bentz, D.P., 1994. Universal scaling of fluid permeability for sphere packings. Phys. Rev. E 50, 403.

Matter, J.M., Broecker, W.S., Gislason, S.R., Gunnlaugsson, E., Oelkers, E.H., Stute, M., Sigurdardóttir, H., Stefansson, A., Alfre\dhsson, H.A., Aradóttir, E.S., others, 2011. The CarbFix Pilot Project--storing carbon dioxide in basalt. Energy Procedia 4, 5579–5585.

Maxwell, J.C., 1867. Iv. on the dynamical theory of gases. Philos. Trans. R. Soc. London 49–88.

Mayer, K., Scheu, B., Gilg, H.A., Heap, M.J., Kennedy, B.M., Lavallée, Y., Letham-Brake, M., Dingwell, D.B., 2015. Experimental constraints on phreatic eruption processes at Whakaari (White Island volcano). J. Volcanol. Geotherm. Res. 302, 150–162.

McGowan, E., 2016. Magma emplacement and deformation in rhyolitic dykes: insight into magmatic outgassing. Lancaster University.

McIntosh, I.M., Llewellin, E.W., Humphreys, M.C.S., Nichols, A.R.L., Burgisser, A., Schipper, C.I., Larsen, J.F., 2014. Distribution of dissolved water in magmatic glass records growth and resorption of bubbles. Earth Planet. Sci. Lett. 401, 1–11.

McNamara, D.D., Lister, A., Prior, D.J., 2016. Calcite sealing in a fractured geothermal reservoir: Insights from combined EBSD and chemistry mapping. J. Volcanol. Geotherm. Res. 323, 38–52.

Melnik, O., Barmin, A.A., Sparks, R.S.J., 2005. Dynamics of magma flow inside volcanic conduits with bubble overpressure buildup and gas loss through permeable magma. J. Volcanol. Geotherm. Res. 143, 53–68.

Mielke, P., Nehler, M., Bignall, G., Sass, I., 2015. Thermo-physical rock properties and the impact of advancing hydrothermal alteration—A case study from the Tauhara geothermal field, New Zealand. J. Volcanol. Geotherm. Res. 301, 14–28.

Milliken, R.E., Mustard, J.F., 2005. Quantifying absolute water content of minerals using near-infrared reflectance spectroscopy. J. Geophys. Res. Planets 110.

Mitchell, N.C., 2003. Susceptibility of mid-ocean ridge volcanic islands and seamounts to large-scale landsliding. J. Geophys. Res. Solid Earth 108.

Mordensky, S.P., Kennedy, B.M., Villeneuve, M.C., Lavallée, Y., Reichow, M.K., Wallace, P.A.,

Siratovich, P.A., Gravley, D.M., 2019. Increasing the permeability of hydrothermally altered andesite by transitory heating. Geochemistry, Geophys. Geosystems.

Mortensen, A.K., Egilson, \TH, Gautason, B., Árnadóttir, S., Gu\dhmundsson, Á., 2014. Stratigraphy, alteration mineralogy, permeability and temperature conditions of well IDDP-1, Krafla, NE-Iceland. Geothermics 49, 31–41.

Mosser-Ruck, R., Devineau, K., Charpentier, D., Cathelineau, M., 2005. Effects of ethylene glycol saturation protocols on XRD patterns: a critical review and discussion. Clays Clay Miner. 53, 631–638.

Mueller, S., Melnik, O., Spieler, O., Scheu, B., Dingwell, D.B., 2005. Permeability and degassing of dome lavas undergoing rapid decompression: an experimental determination. Bull. Volcanol. 67, 526–538.

Mysen, B.O., 1990. Relationships between silicate melt structure and petrologic processes. Earth-Science Rev. 27, 281–365.

Navon, O., Lyakhovsky, V., 1998. Vesiculation processes in silicic magmas. Geol. Soc. London, Spec. Publ. 145, 27–50.

Neuberg, J.W., Tuffen, H., Collier, L., Green, D., Powell, T., Dingwell, D., 2006. The trigger mechanism of low-frequency earthquakes on Montserrat. J. Volcanol. Geotherm. Res. 153, 37–50. https://doi.org/10.1016/J.JVOLGEORES.2005.08.008

Newman, S., Lowenstern, J.B., 2002. VolatileCalc: a silicate melt--H2O--CO2 solution model written in Visual Basic for excel. Comput. \& Geosci. 28, 597–604.

Nichols, A.R.L., Potuzak, M., Dingwell, D.B., 2009. Cooling rates of basaltic hyaloclastites and pillow lava glasses from the HSDP2 drill core. Geochim. Cosmochim. Acta 73, 1052–1066.

Nielson, D.L., Stiger, S.G., 1996. Drilling and evaluation of Ascension# 1, a geothermal exploration well on Ascension Island, South Atlantic Ocean. Geothermics 25, 543–560.

Oelkers, E.H., Gislason, S.R., 2001. The mechanism, rates and consequences of basaltic glass dissolution: I. An experimental study of the dissolution rates of basaltic glass as a function of aqueous Al, Si and oxalic acid concentration at 25 C and pH= 3 and 11. Geochim. Cosmochim. Acta 65, 3671–3681.

Ohsawa, S., Yusa, Y., Oue, K., Amita, K., 2000. Entrainment of atmospheric air into the volcanic system during the 1995 phreatic eruption of Kuju Volcano, Japan. J. Volcanol. Geotherm. Res. 96, 33–43.

Okumura, S., Sasaki, O., 2014. Permeability reduction of fractured rhyolite in volcanic conduits and its control on eruption cyclicity. Geology 42, 843–846.

Otsuki, S., Nakamura, M., Okumura, S., Sasaki, O., 2015. Interfacial tension-driven relaxation of magma foam: An experimental study. J. Geophys. Res. Solid Earth 120, 7403–7424.

Parikh, N.M., 1958. Effect of atmosphere on surface tension of glass. J. Am. Ceram. Soc. 41, 18–22.

Paterson, M.S., Wong, T., 2005. Experimental rock deformation-the brittle field. Springer Science \& Business Media.

Perera, G., Doremus, R.H., Lanford, W., 1991. Dissolution rates of silicate glasses in water at pH 7. J. Am. Ceram. Soc. 74, 1269–1274.

Pitzer, K.S., Sterner, S.M., 1994. Equations of state valid continuously from zero to extreme pressures for H2O and CO2. J. Chem. Phys. 101, 3111–3116.

Potuzak, M., Nichols, A.R.L., Dingwell, D.B., Clague, D.A., 2008. Hyperquenched volcanic glass from Loihi seamount, Hawaii. Earth Planet. Sci. Lett. 270, 54–62.

Prousevitch, A.A., Sahagian, D.L., Anderson, A.T., 1993. Dynamics of diffusive bubble growth in magmas: Isothermal case. J. Geophys. Res. Solid Earth 98, 22283–22307.

Proussevitch, A.A., Sahagian, D.L., 1998. Dynamics and energetics of bubble growth in magmas: Analytical formulation and numerical modeling. J. Geophys. Res. Solid Earth 103, 18223–18251.

Quane, S.L., Russell, J.K., Friedlander, E.A., 2009. Time scales of compaction in volcanic systems. Geology 37, 471–474.

Rahromostaqim, M., Sahimi, M., 2020. Molecular Dynamics Study of the Effect of Layer Charge and Interlayer Cations on Swelling of Mixed-Layer Chlorite--Montmorillonite Clays. J. Phys. Chem. C 124, 2553–2561.

Reiner, M., 1964. The deborah number. Phys. Today 17, 62.

Richter, D., Simmons, G., 1974. Thermal expansion behavior of igneous rocks, in: International Journal of Rock Mechanics and Mining Sciences & Geomechanics Abstracts. pp. 403–411.

Rman, N., Lapanje, A., Prestor, J., O'Sullivan, M.J., 2016. Mitigating depletion of a porous geothermal aquifer in the Pannonian sedimentary basin. Environ. Earth Sci. 75, 723.

Robert, G., Whittington, A.G., Stechern, A., Behrens, H., 2014. Heat capacity of hydrous basaltic glasses and liquids. J. Non. Cryst. Solids 390, 19–30.

Ross, P.-S., Núñez, G.C., Hayman, P., 2017. Felsic maar-diatreme volcanoes: a review. Bull. Volcanol. 79, 20.

Russell, J.D. t, Farmer, V.C., 1964. Infra-red spectroscopic study of the dehydration of montmorillonite and saponite. Clay Miner. Bull. 5, 443–464.

Rust, A.C., Cashman, K. V, Wallace, P.J., 2004. Magma degassing buffered by vapor flow through brecciated conduit margins. Geology 32, 349–352.

Rust, A.C., Manga, M., 2002. Effects of bubble deformation on the viscosity of dilute suspensions. J. Nonnewton. Fluid Mech. 104, 53–63.

Rutter, E.H., 1986. On the nomenclature of mode of failure transitions in rocks. Tectonophysics 122, 381–387.

Ryan, A.G., Heap, M.J., Russell, J.K., Kennedy, L.A., Clynne, M.A., 2020. Cyclic shear zone cataclasis and sintering during lava dome extrusion: Insights from Chaos Crags, Lassen Volcanic Center (USA). J. Volcanol. Geotherm. Res. 401, 106935.

Ryan, A.G., Russell, J.K., Hess, K.-U., Phillion, A.B., Dingwell, D.B., 2015a. Vesiculation in rhyolite at low H 2 O contents: A thermodynamic model. Geochemistry, Geophys. Geosystems 16, 4292–4310.

Ryan, A.G., Russell, J.K., Nichols, A.R.L., Hess, K.-U., Porritt, L.A., 2015b. Experiments and models on H2O retrograde solubility in volcanic systems. Am. Mineral. 100, 774–786.

Sahagian, D.L., Proussevitch, A.A., 1998. 3D particle size distributions from 2D observations:

stereology for natural applications. J. Volcanol. Geotherm. Res. 84, 173–196.

Sahini, M., Sahimi, M., 1994. Applications of percolation theory. CRC Press.

Sakai, M., Shimizu, S., 2001. Indentation rheometry for glass-forming materials. J. Non. Cryst. Solids. https://doi.org/10.1016/S0022-3093(01)00316-7

Sammis, C.G., Ashby, M.F., 1986. The failure of brittle porous solids under compressive stress states. Acta Metall. 34, 511–526.

Sanchez-Alfaro, P., Reich, M., Arancibia, G., Pérez-Flores, P., Cembrano, J., Driesner, T., Lizama, M., Rowland, J., Morata, D., Heinrich, C.A., others, 2016. Physical, chemical and mineralogical evolution of the Tolhuaca geothermal system, southern Andes, Chile: insights into the interplay between hydrothermal alteration and brittle deformation. J. Volcanol. Geotherm. Res. 324, 88–104.

Saubin, E., Kennedy, B., Tuffen, H., Villeneuve, M., Davidson, J., Burchardt, S., 2019. Comparative field study of shallow rhyolite intrusions in Iceland: Emplacement mechanisms and impact on country rocks. J. Volcanol. Geotherm. Res. 388, 106691.

Saubin, E., Tuffen, H., Gurioli, L., Owen, J., Castro, J.M., Berlo, K., McGowan, E.M., Schipper, C.I., Wehbe, K., 2016. Conduit dynamics in transitional rhyolitic activity recorded by tuffisite vein textures from the 2008--2009 Chaitén Eruption. Front. Earth Sci. 4, 59.

Schaefer, L.N., Kendrick, J.E., Oommen, T., Lavallée, Y., Chigna, G., 2015. Geomechanical rock properties of a basaltic volcano. Front. Earth Sci. 3, 29.

Schauroth, J., Wadsworth, F.B., Kennedy, B., von Aulock, F.W., Lavallée, Y., Damby, D.E., Vasseur, J., Scheu, B., Dingwell, D.B., 2016. Conduit margin heating and deformation during the AD 1886 basaltic Plinian eruption at Tarawera volcano, New Zealand. Bull. Volcanol. 78, 12.

Schiffman, P., Watters, R.J., Thompson, N., Walton, A.W., 2006. Hyaloclastites and the slope stability of Hawaiian volcanoes: Insights from the Hawaiian Scientific Drilling Project's 3-km drill core. J. Volcanol. Geotherm. Res. 151, 217–228.

Schipper, C.I., Castro, J.M., Kennedy, B.M., Tuffen, H., Whattam, J., Wadsworth, F.B., Paisley, R., Fitzgerald, R.H., Rhodes, E., Schaefer, L.N., others, 2021. Silicic conduits as supersized tuffisites: Clastogenic influences on shifting eruption styles at Cordón Caulle volcano (Chile). Bull. Volcanol. 83, 1–22.

Schipper, C.I., Castro, J.M., Tuffen, H., James, M.R., How, P., 2013. Shallow vent architecture during hybrid explosive--effusive activity at Cordón Caulle (Chile, 2011--12): evidence from direct observations and pyroclast textures. J. Volcanol. Geotherm. Res. 262, 25–37.

Schopka, H.H., Gudmundsson, M.T., Tuffen, H., 2006. The formation of Helgafell, southwest Iceland, a monogenetic subglacial hyaloclastite ridge: sedimentology, hydrology and volcano--ice interaction. J. Volcanol. Geotherm. Res. 152, 359–377.

Scott, S.W., Covell, C., Júl\'\iusson, E., Valfells, Á., Newson, J., Hrafnkelsson, B., Pálsson, H., Gudjónsdóttir, M., 2019. A probabilistic geologic model of the Krafla geothermal system constrained by gravimetric data. Geotherm. Energy 7, 1–30.

Scott, S.W., O'Sullivan, J.P., Maclaren, O.J., Nicholson, R., Covell, C., Newson, J., Gu\dhjónsdótt\'\ir, M.S., 2022. Bayesian calibration of a natural state geothermal reservoir model, Krafla, north Iceland. Water Resour. Res. 58, e2021WR031254.

Segall, P., Fitzgerald, S.D., 1998. A note on induced stress changes in hydrocarbon and

geothermal reservoirs. Tectonophysics 289, 117–128.

Senger, K., Tveranger, J., Planke, S., Ogata, K., Braathen, A., Wheeler, W., Chevallier, L., 2012. Fluid flow around igneous intrusions: from outcrop to simulator, in: LASI 5 Conference, 29--30 October, Port Elizabeth, South Africa. pp. 2–3.

Shaw, H.R., 1972. Viscosities of magmatic silicate liquids; an empirical method of prediction. Am. J. Sci. 272, 870–893.

Shirozu, H., Sakasegawa, T., Katsumoto, N., Ozaki, M., 1975. Mg-chlorite and interstratified Mg-chlorite/saponite associated with Kuroko deposits. Clay Sci. 4, 305–321. https://doi.org/10.11362/jcssjclayscience1960.4.305

Siratovich, P.A., Heap, M.J., Villeneuve, M.C., Cole, J.W., Kennedy, B.M., Davidson, J., Reuschlé, T., 2016. Mechanical behaviour of the Rotokawa Andesites (New Zealand): Insight into permeability evolution and stress-induced behaviour in an actively utilised geothermal reservoir. Geothermics 64, 163–179.

Siratovich, P.A., Heap, M.J., Villenueve, M.C., Cole, J.W., Reuschlé, T., 2014. Physical property relationships of the Rotokawa Andesite, a significant geothermal reservoir rock in the Taupo Volcanic Zone, New Zealand. Geotherm. Energy 2, 10.

Siratovich, P.A., Sass, I., Homuth, S., Bjornsson, A., 2011. Thermal stimulation of geothermal reservoirs and laboratory investigation of thermally-induced fractures, in: Proc., Geothermal Resources Council Annual Meeting. pp. 1529–1535.

Siratovich, P.A., Villeneuve, M.C., Cole, J.W., Kennedy, B.M., Bégué, F., 2015. Saturated heating and quenching of three crustal rocks and implications for thermal stimulation of permeability in geothermal reservoirs. Int. J. Rock Mech. Min. Sci. 80, 265–280.

Skilling, I.P., White, J.D.L., McPhie, J., 2002. Peperite: a review of magma--sediment mingling. J. Volcanol. Geotherm. Res. 114, 1–17.

Smith, J. V, 1996. Ductile-brittle transition structures in the basal shear zone of a rhyolite lava flow, eastern Australia. J. Volcanol. Geotherm. Res. 72, 217–223.

Sparks, R.S.J., 2003. Dynamics of magma degassing. Geol. Soc. London, Spec. Publ. 213, 5–22.

Sparks, R.S.J., 1978. The dynamics of bubble formation and growth in magmas: a review and analysis. J. Volcanol. Geotherm. Res. 3, 1–37.

Sparks, R.S.J., Tait, S.R., Yanev, Y., 1999. Dense welding caused by volatile resorption. J. Geol. Soc. London. 156, 217–225.

Sparks, R.S.J., Wright, J. V, 1979. Welded air-fall tuffs.

Spera, F.J., 2000. Encyclopedia of Volcanoes, H. Sigurdsson, Ed.

Spieler, O., Kennedy, B., Kueppers, U., Dingwell, D.B., Scheu, B., Taddeucci, J., 2004. The fragmentation threshold of pyroclastic rocks. Earth Planet. Sci. Lett. 226, 139–148.

Stasiuk, M. V, Barclay, J., Carroll, M.R., Jaupart, C., Ratté, J.C., Sparks, R.S.J., Tait, S.R., 1996. Degassing during magma ascent in the Mule Creek vent (USA). Bull. Volcanol. 58, 117–130.

Stevenson, R.J., Bagdassarov, N.S., Romano, C., 1997. Vesiculation processes in a water-rich calc-alkaline obsidian. Earth Planet. Sci. Lett. 146, 555–571.

Stroncik, N.A., Schmincke, H.-U., 2001. Evolution of palagonite: Crystallization, chemical

changes, and element budget. Geochemistry, Geophys. Geosystems 2.

Sturchio, N.C., Muehlenbachs, K., Seitz, M.G., 1986. Element redistribution during hydrothermal alteration of rhyolite in an active geothermal system: Yellowstone drill cores Y-7 and Y-8. Geochim. Cosmochim. Acta 50, 1619–1631.

Taddeucci, J., Cimarelli, C., Alatorre-Ibargüengoitia, M.A., Delgado-Granados, H., Andronico, D., Del Bello, E., Scarlato, P., Di Stefano, F., 2021. Fracturing and healing of basaltic magmas during explosive volcanic eruptions. Nat. Geosci. 14, 248–254.

Thien, B.M.J., Kosakowski, G., Kulik, D.A., 2015. Differential alteration of basaltic lava flows and hyaloclastites in Icelandic hydrothermal systems. Geotherm. Energy 3, 11.

Truby, J.M., Mueller, S.P., Llewellin, E.W., Mader, H.M., 2015. The rheology of three-phase suspensions at low bubble capillary number. Proc. R. Soc. A Math. Phys. Eng. Sci. 471, 20140557.

Tuffen, H., Castro, J.M., 2009. The emplacement of an obsidian dyke through thin ice: Hrafntinnuhryggur, Krafla Iceland. J. Volcanol. Geotherm. Res. 185, 352–366.

Tuffen, H., Dingwell, D., 2005. Fault textures in volcanic conduits: evidence for seismic trigger mechanisms during silicic eruptions. Bull. Volcanol. 67, 370–387. https://doi.org/10.1007/s00445-004-0383-5

Tuffen, H., Dingwell, D.B., Pinkerton, H., 2003. Repeated fracture and healing of silicic magma generate flow banding and earthquakes? Geology 31, 1089–1092. https://doi.org/10.1130/G19777.1

Tulinius, H., Correia, H., Sigurdsson, O., 2000. Stimulating a high enthalpy well by thermal cracking, in: World Geothermal Congress.

Unwin, H.E., Tuffen, H., Phillips, E., Wadsworth, F.B., James, M.R., 2021. Pressure-driven opening and filling of a volcanic hydrofracture recorded by tuffisite at Húsafell, Iceland: A potential seismic source. Front. Earth Sci. 9, 347.

Van Otterloo, J., Cas, R.A.F., Scutter, C.R., 2015. The fracture behaviour of volcanic glass and relevance to quench fragmentation during formation of hyaloclastite and phreatomagmatism. Earth-Science Rev. 151, 79–116.

Vasseur, J., Wadsworth, F.B., Dingwell, D.B., 2020. Permeability of polydisperse magma foam. Geology 48, 536–540.

Vasseur, J., Wadsworth, F.B., Lavallée, Y., Hess, K.-U., Dingwell, D.B., 2013a. Volcanic sintering: timescales of viscous densification and strength recovery. Geophys. Res. Lett. 40, 5658–5664.

Vasseur, J., Wadsworth, F.B., Lavallée, Y., Hess, K.U., Dingwell, D.B., 2013b. Volcanic sintering: Timescales of viscous densification and strength recovery. Geophys. Res. Lett. 40, 5658–5664. https://doi.org/10.1002/2013GL058105

Vidal, O., Dubacq, B., 2009. Thermodynamic modelling of clay dehydration, stability and compositional evolution with temperature, pressure and H2O activity. Geochim. Cosmochim. Acta 73, 6544–6564.

von Aulock, F.W., Kennedy, B.M., Maksimenko, A., Wadsworth, F.B., Lavallée, Y., 2017. Outgassing from open and closed magma foams. Front. Earth Sci. 5, 46.

Von Aulock, F.W., Nichols, A.R.L., Kennedy, B.M., Oze, C., 2013. Timescales of texture

development in a cooling lava dome. Geochim. Cosmochim. Acta 114, 72–80.

Wadge, G., Ryan, G., Calder, E.S., 2009. Clastic and core lava components of a silicic lava dome. Geology 37, 551–554.

Wadsworth, F.B., Llewellin, E.W., Vasseur, J., Gardner, J.E., Tuffen, H., 2020a. Explosive-effusive volcanic eruption transitions caused by sintering. Sci. Adv. 6, eaba7940.

Wadsworth, F.B., Vasseur, J., Llewellin, E.W., Brown, R.J., Tuffen, H., Gardner, J.E., Kendrick, J.E., Lavallée, Y., Dobson, K.J., Heap, M.J., others, 2021. A model for permeability evolution during volcanic welding. J. Volcanol. Geotherm. Res. 409, 107118.

Wadsworth, F.B., Vasseur, J., Llewellin, E.W., Dingwell, D.B., 2017a. Sintering of polydisperse viscous droplets. Phys. Rev. E 95, 33114.

Wadsworth, F.B., Vasseur, J., Llewellin, E.W., Dobson, K.J., Colombier, M., Von Aulock, F.W., Fife, J.L., Wiesmaier, S., Hess, K.-U., Scheu, B., others, 2017b. Topological inversions in coalescing granular media control fluid-flow regimes. Phys. Rev. E 96, 33113.

Wadsworth, F.B., Vasseur, J., Llewellin, E.W., Schauroth, J., Dobson, K.J., Scheu, B., Dingwell, D.B., 2016a. Sintering of viscous droplets under surface tension. Proc. R. Soc. A Math. Phys. Eng. Sci. 472, 20150780.

Wadsworth, F.B., Vasseur, J., Schauroth, J., Llewellin, E.W., Dobson, K.J., Havard, T., Scheu, B., von Aulock, F.W., Gardner, J.E., Dingwell, D.B., others, 2019. A general model for welding of ash particles in volcanic systems validated using in situ X-ray tomography. Earth Planet. Sci. Lett. 525, 115726.

Wadsworth, F.B., Vasseur, J., Scheu, B., Kendrick, J.E., Lavallée, Y., Dingwell, D.B., 2016b. Universal scaling of fluid permeability during volcanic welding and sediment diagenesis. Geology 44, 219–222.

Wadsworth, F.B., Vasseur, J., von Aulock, F.W., Hess, K.-U., Scheu, B., Lavallée, Y., Dingwell, D.B., 2014. Nonisothermal viscous sintering of volcanic ash. J. Geophys. Res. Solid Earth 119, 8792–8804.

Wadsworth, F.B., Vossen, C.E.J., Schmid, D., Colombier, M., Heap, M.J., Scheu, B., Dingwell, D.B., 2020b. Determination of permeability using a classic Darcy water column. Am. J. Phys. 88, 20–24.

Wang, W.-H., Wong, T., 2003. Effects of reaction kinetics and fluid drainage on the development of pore pressure excess in a dehydrating system. Tectonophysics 370, 227–239.

Watkins, J.M., Gardner, J.E., Befus, K.S., 2017. Nonequilibrium degassing, regassing, and vapor fluxing in magmatic feeder systems. Geology 45, 183–186.

Webb, S.L., Dingwell, D.B., 1990. The onset of non-Newtonian rheology of silicate melts. Phys. Chem. Miner. 17, 125–132.

White, J.D.L., Houghton, B.F., 2006. Primary volcaniclastic rocks. Geology 34, 677–680.

Whittington, A.G., Hellwig, B.M., Behrens, H., Joachim, B., Stechern, A., Vetere, F., 2009. The viscosity of hydrous dacitic liquids: implications for the rheology of evolving silicic magmas. Bull. Volcanol. 71, 185–199.

Wilding, M., Dingwell, D., Batiza, R., Wilson, L., 2000. Cooling rates of hyaloclastites: applications of relaxation geospeedometry to undersea volcanic deposits. Bull. Volcanol.

61, 527–536.

Wohletz, K., 2002. Water/magma interaction: some theory and experiments on peperite formation. J. Volcanol. Geotherm. Res. 114, 19–35.

Wohletz, K.H., 1986. Explosive magma-water interactions: Thermodynamics, explosion mechanisms, and field studies. Bull. Volcanol. 48, 245–264.

Wohletz, K.H., Sheridan, M.F., 1983. Hydrovolcanic explosions; II, Evolution of basaltic tuff rings and tuff cones. Am. J. Sci. 283, 385–413.

Wolff, J.A., Wright, J. V, 1981. Rheomorphism of welded tuffs. J. Volcanol. Geotherm. Res. 10, 13–34.

Wright, H.M., Cashman, K. V, 2014. Compaction and gas loss in welded pyroclastic deposits as revealed by porosity, permeability, and electrical conductivity measurements of the Shevlin Park Tuff. Bulletin 126, 234–247.

Wright, H.M.N., Cashman, K. V, Gottesfeld, E.H., Roberts, J.J., 2009. Pore structure of volcanic clasts: measurements of permeability and electrical conductivity. Earth Planet. Sci. Lett. 280, 93–104.

Yariv, S., Ovadyahu, D., Nasser, A., Shuali, U., Lahav, N., 1992. Thermal analysis study of heat of dehydration of tributylammonium smectites. Thermochim. Acta 207, 103–113.

Yen, A.S., Murray, B.C., Rossman, G.R., 1998. Water content of the Martian soil: Laboratory simulations of reflectance spectra. J. Geophys. Res. Planets 103, 11125–11133.

Yong, C., Wang, C., 1980. Thermally induced acoustic emission in Westerly granite. Geophys. Res. Lett. 7, 1089–1092.

Yoshimura, S., Nakamura, M., 2010. Fracture healing in a magma: An experimental approach and implications for volcanic seismicity and degassing. J. Geophys. Res. Solid Earth 115.

Yoshimura, S., Nakamura, M., 2008. Diffusive dehydration and bubble resorption during open-system degassing of rhyolitic melts. J. Volcanol. Geotherm. Res. 178, 72–80.

Zakharova, O.K., Spichak, V. V, 2012. Geothermal fields of Hengill Volcano, Iceland. J. Volcanol. Seismol. 6, 1–14.

Zhang, J., Wong, T.-F., Davis, D.M., 1990. Micromechanics of pressure-induced grain crushing in porous rocks. J. Geophys. Res. Solid Earth 95, 341–352.

Zhang, Y., 1999a. $H_2O$ in rhyolitic glasses and melts: measurement, speciation, solubility, and diffusion. Rev. Geophys. 37, 493–516.

Zhang, Y., 1999b. A criterion for the fragmentation of bubbly magma based on brittle failure theory. Nature 402, 648.

Zhang, Y., Ni, H., 2010. Diffusion of H, C, and O components in silicate melts. Rev. Mineral. Geochemistry 72, 171–225.

Zhu, W., Baud, P., Wong, T., 2010. Micromechanics of cataclastic pore collapse in limestone. J. Geophys. Res. Solid Earth 115.
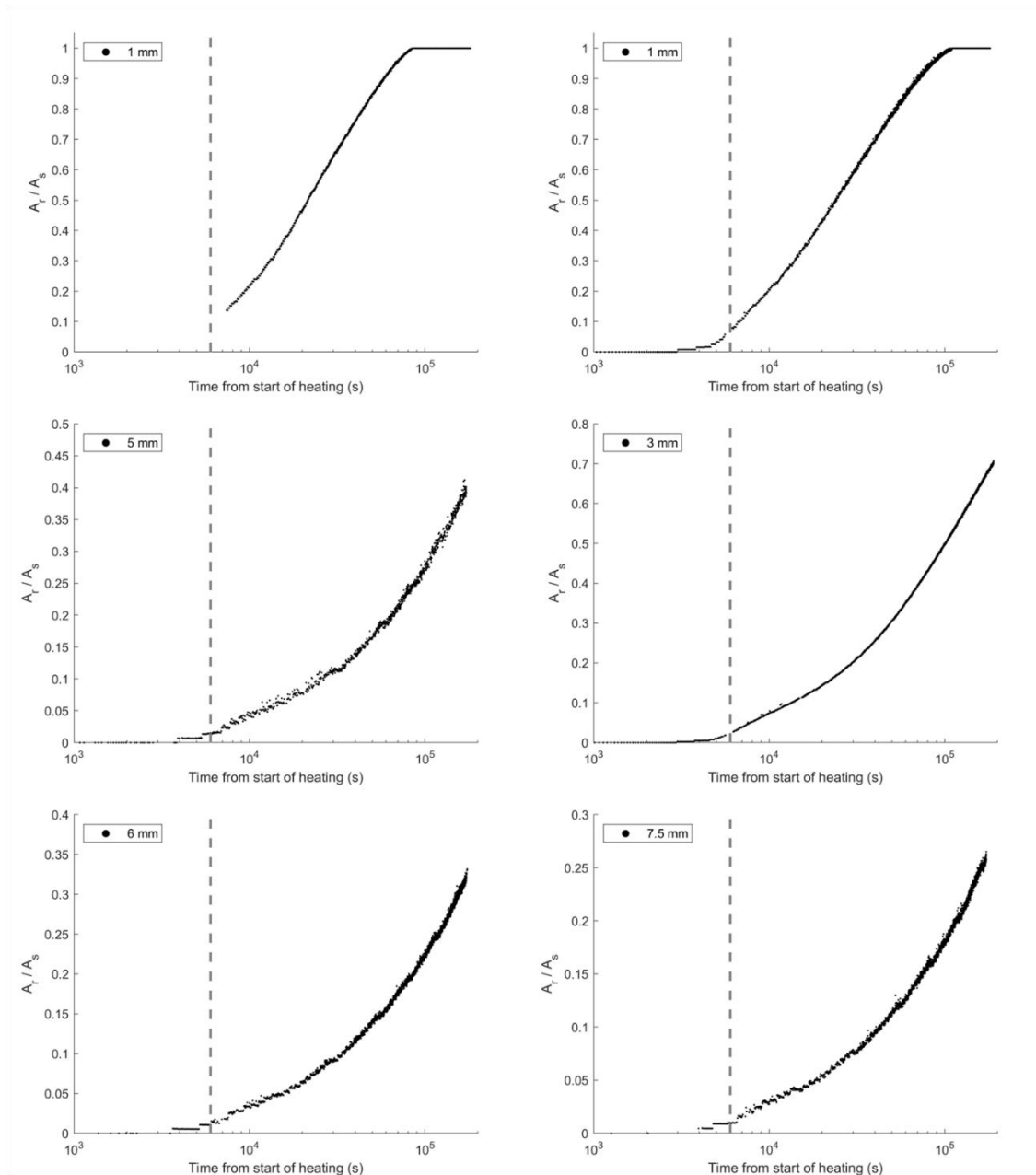
# Appendix I: Chapter 2
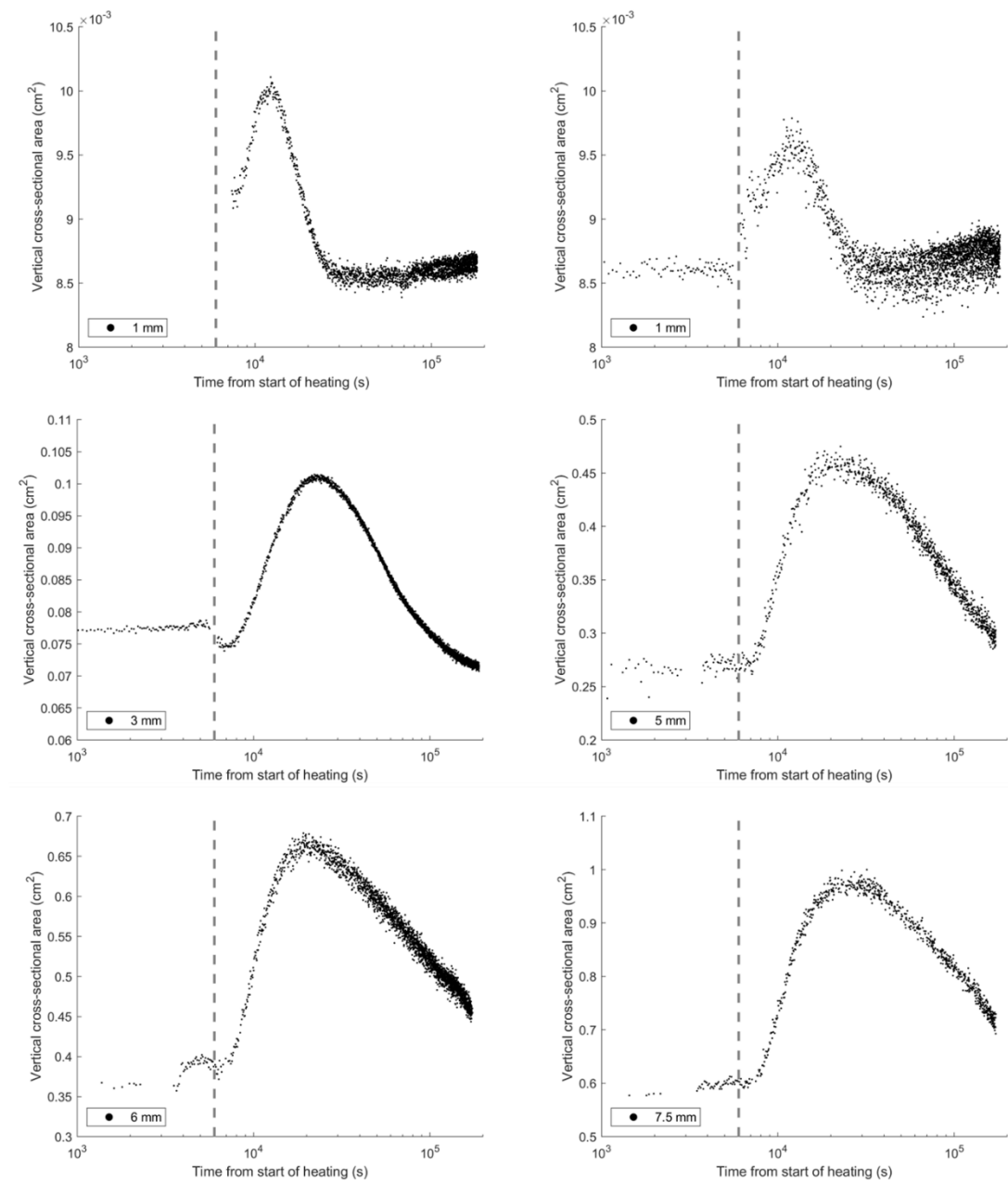


Supplementary Figure A.I-1: Individual plots for the vertical cross-sectional area of each sample presented in Figure 2-2:, as estimated using the segmented sample images. The grey dashed line signifies the start of the isothermal period (1006 °C).
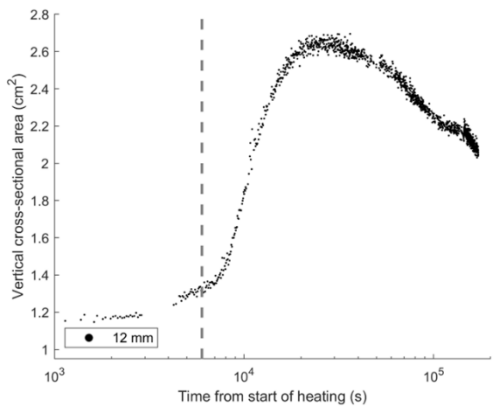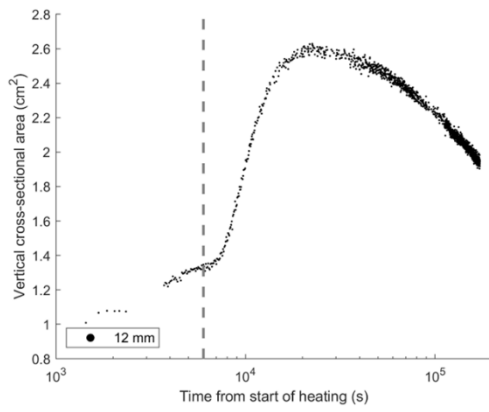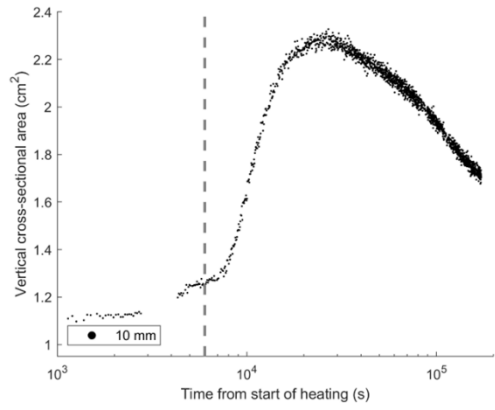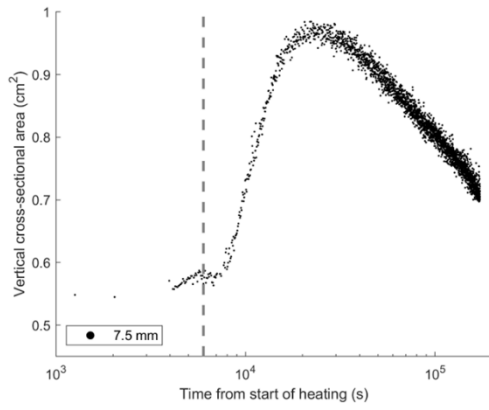
*Supplementary Figure A.I-1: continued.*

*Supplementary Figure A.I-2: Individual plots for the ratio of dense rind area $A_r$ to sample cross-sectional area $A_s$ presented in Figure 2-4, as estimated for each sample using Equation 2-2 and the segmented sample images. The grey dashed line signifies the start of the isothermal period (1006 °C).*
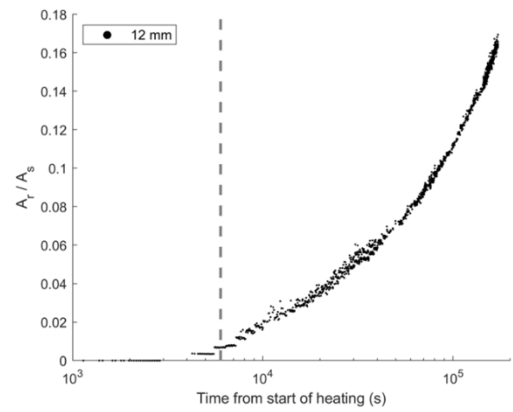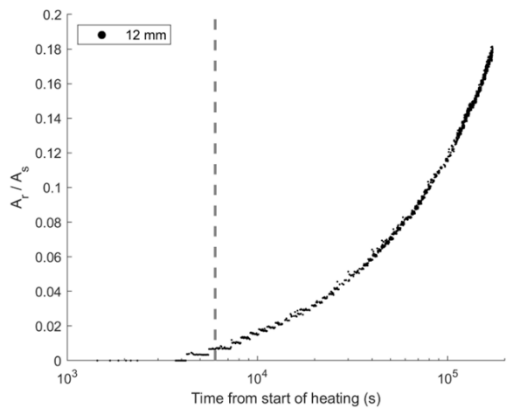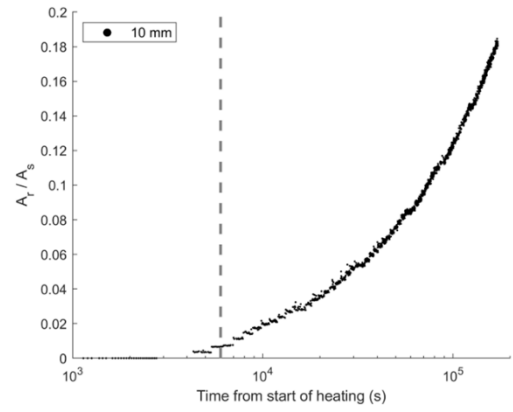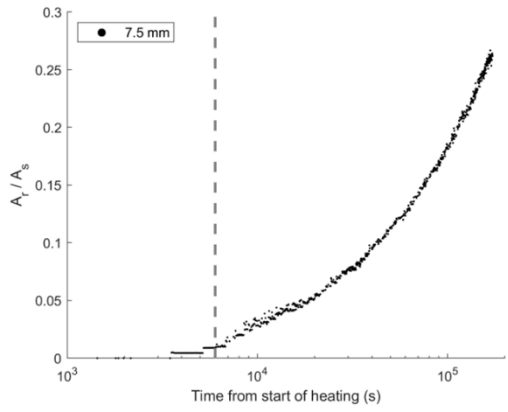
*Supplementary Figure A.I-2: continued.*

*Supplementary Figure A.I-3: Individual plots for bulk sample vesicularity and interior sample vesicularity, as presented in Figure 2-5. Each row corresponds to a single sample. The grey shaded region highlights the vesicularity as expected from closed system bubble growth. The grey dashed line signifies the start of the isothermal period (1006 °C).*
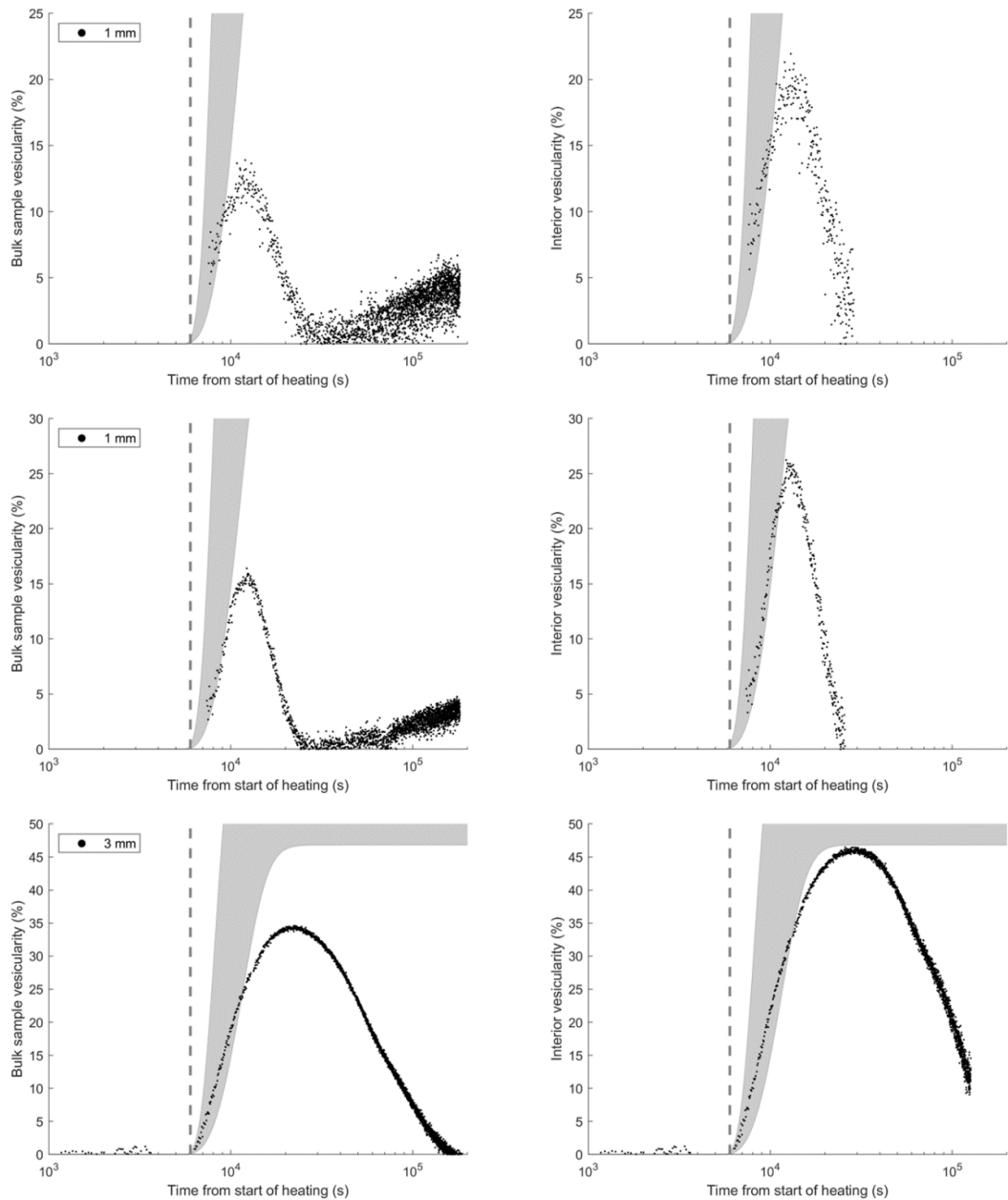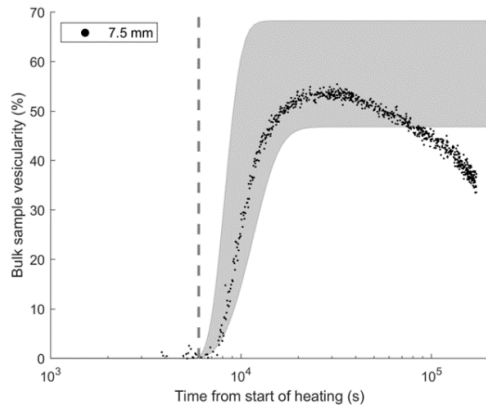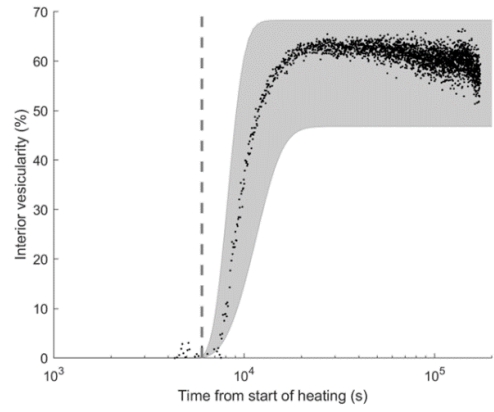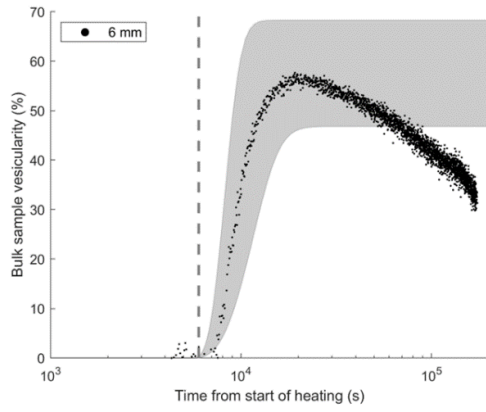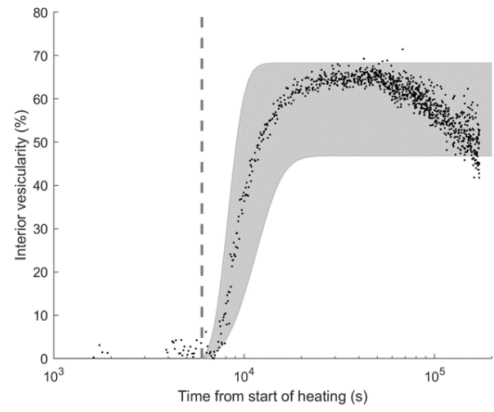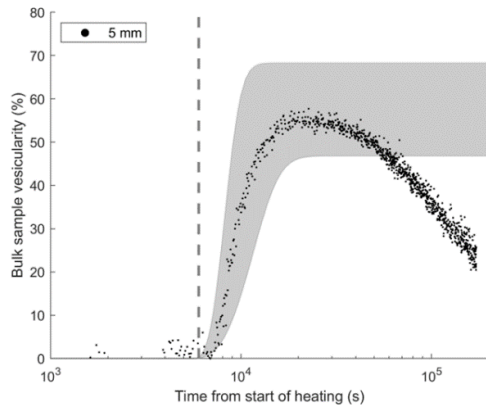
*Supplementary Figure A.I-3: continued.*

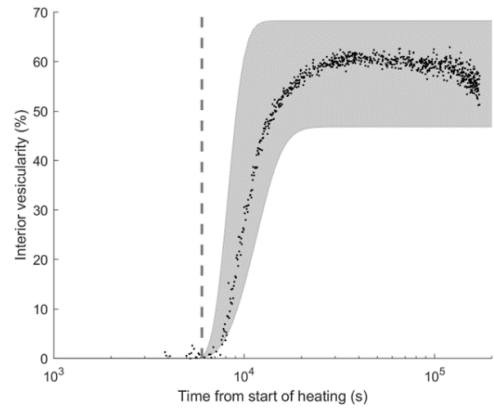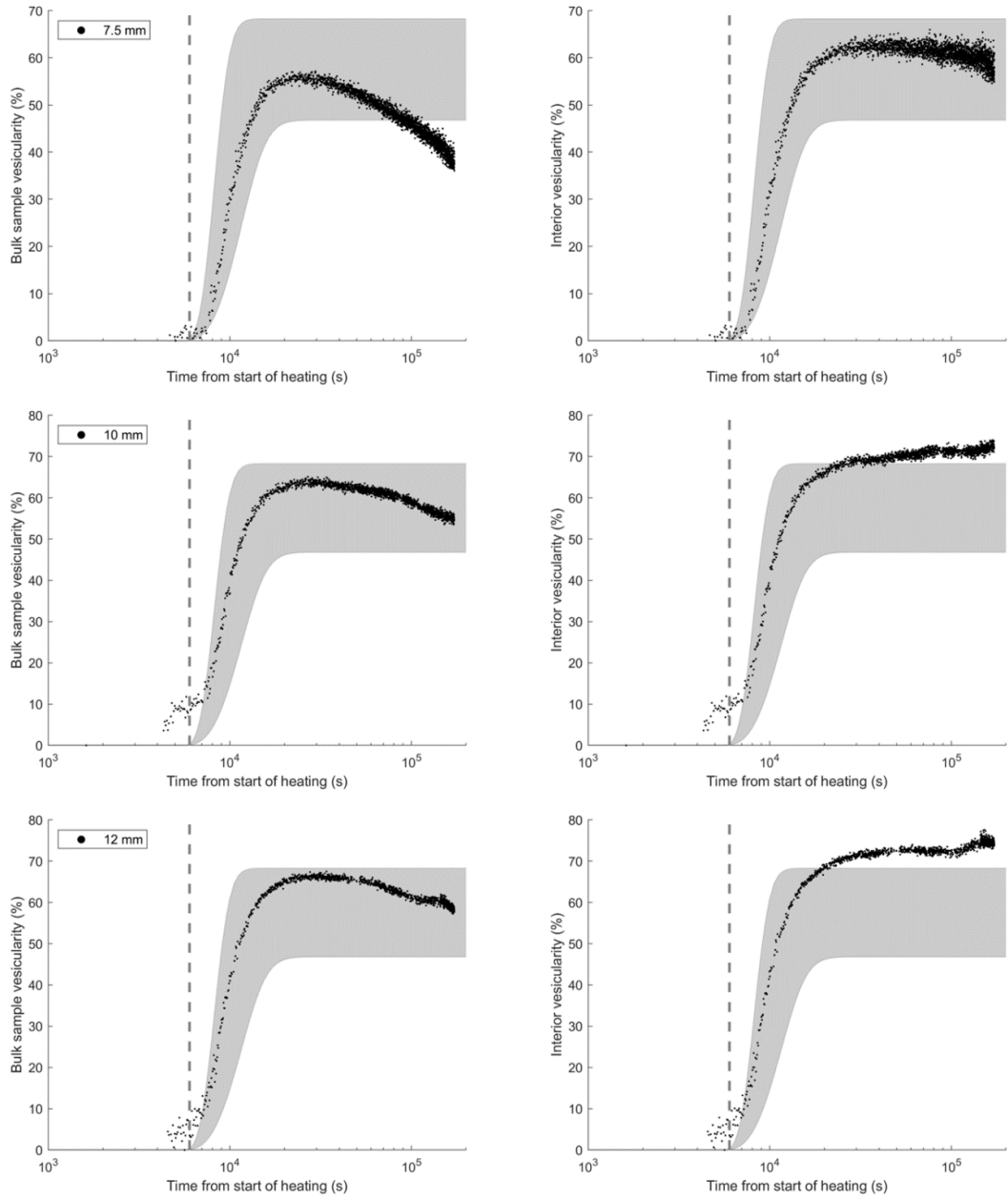*Supplementary Figure A.I-3: continued.*
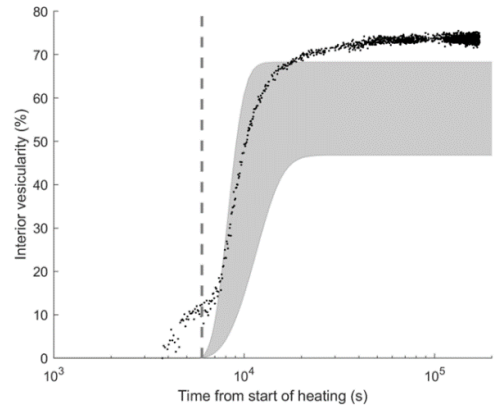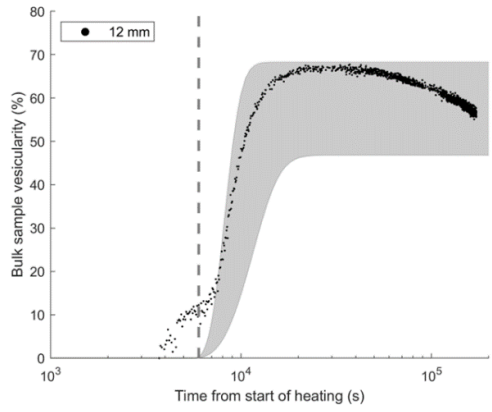
*Supplementary Figure A.I-3: continued.*
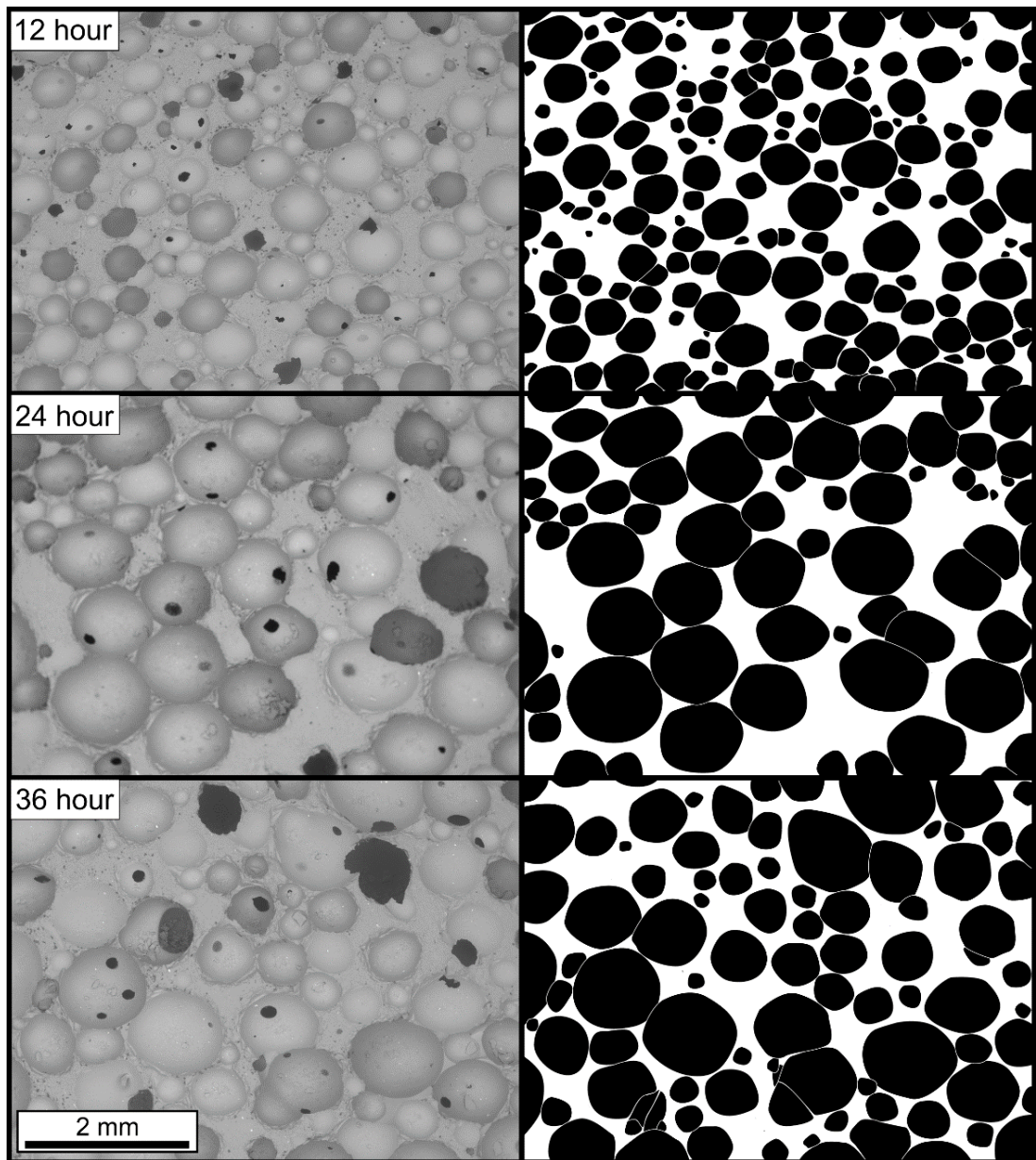
*Supplementary Figure A.I-4: Backscatter electron images (left) of our experimental products, taken from the interior of 12 mm diameter samples. The bubble extents in these images were manually defined and the images were segmented (right) for estimations of bubble number density.*

# Appendix II: Chapter 3
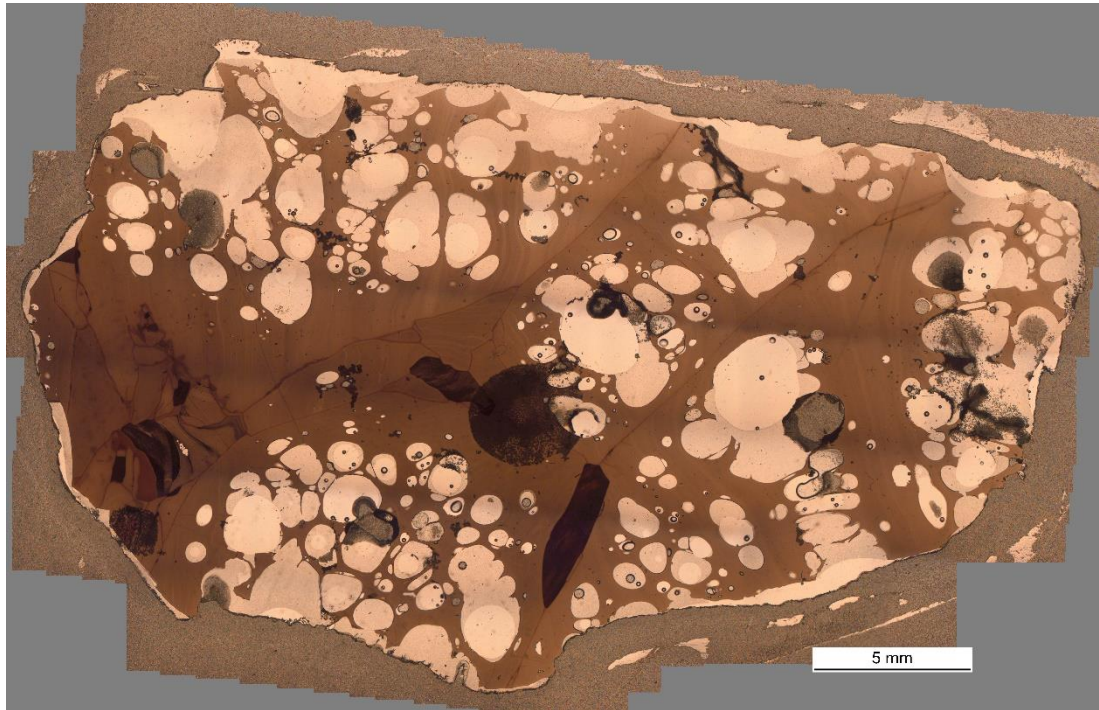


*Supplementary Figure A.II-1: Photomicrograph of naturally sintered glass fragments from Krafla, showing dense rinds, vesicular interiors (white), and fragment interfaces (highlighted green in Figure 3-1:).*

0.50 - 1.00 mm
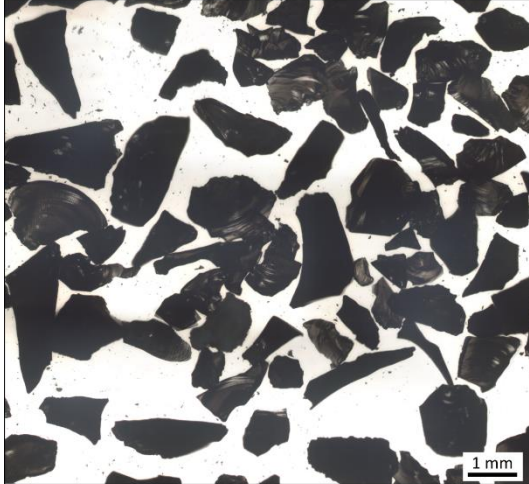
1.00 - 1.40 mm
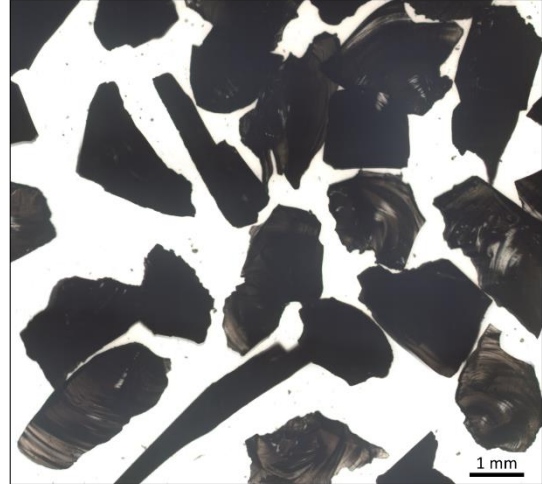
1.40 - 2.00 mm
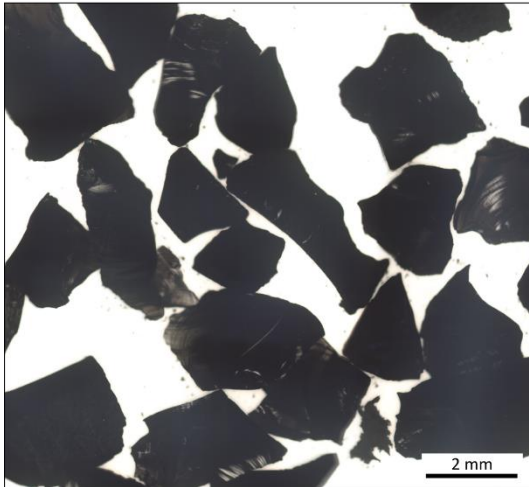
2.00 - 2.36 mm



*Supplementary Figure A.II-2: Reflected light photomicrographs of the four sieved glass fragment populations, prior to experimentation.*

# Appendix III: Chapter 4

## 1. Sample Physical and Mechanical Data

*Supplementary Table A.III-1: A summary of water permeability values at a range of confining pressures.*

| Sample | Confining pressure (MPa) | $k$ (m$^2$) | Porosity reduction (%) |
|---|---|---|---|
| HYA_0m_002 130 °C | 3.73 | 8.05E-14 | n/a |
| | 7.95 | 7.51E-14 | 0.32 |
| | 12.53 | 6.46E-14 | 0.83 |
| | 16.96 | 4.87E-14 | 1.27 |
| | 23.75 | 2.18E-15 | 2.3 |
| | 28.8 | 1.13E-15 | 3.44 |
| HYA_0m_006 185 °C | 3.55 | 4.68E-14 | n/a |
| | 9.04 | 5.58E-14 | 0.41 |
| | 13.96 | 7.18E-14 | 1.09 |
| | 18.91 | 4.96E-14 | 1.86 |
| | 23.84 | 2.25E-14 | 2.82 |
| | 29.04 | 8.13E-15 | 4.04 |
| HYA_0m_008 185 °C | 3.94 | 7.87E-14 | n/a |
| | 8.78 | 7.15E-14 | 0.61 |
| | 13.83 | 6.28E-14 | 1.61 |
| | 18.78 | 5.07E-14 | 2.58 |
| | 23.67 | 3.65E-14 | 3.63 |
| | 27.9 | 2.14E-14 | 4.7 |
| HYA_0m_015 Untreated | 3.55 | 1.56E-14 | n/a |
| | 8.65 | 1.85E-14 | 0.26 |
| | 13.6 | 1.68E-14 | 0.63 |
| | 18.65 | 1.63E-14 | 1.12 |
| | 23.7 | 1.26E-14 | 1.98 |
| | 28.65 | 4.37E-15 | 3.36 |
| HYA_0m_020 Untreated | 3.58 | 5.48E-16 | n/a |
| | 8.53 | 4.42E-16 | 0.31 |
| | 13.61 | 3.98E-16 | 0.75 |
| | 18.51 | 7.72E-16 | 1.27 |
| | 23.56 | 2.67E-16 | 2.09 |
| | 28.21 | 8.93E-16 | 3.27 |

| Sample | Confining pressure (MPa) | $k$ (m$^2$) | Porosity reduction (%) |
|---|---|---|---|
| HYA_0m_021 130 °C | 3.89 | 1.63E-14 | n/a |
| | 8.84 | 1.61E-14 | 0.56 |
| | 13.54 | 1.56E-14 | 1.37 |
| | 18.5 | 1.47E-14 | 2.22 |
| | 23.46 | 1.24E-14 | 3.37 |
| | 28.4 | 3.59E-15 | 4.89 |
| HYA_0m_035 600 °C | 3.27 | 2.28E-15 | n/a |
| | 8.85 | 5.20E-15 | 0.83 |
| | 13.89 | 6.06E-15 | 2.27 |
| | 19.28 | 6.58E-15 | 3.56 |
| | 23.97 | 7.01E-15 | 4.67 |
| | 28.36 | 6.00E-15 | 5.57 |
| HYA_0m_068 400 °C | 3.71 | 5.77E-15 | n/a |
| | 8.58 | 4.66E-15 | 0.74 |
| | 13.78 | 1.28E-14 | 2.01 |
| | 18.75 | 1.78E-14 | 3.15 |
| | 23.45 | 1.53E-14 | 3.7 |
| | 28.59 | 1.31E-14 | 4.39 |
| HYA_0m_072 600 °C | 3.78 | 2.24E-13 | n/a |
| | 8.89 | 1.59E-13 | 0.8 |
| | 13.7 | 1.37E-13 | 2.2 |
| | 18.98 | 1.08E-13 | 3.48 |
| | 23.7 | 1.04E-13 | 4.72 |
| | 28.79 | 8.21E-14 | 5.84 |
| HYA_0m_076 400 °C | 3.46 | 1.10E-13 | n/a |
| | 8.82 | 8.96E-14 | 0.83 |
| | 13.78 | 8.01E-14 | 2.27 |
| | 18.35 | 6.93E-14 | 3.56 |
| | 23.47 | 5.82E-14 | 4.67 |
| | 28.51 | 4.78E-14 | 5.57 |

*Supplementary Table A.III-2: A summary of all porosity, gas permeability, compressive strength, and Young's Modulus values for as-collected and thermally treated cores.*

| Sample | As-collected | | | | Post-thermal treatment | | | | | | |
|---|---|---|---|---|---|---|---|---|---|---|---|
| | Density (g.cm$^{-3}$) | Connected Porosity (%) | Gas $k$ (m$^2$) | TT (°C) | Density (g.cm$^{-3}$) | Mass reduction (g) | Connected Porosity (%) | Gas $k$ (m$^2$) | UCS (MPa) | TXL (MPa) | Young's Modulus (GPa) |
| HYA_0m_001 | 2.5084 | 37.17 | 1.81E-13 | n/a | n/a | n/a | n/a | n/a | n/a | n/a | n/a |
| HYA_0m_002 | 2.5016 | 37.58 | 1.33E-13 | 130 | 2.5876 | 1.94 | 40.7 | 1.65E-13 | n/a | n/a | n/a |
| HYA_0m_003 | 2.5383 | 39.99 | 2.95E-13 | 130 | 2.6197 | 1.51 | 42.1 | 3.66E-13 | n/a | n/a | n/a |
| HYA_0m_004 | 2.5397 | 38.4 | 2.18E-13 | 130 | 2.628 | 1.65 | 41.5 | 2.66E-13 | n/a | n/a | n/a |
| HYA_0m_005 | 2.5405 | 38.24 | 2.89E-13 | 130 | 2.6247 | 1.5 | 42.4 | 3.63E-13 | n/a | n/a | n/a |
| HYA_0m_006 | 2.5527 | 36.75 | 1.53E-13 | 185 | 2.6204 | 1.02 | 42.2 | 2.30E-13 | n/a | n/a | n/a |
| HYA_0m_007 | 2.5015 | 34.38 | 7.21E-14 | 185 | 2.6145 | 2.06 | 40.2 | 1.24E-13 | n/a | n/a | n/a |
| HYA_0m_008 | 2.506 | 36.08 | 1.34E-13 | 185 | 2.6222 | 1.95 | 41.8 | 2.23E-13 | n/a | n/a | n/a |
| HYA_0m_009 | 2.5515 | 39.06 | 1.87E-13 | 185 | 2.6173 | 0.94 | 42 | 2.47E-13 | n/a | n/a | n/a |
| HYA_0m_010 | 2.5691 | 40.29 | 2.72E-13 | n/a | n/a | n/a | n/a | n/a | n/a | n/a | n/a |
| HYA_0m_011 | 2.5496 | 38.48 | 2.76E-13 | n/a | n/a | n/a | n/a | n/a | n/a | n/a | n/a |
| HYA_0m_012 | 2.5719 | 40.93 | 3.20E-13 | 130 | 2.6214 | 0.76 | 43.1 | 3.71E-13 | 8.8 | n/a | 1.58 |
| HYA_0m_013 | 2.5219 | 38.7 | 2.14E-13 | n/a | n/a | n/a | n/a | n/a | n/a | n/a | n/a |
| HYA_0m_014 | 2.5396 | 36.75 | 2.45E-13 | n/a | n/a | n/a | n/a | n/a | n/a | n/a | n/a |
| HYA_0m_015 | 2.4945 | 36.76 | 1.50E-13 | n/a | n/a | n/a | n/a | n/a | n/a | n/a | n/a |
| HYA_0m_016 | 2.5639 | 37.69 | 3.69E-13 | n/a | n/a | n/a | n/a | n/a | n/a | n/a | n/a |
| HYA_0m_017 | 2.5818 | 38.33 | 4.12E-13 | n/a | n/a | n/a | n/a | n/a | n/a | n/a | n/a |
| HYA_0m_018 | 2.5358 | 38.24 | 2.61E-13 | 185 | 2.6452 | 1.71 | 43.3 | 3.68E-13 | n/a | n/a | n/a |
| HYA_0m_019 | 2.5099 | 37.62 | 1.31E-13 | 185 | 2.6298 | 2.04 | 43.5 | 2.14E-13 | n/a | n/a | n/a |

*Supplementary Table A.III-2: continued.*

| | As-collected | | | | Post-thermal treatment | | | | | | |
|---|---|---|---|---|---|---|---|---|---|---|---|
| Sample | Density (g.cm$^{-3}$) | Connected Porosity (%) | Gas $k$ (m$^2$) | TT (°C) | Density (g.cm$^{-3}$) | Mass reduction (g) | Connected Porosity (%) | Gas $k$ (m$^2$) | UCS (MPa) | TXL (MPa) | Young's Modulus (GPa) |
| HYA_0m_020 | 2.5017 | 36.65 | 1.47E-13 | n/a | n/a | n/a | n/a | n/a | n/a | n/a | n/a |
| HYA_0m_021 | 2.5153 | 37.65 | 1.85E-13 | 130 | 2.6033 | 1.62 | 42.1 | 2.48E-13 | n/a | n/a | n/a |
| HYA_0m_022 | 2.5067 | 38.29 | 1.86E-13 | n/a | n/a | n/a | n/a | n/a | n/a | n/a | n/a |
| HYA_0m_023 | 2.5323 | 36.14 | 1.81E-13 | 185 | 2.6433 | 1.88 | 41.5 | 2.77E-13 | n/a | n/a | n/a |
| HYA_0m_024 | 2.5975 | 41.82 | 3.72E-13 | n/a | n/a | n/a | n/a | n/a | 8 | n/a | 1.15 |
| HYA_0m_025 | 2.5596 | 39.86 | 2.42E-13 | 185 | 2.6195 | 0.79 | 42.4 | 3.02E-13 | 92 | n/a | 0.95 |
| HYA_0m_026 | 2.5767 | 39.67 | 2.21E-13 | 130 | 2.612 | 0.51 | 41.2 | 2.54E-13 | 11.5 | n/a | 1.91 |
| HYA_0m_027 | 2.5568 | 40.45 | 1.91E-13 | 130 | 2.5925 | 0.45 | 42.1 | 2.21E-13 | 8.7 | n/a | 1 |
| HYA_0m_028 | 2.5686 | 41.75 | 2.41E-13 | 185 | 2.6314 | 0.74 | 44.2 | 3.07E-13 | 6.3 | n/a | 0.66 |
| HYA_0m_029 | 2.5631 | 39.98 | 1.98E-13 | n/a | n/a | n/a | n/a | n/a | 10.1 | n/a | 1.43 |
| HYA_0m_030 | 2.5592 | 41.31 | 2.03E-13 | n/a | n/a | n/a | n/a | n/a | 8.3 | n/a | 1.18 |
| HYA_0m_031 | 2.5531 | 39.84 | 1.75E-13 | 130 | 2.5938 | 0.54 | 41.6 | 2.03E-13 | 8.4 | n/a | 1.3 |
| HYA_0m_032 | 2.5471 | 40.24 | 1.30E-13 | 185 | 2.6178 | 0.86 | 43.1 | 1.74E-13 | 10.5 | n/a | 1.41 |
| HYA_0m_033 | 2.6043 | 40.8 | 4.13E-13 | 185 | 2.6558 | 0.7 | 43 | 4.90E-13 | 7 | n/a | 0.85 |
| HYA_0m_034 | 2.5514 | 44.13 | 2.50E-13 | 600 | 2.7653 | 2.77 | 45.9 | 5.90E-13 | 6.6 | n/a | 0.73 |
| HYA_0m_035 | 2.5036 | 37.96 | 1.70E-13 | 600 | 2.7355 | 3.58 | 47.9 | 5.46E-13 | n/a | n/a | n/a |
| HYA_0m_036 | 2.5119 | 41.36 | 1.79E-13 | 600 | 2.7273 | 3.02 | 50.3 | 5.56E-13 | 4.2 | n/a | 0.49 |
| HYA_0m_037 | 2.5027 | 37.66 | 2.08E-13 | 600 | 2.7279 | 2.74 | 47.1 | 5.55E-13 | n/a | n/a | n/a |
| HYA_0m_038 | 2.527 | 37.89 | 2.17E-13 | 600 | 2.7489 | 2.92 | 47 | 5.68E-13 | n/a | n/a | n/a |
| HYA_0m_039 | 2.5107 | 39.42 | 1.94E-13 | 600 | 2.7325 | 3.21 | 48.7 | 5.86E-13 | 5.3 | n/a | 0.47 |

*Supplementary Table A.III-2: continued.*

| Sample | As-collected | | | | Post-thermal treatment | | | | | | |
|---|---|---|---|---|---|---|---|---|---|---|---|
| | Density (g.cm$^{-3}$) | Connected Porosity (%) | Gas $k$ (m$^2$) | TT (°C) | Density (g.cm$^{-3}$) | Mass reduction (g) | Connected Porosity (%) | Gas $k$ (m$^2$) | UCS (MPa) | TXL (MPa) | Young's Modulus (GPa) |
| HYA_0m_040 | 2.4976 | 35.7 | 1.73E-13 | 130 | 2.5302 | 0.38 | 39 | 2.13E-13 | n/a | n/a | n/a |
| HYA_0m_041 | 2.5636 | 37.66 | 3.60E-13 | 600 | 2.7633 | 2.64 | 46 | 7.04E-13 | n/a | 23.1 | 0.56 |
| HYA_0m_042 | 2.5348 | 40.85 | 2.12E-13 | 185 | 2.6498 | 0.61 | 44.3 | n/a | n/a | 23.8 | 1.79 |
| HYA_0m_043 | 2.5488 | 40.33 | 2.23E-13 | 185 | 2.62 | 1.16 | 43.7 | n/a | n/a | 26.3 | 1.38 |
| HYA_0m_044 | 2.5556 | 40.23 | 2.29E-13 | 130 | 2.5878 | 0.42 | 41.6 | n/a | n/a | 27.7 | 2.51 |
| HYA_0m_045 | 2.5548 | 40.76 | 2.51E-13 | n/a | n/a | n/a | n/a | n/a | n/a | n/a | n/a |
| HYA_0m_046 | 2.5687 | 40.59 | 2.81E-13 | n/a | n/a | n/a | n/a | n/a | n/a | n/a | n/a |
| HYA_0m_047 | 2.5582 | 39.91 | 2.60E-13 | n/a | n/a | n/a | n/a | n/a | n/a | 29.5 | 3.44 |
| HYA_0m_048 | 2.5523 | 40.37 | 2.08E-13 | n/a | n/a | n/a | n/a | n/a | n/a | n/a | n/a |
| HYA_0m_049 | 2.5345 | 38.59 | 1.44E-13 | n/a | n/a | n/a | n/a | n/a | n/a | n/a | n/a |
| HYA_0m_050 | 2.5426 | 39.04 | 2.39E-13 | n/a | n/a | n/a | n/a | n/a | n/a | n/a | n/a |
| HYA_0m_051 | 2.5562 | 39.35 | 1.69E-13 | n/a | n/a | n/a | n/a | n/a | n/a | n/a | n/a |
| HYA_0m_052 | 2.532 | 39.92 | 1.47E-13 | n/a | n/a | n/a | n/a | n/a | n/a | n/a | n/a |
| HYA_0m_053 | 2.5858 | 40.02 | 3.35E-13 | 400 | 2.7271 | 1.9 | 45.8 | 5.47E-13 | n/a | n/a | n/a |
| HYA_0m_054 | 2.5386 | 38.23 | 2.11E-13 | 400 | 2.6862 | 1.99 | 44.2 | 3.61E-13 | n/a | 26.3 | 1.33 |
| HYA_0m_055 | 2.6033 | 40.35 | 4.80E-13 | 400 | 2.7385 | 1.84 | 45.8 | 7.53E-13 | n/a | n/a | n/a |
| HYA_0m_056 | 2.5337 | 39.83 | 1.86E-13 | 600 | 2.7103 | 2.3 | 47 | 4.50E-13 | n/a | 24.1 | 0.68 |
| HYA_0m_057 | 2.5467 | 40.02 | 2.39E-13 | 400 | 2.6791 | 1.84 | 45.7 | 4.27E-13 | 6.8 | n/a | 1.27 |
| HYA_0m_058 | 2.5504 | 39.76 | 2.54E-13 | 400 | 2.685 | 1.79 | 45.5 | 4.33E-13 | n/a | n/a | n/a |
| HYA_0m_059 | 2.5885 | 38.33 | 3.54E-13 | 400 | 2.7295 | 1.82 | 44.2 | 5.69E-13 | 6.3 | n/a | 1.32 |

*Supplementary Table A.III-2: continued.*

| | As-collected | | | | Post-thermal treatment | | | | | | |
|---|---|---|---|---|---|---|---|---|---|---|---|
| Sample | Density (g.cm$^{-3}$) | Connected Porosity (%) | Gas $k$ (m$^2$) | TT (°C) | Density (g.cm$^{-3}$) | Mass reduction (g) | Connected Porosity (%) | Gas $k$ (m$^2$) | UCS (MPa) | TXL (MPa) | Young's Modulus (GPa) |
| HYA_0m_060 | 2.543 | 41.08 | 2.11E-13 | 400 | 2.6927 | 1.85 | 47.1 | 4.01E-13 | n/a | n/a | n/a |
| HYA_0m_061 | 2.5482 | 40.6 | 2.14E-13 | 400 | 2.6909 | 1.91 | 46.6 | 4.13E-13 | n/a | n/a | n/a |
| HYA_0m_062 | 2.4618 | 36.8 | n/a | n/a | n/a | n/a | n/a | n/a | n/a | n/a | n/a |
| HYA_0m_063 | 2.4676 | 37.79 | n/a | n/a | n/a | n/a | n/a | n/a | n/a | n/a | n/a |
| HYA_0m_064 | 2.4674 | 36.81 | n/a | n/a | n/a | n/a | n/a | n/a | n/a | n/a | n/a |
| HYA_0m_065 | 2.5072 | 39.93 | n/a | n/a | n/a | n/a | n/a | n/a | n/a | n/a | n/a |
| HYA_0m_066 | 2.5087 | 36.96 | n/a | n/a | n/a | n/a | n/a | n/a | n/a | n/a | n/a |
| HYA_0m_067 | 2.5482 | 39.29 | 1.82E-13 | 400 | 2.6286 | 0.9 | 42.5 | 3.10E-13 | n/a | n/a | n/a |
| HYA_0m_068 | 2.5449 | 38.61 | 1.56E-13 | 400 | 2.6479 | 1.1 | 42.6 | 2.90E-13 | n/a | n/a | n/a |
| HYA_0m_069 | 2.5515 | 39.27 | 1.82E-13 | n/a | n/a | n/a | n/a | n/a | n/a | n/a | n/a |
| HYA_0m_070 | 2.5497 | 38.46 | 2.51E-13 | n/a | n/a | n/a | n/a | n/a | n/a | 31 | 2.17 |
| HYA_0m_071 | 2.5376 | 39.01 | 1.97E-13 | 130 | 2.5678 | 0.61 | 40.6 | 2.29E-13 | n/a | 29.6 | 1.52 |
| HYA_0m_072 | 2.5956 | 38.86 | 3.96E-13 | 600 | 2.7501 | 1.91 | 45.1 | 7.42E-13 | n/a | n/a | n/a |
| HYA_0m_073 | 2.5492 | 40 | 2.12E-13 | 400 | 2.6811 | 1.89 | 45.6 | 3.82E-13 | n/a | 24.7 | 1.1 |
| HYA_0m_074 | 2.5405 | 38.77 | 3.45E-13 | n/a | n/a | n/a | n/a | n/a | n/a | n/a | n/a |
| HYA_0m_075 | 2.536 | 40.02 | 2.11E-13 | 400 | 2.6878 | 2.32 | 46.5 | 4.18E-13 | 5.9 | n/a | 0.8 |
| HYA_0m_076 | 2.5992 | 38.34 | 4.27E-13 | 400 | 2.6612 | 1.04 | 41.3 | 6.46E-13 | n/a | n/a | n/a |

*Supplementary Table A.III-3: A summary of the Brazilian disc parameters for as-collected and TT samples.*

| | As-collected | | | Post-thermal treatment | | | |
| --- | --- | --- | --- | --- | --- | --- | --- |
| Sample | Density (g.cm$^{-3}$) | Connected porosity (%) | TT (°C) | Density (g.cm$^{-3}$) | Mass loss (g) | Connected porosity (%) | UTS (MPa) |
| HYA_0m_001_Br | 2.4899 | 31.09 | n/a | n/a | n/a | n/a | 1.53 |
| HYA_0m_002_Br | 2.5139 | 33.67 | n/a | n/a | n/a | n/a | 1.21 |
| HYA_0m_003_Br | 2.4877 | 32.05 | n/a | n/a | n/a | n/a | 1.69 |
| HYA_0m_004_Br | 2.545 | 33.04 | n/a | n/a | n/a | n/a | 1.5 |
| HYA_0m_005_Br | 2.5824 | 32.28 | 130 | 2.6346 | 0.32 | 35.67 | 0.98 |
| HYA_0m_006_Br | 2.5626 | 36.44 | 130 | 2.6214 | 0.39 | 39.95 | 0.96 |
| HYA_0m_007_Br | 2.562 | 38.9 | 130 | 2.6166 | 0.42 | 42.4 | 0.92 |
| HYA_0m_008_Br | 2.5598 | 34.78 | 130 | 2.6157 | 0.36 | 38.41 | 1.07 |
| HYA_0m_009_Br | 2.5453 | 38.07 | 130 | 2.6059 | 0.39 | 41.69 | 0.79 |
| HYA_0m_010_Br | 2.5122 | 37.56 | 185 | 2.5993 | 0.47 | 42.36 | 0.97 |
| HYA_0m_011_Br | 2.6096 | 36.32 | 185 | 2.6402 | 0.33 | 38.99 | 0.82 |
| HYA_0m_012_Br | 2.52 | 41.33 | 185 | 2.6095 | 0.42 | 45.86 | 0.86 |
| HYA_0m_013_Br | 2.524 | 39.53 | 185 | 2.6098 | 0.49 | 43.86 | 0.91 |
| HYA_0m_014_Br | 2.4942 | 36.79 | 185 | 2.5956 | 0.59 | 42.22 | 1 |
| HYA_0m_015_Br | 2.5498 | 36.18 | 400 | 2.7235 | 0.76 | 44.47 | 0.7 |
| HYA_0m_016_Br | 2.568 | 39.51 | 400 | 2.6707 | 0.66 | 45.59 | 0.63 |
| HYA_0m_017_Br | 2.5964 | 35.17 | 400 | 2.707 | 0.66 | 41.5 | 0.68 |
| HYA_0m_018_Br | 2.518 | 40.18 | 400 | 2.6618 | 0.75 | 47.3 | 0.69 |
| HYA_0m_019_Br | 2.5002 | 36.55 | 400 | 2.6419 | 0.82 | 44.19 | 0.8 |
| HYA_0m_020_Br | 2.5171 | 39.02 | 600 | 2.6952 | 0.73 | 46.69 | 0.7 |
| HYA_0m_021_Br | 2.5885 | 35.91 | 600 | 2.776 | 0.79 | 40.97 | 0.66 |
| HYA_0m_022_Br | 2.5028 | 38.59 | 600 | 2.7167 | 0.98 | 48.32 | 0.57 |
| HYA_0m_023_Br | 2.5168 | 38.59 | 600 | 2.717 | 1.01 | 47.64 | 0.66 |
| HYA_0m_024_Br | 2.5295 | 35.99 | 600 | 2.7473 | 0.94 | 46.16 | 0.54 |

## 2. Clay-separated XRD

Clay separated XRD measurements were performed on as-collected, surficial hyaloclastite for unglycolated and glycolated samples. The d(060) peak is at 60.35°, whilst the d(001) peak transitions from 15 Å to 16.2 Å, upon glycolation. Raw X-ray diffractograms are presented in Supplementary Figure A.III-1.
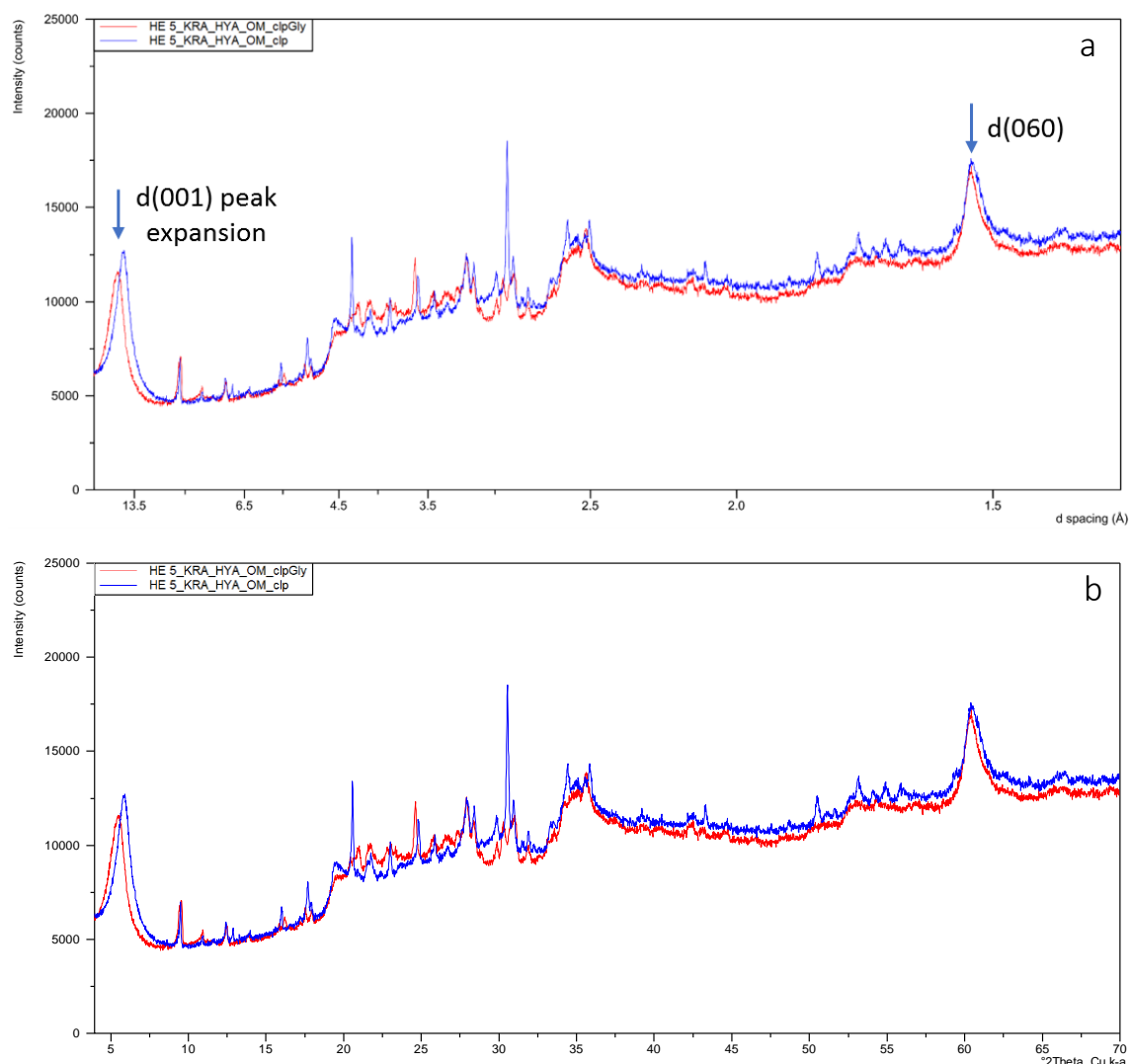


*Supplementary Figure A.III-1: X-ray diffractograms of as-collected, gylcolated and unglycolated surficial hyaloclastite; a. intensity presented against °2Theta Cu k-a; b. intensity presented against angstroms.*

## 3. QEMSCAN Images

We present here the full QEMSCAN images, acquired at 20 μm for as-collected (Supplementary Figure A.III-2) and thermally treated (TT) samples (Supplementary Figure A.III-3 - A.III-6), that are used in the quantification of the mineral distribution Table 4-2.
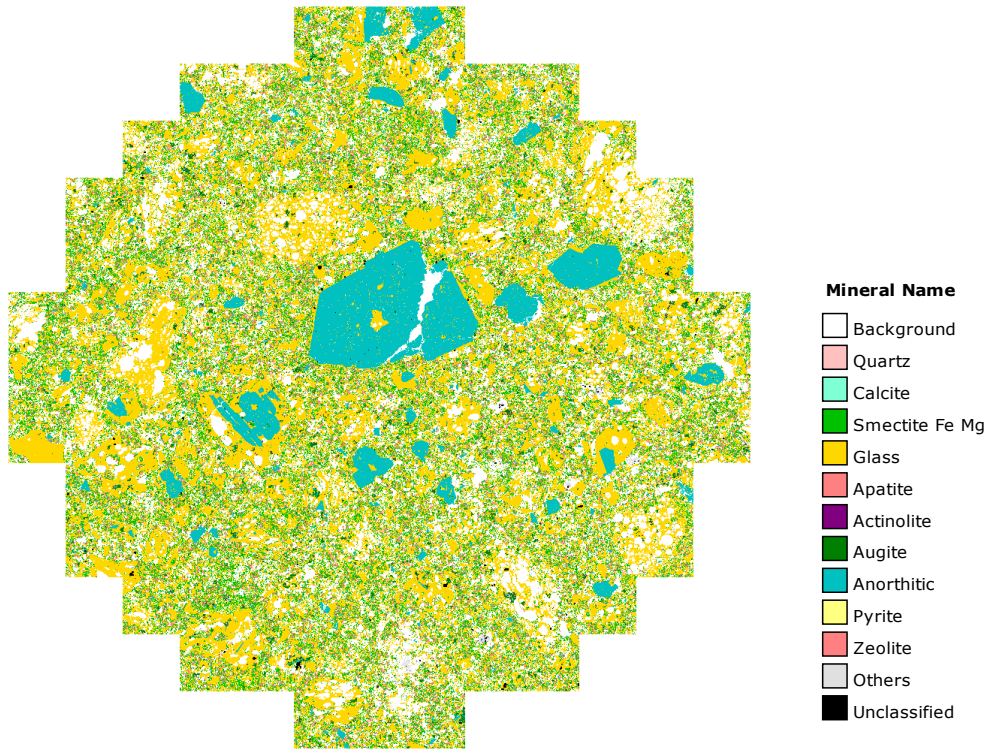
Supplementary Figure A.III-7 provides an annotated example of the various petrographic images presented in Figure 4-3.
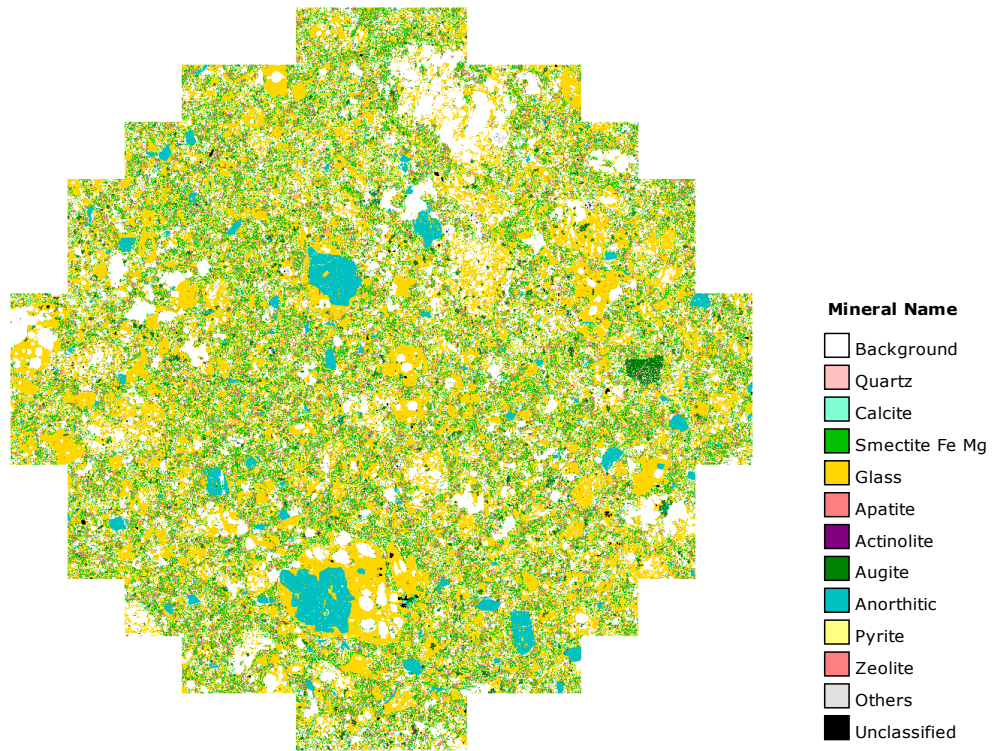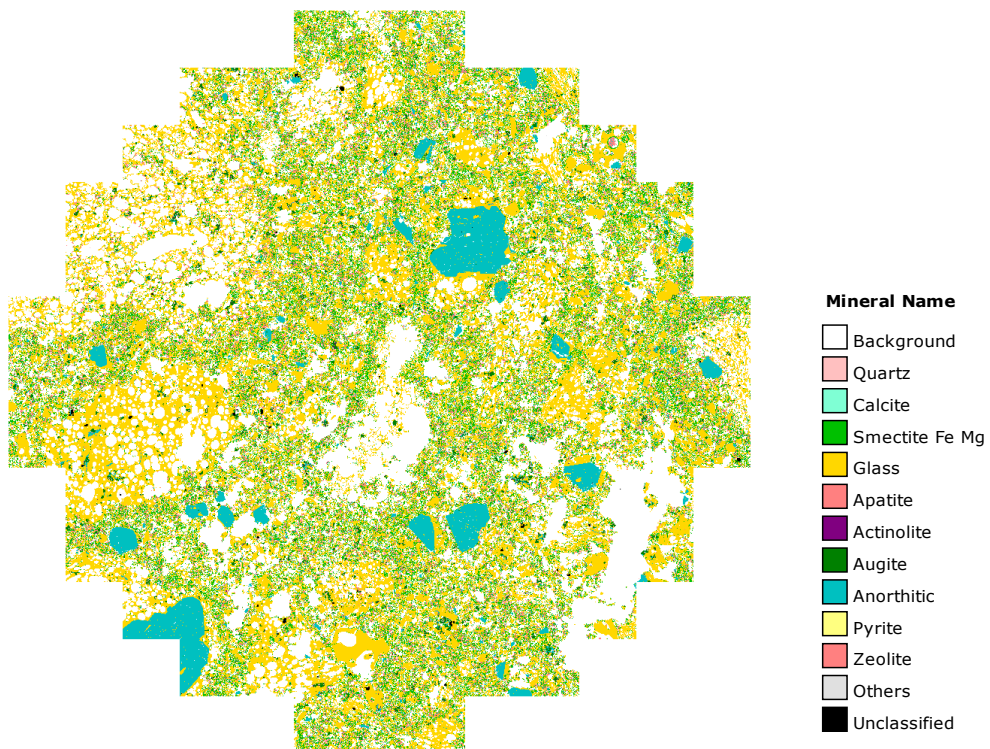


*Supplementary Figure A.III-2: Mineral distribution of as-collected hyaloclastite, acquired using QEMSCAN at 20 μm resolution.*
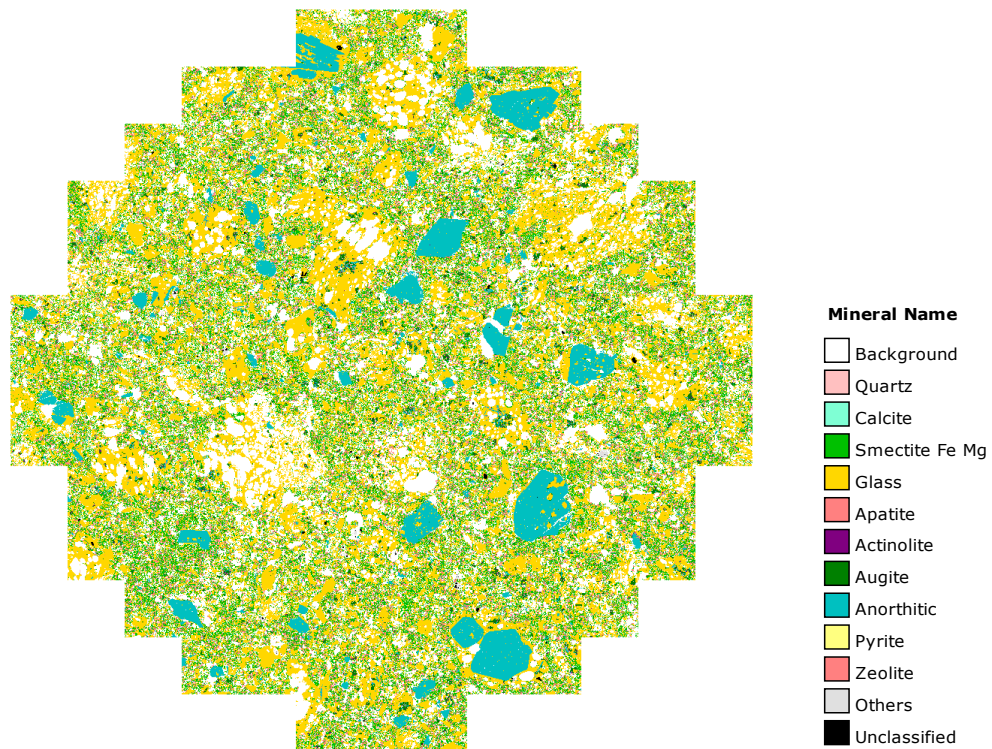
*Supplementary Figure A.III-3: Mineral distribution of hyaloclastite, TT to 130 °C for 12 hours, and acquired using QEMSCAN at 20 μm resolution.*



**Mineral Name**
- Background
- Quartz
- Calcite
- Smectite Fe Mg
- Glass
- Apatite
- Actinolite
- Augite
- Anorthitic
- Pyrite
- Zeolite
- Others
- Unclassified

*Supplementary Figure A.III-4: Mineral distribution of hyaloclastite, TT to 185 °C for 12 hours, and acquired using QEMSCAN at 20 μm resolution.*



**Mineral Name**
- Background
- Quartz
- Calcite
- Smectite Fe Mg
- Glass
- Apatite
- Actinolite
- Augite
- Anorthitic
- Pyrite
- Zeolite
- Others
- Unclassified

*Supplementary Figure A.III-5: Mineral distribution of hyaloclastite, TT to 400 °C for 12 hours, and acquired using QEMSCAN at 20 μm resolution.*
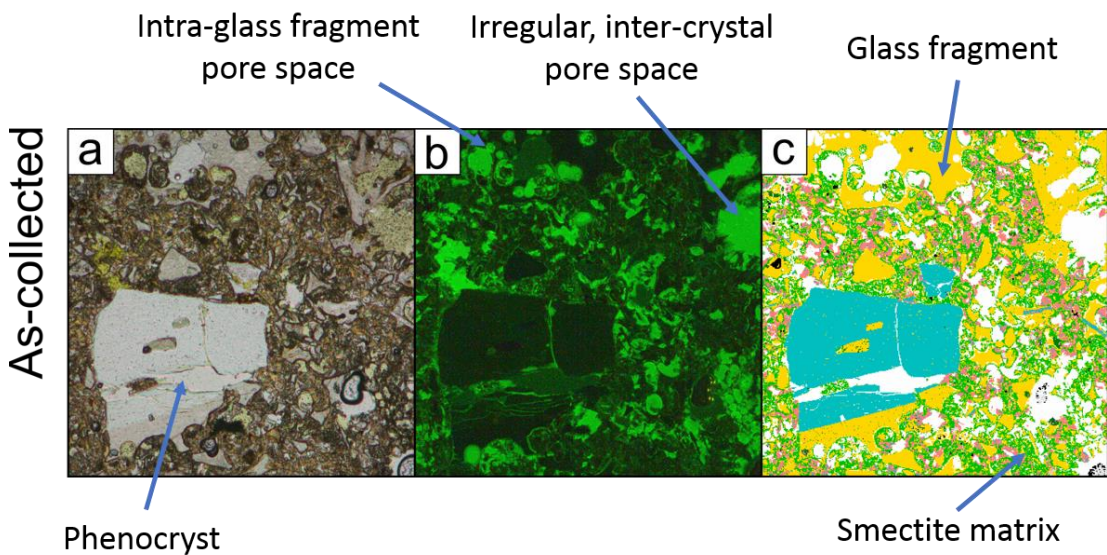


**Mineral Name**
- Background
- Quartz
- Calcite
- Smectite Fe Mg
- Glass
- Apatite
- Actinolite
- Augite
- Anorthitic
- Pyrite
- Zeolite
- Others
- Unclassified

*Supplementary Figure A.III-6: Mineral distribution of hyaloclastite, TT to 600 °C for 12 hours, and acquired using QEMSCAN at 20 μm resolution.*



Intra-glass fragment pore space

Irregular, inter-crystal pore space

Glass fragment

As-collected

Phenocryst

Smectite matrix

*Supplementary Figure A.III-7: Annotated example from Figure 4-3. a. Plain polarised light image from an optical microscope; b. Ultraviolet pore space map using florescent dyed thin section; c. QEMSCAN image showing mineral distribution.*

## 4. Additional Strength Curves

Figure 4-6 presents a subset of the total tensile strength dataset, for easier viewing. Here, we present the other strength curves not shown in the main paper.
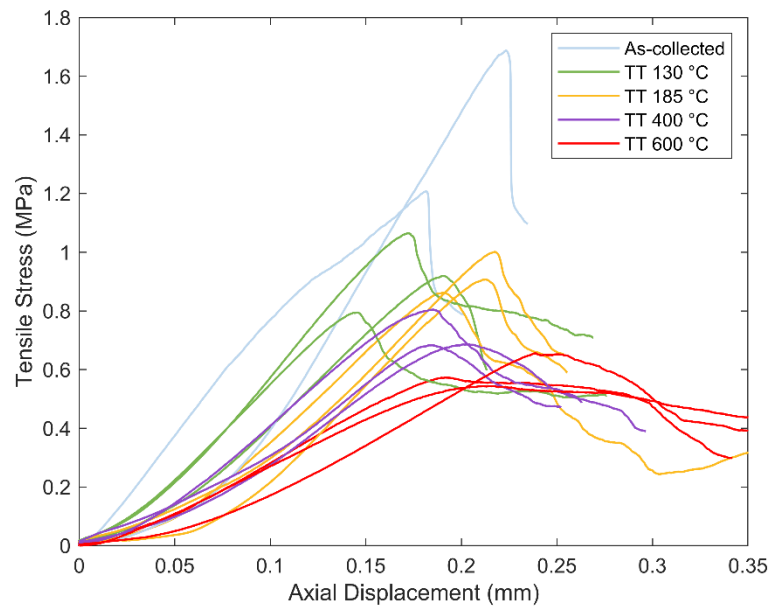


*Supplementary Figure A.III-8: Additional tensile strength curves for as-collected and TT surficial material.*